

PHOTODISSOCIATION STUDIES OF CH₃I AND CF₃I IN FLUID ⁴HELIUM NANODROPLETS

THÈSE N° 2967 (2004)

PRÉSENTÉE À LA FACULTÉ SCIENCES DE BASE

Institut des sciences et ingénierie chimique

SECTION DE CHIMIE ET GÉNIE CHIMIQUE

ÉCOLE POLYTECHNIQUE FÉDÉRALE DE LAUSANNE

POUR L'OBTENTION DU GRADE DE DOCTEUR ÈS SCIENCES

PAR

Andreas BRAUN

Diplom-Physiker, Freie Universität Berlin, Allemagne
et de nationalité allemande

acceptée sur proposition du jury:

Dr M. Drabbels, directeur de thèse
Prof. M. Chergui, rapporteur
Prof. Th. Rizzo, rapporteur
Dr A. Slenczka, rapporteur
Prof. J. Toennies, rapporteur

Lausanne, EPFL
2004

Abstract

A novel experimental apparatus to study the dynamics of photodissociation and photoionization processes in the interior or at the surface of helium droplets by means of imaging techniques has been designed, built and characterized. This molecular beam machine combines a versatile cryogenic cluster source with a cross beam scattering stage to introduce impurities into the droplets and a velocity map imaging instrument as the principal analysis tool. In a first series of experiments we have used this apparatus to examine the 266 nm A band photolysis of CH₃I and CF₃I embedded in liquid ⁴He clusters with selected mean sizes in the range from ≈ 2000 to ≈ 20000 atoms. The *in-situ* creation of photofragments in the droplet interior constitutes an original approach to studying the translational dynamics of neutral microscopic particles in the quantum liquid, which until now were poorly characterized. For all mean droplet sizes under investigation we observe that fragments of every studied species can escape from the droplets. A predominantly thermally driven fragment release clearly is not compatible with the three-dimensional velocity distributions of the products. Accordingly, the vast majority of departing photofragments is thought to escape from the clusters simply by pushing away helium atoms, an escape process which we designate “direct”. It is found that the translational and angular relaxation of the escaping products generally increases both with decreasing fragment mass and increasing mean droplet size. We furthermore show that droplet angular momenta can at most have a minor effect on the measured angular product distributions which therefore are thought to mainly reveal deflections of the fragment trajectories inside the droplets. Accompanying classical Monte Carlo simulations based on independent pairwise hard-sphere scattering can reproduce qualitative and quantitative properties of the observed speed and angular distributions and suggest strongly that binary fragment–helium collisions are at the origin of the translational and angular relaxation of the escaping products. By state-specifically detecting methyl fragments in the vibrational ground and in the first umbrella mode (ν_2) excited state we show that vibrational cooling in the course of the fragment escape is not complete and that the mean relative kinetic energy loss of departing molecular fragments does not depend significantly on the level of vibrational excitation. Departing iodine and CH₃ fragments are found to leave the helium droplets as fragment–He_{*n*} complexes with sizes *n* of up to 15 and more helium atoms. These partially solvated fragments exhibit characteristic droplet frame speeds that strongly correlate with the complex size *n*: Larger structures escape with lower speeds from the helium clusters. The velocity map images of size-selected IHe_{*n*} products show furthermore that the characteristic complex speeds depend little on the initial kinetic energy of the nascent iodine fragments or on the helium droplet size. Instead, the variation of the latter parameters is shown to profoundly affect the size distribution of the escaping IHe_{*n*} products. We present evidence that these complexes build up already in the droplet interior and argue that their formation should be regarded as the dynamical development of helium solvation shells around the translationally relaxing radicals. It is proposed that both the speed of a moving fragment relative to the helium bath and the strength of the fragment–He interaction determine the instantaneous size of a forming complex structure to a good degree of approximation. By velocity mapping bare parent molecules we furthermore demonstrate the occurrence of CH₃–I fragment recombination in helium droplets with mean sizes of more than ≈ 3000 atoms. The (CH₃I)⁺ ion signal appears with a time constant of ≈ 5 ns and shows a finite kinetic energy

release which is thought to arise from a complete evaporation of the solvent atoms as a result of the internal cooling of the recombined molecules. For CF_3I no recombination signal is observed. This effect is attributed to the different fragment masses and the dissimilar partitioning of the total kinetic energy in the CF_3I photolysis reaction.

Version Abrégée

Un nouveau dispositif expérimental a été conçu, construit et caractérisé afin d'étudier, par des méthodes d'imagerie, la dynamique des processus de photodissociation et de photo-ionisation à l'intérieur ou en surface de gouttelettes d'hélium. Notre appareil à jet moléculaire comprend une source cryogénique polyvalente permettant la formation d'agrégats d'hélium, une chambre de dopage des gouttelettes d'hélium équipée d'un jet croisé, et, comme outil principal d'analyse, un instrument d'imagerie des champs de vitesse. Cet appareil a été utilisé, dans une première série d'expériences, pour l'étude de la photolyse (par excitation à 266 nm de la bande A d'absorption) de CH_3I et CF_3I incorporés dans les agrégats de ^4He liquide, de tailles moyennes choisies entre ≈ 2000 et ≈ 20000 atomes. La création *in situ* de photofragments à l'intérieur de gouttelettes constitue une approche originale dans l'étude de la dynamique translationnelle de particules microscopiques neutres dans ce fluide quantique, peu caractérisée jusqu'à présent. Pour les molécules étudiées, on a observé que tous les fragments formés s'échappent des gouttelettes, quelle que soit la taille moyenne de ces dernières. Un processus de libération des fragments essentiellement sous contrôle thermique est en contradiction avec la distribution tridimensionnelle des vecteurs vitesse obtenue pour les produits. Une hypothèse plus probable est que les photofragments se fraient un chemin hors des gouttelettes en repoussant les atomes d'hélium, processus que l'on définit comme "direct". En outre, on a observé une relaxation translationnelle et angulaire des produits issus des gouttelettes plus importante pour des fragments de faible masse, de même que pour des gouttelettes de plus grande taille. Nous avons montré par ailleurs que le moment angulaire des gouttelettes ne peut avoir qu'un effet mineur sur les distributions angulaires mesurées des produits, ces dernières révélant principalement des déviations de trajectoire des fragments à l'intérieur des gouttelettes. Des calculs de simulation classique Monte Carlo, reposant sur le modèle de collision de noyaux durs à deux corps, sont en mesure de reproduire les propriétés qualitatives et quantitatives des distributions angulaires et de vitesses observées expérimentalement, suggérant ainsi que les collisions individuelles entre fragments et atomes d'hélium sont à l'origine de la relaxation translationnelle et angulaire des produits sortant des gouttelettes. La détection état-spécifique des fragments méthyle dans l'état vibrationnel fondamental et dans le premier état excité du mode parapluie (ν_2) nous a permis de montrer que la relaxation vibrationnelle au cours de l'émergence des fragments est inachevée et que la perte relative moyenne d'énergie cinétique des fragments moléculaires ne dépend pas de façon significative du niveau d'excitation vibrationnelle. Les fragments iode et méthyle quittent les gouttelettes d'hélium sous la forme de complexes d'hélium (fragment- He_n) dont la taille varie jusqu'à $n = 15$ atomes d'hélium, voire plus. Ces fragments partiellement solvatés présentent des vitesses caractéristiques, dans le référentiel des gouttelettes, fortement corrélées à la taille n du complexe: les plus grands complexes s'échappent des gouttelettes d'hélium avec des vitesses plus faibles. Les cartes de vitesses des produits IHe_n sélectionnés par taille montrent que les vitesses caractéristiques dépendent peu de la taille de la gouttelette d'hélium ou de l'énergie cinétique initiale des fragments d'iode. Par contre, la variation de ces paramètres semble affecter profondément la distribution de tailles des produits IHe_n issus des gouttelettes. Nous avons démontré que ces agrégats se forment déjà à l'intérieur de la gouttelette, et proposons un processus de formation fondé sur le développement dynamique de couches de solvation d'hélium autour de radicaux en relaxation translationnelle. Il apparaît ainsi que la vitesse du

fragment en mouvement par rapport au bain d'hélium et la force d'interaction fragment-hélium déterminent, dans une bonne approximation, la taille instantanée du complexe naissant. Par ailleurs, les cartes de vitesses des molécules parentes dénuées de solvant, nous ont permis de mettre en évidence la recombinaison des fragments CH_3 et I dans des gouttelettes d'hélium de taille moyenne supérieure à ≈ 3000 atomes. En effet, le signal de l'ion $(\text{CH}_3\text{I})^+$ apparaît avec une constante de temps de l'ordre de ≈ 5 ns et possède une énergie cinétique non nulle, ce qui est vraisemblablement dû à l'évaporation complète des atomes de solvant résultant de la relaxation interne des molécules recombinaison. Aucune recombinaison n'a cependant été observée pour CF_3I , ce qui s'explique probablement par la différence de masse des fragments et de la distribution inégale de l'énergie cinétique totale au cours de la réaction de photolyse de CF_3I .

Contents

1	Introduction	1
2	Concepts	13
2.1	The making of helium droplet beams	13
2.2	Evaporative cooling	16
2.3	Droplet sizes	20
2.4	Capture of foreign atoms and molecules	23
2.4.1	Cross sections	23
2.4.2	Poisson distributions	26
2.4.3	Evaporation of helium atoms subsequent to a pick-up process	32
2.5	Photodissociation of CF_3I and CH_3I in the gas phase	34
2.5.1	Introduction	34
2.5.2	Photodissociation in the A band	35
3	Experimental Setup	43
3.1	Droplet Beam Apparatus	43
3.2	Geometry and fluxes of the droplet beam	47
3.3	Cluster Source	51
3.3.1	Construction	51
3.3.2	Heat loads	57
3.3.3	Stagnation temperature	60
3.3.4	Performance	62
3.4	Cross beam doping	63
3.4.1	Introduction	63
3.4.2	Setup	65
3.4.3	Calibration	65
3.5	Ion Imaging	70
3.5.1	Introduction	70
3.5.2	Conventional ion imaging	71
3.5.3	Velocity map imaging	73
3.5.4	Image magnification by an einzel lens	74
3.5.5	Properties	75
3.5.6	Setup	75

3.5.7	Data analysis	77
3.5.8	Calibration	79
3.5.9	Observable kinetic energies	85
3.6	Lasers	85
3.6.1	Photolysis	86
3.6.2	Ionization	86
3.7	Electronics	87
3.7.1	Imaging experiments	87
3.7.2	Time-of-flight measurements	89
4	Photodissociation in ^4He droplets	91
4.1	Introduction	91
4.2	Iodine fragments	95
4.2.1	Time-of-flight mass spectra	95
4.2.2	Imaging the IHe_n product complexes	101
4.2.3	Discussion	115
4.2.3.1	Escape process	115
4.2.3.2	A possible model	119
4.2.3.3	Complex formation	119
4.3	Alkyl fragments	123
4.3.1	The CF_3 radical	123
4.3.2	The CH_3 radical	128
4.3.3	Discussion	135
4.3.3.1	Escape process	135
4.4	Discussion: iodine and alkyl fragments	137
4.4.1	Angular broadening	137
4.4.2	The role of the fragment mass	138
4.4.3	Mean total kinetic energy transfer	139
4.4.4	Complex formation	140
4.5	Recombination	142
4.5.1	Droplet size effects	144
4.5.2	Time dependence	149
4.5.3	Discussion	152
4.6	Simulations	155
4.6.1	The model	156
4.6.2	Results	158
4.6.3	Discussion	161
4.7	Other experimental results	163
4.7.1	Droplet beam speed	163
4.7.2	Background reduction	163
5	Summary and Outlook	167
5.1	Summary	167
5.2	Outlook	170

A	Properties of the log-normal distribution	175
B	Abel inversion	177
C	Pick-up induced droplet angular momenta	183
D	Modeling fragment motion in helium droplets	187
	D.1 Viscous flow	187
	D.2 Elastic hard-sphere collisions	188
	List of figures	191
	List of tables	197
	List of abbreviations	199
	Bibliography	201

Chapter 1

Introduction

The two stable isotopes of helium, ${}^4\text{He}$ and ${}^3\text{He}$, are in many respects unique among the chemical elements. Most remarkably, they do not exhibit a triple point and, accordingly, remain liquid under their saturated vapor pressure down to the lowest temperatures. This reluctance to solidify is a result of both the extremely weak He–He interactions and the small mass of the helium atoms. The latter aspect causes a high zero-point energy which dominates the total energy of the system at the low atomic volumes associated with a solid lattice.¹ Consequently, a low-density liquid becomes energetically favorable while solidification is effectively impeded unless considerable external pressures in excess of 25 bar are applied. The extraordinarily weak van der Waals interactions between the atoms furthermore cause the two helium isotopes to have the lowest boiling points of all substances, that is 4.21 K for ${}^4\text{He}$ and 3.19 K for ${}^3\text{He}$.² At temperatures immediately below these values, both ${}^4\text{He}$ and ${}^3\text{He}$ behave to a good degree of approximation as ordinary liquids with small but finite viscosities. When the temperature is lowered further, however, liquid ${}^4\text{He}$ and liquid ${}^3\text{He}$ reveal fundamentally different characteristics that can be linked to the dissimilar quantum statistics governing the two isotopes. Around 2.18 K and under its saturated vapor pressure, the bosonic ${}^4\text{He}$ liquid undergoes a phase transition from the normal (He I) into a superfluid (He II) state, which is not shared by the fermionic ${}^3\text{He}$. This unique phase transition is believed to be directly related to Bose-Einstein condensation and causes many properties of the liquid to change abruptly. The specific heat, for instance, exhibits a characteristic anomaly (see Figure 1.1), the shape of which led to the term “ λ -point” to denote the transition temperature. The fascinating properties of bulk He II include an exceptionally high heat conductivity, a vanishing viscosity for the flow through fine capillaries, and a new type of heat propagation known as “second sound”. In contrast to ${}^4\text{He}$, no similar phase transition is observed for the ${}^3\text{He}$ isotope unless the temperature of the liquid is lowered to three orders of magnitude below the boiling point. Here, at temperatures around 2.6 mK, a transition to a superfluid phase occurs, which is thought to arise due to the formation of bosonic ${}^3\text{He}$ pairs, analogous to Cooper pairs of electrons in a superconducting solid.³

Many macroscopic thermodynamic and hydrodynamic properties of bulk He II can be explained in terms of a so-called “two-fluid model” as first suggested by Tisza.⁴ The equations of motion were developed later on by Landau^{5,6} in the context of quantum hydrodynamics. The model is based on the assumption that He II behaves *as if* it were a mixture of a *normal*,

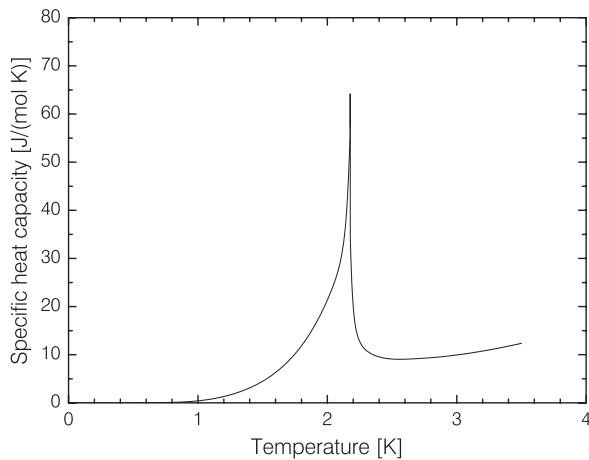


FIGURE 1.1: Specific heat capacity of liquid ${}^4\text{He}$ as a function of temperature at saturated vapor pressure. The curve illustrates the anomaly associated with the phase transition to the superfluid state around $T_\lambda \approx 2.18$ K. The graph is based on the recommended values from reference [8].

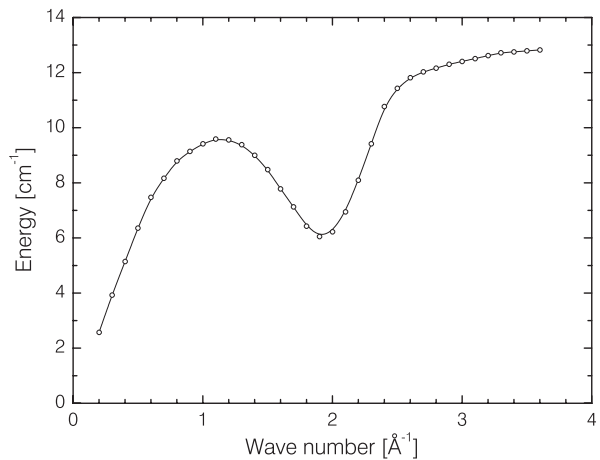


FIGURE 1.2: Dispersion curve of bulk He II at a temperature of 1.1 K and under its saturated vapor pressure as measured by neutron scattering experiments. The displayed data is taken from reference [9].

viscous fluid with density ϱ_n and a *superfluid*^a with density ϱ_s , the latter capable of frictionless flow and carrying zero entropy. The two mass densities ϱ_n and ϱ_s are functions of temperature and obey

$$\varrho_{\text{bulk}} = \varrho_n + \varrho_s, \quad (1.1)$$

where ϱ_{bulk} denotes the real mass density of bulk He II. The normal density ϱ_n is zero at absolute zero and increases to the value ϱ_{bulk} at the λ -point. By assigning an individual local velocity, \mathbf{v}_n and \mathbf{v}_s , to each of its physically inseparable components, the bulk liquid is formally allowed to carry out two different motions at the same time. Accordingly, the mass flux density \mathbf{j} may be written as

$$\mathbf{j} = \varrho_n \mathbf{v}_n + \varrho_s \mathbf{v}_s. \quad (1.2)$$

The superfluid fraction is assumed to be free of turbulence and therefore must exhibit irrotational flow with its velocity \mathbf{v}_s obeying

$$\text{curl } \mathbf{v}_s = 0, \quad (1.3)$$

which, together with equations (1.1) and (1.2), is an element of the complete set of equations constituting the two-fluid model. The soundness of the model assumptions was confirmed in 1946 in an elegant experiment by Andronikashvili.⁷ Monitoring the period of a multiple-disk torsional oscillator immersed in liquid ${}^4\text{He}$ he observed a decrease of the oscillator's moment of inertia as the temperature of the bath was reduced below the λ -point. In agreement with the two-fluid model this result could be interpreted assuming that the superfluid fraction remains

^aNote the ambiguous meaning of the term “superfluid”. In the context of the two-fluid model it refers to the superfluid fraction only, whereas elsewhere it is used to designate the whole He II liquid.

stationary and does not couple by viscous forces to the oscillatory motion of the disks. The normal fluid fraction $\varrho_n/\varrho_{\text{bulk}}$ derived from these experiments decreases sharply below the λ -point and becomes smaller than $\approx 10\%$ at temperatures lower than 1.4 K. Further phenomena the two-fluid model can successfully account for include the (inverse) fountain effect and the various sound modes in He II, a documentation of which can be found in references [2, 3].

The understanding of helium II on a microscopic level is closely related to the spectrum of elementary excitations in the superfluid. The dispersion curve for these excitations was first measured comprehensively in 1960 by Henshaw and Woods¹⁰ using inelastic neutron scattering and is shown in Figure 1.2. The experimentally found shape fully confirmed the brilliant theoretical predictions made by Landau^{5,6} more than a decade earlier. At small wave numbers k and low energies ε the only excitations are phonons that approximately follow a linear relation $\varepsilon = c \cdot \hbar k$, with c as the speed of sound. One of the most remarkable features of the dispersion curve is however the local minimum at wave numbers around 1.9 \AA^{-1} which is attributed to excitations known as rotons. As pointed out by Landau,⁵ a finite critical flow velocity, termed v_L , below which no elementary excitations can be generated, is essential for the occurrence of superfluidity. Since only relative velocities between the liquid and its surroundings are of relevance here, it is instructive to consider an object much heavier than a ^4He atom, traveling with speed v through motionless helium II. Based on the energy and momentum conservation laws it can easily be shown¹¹ that such an object can only create an excitation of energy ε and momentum $\hbar k$ if the condition

$$v \geq \frac{\varepsilon}{\hbar k} \quad (1.4)$$

is fulfilled. The peculiar shape of the dispersion curve of the elementary excitations in He II ensures that the lowest values of the ratio $\varepsilon/(\hbar k)$ occur in the vicinity of the roton minimum. Taking the corresponding momentum $k = 1.95 \text{ \AA}^{-1}$ and energy $\varepsilon = 6.008 \text{ cm}^{-1}$ from the recommended values in reference [8] one finds a critical velocity

$$v_L \approx 58 \text{ m/s} \quad (1.5)$$

for bulk He II at saturated vapor pressure. Note that the shape of the dispersion curve changes slightly with pressure. As a consequence, the critical velocity is smaller for higher pressures and reaches a value of $v_L = 46 \text{ m/s}$ at a pressure of 25 bar.¹¹ Below this relative velocity the object's motion thus is predicted to be frictionless as the dissipation of kinetic energy via the creation of elementary excitations is forbidden. Initial attempts to experimentally confirm Landau's critical velocity in superfluid helium were based on monitoring the helium flow in confined geometries or on measuring the drag on positive or negative helium ions moved through stationary He II with the aid of electric fields. These early experiments were, however, impaired by the creation of quantized vortices in the liquid that led to critical velocities substantially lower than the predicted values. In the late 1970s Allum *et al.*¹¹ demonstrated that the generation of vortices by the motion of negative ions can be suppressed if high pressures close to the solidification limit are applied. Under such conditions excess electrons in He II, which in fact are "bubble" structures with a large hydrodynamic mass about 240 times the mass of a single ^4He atom,^{12,13} are indeed found to drift freely through the medium unless velocities of the order of 50 m/s are reached. This direct measurement of the critical velocity is illustrated in Figure 1.3. For

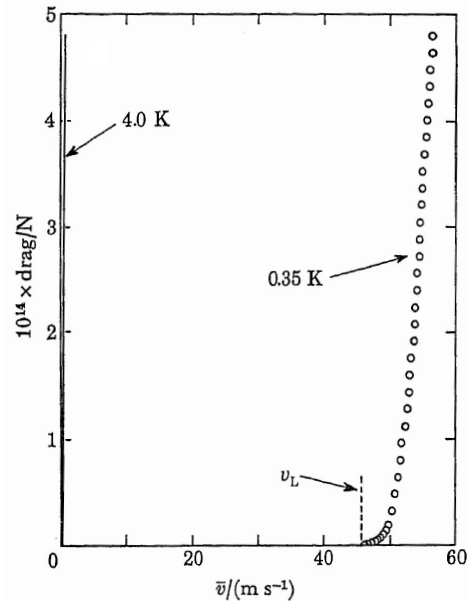


FIGURE 1.3: Drag force on intrinsic negative ions moving through highly pressurized He II kept at a temperature of 0.35 K as a function of the ions' mean speed \bar{v} (circles). The drag forces observed in an analogous experiment in non-superfluid ^4He at 4.0 K are given for comparison (solid line). The onset of drag in the superfluid coincides with the critical velocity v_L predicted by Landau (see text). The graph is reproduced from reference [11].

comparison, the figure also shows the result of a drift experiment carried out in non-superfluid ^4He above the λ -point, where viscous drag is apparent even at the lowest relative speeds.

The spectroscopic interrogation of foreign species immersed into the bulk constitutes an alternative and powerful means to probe the microscopic properties of the He I or He II quantum liquids.¹⁴ The implantation of extrinsic impurities into bulk liquid ^4He is, however, associated with substantial experimental complications, mainly since solvated atoms or molecules tend to aggregate to larger structures that preferentially bind to the container walls.¹⁵ Over the last years, however, several new techniques to efficiently introduce metal atoms and ions into the bulk liquid have emerged. With these methods, which include the condensation of atomic or ionic beams in liquid ^4He as well as the laser ablation directly in the bulk interior,¹⁶ relatively high monomer concentrations above 10^8 cm^{-3} could be achieved. A very recent development is the injection of impurities by colliding doped helium clusters with the surface of the bulk liquid.¹⁷ However, to the best of our knowledge, no techniques to produce considerable concentrations of molecular monomers in bulk liquid helium have been reported yet.

Helium droplets

Many of the difficulties connected to the poor solubility of foreign species in the bulk liquid can be overcome using finite size helium clusters as a solvent. These clusters can easily be produced in jet expansions and, depending on the expansion conditions, have typical mean

sizes of 10^3 to 10^8 atoms (see Section 2.1). The internal pressures of those clusters is with less than 2 bar^{18,19} considerably lower than the solidification pressure of about 25 bar, which makes helium the only substance whose clusters are definitely liquid. Consequently, clusters of helium atoms are commonly referred to as “droplets”. Free helium droplets cool by evaporation of atoms from their surface and reach temperatures of about 0.4 K in case of ^4He , and 0.15 K in case of ^3He clusters (see Section 2.2). Whereas ^4He droplets thus exist at temperatures below the λ -point and, as we will point out below, have been demonstrated to exhibit superfluid behaviour, ^3He droplets are definitely too warm to become superfluid. Assuming a spherical shape and bulk densities the radius R of a helium droplet composed of N atoms can be estimated from

$$R = r_0 \cdot N^{\frac{1}{3}}, \quad (1.6)$$

where r_0 , the so-called unit radius, equals 2.22 Å for ^4He and 2.44 Å for ^3He .¹⁸ Helium clusters thus have typical diameters ranging from a few to some hundred nanometers. These cold “nanodroplets” have the advantage of readily capturing atomic or molecular impurities from the gas phase via inelastic collisions (see Section 2.4). Compared to the bulk liquids, the immersion of foreign species, e.g. as an indirect probe of quantum statistical phenomena, thus is largely facilitated. As finite systems, helium droplets also offer the unique possibility to study how these phenomena vary as a function of cluster size at a nanoscale level and therefore have attracted a high degree of fundamental interest from both experimentalists and theoreticians in recent years. Since virtually any impurity can easily be trapped inside or on the surface of helium droplets, they may also serve as a powerful tool to assemble and stabilize weakly bound species, or to perform high-resolution spectroscopic experiments on large molecules or clusters that otherwise can not be cooled to such low temperatures. The large and rapidly expanding body of literature has been reviewed regularly with a focus on experimental^{20–24} as well as theoretical^{25–33} studies, and shows the great interest of both the physics and the chemistry community in these highly quantum van der Waals clusters. In order to put this thesis in the context of past and ongoing work by other groups we give a brief summary of relevant experimental and theoretical studies in the following paragraph.

The first experimental record of helium droplets dates back to 1908 and is attributed to H. Kamerlingh Onnes. In the course of the initial attempts to liquefy the rare gas in Leiden he observed a “dense gray cloud [...] resembling partly cotton wool” in an expansion of cold, gaseous helium.³⁴ This observation was, however, quickly followed by his discovery of liquid helium only three months later.³⁵ Subsequent research consequently focused on the properties of bulk ^4He , the superfluid state of which was found in 1938 by Allen, Misener and Kapitza.^{36,37}

New interest in helium clusters emerged when, owing to the pioneering work of Becker and coworkers, molecular beams of atomic and molecular clusters became available in the late 1950s.^{38,39} In 1959, at a time when the experimental apparatus to create helium clusters was not yet operational, Becker proposed that ^4He droplets could be used to examine how superfluidity scales with cluster size.^{40,41} He suggested that superfluid behaviour might be observed by scattering atoms from pure ^4He quantum clusters and thus laid the foundations for experiments on the translational motion of foreign neutral species in helium droplets. Following improvements of their source setup^{39,42} Becker and coworkers eventually produced the first beam of ^4He clusters in 1961.⁴³ In the 1970s and 80s, Becker, Gspann and coworkers carried out a

series of crossed beam experiments in order to elucidate the interaction of impinging atomic and molecular species with helium clusters.^{44–49} As part of their efforts to verify suspected signatures of superfluidity in ^4He clusters, the first beam of ^3He droplets was generated in 1977.⁴⁵ It was shown that large droplets of 10^4 to 10^8 atoms can be deflected by multiple collisions with atomic or molecular beams.^{46,48} Drag coefficients derived from these measurements indicated an incomplete momentum transfer from the impinging particles to both ^4He and ^3He droplets, a phenomenon which henceforth became known as droplet “momentum transparency”.^{49,50} However, no conclusive evidence for superfluidity in ^4He clusters was obtained in these experiments.

Mass-spectrometric studies of small and pure helium clusters were first undertaken in 1975 by van Deursen and Reuss,⁵¹ followed some years later by Stephens and King.⁵² The latter authors found enhanced ion stability, *i.e.* “magic numbers”, of 7, 10, 14 and 30 for both ^4He and ^3He cluster cations. Electron-impact studies on larger clusters led to the discovery of electronically metastable neutral droplets of either isotope by Gspann.^{48,53}

An important breakthrough was made when in 1990 the Toennies group in Göttingen reported the first conclusive evidence that helium clusters readily capture foreign particles. Similar to solid argon clusters, for which the effect was demonstrated by Scoles and coworkers in 1985,⁵⁴ doped helium droplets can be formed by passing the pure clusters through a low-pressure ($\approx 10^{-5}$ mbar) scattering cell or, alternatively, a crossing molecular beam. Using electron impact mass-spectrometry Toennies and coworkers not only showed that both atomic and molecular guest species can be introduced effortlessly this way,^{55–57} but also that the aggregation of impurities to subclusters inside the droplets can be controlled in a quantitative manner.¹⁹

The significance of doped helium droplets as a model system for investigating finite-size quantum statistical behaviour grew tremendously when the Scoles group in Princeton successfully carried out the first spectroscopic experiment on a dissolved impurity in 1992. Using line-tunable N_2O and CO_2 lasers they measured the infrared absorption of both SF_6 and $(\text{SF}_6)_2$ in the spectral region of the ν_3 fundamental transition of SF_6 .^{58–60} Absorption was detected by measuring the attenuation of the droplet beam in the forward direction (“beam depletion spectroscopy”). This method relies on non-radiative transfer of energy from the optically excited impurity to the solvent, causing evaporation of helium atoms and, consequently, a reduction in cluster size. The latter effect can then easily be detected using mass-spectrometric or bolometric techniques.

A few years afterwards the Toennies group recorded the first high resolution spectra of the same infrared transition for SF_6 in pure ^4He ^{61,62} and mixed $^4\text{He}/^3\text{He}$ clusters⁶³ using continuously tunable diode lasers. These measurements revealed the presence of a rotational fine structure with an unexpectedly narrow linewidth of only ≈ 300 MHz for the pure ^4He droplets.⁶² In the mixed clusters the helium isotopes segregate spatially, since the heavier ^4He atoms, associated with lower zero-point energy, bind more strongly to themselves and to any dissolved impurity than the ^3He isotope. Therefore, a doped ^4He subcluster is expected to form inside,^{64,65} while the outer ^3He layer determines the temperature of the entire system by evaporation from its surface. In each case, the rovibrational Hamiltonian of the free molecule was found to provide an excellent fit to the experimental spectrum, indicating that the solvation in liquid ^4He does not alter the symmetry of the rotor. Moreover, the analysis of the relative

intensities of the rotational lines provided a direct measure of the droplet temperatures. With 0.38 ± 0.01 K for ^4He and 0.15 ± 0.01 K for low-purity ^3He droplets,⁶³ the experimentally found temperatures were in good agreement with earlier predictions.^{66,67} The rotational constant extracted from the spectra were, however, about a factor of 2.7 lower than in the gas phase,^{62,63} which initially was explained by the rigid attachment of a limited number of ^4He atoms to the rotating molecule.⁶² The nearly free rotation of the molecule was taken as a indication of superfluidity in the finite-size droplets, although it was not fully clear at the time whether this phenomenon might simply be a consequence of the extremely weak solute–solvent van der Waals interaction. Most importantly, however, these experiments established helium droplets as a supremely cold and gentle matrix for high-resolution spectroscopic studies on individually solvated molecules.⁶⁸ In contrast to the more traditional solid cryogenic hosts, e.g. rare gas matrices, inhomogeneous line broadening due to different local binding sites does not occur in liquid helium. This technique, termed “helium nanodroplet isolation spectroscopy” (HENDI) thus opened up new possibilities to carry out high-resolution spectroscopic measurements, particularly on unstable species or on large, biologically relevant molecules.

The first conclusive experimental evidence of superfluidity in ^4He droplets came from electronic spectroscopy. The spectrum of the $S_1 \leftarrow S_0$ transition of glyoxal ($\text{C}_2\text{H}_2\text{O}_2$) in pure ^4He droplets was found to contain a phonon wing, the shape of which could be attributed to the unique elementary phonon and roton excitations in superfluid He II.⁶⁹ In particular, the zero-phonon line, arising from the purely electronic 0_0^0 transition, is separated from the maximum in the phonon wing by a well-defined gap which corresponds approximately to the roton energy of about 6 cm^{-1} in He II. Since the occurrence of a roton minimum in the dispersion curve is intimately related to the superfluid state of ^4He , the characteristic shape of the vibronic spectrum was identified as a signature of superfluidity in the finite size droplets. This interpretation was substantiated by recent measurements on glyoxal embedded in pure ^3He clusters.^{21,22} At a temperature of 0.15 K ^3He is known to behave similar to a normal fluid with a broad particle-hole excitation branch. Solvation in liquid ^3He should therefore not give rise to a gap in the vibronic spectrum, which was fully confirmed by the experiments. Moreover, the roton gap was experimentally shown to reappear once on average about 120 ^4He atoms, predicted to localize around the impurity, were added to the ^3He droplets. This result agrees well with a large number of calculations that, based on manifestations such as the specific heat anomaly^{25,70} or the dispersion curve,^{26,30,71–74} predict superfluid behaviour to occur for ^4He clusters containing more than about 10^2 atoms.

In 1998 Grebenev *et al.*⁷⁵ carried out a beautiful experiment which unambiguously showed that the free rotations of molecules in ^4He droplets can indeed be regarded as a microscopic manifestation of superfluidity. Using OCS as a dopant molecule they demonstrated that the sharp rotational lines characterizing the rovibrational spectrum in pure ^4He clusters collapse to a broad peak in pure ^3He droplets, thereby indicating normal fluid behaviour. Subsequently, a few ^4He atoms were gradually added to the doped ^3He droplets, similar to the experiment on glyoxal described above. Upon the insertion of on average 60 ^4He atoms, corresponding to roughly two ^4He solvation shells, narrow rotational lines emerged again. This was taken as evidence that the local superfluid environment involves the innermost solvation shell closest to the impurity, into which no ^3He atom can infiltrate.⁷⁵ Similar to the SF_6 , the measurements on OCS in ^4He yielded a rotational constant a factor of 2.8 smaller than for the free molecule.^{75,76}

Due to the association of superfluidity with unhindered rotational motion, this experiment became known as the microscopic version of the famous Andronikashvili experiment.⁷

In the few years since the first publication of a high-resolution spectrum of an impurity embedded in helium clusters, a large number of rotationally resolved infrared spectra of various molecular solutes have been measured (for a recent overview see e.g. references [32, 77]). In each case, the spectrum could be described by a free rotor Hamiltonian with rotational constants B equal to or smaller than the corresponding gas phase values B_0 . Generally, the rotational constants of light molecules with relatively large values of B_0 are found to change only slightly upon solvation, *i.e.* $B \approx B_0$. Typical examples are HF⁷⁸ or H₂O⁷⁹ which virtually conserve the vacuum rotational constants in the interior of ⁴He droplets. Heavier molecules with small B_0 , such as SF₆,^{63,80} OCS,⁷⁶ or propyne (HCCCH₃)⁸¹ are found to have rotational constants B as low as $\approx 25\%$ of the vacuum value. While other spectral features such as the line shifts with respect to the spectra of the free molecules, the shape of the rovibrational lines⁸² and the centrifugal distortion constants⁸³ have also been examined theoretically, the solute dependent ratio B/B_0 has received by far the highest interest. Aside the originally proposed simplistic picture of rigidly attached helium atoms,⁶² essentially two different models have been put forward to explain the increased moment of inertia of the solvated molecule.

The first model has been developed by Lehmann and coworkers^{84,85} in Princeton and is based on classical continuum hydrodynamics. In this description, the anisotropic ground state helium density is assumed to adiabatically follow the classical rotation of the solute and thus appears stationary in the molecular frame. In the laboratory frame, however, the density is time-dependent and drives the helium flow which is treated as fully superfluid, *i.e.* inviscid and irrotational. Accordingly, the solution to this problem may be given in form a scalar velocity potential ϕ from which the hydrodynamic contribution to the solvent's moment of inertia can be derived. With the aid of this model many experimentally found rotational constants of linear or rod-like molecules in liquid helium could be roughly reproduced. Nevertheless, it remains highly uncertain whether continuum hydrodynamics can provide a good microscopic description of the system, particularly with respect to the atomic-scale quantum solvation structure nearest to the impurity. Moreover, this so-called "superfluid hydrodynamic model" neglects the reduction of the superfluid density near the impurity, an effect that is well known from "healing length" measurements on solid substrates.^{86,87}

A more complex microscopic picture emerged from the theoretical simulations performed by the group of Whaley in Berkeley.^{32,88} Using $T = 0$ K diffusion Monte Carlo (DMC) methods they demonstrated that the unhindered molecular rotations in the ⁴He droplets are due to an inefficient transfer of angular momentum from the solute to the solvent. Complementary finite temperature path integral Monte Carlo calculations indicated that the solute-solvent interaction induces an increased non-superfluid density in the first solvation layer around the dopant molecule. Since superfluidity may be associated with long exchange cycles in imaginary time,⁸⁹ Kwon and Whaley identify the local non-superfluid density considering only particles participating in exchange cycles that involve less than a critical number of atoms.⁸⁸ This microscopic two-fluid description leads to three contributions to the total moment of inertia of the solvated molecule, *i.e.*

$$I = I_0 + I_n + I_s . \quad (1.7)$$

Here, I_0 is the moment of inertia of the free molecule, I_n is the contribution from the non-superfluid component, and I_s arises from the irrotational flow of the superfluid density. For heavy molecules such as SF_6 and OCS , very good agreement with the experimentally observed rotational constants can be achieved if a rigid coupling of the well-localized non-superfluid density to the rotating molecule is assumed. For those rotors the contribution of the superfluid density is estimated to be negligible, indicating that adiabatic following holds only for the non-superfluid component of the fluid. In case of lighter molecules with larger vacuum rotational constants such as HCN , the microscopic two-fluid model fails since adiabatic following breaks down even for the non-superfluid component.³²

Very recently it became possible to produce small doped helium clusters containing up to 20 ^4He atoms in pulsed supersonic jet expansions.^{90,91} Such aggregates partially bridge the gap to the much larger droplets described above and constitute an important benchmark system for microscopic theoretical approaches. Using both high-resolution infrared and microwave techniques McKellar, Jäger and coworkers unambiguously assigned IR absorption spectra of small $\text{OCS-}^4\text{He}_N$ ^{92,93} as well as $\text{N}_2\text{O-}^4\text{He}_N$ ⁹⁴ van der Waals complexes in the range $N \lesssim 10$. Measuring the rotational constants as a function of cluster size N they were able to directly observe the evolution from a rigid chromophore–helium complex towards a quantum solvated impurity. In agreement with recent quantum Monte Carlo calculations^{95,96} the rotational constants of the $\text{OCS-}^4\text{He}_N$ complexes were found to decrease with increasing N , reaching the limiting droplet value around $N = 5$ and then undershooting it for $N = 6, 7, 8$. For N_2O the rotational constants approach the asymptotic droplet value at $N \approx 6$ and show oscillatory behaviour for larger complex sizes. These results prove that even helium density in the first solvation shell closest to a molecular impurity can become decoupled from the rotational motion of the solute. In the context of the microscopic two-fluid model by Kwon and Whaley^{32,88} the experimental findings thus indicate the presence of a substantial superfluid fraction in the intimate vicinity of a fully solvated molecule.

The possibility to use helium droplets as a means to grow and stabilize weakly bound species in geometries outside the global potential energy minimum has been demonstrated by Nauta and Miller both for complexes of HCN ⁹⁷ and of water molecules.⁹⁸ In seeded supersonic jet expansions, which are known to produce preferentially complexes in the most stable geometry, HCN clusters containing more than three molecules form exclusively non-polar, presumably cyclic structures. The sequential aggregation in the interior of helium droplets, however, leads only to strongly polar, linear chains of HCN molecules. This phenomenon is attributed to the absence of thermal motion in the interior of helium droplets which ensures that an introduced HCN molecule and any preexisting complex can align due to the long-range dipole–dipole interaction and mutually approach in a head-to-tail configuration.⁹⁷ The growth of H_2O complexes in helium droplets led preferentially to a cyclic hexamer,⁹⁸ a structure previously unseen in jet expansions. These studies vividly demonstrated the largely unexplored potential of helium droplets as a means to construct novel nanoscale complex species.

Motivation

The brief overview presented above gives evidence of the large number of experimental and theoretical studies that, over the last decade, have considerably advanced our understanding

of the *rotational* motion of helium-solvated molecular species. About a century after its first liquefaction, however, surprisingly little is known about the *translational* dynamics of *neutral* atoms and molecules inside liquid helium. This lack of information is mainly due to the substantial experimental difficulties associated with monitoring the motion of uncharged particles in the bulk fluid. In particular, important observables, such as the kinetic energy or the direction of travel, are difficult to obtain. The velocity of charged species in solution can however be manipulated and measured with much greater facility. Many important phenomena related to translational motion in bulk He II, such as the formation of quantum vortices⁹⁹ as well as the significance of Landau’s critical velocity,¹¹ therefore have been investigated by carrying out drift experiments on intrinsic ions.

As opposed to the bulk liquid, finite-size free helium clusters constitute a medium for translational motion with simple access to both the speed and the angular distribution of departing neutral particles. Moreover, the mean size of the droplets in a beam can readily be controlled by changing the stagnation conditions of the expansion. Consequently, it becomes feasible to systematically vary the distance of travel inside the quantum liquid. Essentially, two alternative methods to study the interaction of a traveling neutral particle with helium droplets are possible. In the first method the scattering of *external* species from *pure* helium droplets is investigated. This traditional approach was already suggested by Becker⁴⁰ in 1959 and has since been employed in various experiments that mainly measured the deflection of the droplet beam.^{46, 48, 100} Recently, Harms *et al.*¹⁰¹ found indications for superfluidity in ⁴He droplets in scattering experiments with ³He atoms. The second method relies on dissociating molecular impurities solvated *inside* the helium droplets. The outcome of such an experiment was very recently predicted by Takayanagi *et al.*¹⁰² In this study the photodissociation of Cl₂ in small ⁴He₂₀₀ droplets is simulated at a finite temperature of 4 K, where superfluid phenomena do not occur. It is found that the chlorine fragments depart from the cluster environment in virtually all cases, resulting in a negligible probability for recombination. This result is in stark contrast to the behaviour of nascent fragments generally observed in solid clusters. For instance, photodissociation experiments of halogen molecules in anionic systems such as I₂⁻(Ar)_n,¹⁰³ I₂⁻(CO₂)_n,¹⁰⁴ I₂⁻(OCS)_n,¹⁰⁵ and Br₂⁻(CO₂)_n¹⁰⁶ have shown that caging^b is essentially complete once about one entire solvent shell is formed around the parent molecule. A similar behaviour is found for the extensively studied dissociation reactions of hydrogen halide molecules in the interior of small rare gas clusters (for a recent review see reference [107]). In case of HBr embedded in argon clusters, both theoretical and experimental results indicate an efficient caging of the initially fast and highly mobile hydrogen fragment once the third solvent shell is filled.¹⁰⁸ Takayanagi *et al.*¹⁰² attribute the lack of caging found in their calculations not only to the weak He–He interaction, but also to structural and dynamical quantum effects in ⁴He droplets. It is therefore of great interest to obtain more detailed information on the interaction of liquid helium with translationally excited impurities. Moreover, the photodissociation of stable solute molecules inside helium droplets opens the door towards investigating chemical reactions involving radicals at ultralow temperatures. The study of such reactions is a largely unexplored field and constitutes a possible direction for future research in our group.

^bThe term “caging” is used here to denote the ability of a finite-size solvent to impede the departure of a specific photofragment, thereby possibly causing recombination of the parent molecule.

This thesis aims to shed light on some of these aspects by investigating the 266 nm photodissociation of CH_3I and CF_3I in the interior of ^4He droplets containing on average 2000–20000 atoms. The parent molecules were chosen because of their similar and well-known gas phase UV photodissociation dynamics (see Section 2.5). Moreover, the dissimilar masses of the CH_3 and CF_3 fragments result in a very different energy partitioning in the photolysis of these two molecules. As a consequence, iodine fragments from CH_3I have a substantially lower initial kinetic energy than those from a CF_3I parent, which permits studying the influence of the initial kinetic energy on the translational dynamics of iodine atoms inside liquid ^4He . In the experiments presented in this work, photodissociation products escaping from the cluster environment are laser-ionized and detected with the aid of a velocity map imaging setup. From the recorded ion images both the speed distribution and the angular distribution of the departing neutral species can be recovered. This way, the relaxation of both the kinetic energy and the velocity vector in the course of the motion through the finite-size droplets can be assessed.

Outline

The material in this thesis is ordered as follows: In Chapter 2 important mechanisms related to the the formation and subsequent doping of helium droplets in a molecular beam apparatus are explained. The quantitative description of evaporative cooling given in this chapter includes estimations of the the droplet heat capacities and evaporation rates at finite temperatures that will be valuable for the interpretation of the experimental data. Chapter 2 moreover provides a brief review of the work on the dissociation of the free alkyl iodides CH_3I and CF_3I in the gas phase. From the available data in the literature the expected mean kinetic energies and angular distributions of both the (fluorinated) methyl and iodine fragments at the relevant photolysis wavelength of 266 nm are determined. The results serve as an estimate for the initial properties of the nascent fragments created by the 266 nm dissociation of CH_3I and CF_3I inside ^4He droplets. In Chapter 3 we describe the experimental setup with a focus on the helium droplet beam machine designed and constructed as part of this thesis work. Particularly detailed accounts are given for the cryogenic droplet source and the velocity map imaging setup, the latter of which was used to acquire the vast majority of data presented and interpreted in Chapter 4. In the latter chapter we separately show and discuss the experimental results for each photofragment in order to gradually establish an increasingly comprehensive picture of the fragment dynamics. A valuable contribution to our understanding of the fragment motion inside the helium clusters comes from classical Monte Carlo simulations presented in the same chapter. In Chapter 5 we finally summarize the most important results obtained in this work and give suggestions for future experiments.

The appendices cover supplementary and often lengthy material that is referred to in Chapters 2–4. In Appendix A we list important mathematical properties of the log-normal distribution that is used to describe the distribution of cluster sizes in the helium droplet beam. The numerical algorithms used to perform Abel inversions on the recorded ion images and hence to obtain both the speed and the angular distributions of the detected particles are discussed in some detail in Appendix B. In Appendix C estimates of the droplet rotational frequency as induced by a single collision with a dopant molecule in a scattering cell are given. Appendix D finally provides the mathematical background for the hard-sphere scattering Monte Carlo sim-

ulations carried out to elucidate elementary properties of the fragment motion through the liquid environment. Additionally, an alternative description based on viscous Stokes flow past a sphere is explained briefly.

Chapter 2

Concepts

The main goal of this chapter is to quantitatively examine important properties of the doped helium droplets before and after the absorption of a UV photolysis photon. Knowing these properties allows us to choose appropriate experimental conditions and will be vital for the interpretation of the obtained data. The chapter begins with a description of how beams of helium clusters are produced experimentally in Section 2.1. In order to understand the droplet temperatures as well as the response of helium clusters to heat input, we explain the evaporative cooling of the droplets in Section 2.2. After estimating the mean droplet sizes produced in our setup in Section 2.3, some effort is made to quantify various aspects of the pick-up process by which impurities are introduced into the helium droplets. This part, presented in Section 2.4, is of great importance to our experiments as doping a significant number of droplets with more than one impurity must be avoided. Finally, we discuss the current understanding of the 266 nm photodissociation of CH_3I and CF_3I in the gas phase in Section 2.5. This analysis establishes the initial angular and kinetic energy distributions of the nascent photofragments in helium droplets.

2.1 The making of helium droplet beams

Nowadays, molecular beams of ^4He and ^3He droplets are routinely obtained from jet expansions of precooled high purity helium into vacuum.^{51,52,75,109} In contrast to the early works of Becker, Gspann and coworkers who used conventional nozzles of 0.1–0.15 mm diameter and low stagnation pressures of the order of 1 bar to produce helium cluster beams,^{39,45} current experimental apparatus rely on expansions through small orifices of 5–10 μm diameter.^{59,97,109,112,113} Such orifice dimensions require both high stagnation pressures $p_o \approx 5\text{--}200$ bar and low stagnation temperatures $T_o \approx 3\text{--}30$ K for cluster formation to occur. As will be shown below, these typical source conditions give access to three qualitatively different expansion regimes. Moreover, carefully setting the stagnation conditions (p_o, T_o) permits gaining control over important droplet beam properties such as the speed v_D and the mean cluster size \bar{N} .

In the course of an expansion, density and temperature of the expanding matter drop rapidly as the distance to the orifice increases. The accompanying change of thermodynamic state

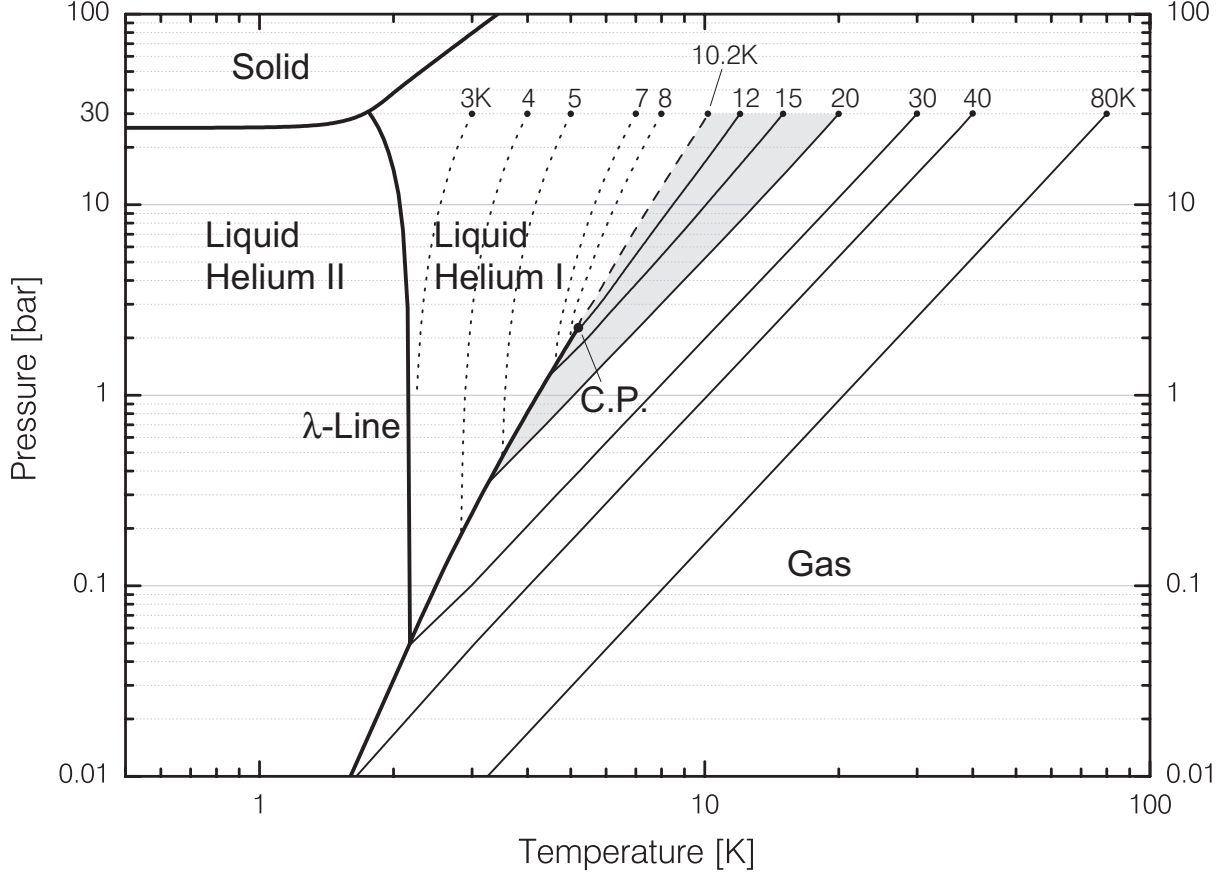


FIGURE 2.1: Phase diagram of ${}^4\text{He}$ in a doubly logarithmic pressure-temperature representation.^{110, 111} Phases are separated by thick solid lines. Thin lines represent isentropes starting at a stagnation pressure of 30 bar and a selection of stagnation temperatures ranging from 3 K to 80 K. Isentropes intersecting the liquid–gas phase line from the liquid side (dotted lines) and from the gas phase side (solid lines) are graphically distinguished. The isentrope passing through the critical point (C.P.) at 5.2014 K and 2.275 bar starts from 10.2 K and is shown as a dashed line. The shaded region approximately illustrates the expansion conditions employed in this work to create mean droplet sizes of about $2 \cdot 10^3$ to $2 \cdot 10^4$ atoms.

is approximately adiabatic. It is instructive to view the resulting trajectories in a pressure-temperature phase diagram, which can easily be obtained from tables of the well-known thermodynamic properties of ${}^4\text{He}$ at low temperatures.^{110, 111} Figure 2.1 shows the phase boundaries of ${}^4\text{He}$ as well as a set of isentropes starting at a stagnation pressure of $p_o = 30$ bar and at various stagnation temperatures $T_o = 3\text{--}80$ K. Based on Figure 2.1 three principal expansion regimes can be identified:¹⁰⁹

- I. At low stagnation temperatures T_o the real fluid properties of helium lead to curved isentropes (\cdots) that bend towards the saturation curve. The isentropes therefore do not intersect the λ -line and approach the line of equilibrium coexistence from the normal liquid side. Local temperatures and pressures at the intersection point are below the

critical point values (“supercritical regime”).

- II. Temperature T_o and pressure p_o in the source correspond to the critical specific entropy of $S_c = 22.81 \text{ JK}^{-1}\text{mol}^{-1}$. Consequently, the isentrope (---) passes through the critical point around 5.2 K and 2.3 bar (“critical expansion”).
- III. For high stagnation temperatures T_o the isentropes (—) meet the gas–liquid phase boundary from the vapor side. Local temperatures and pressures at the point of intersection with the saturation curve are below the critical point values (“subcritical regime”).

Supercritical expansions

In the course of supercritical expansions the isentropes can reach the vicinity of the λ -line which is characterized by a sharp increase of the specific heat. Hence, an ideal gas approximation fails and the thermodynamic trajectories bend downward to cross into the two-phase region from the liquid side where clusters are produced by fragmentation of the He I normal fluid. For supercritical expansion conditions bimodal speed and size distributions have been found.^{109,112,114} The major contribution to these distributions is thought to arise indeed from droplets formed by fragmentation of the liquid. Such clusters have been shown to be very large, containing about 10^6 to 10^8 atoms,¹¹⁵ and to exhibit an exponential size distribution.¹¹⁶ However, in addition to the fragmentation droplets, smaller clusters are created by a different mechanism. Subsequent to the disintegration of the liquid, helium atoms evaporating from the droplets may feed the monoatomic gas expansion which can lead to cluster formation by recondensation.^{109,114} Speeds and speed ratios^a of both types of clusters formed in supercritical expansions have been obtained by Buchenau *et al.*¹⁰⁹ from time-of-flight measurements. For stagnation pressures p_o well above the critical point speed ratios $S \gtrsim 40$ were found for clusters formed by fragmentation.

Critical expansions

Expansions through the critical point are expected to have special properties as the surface tension vanishes⁸ and the speed of sound goes through a minimum.¹¹¹ Using time-of-flight mass spectrometry Harms *et al.*¹¹⁸ more closely inspected the properties of ^4He droplets produced from stagnation conditions in the vicinity of the critical point. At a stagnation pressure of $p_0 = 2.3$ bar they found a sharp reduction of droplet speed as the stagnation temperature was lowered through the critical-point temperature of 5.2 K. At the same time the mean cluster size was observed to increase dramatically, thereby indicating a sudden change from condensation- to fragmentation-formed droplets. For stagnation pressures above about 7 bar the marked change in droplet speed was found to disappear, while at lower stagnation pressures droplet speeds below 50 m/s were observed. Expansions starting from around the critical point were found to yield a surprisingly small speed ratio $S \approx 5$. It is however possible that this observation

^aThe speed ratio S of a collimated molecular beam is defined as $S = [\frac{1}{2}mv^2 / (k_B T_{\parallel})]^{1/2}$, where m is the molecular mass, k_B denotes the Boltzmann constant, and T_{\parallel} is the parallel temperature of the beam propagating with an average speed v in the laboratory frame. In case of monoatomic species and high speed ratios $S \gtrsim 10$ the following approximations¹¹⁷ may be used: $(\Delta v/v) \approx (1.65/S)$ and $(T_{\parallel}/T_o) \approx (2.5/S^2)$. In the latter expressions Δv denotes the FWHM of the speed distribution and T_o is the stagnation temperature.

was brought about by an imperfect thermal stabilization of the droplet source that caused the stagnation conditions to rapidly alternate between the sub- and the supercritical regime.¹¹⁸

Subcritical expansions

The subcritical regime is the most common mode of operation for helium droplet machines and has been used exclusively for the dissociation experiments presented in this work (see shaded area in Figure 2.1). For this expansion regime the ensuing molecular beam is found to contain both helium atoms and clusters composed of up to some 10^4 atoms.¹⁰⁰ The mean size \bar{N} of the droplets grows if the stagnation temperature T_o is lowered or the stagnation pressure p_o is raised. For high stagnation pressures p_o and temperatures T_o the expanding helium behaves approximately like an ideal gas. In this limit, the local temperature T and pressure p of the system evolve along a line of constant entropy according to¹¹⁹

$$p \cdot T^{\frac{\gamma}{1-\gamma}} = p_o \cdot T_o^{\frac{\gamma}{1-\gamma}} = \text{const} , \quad (2.1)$$

where γ is the ratio of the specific heats and equals 5/3 for a monoatomic gas. In the doubly logarithmic plot this approximation gives rise to linear trajectories which eventually meet the saturation curve from the vapor side as the expansion proceeds. Although the system is thought to temporarily cross the saturation curve while maintaining a supercooled gaseous state, condensation will eventually commence if the density is still sufficiently high for the necessary three-body collisions to occur. As the droplets grow in size the trajectories rejoin the saturation curve due to the accompanying heat release.⁷⁷ Further downstream collisions cease and the then freely moving droplets cool by evaporation along the gas-liquid phase line (see Section 2.2).

Under slightly subcritical conditions and for high stagnation pressures p_o well above the critical point Buchenau *et al.*¹⁰⁹ found speed ratios $S \gtrsim 100$. This value is consistent with speed ratios measured by the same authors for clusters formed by recondensation in the supercritical regime and with the findings of Lewerenz *et al.*¹⁰⁰ who report a speed ratio of $S = 110$ for a subcritical expansion from $p_o = 80$ bar and $T_o = 24$ K. As a consequence of these high speed ratios the droplet beam velocity spread can in many applications be neglected. Accordingly, we assign a single velocity v_D to the subcritically formed droplet beam which henceforth is treated as quasi-monochromatic. In this work we will exploit the high speed ratio to obtain sharp ion images for products of reactions in ^4He droplets although the detector surface is parallel to the droplet beam axis (see Section 3.5). Typical droplet speeds in the subcritical expansion regime are 250–450 m/s depending on stagnation pressure and temperature. Figure 2.2 illustrates speeds observed in the Toennies group for a stagnation pressure of 20 bar. Droplet beam speeds v_D measured in our apparatus using velocity map imaging will be presented in Section 4.7.1.

2.2 Evaporative cooling

Thermally excited helium droplets cool by evaporation of atoms from their surface as each emission event reduces the excitation energy E of the cluster by the sum of the kinetic energy

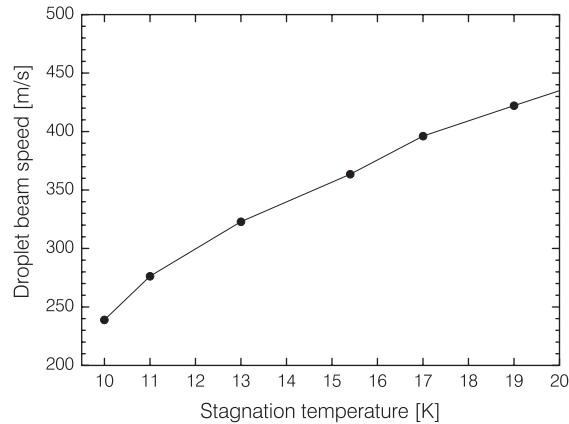


FIGURE 2.2: Droplet beam speeds observed by Schilling¹²⁰ in the subcritical expansion regime. The stagnation pressure is $p_o = 20$ bar.

and the negative chemical potential $-\mu_N$ of the released atom. This consideration is summarized in the statistical relation

$$\frac{dE}{dt} = - \left(\frac{3}{2} k_B T - \mu_N \right) \frac{dN}{dt} \quad (2.2)$$

which serves as a starting point of our description. As always, N denotes the number of helium atoms forming the cluster. For a given droplet temperature T the rate of evaporation $-dN/dt$ from large helium clusters of either isotope can be calculated from

$$\frac{dN}{dt} = -g \frac{m r_0^2 N^{\frac{2}{3}}}{\pi \hbar^3} (k_B T)^2 \exp \left[\frac{\mu_N}{k_B T} \right]. \quad (2.3)$$

This expression first was derived by Brink and Stringari⁶⁶ from the well-known Weisskopf formula¹²¹ describing the evaporation of neutrons from nuclei, and becomes equivalent to the predictions of gas kinetic theory in the limit of large clusters and high excitation energies. Here, r_0 is the bulk unit radius as defined in equation (1.6), while g and m are the the spin degeneracy and the mass of the evaporating atom, respectively. For both ^4He and ^3He droplets the thermal effect on the chemical potential

$$\mu_N = -T \left(\frac{\partial S}{\partial N} \right)_E - E_0(N) \cong -E_0(N), \quad (2.4)$$

where S denotes the entropy of the system, is negligible.⁶⁶ As a consequence, the chemical potential μ_N reduces to the size dependent negative binding energy $-E_0$.

In order to predict the evolution of the cluster temperature in time $T(t)$ one furthermore has to provide the microscopic heat capacity of the droplet or, in other words, express the excitation energy E as a function of droplet size N and temperature T . Together with equations (2.2) and (2.3) this final relation yields a closed system of coupled differential equations. From the solution $T(t)$ one subsequently can calculate the evaporation rates $-dN/dt$ at any point in the cooling process using equation (2.3).

The experimental studies described in this work deal with droplets composed of bosonic ^4He atoms. We therefore proceed to address the specific properties of this isotope. A simple expression¹²² for the size dependent binding energy E_0 is given by

$$E_0(N) = 7.15 \text{ K} - 11.30 \text{ K} \cdot N^{-\frac{1}{3}}, \quad (2.5)$$

the second term of which represents the surface energy correction. This expression predicts $E_0 \approx 6.02 \text{ K}$ (4.2 cm^{-1}) and 6.63 K (4.6 cm^{-1}) for $N = 1000$ and $N = 10000$ atoms, respectively.

For the ^4He isotope the heat content of a droplet conveniently is divided into contributions E_{bulk} and E_{surf} from bulk and surface modes, respectively. In the classical picture the surface vibrational modes, termed “rippbons”, are lower in energy than the bulk compression modes.¹²³ In the relevant droplet size range $N \lesssim 20000$ and for temperatures below about 1 K therefore little population of the bulk modes is predicted and the droplet excitation energy E is almost exclusively based on surface vibrations. Hence, we note

$$E \cong \begin{cases} E_{\text{surf}} & \text{for } T \lesssim 1 \text{ K} \\ E_{\text{bulk}} + E_{\text{surf}} & \text{for } T \gtrsim 1 \text{ K} \end{cases} \quad (2.6)$$

and will consider bulk contributions only at temperatures above 1 K. The surface mode heat content E_{surf} can be estimated from the classical density of states. For a given surface tension σ_t one finds⁶⁶

$$E_{\text{surf}} \leq 0.864 \cdot k_{\text{B}} \left(\frac{k_{\text{B}}^2 m}{\hbar^2 \sigma_t} \right)^{\frac{2}{3}} T^{\frac{7}{3}} N^{\frac{2}{3}}, \quad (2.7)$$

both sides of which are equal up to a temperature of roughly 2 K.

With this information at hand the cooling of thermally excited ^4He droplets with initial temperatures $T \lesssim 1 \text{ K}$ can be calculated by solving the coupled equations (2.2), (2.3), (2.6) and (2.7) simultaneously. For low droplet temperatures the kinetic energy term in equation (2.2) may be neglected. The solution $T(t)$ to this system of equations was first reported by Brink and Stringari.⁶⁶ Figure 2.3 shows the calculated cooling of large ^4He droplets for two different initial temperatures of 1 K and 0.7 K. The behaviour of the internal temperature depends little on the cluster size and, as illustrated, becomes independent of the initial temperature after a cooling time of about 10^{-7} s . A good value for the typical experimental flight time is 1 ms as determined by the length of the apparatus and the droplet speed. Within this flight time ^4He droplets are predicted to reach internal temperatures of about 0.3 K. A similar model⁶⁷ for ^3He clusters yields a calculated temperature of 0.15 K. These temperatures are in good agreement with earlier estimations by Gspann⁴⁸ and have been confirmed by later experiments.^{62,63,75,124} Figure 2.4 illustrates the evaporation from a ^4He droplet initially composed of $N = 10000$ atoms and heated to a temperature of 1 K. While almost no change in droplet size occurs in the first 100 ps following the excitation, about 75% of the atoms are released between 100 ps and 100 ns. The evaporation rate peaks at $t = 0$ where a value of 10^{10} s^{-1} is reached and subsequently drops rapidly. After about 10^{-5} to 10^{-4} s the droplet size therefore practically stays constant.

With respect to the experimental results of this work it is instructive to estimate the temperatures and the evaporation rates of ^4He droplets with much higher internal energy content.

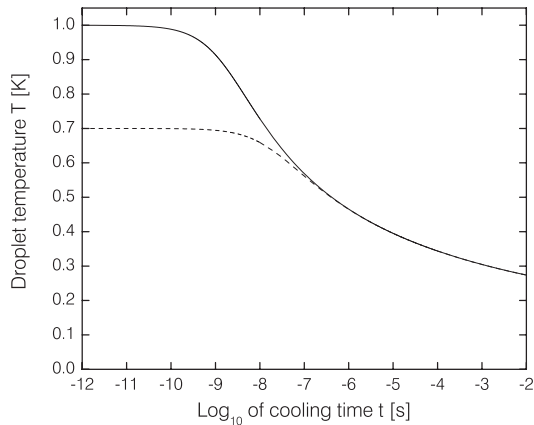


FIGURE 2.3: Cooling of large ($N \gtrsim 3000$) ^4He droplets due to evaporation from the surface. Starting from 1 K (solid line) and 0.7 K (dashed line) the internal temperature falls rapidly to eventually become independent of the initial conditions after about 10^{-7} s. The droplets are predicted to attain temperatures of about 0.3 K within a typical experimental flight time of 1 ms.

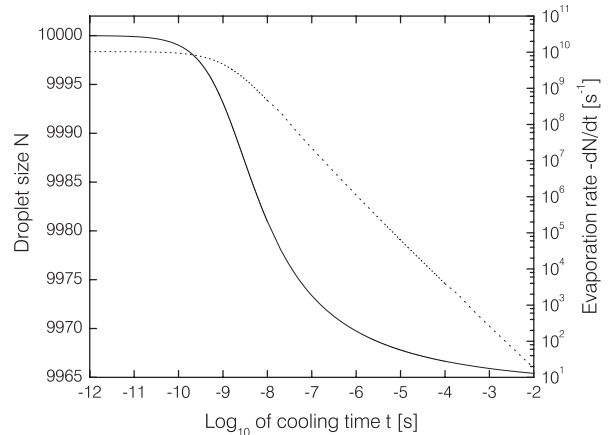


FIGURE 2.4: Size (solid line) and evaporation rate (dotted line) of a thermally excited ^4He droplet as a function of time. In the course of the cooling process about 35 particles are emitted from the droplet that initially, at a temperature of 1 K, was composed of $N = 10000$ atoms. The evaporation rate has a peak value of 10^{10} s^{-1} and falls continuously with time.

Under those conditions both bulk and surface modes become populated and the density of states based on surface modes only, as presented in reference [66], is no longer valid. Given an elevated excitation energy, the initial temperature of large droplets can, however, be estimated from the thermodynamic properties of bulk ^4He .⁸ The bulk mode contribution to the internal energy content of a droplet is obtained by integrating the experimental bulk specific heat. An estimate of E_{Surf} at a given temperature T can be obtained from the experimental data on the surface tension σ_t using equation (2.7). At $T = 2$ K we find the contribution of the surface modes to the total excitation energy to be inferior to 25% for all $N \geq 1000$. Therefore only a small error is introduced by using the right hand side of equation (2.7) at more elevated temperatures than 2 K. The estimated contributions to the internal energy at different temperatures are plotted in Figure 2.5 for a droplet size of $N = 10000$. It can easily be seen that the energy content of the surface modes E_{Surf} becomes relatively less important as the temperature increases. At temperatures above about 1 K bulk modes become significant and eventually carry most of the internal energy as the temperature increases further. The abrupt change in the slope of the bulk contribution at 2.177 K is caused by the specific heat anomaly at the λ -transition.

The thus estimated internal energy from both surface and bulk contributions is given in Table 2.1 for various droplet sizes N and temperatures T . As an example we examine a rather typical case for the dissociation experiments presented in this work. Let us assume an energy of 12000 cm^{-1} is deposited in a ^4He droplets containing $N = 5000$ atoms. According to Table 2.1 this gives rise to an initial temperature of about 3.5 K, *i.e.* the droplet is predicted to undergo a transition into the normal He I phase. For this temperature and droplet size the initial and highest evaporation rates $-dN/dt$ can be estimated from equation (2.3) to be approximately

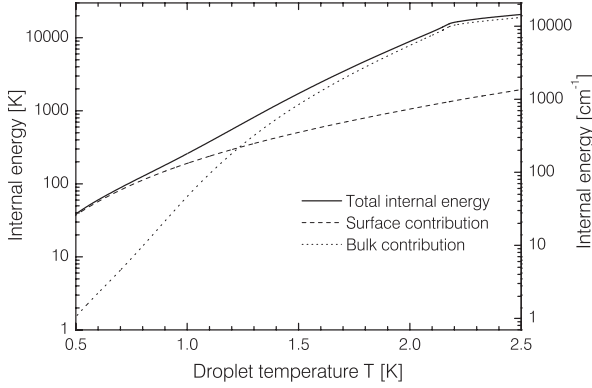


FIGURE 2.5: Plot of the internal energy of a $N = 10000$ ${}^4\text{He}$ droplet at elevated temperatures between 0.5 K and 2.5 K. The contributions from surface and bulk modes are estimated from experimental data.⁸

T [K]	$N = 1000$	2000	5000	10000
1.5	160	290	645	1199
2.0	705	1344	3195	6200
2.177	1194	2306	5557	10874
2.5	1607	3094	7429	14506
3.0	2214	4219	10016	19418
3.5	3048	5733	13413	25763

TABLE 2.1: Estimate of the internal energy of ${}^4\text{He}$ droplets at elevated temperatures based on experimental data of the bulk properties. The total internal energy is given in units of cm^{-1} as a function of droplet size N and temperature T .

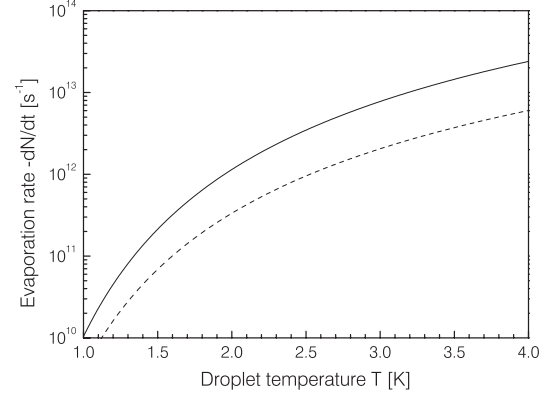


FIGURE 2.6: Evaporation rates of ${}^4\text{He}$ clusters as a function of droplet temperature T . The rates have been calculated from equation (2.3) for $N = 10000$ (solid line) and $N = 1000$ (dashed line).

T_o [K]	\bar{N}	T_o [K]	\bar{N}
11	20060	17	3540
12	14710	18	2750
13	10860	19	2150
14	8080	20	1710
15	6080	21	1370
16	4620	22	1100

TABLE 2.2: Prediction of the mean droplet size \bar{N} for a stagnation pressure of $p_o = 30$ bar and various stagnation temperatures T_o . The data is calculated for an orifice diameter of $5 \mu\text{m}$.

$9.5 \cdot 10^{12} \text{ s}^{-1}$. For further reference we show the calculated evaporation rates for a wide range of temperatures and two relevant droplet sizes in Figure 2.6.

2.3 Droplet sizes

Atom number distributions $f(N)$ (also termed size distributions) of helium clusters produced by condensation from the gas phase have been determined from the angular distribution of clusters scattered by a single collision with a secondary beam of SF_6 ,¹⁰⁰ argon and krypton.¹²⁵ By means of a thorough mass-spectrometric analysis of the scattered clusters it was shown that the angular distribution of deflected droplets does not depend on whether or not the colliding particle sticks to the droplet. Lewerenz *et al.*¹⁰⁰ therefore concluded that under the experimental conditions

used, complete momentum transfer in each single collision can be assumed.^b Since the speed ratio of the droplet beam in the subcritical expansion regime is very high (see Section 2.1), the experimentally found deflection angle θ and the number N of helium atoms in the droplet are directly related by a $N(\theta) \propto 1/\theta$ rule.¹²⁰

The measured atom number distributions have been shown to fit very well to a log-normal distribution^{100,120}

$$f(N) = \frac{1}{N\delta\sqrt{2\pi}} \exp\left[-\frac{(\ln N - \mu)^2}{2\delta^2}\right], \quad (2.8)$$

where $\delta > 0$ and μ are parameters. The mean droplet size \bar{N} and the standard deviation S of the distribution $f(N)$ are given by

$$\bar{N} = \exp(\mu + \delta^2/2) \quad (2.9a)$$

and

$$S = \bar{N}\sqrt{\exp(\delta^2) - 1}. \quad (2.9b)$$

Measurements for a wide range of subcritical expansion conditions show that the standard deviation S and the mean number of helium atoms per droplet \bar{N} are approximately linearly related:^{120,125}

$$S/\bar{N} \approx 0.60 \pm 0.04 \quad (2.10a)$$

which according to equation (2.9b) translates to

$$\delta \approx 0.55 \pm 0.03. \quad (2.10b)$$

Using equation (A.8) the same relation can also conveniently be expressed in terms of the full width at half maximum (FWHM) $\Delta N_{1/2}$ of the distribution $f(N)$ which obeys

$$\Delta N_{1/2}/\bar{N} \approx 0.88 \pm 0.02, \quad (2.10c)$$

and therefore is comparable to \bar{N} . A more complete overview of the mathematical properties of log-normal distributions can be found in Appendix A.

In many experiments on helium droplets and other clusters the reliable prediction of mean cluster sizes \bar{N} for a particular orifice and given stagnation conditions is of great importance. For this purpose various semi-empirical scaling laws have been suggested.^{126–129} Figure 2.7 shows a plot of the mean cluster sizes \bar{N} measured by molecular beam scattering experiments in the Toennies group^{100,125} as a function of the scaling parameter Γ developed by Knuth *et al.*¹²⁶ The calculation of Γ involves the evaluation of the real fluid properties of ${}^4\text{He}$ ^{110,111} under the

^bGspann⁵⁰ does not agree with this interpretation. In the light of the “momentum transparency” found in earlier works of his^{47,49} he reasons that a sticking collision does not necessarily imply full momentum transfer to the droplet. It is argued that instead of being transferred to the droplet, part of the impinging particle’s momentum might be lost by anisotropic evaporation from the backside of the cluster. As a consequence, the droplet sizes reported by Lewerenz *et al.* would be too large. Their findings are, however, supported by recent independent measurements of mean droplet sizes using a spectroscopic technique.⁸⁰ We will therefore use the widely accepted results of Lewerenz *et al.*

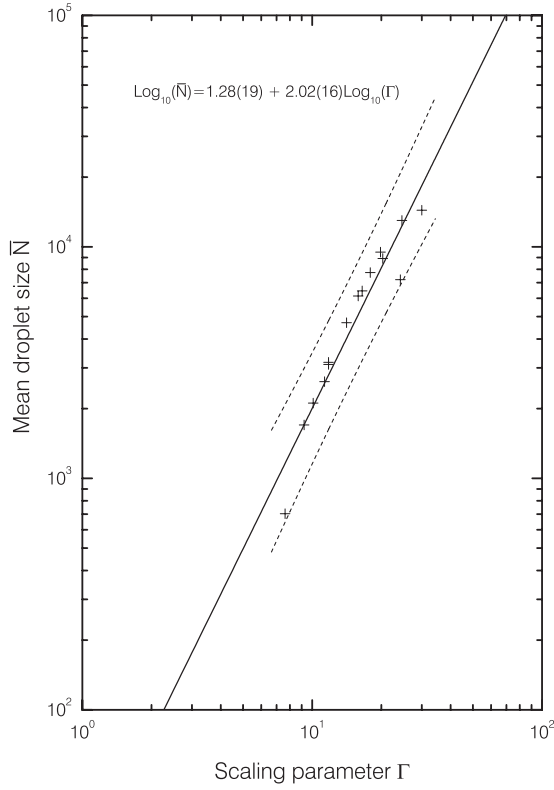


FIGURE 2.7: Mean size \bar{N} of droplets formed in subcritical expansions^{100,125} as a function of the scaling parameter Γ .¹²⁶ A linear fit to the data is shown as solid line as well as in equational form. The 95% prediction band resulting from the fit is indicated by the dashed lines.

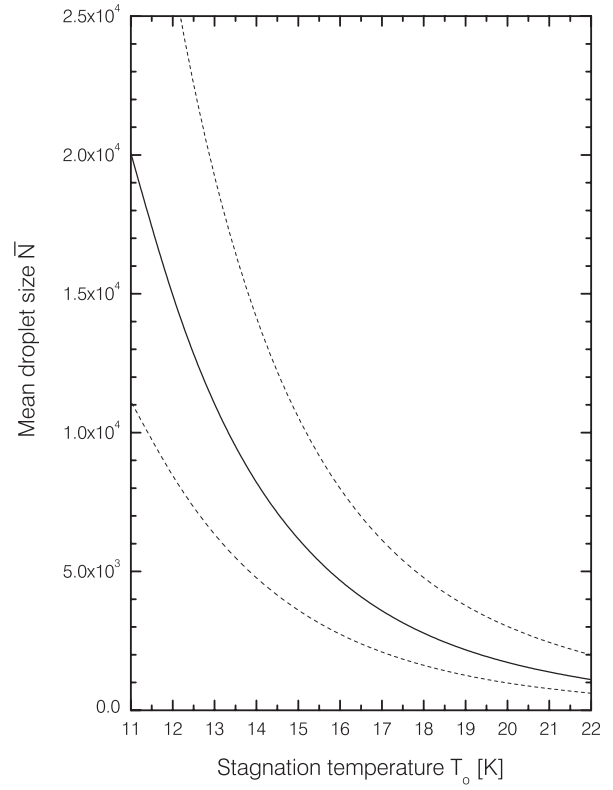


FIGURE 2.8: Prediction of mean droplet sizes \bar{N} produced in subcritical expansions through a $5\mu\text{m}$ orifice from a stagnation pressure $p_o = 30$ bar and stagnation temperatures T_o from 11 to 22 K. The diagram shows the best guess (solid line) as well as the 95% prediction band (dashed line).

stagnation pressure p_o and temperature T_o . Linear regression yields a relation between $\log(\bar{N})$ and $\log(\Gamma)$ which subsequently can be used to estimate mean droplet sizes for other expansion conditions. Figure 2.8 shows the result for a fixed stagnation pressure $p_o = 30$ bar and an orifice diameter of $5\mu\text{m}$. In the experimentally relevant temperature range from $T_o = 11$ – 22 K mean droplet sizes \bar{N} from about 20000 to 1000 atoms are predicted. For convenience they are tabulated in Table 2.2.

Based on the reported ratio $S/\bar{N} \approx 0.60$ and the predicted mean droplet sizes \bar{N} in Table 2.2 the atom number distribution $f(N)$ of pure ${}^4\text{He}$ droplets can be calculated. Figure 2.9 shows the resulting log-normal distributions for a fixed stagnation pressure $p_o = 30$ bar and some selected stagnation temperatures. Assuming uniform bulk density and a spherical shape the atom numbers are easily converted to droplet radii using equation (1.6). The resulting radius distributions are depicted in Figure 2.10. As will be shown below in Section 2.4.1 the classical radii corresponding to the observed integral cross sections are by about 6.5 \AA larger.

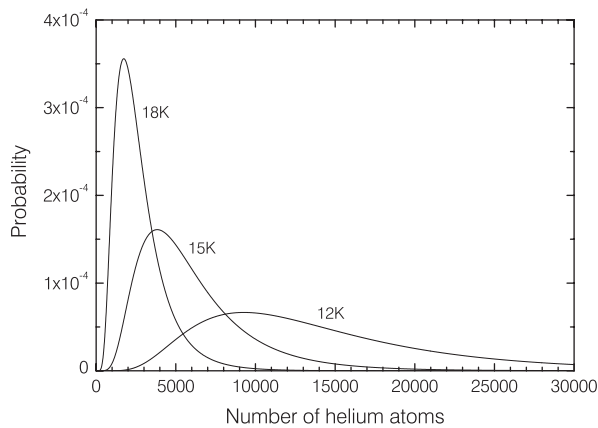


FIGURE 2.9: Predicted atom number distributions $f(N)$ for a stagnation pressure of $p_o = 30$ bar and stagnation temperatures $T_o = 12, 15$ and 18 K. The corresponding mean droplet sizes are given in Table 2.2.

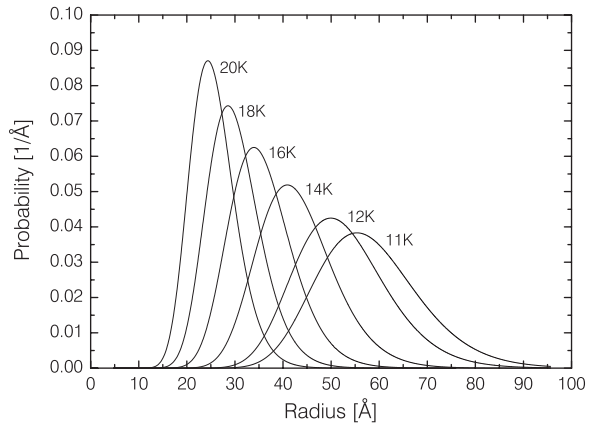


FIGURE 2.10: Distributions of droplet radii for a stagnation pressure of $p_o = 30$ bar and various stagnation temperatures T_o from 11 to 20 K. The reported radii are obtained assuming that the droplets are uniform and have bulk density.

2.4 Capture of foreign atoms and molecules

Foreign species can readily be introduced into helium clusters by passing the droplet beam through a scattering cell. Upon collision the impurities are “picked-up” by the generally much heavier droplets. If the scattering gas pressure is sufficiently high multiple collisions occur and may lead to the successive introduction of several impurities. The long range dispersion interaction between the foreign particles is expected to quickly lead to coagulation and formation of subclusters within 10^{-10} to 10^{-8} s.¹⁹

2.4.1 Cross sections

We begin the discussion of the pick-up process considering the total scattering cross section $\sigma_{\text{tot}}(N)$ of a droplet containing N helium atoms. Due to the atom number distribution $f(N)$ in the cluster beam, only its mean value

$$\bar{\sigma} = \int_0^{\infty} \sigma_{\text{tot}}(N) f(N) dN \quad (2.11)$$

is experimentally accessible.^c A good approximation of σ_{tot} is obtained by assuming a uniform spherical droplet of bulk density. Using the classical droplet radius R and the bulk unit radius r_0 as defined as in equation (1.6) we find

$$\sigma_{\text{tot}} = \pi R^2 = \pi r_0^2 N^{\frac{2}{3}}, \quad (2.12a)$$

^cThe limited angular resolution of the scattering experiments performed to measure $\bar{\sigma}$ impairs the detection of the full quantum mechanical total scattering cross-section. Instead, experiments are shown to yield values very close to the *classical* cross section.¹²⁵

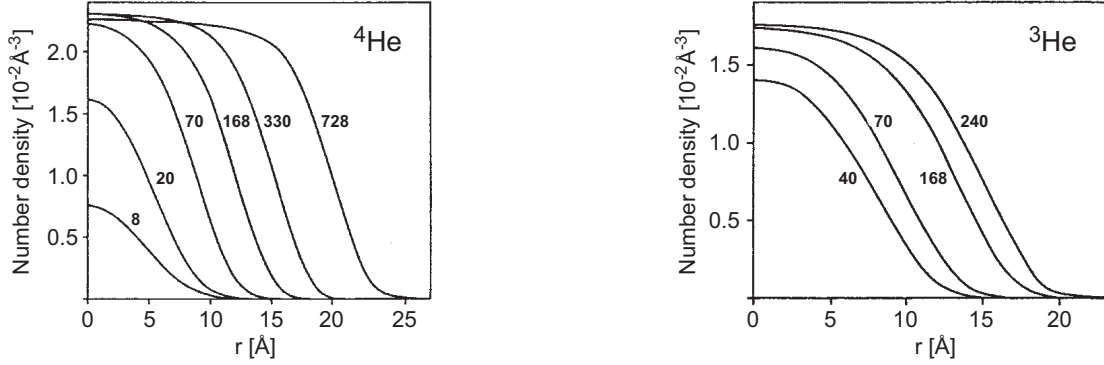


FIGURE 2.11: Calculated radial density profiles of various small and medium size ${}^4\text{He}$ and ${}^3\text{He}$ droplets. Numbers denote the droplet size N . The figures are reproduced from reference [18].

an expression which readily is generalized to different but still uniform densities ρ :

$$\sigma_{\text{tot}}(N) = \pi r_0^2 \left(\frac{\rho_{\text{bulk}}}{\rho} \right)^{\frac{2}{3}} N^{\frac{2}{3}} =: \sigma_0 N^{\frac{2}{3}}. \quad (2.12b)$$

This $\sigma_{\text{tot}} \propto N^{2/3}$ rule allows one to evaluate the integral (2.11) analytically. With the aid of equation (A.5) in Appendix A one obtains

$$\bar{\sigma} = \sigma_0 \overline{N^{\frac{2}{3}}} \exp(-\delta^2/9) = \sigma_{\text{tot}}(\overline{N}) \exp(-\delta^2/9). \quad (2.13)$$

With the established mean properties of the log-normal distribution (see equations (2.10)) the factor $\exp(-\delta^2/9)$ takes on the value 0.966 ± 0.004 and hence is very close to unity. It is therefore common practice to use

$$\bar{\sigma} \approx \sigma_{\text{tot}}(\overline{N}) \quad (2.14)$$

as a simple approximation.

A more profound analysis of σ_{tot} is obtained by considering the dependence of the helium droplet density on the radial coordinate. Radial density profiles in ${}^3\text{He}$ and ${}^4\text{He}$ droplets have been investigated by means of various theoretical methods^{18, 25, 28, 30, 72–74, 125, 130–133} for a wide range of cluster sizes. Rather than being uniform, the density is found to decrease with increasing radial position. With the exception of small clusters composed of less than about 10^2 atoms the computed densities are found to approach the bulk values¹⁸ of $\rho_{\text{bulk}} = 0.0219 \text{ \AA}^{-3}$ for ${}^4\text{He}$ and $\rho_{\text{bulk}} = 0.0165 \text{ \AA}^{-3}$ for ${}^3\text{He}$ in the central part the of droplets. Figure 2.11 shows the radial density profiles of ${}^4\text{He}$ and ${}^3\text{He}$ droplets as computed by early density functional (DFT) calculations.¹⁸

This radial density profile has consequences for the probability of capturing foreign particles in a helium droplet. As the average density ρ is lower, the cross sections σ_{tot} are larger than those predicted for a uniform sphere of bulk density. Experimentally, the mean droplet size \overline{N} and the mean total scattering cross section $\bar{\sigma}$ can be determined simultaneously in crossed beam scattering experiments. Using krypton and argon as scattering species, Harms *et al.*¹²⁵

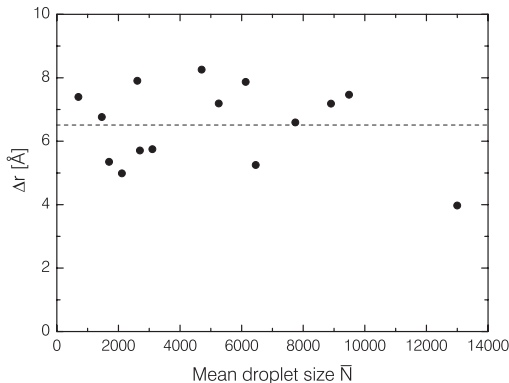


FIGURE 2.12: Plot of the surface thickness correction parameter Δr as a function of mean droplet size \bar{N} . The data is taken from reference [125]. The dashed line illustrates the mean value of $\Delta r = 6.51 \text{ \AA}$.

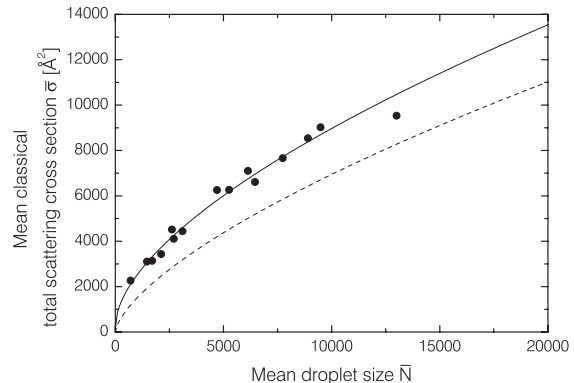


FIGURE 2.13: Prediction of the mean classical total scattering cross section $\bar{\sigma}$ as a function of the mean droplet size \bar{N} in the beam. The diagram shows the predicted cross sections according to the improved equation (2.15) (solid line) as well as the simple relation (2.12a) (dashed line). The experimental values are shown as filled circles.

have provided a unique set of data where $\bar{\sigma}(\bar{N})$ and the atom number distribution $f(N)$ of a ^4He droplet beam were measured under identical conditions in the $\bar{N} \approx 10^3\text{--}10^4$ size range. As stated in Section 2.3, the size distribution $f(N)$ is extracted from the angularly resolved deflection signal, whereas $\bar{\sigma}$ is obtained from the attenuation of the forward peak in the deflection pattern. The measured mean classical total scattering cross sections were subsequently demonstrated to agree well with cross sections predicted on the basis of density profiles obtained from accompanying DFT calculations. Most importantly, both data and theory were shown to be compatible with a liquid–vapor interface of *constant thickness*, independent of droplet size N . For a surface layer defined by a density change from 10% to 90% of the bulk value, a thickness of $6.4 \pm 1.3 \text{ \AA}$ could be extracted from the data.

Harms *et al.*¹²⁵ relate the average total scattering cross section $\bar{\sigma}$ of the droplet beam to a mean droplet density $\bar{\rho}$ which was found to increase with mean droplet size \bar{N} . The prediction of $\bar{\sigma}$ for a given mean droplet size \bar{N} hence requires a knowledge of the function $\bar{\rho}(\bar{N})$. More intuitively, $\bar{\sigma}$ may directly be estimated assuming a liquid–vapor interface of size independent thickness. In this approximation the classical total scattering cross section σ_{tot} of a size N droplet is calculated by increasing the uniform sphere radius R (see equation (1.6)) by a fixed amount Δr :

$$\sigma_{\text{tot}} = \pi \left(r_0 \cdot N^{\frac{1}{3}} + \Delta r \right)^2 . \quad (2.15)$$

Again, the mean integral cross sections $\bar{\sigma}$ is obtained analytically from the integral (2.11). We find

$$\bar{\sigma} = \pi \left[r_0^2 \bar{N}^{\frac{2}{3}} + 2r_0 \Delta r \bar{N}^{\frac{1}{3}} \right] \exp(-\delta^2/9) + \pi (\Delta r)^2 . \quad (2.16)$$

Inversely, the surface thickness correction Δr can be calculated from the data on $\bar{\sigma}$ and the simultaneously determined parameters \bar{N} and δ of the log-normal distribution. Figure 2.12 shows

the resulting plot of Δr as a function of mean droplet size \overline{N} , obtained from the experimental data given in reference [125]. The mean value of the distribution is found to be

$$\Delta r = 6.51 \pm 0.33 \text{ \AA}. \quad (2.17)$$

As shown in Figure 2.13, this result considerably improves the prediction of the mean integral cross sections $\overline{\sigma}$ compared to the simple bulk density model. The predictions are based on a constant parameter δ for the log-normal distributions as given by equation (2.10b).

A collision between a helium cluster and the scattering gas does, however, not always lead to an absorption of the foreign particle by the droplet. Deflection experiments in the Toennies group found the cross section σ_{cap} for capturing an impurity to be inferior to the total scattering cross section σ_{tot} , thus indicating that an impinging atom or molecule may traverse the droplet and subsequently leave the helium environment again.^{19,120,134,135} These events are characterized by a partial transfer of the scattering particle's momentum and kinetic energy to the droplet. The ratio $\sigma_{\text{cap}}/\sigma_{\text{tot}}$ has been found to depend on the impurity mass as well as on the interaction potential of the foreign particle with the helium environment.^{19,136} Consequently, for a given scattering species this effect can be accounted for by introducing an size dependent mean sticking coefficient $S(N) \in [0, 1]$ which represents an average over all impact geometries. The capture cross section σ_{cap} for an individual collision between a foreign particle and a helium cluster can then be written as

$$\sigma_{\text{cap}}(N) = S(N) \cdot \sigma_{\text{tot}}(N) . \quad (2.18)$$

2.4.2 Poisson distributions

Having characterized the capture cross section $\sigma_{\text{cap}}(N)$ we proceed to write down a differential expression for the probability $dP_{\text{cap}}(N)$ of a capture event occurring to a droplet of size N traveling a small distance dz along the z -axis. In case of a *static* scattering gas of uniform density n_S this probability is given by

$$\frac{dP_{\text{cap}}(N)}{dz} = n_S \sigma_{\text{cap}}(N) . \quad (2.19)$$

A cluster beam passing through a *moving* scattering gas of kinetic temperature T_S will experience an increased collision probability which can be accounted for by multiplying the right hand side of equation (2.19) by a correction factor $F_{a_0}(\infty, x) \geq 1$. This factor can be obtained by calculating an integral over all collision velocities.¹³⁷ In case of a hard sphere interaction potential one obtains the analytical expression

$$F_{a_0}(\infty, x) = \frac{1}{\sqrt{\pi}} \left\{ \frac{1}{x} e^{-x^2} + \left(2 + \frac{1}{x^2} \right) \frac{\sqrt{\pi}}{2} \text{erf}(x) \right\} , \quad (2.20a)$$

where the usual definition of the error function

$$\text{erf}(x) = \frac{2}{\sqrt{\pi}} \int_0^x e^{-t^2} dt \quad (2.20b)$$

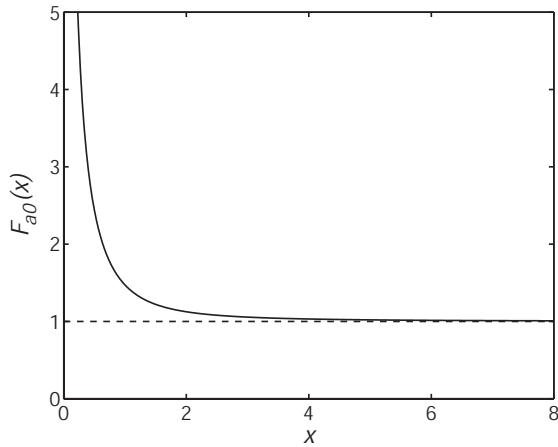


FIGURE 2.14: Plot of the correction factor $F_{a_0}(\infty, x)$ as defined by equation (2.20a). According to equation (2.21) the argument x can be identified as the ratio of droplet speed v_D and the most prominent speed \hat{v}_S of the scattering gas.

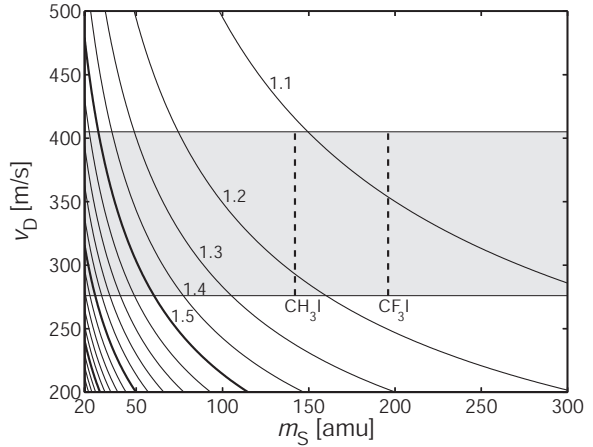


FIGURE 2.15: Contour plot of the correction factor $F_{a_0}(\infty, x)$ as a function of impurity mass m_S and droplet beam speed v_D based on a kinetic temperature of $T_S = 295$ K. The shaded region shows the experimentally accessible droplet beam speeds at a stagnation pressure of 30 bar and nozzle temperatures of 11 K to 19 K.

is employed. The argument x in expression (2.20a) is equal to the ratio of droplet speed v_D and the most probable speed \hat{v}_S of the thermal scattering gas of mass m_S , that is

$$x = \frac{v_D}{\hat{v}_S} = \frac{v_D}{\sqrt{2k_B T_S/m_S}}. \quad (2.21)$$

Consequently, the correction factor obeys

$$\lim_{x \rightarrow \infty} F_{a_0}(\infty, x) = 1 \quad (2.22)$$

as the limit of a static scattering gas requires. This behaviour of $F_{a_0}(\infty, x)$ is illustrated in Figure 2.14.

It is instructive to examine $F_{a_0}(\infty, x)$ for realistic experimental conditions. Figure 2.15 therefore shows a contour plot of the correction factor for a wide range of droplet speeds and masses m_S of the scattering partner. Within the experimentally accessible range of droplet speeds, indicated by the shaded region, the differences between the two principal scattering species CH_3I and CF_3I used in our experiments are less than 6%. As this difference is small compared to other uncertainties of the system, *e.g.* pressure readings, it can often be neglected. Due to their higher thermal speeds collisions with lighter scattering partners such as H_2O or H_2 are, however, much more likely (see Table 2.3) and therefore special care has to be taken to reduce the background pressure of these species in the scattering cell.

Including the correction factor $F_{a_0}(\infty, x)$ equation (2.19) takes on the form

$$\frac{dP_{\text{cap}}(N)}{dz} = F_{a_0}(\infty, x) n_S \sigma_{\text{cap}}(N) \quad (2.23)$$

v_D [m/s]	H ₂	H ₂ O	CH ₃ I	CF ₃ I
276	6.47	2.33	1.22	1.16
405	4.46	1.73	1.11	1.08

TABLE 2.3: Correction factor $F_{a_0}(\infty, x)$ for various scattering gases at room temperature. Values are given for the highest and lowest droplet beam speed v_D used in this work.

which with the aid of the ideal gas law $n_S = p_S / (k_B T_S)$ can be rewritten as

$$\alpha_N \equiv \frac{dP_{\text{cap}}(N)}{dz} = \frac{F_{a_0}(\infty, x) p_S \sigma_{\text{cap}}(N)}{k_B T_S} . \quad (2.24)$$

Here, the size dependent inverse mean free path α_N was introduced to obtain a more compact notation.

We will now use this expression to calculate the intensities $I_{N,k}(z)$ of helium clusters of size N having captured exactly k impurity particles ($k = 0, 1, 2, \dots$) as a function of the droplet position z inside the scattering cell of length L . In order to facilitate these calculations we make the assumption that the size of a helium droplet does not change in the aftermath of a collision with the scattering gas. This assumption implies that the capture cross section is independent of the number k of impurities introduced into the droplet. The evaporative loss of helium atoms following a collision is therefore neglected. As discussed in Section 2.4.3 we expect the capture of a CH₃I or CF₃I molecule to lead to an evaporation of only a few hundred atoms. For large clusters of some thousand atoms this assumption thus certainly is a good approximation.

Having simplified the droplet beam in this manner we note that the intensity $I_{N,0}$ of pure helium droplets of size N will decrease with increasing position z in the scattering chamber, as each capture event signifies an intensity loss in favor of the monomer signal $I_{N,1}$:

$$\frac{dI_{N,0}(z)}{dz} = -\alpha_N I_{N,0}(z) . \quad (2.25a)$$

In contrast to $I_{N,0}$, any signal $I_{N,k}(z)$ with $k \geq 1$ can grow with z , as both losses to more highly doped droplets and gains from droplets containing one impurity less have to be included:

$$\frac{dI_{N,k}(z)}{dz} = \alpha_N [I_{N,k-1}(z) - I_{N,k}(z)] . \quad (2.25b)$$

It is straightforward to show that the solution to the coupled differential equations (2.25) at the end of the scattering cell ($z = L$) for all $k = 0, 1, \dots, \infty$ is given by a Poisson distribution

$$I_{N,k}(L) = I_{\text{tot}}(N) \frac{(\alpha_N z)^k}{k!} \exp(-\alpha_N z) \Big|_{z=L} = I_{\text{tot}}(N) \frac{(\alpha_N L)^k}{k!} \exp(-\alpha_N L) , \quad (2.26)$$

where we implicitly define the position independent total intensity of size N clusters in the droplet beam

$$I_{\text{tot}}(N) = \sum_{k=0}^{\infty} I_{N,k}(z) . \quad (2.27)$$

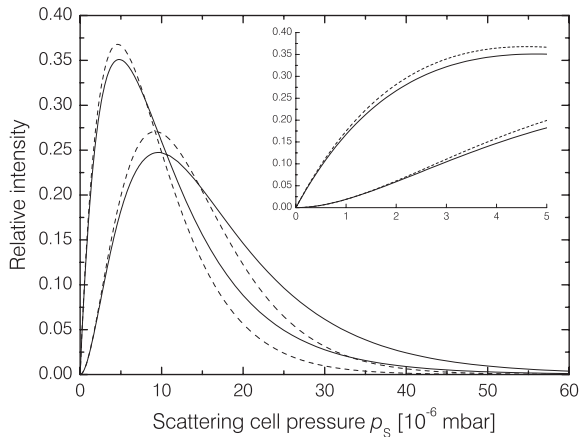


FIGURE 2.16: Comparison of the relative intensities $\overline{P}_k(p_s)$ and $P_{\overline{N},k}(p_s)$ for singly ($k = 1$) and doubly ($k = 2$) doped helium droplets. $\overline{P}_k(p_s)$ (solid lines) represents an average over the droplet size distribution, while $P_{\overline{N},k}(p_s)$ (dashed lines) is a pure Poisson distribution that would be obtained if the droplet beam contained only clusters of size \overline{N} . The curves have been calculated for typical source conditions of $p_o = 30$ bars and $T_o = 15$ K. The scattering gas is CH_3I .

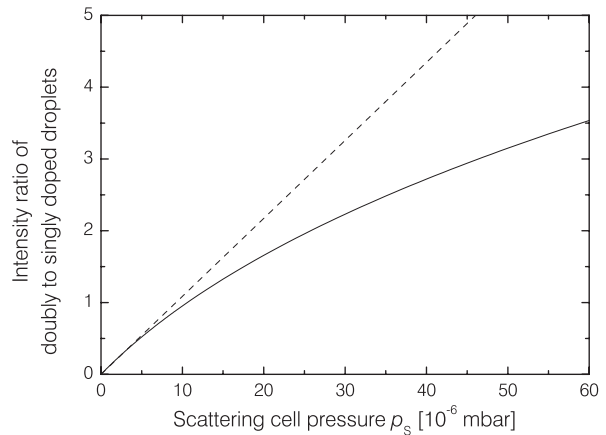


FIGURE 2.17: Intensity ratio of doubly to singly doped helium clusters for the same source conditions as in Figure 2.16. Solid lines show the intensity ratio $\overline{P}_2(p_s)/\overline{P}_1(p_s)$ obtained for a realistic cluster size distribution, while the dashed lines illustrate the result $P_{\overline{N},2}(p_s)/P_{\overline{N},1}(p_s)$ in case of a simplified helium cluster beam containing only droplets of size \overline{N} .

In order to examine the effect of the scattering cell pressure p_s on the individual intensities of size N clusters doped with k foreign particles we rewrite the Poisson distribution given by equations (2.26) and (2.24) in the following way:

$$P_{N,k}(p_s) \equiv \frac{(\beta_N p_s)^k}{k!} \exp(-\beta_N p_s), \quad (2.28a)$$

where

$$\beta_N \equiv \frac{F_{a_0}(\infty, x) L \sigma_{\text{cap}}(N)}{k_B T_S}. \quad (2.28b)$$

Here, $P_{N,k} = I_{N,k}(L)/I_{\text{tot}}(N)$ denotes the relative intensity of droplets containing k impurities among all droplets of size N . The *size independent* relative intensity \overline{P}_k of k -mer doped droplets finally is obtained considering the atom number distribution $f(N)$ given by equation (2.8):

$$\overline{P}_k(p_s) = \int_0^\infty P_{N,k}(p_s) f(N) dN. \quad (2.29)$$

The integral (2.29) over all atom numbers N can easily be evaluated numerically for a given set of parameters. Frequently, however, the pure Poisson distribution $P_{\overline{N},k}(p_s)$ is used as an approximation to $\overline{P}_k(p_s)$. It is instructive to examine the quality of this approximation for realistic experimental conditions. We choose the rather typical expansion conditions of $p_o = 30$ bar and $T_o = 15$ K that correspond to a mean droplet size of 6080 atoms (see Table 2.2). Under

these conditions the droplet beam speed v_D is 355 m/s. The calculations were carried out for the model impurity CH_3I . The total scattering cross section is evaluated according to equation (2.15) and a sticking coefficient $S = 1$ is assumed. Figure 2.16 illustrates the obtained pick-up curves for $k = 1, 2$ in a relevant range of pressures p_S in the room temperature scattering cell of geometrical length $L = 0.112$ m. For the same pressure range the calculated intensity ratio of singly and doubly doped droplets is shown in Figure 2.17. From Figure 2.16 it becomes clear that taking into account the cluster size distribution $f(N)$ results in somewhat wider curves. For high scattering cell pressures p_S the pure Poisson approximation significantly underestimates the relative intensities of both singly and doubly doped helium droplets. However, good agreement is found for small pressures in the rising part of the pick-up curves. Moreover, almost identical peak positions are obtained. This trend is confirmed by the data shown in Figure 2.17. Again, the intensity ratio obtained from pure Poisson distributions is found to be a good approximation in the limit of small pressures.

We conclude that the Poisson distribution $P_{\bar{N},k}(p_S)$ may constitute a good approximation, especially for small scattering cell pressures p_S corresponding to the rising part of the respective pick-up curve. The approximation may even be somewhat improved if the capture cross section of an average size droplet $\sigma_{\text{cap}}(\bar{N})$ is replaced by the slightly smaller value $\bar{\sigma}_{\text{cap}}$ which denotes an average over the atom number distribution. Introducing the more compact notation $P_k(p_S)$ for the relative intensities we thus finally obtain the approximate Poisson description

$$P_k(p_S) \equiv \frac{(\beta p_S)^k}{k!} \exp(-\beta p_S), \quad (2.30a)$$

with

$$\beta \equiv \frac{F_{a_0}(\infty, x) L \bar{\sigma}_{\text{cap}}}{k_B T_S}. \quad (2.30b)$$

Figure 2.18 illustrates the result for the scattering gas CH_3I and the typical source conditions of $p_o = 30$ bar and $T_o = 15$ K. Together with the relative intensities P_k for $k = 0, 1, 2, 3$ the leading terms $(\beta p_S)^k/k!$ of the distributions are plotted, which become an increasingly valid approximation for low scattering gas pressures. We note that in order to efficiently keep the droplets from picking up undesired impurities in the scattering cell, the background pressure of gases other than helium should not exceed about $1 \cdot 10^{-7}$ mbar. For light species such as molecular or atomic hydrogen even more modest background pressures may be needed (see Table 2.3).

From the first derivative of equation (2.30a) the pick-up of k impurities is easily shown to become maximal for $P_k(p_S^{\text{max}}) = P_{k-1}(p_S^{\text{max}})$. Hence, as shown in Figure 2.18, the maxima are given as the crossing points of successive distributions. This leads to a series of equally spaced maxima at pressures

$$p_S^{\text{max}} = \frac{k}{\beta} = k \cdot \frac{k_B T_S}{F_{a_0}(\infty, x) L \bar{\sigma}_{\text{cap}}}, \quad (2.31)$$

which is a useful equation for calibration purposes.

The pressure dependence of the relative intensities P_k has been observed experimentally in both mass-spectrometric¹⁹ and spectroscopic^{68, 138, 139} studies. In spite of the approximations made to derive the functional form (2.30) good agreement with the predicted Poisson distributions is found. Equation (2.31) therefore provides a simple means to assign a mean capture

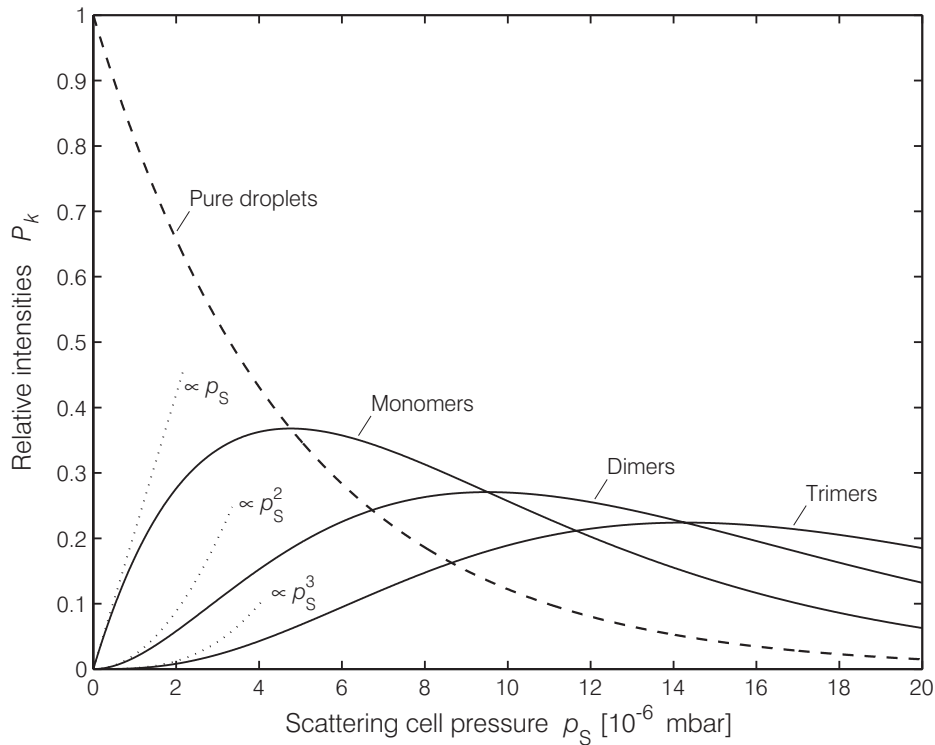


FIGURE 2.18: Plot of the relative intensities P_k of k -mer doped ${}^4\text{He}$ clusters as a function of the scattering cell pressure p_S , estimated for typical source conditions of $p_o = 30$ bar and $T_o = 15$ K. The mean cluster size of $\bar{N} = 6080$ atoms corresponds to an mean integral scattering cross section of 6720 \AA^2 (see equation (2.16)). The relative intensities for $k = 0, 1, 2, 3$ are approximated by Poisson distributions according to the equations (2.30), based on a geometric length $L = 0.112$ m of the cell, a droplet speed $v_D = 355$ m/s and an impurity mass of 142 amu (CH_3I). Furthermore, a sticking coefficient of $S = 1$ is assumed.

cross section to particular source conditions and hence to obtain an estimate of the droplet sizes produced.

Mass-spectrometric studies using electron impact ionization are, however, notoriously impaired by fragmentation of the impurity complexes. Although early studies seemed to indicate that fragmentation of subclusters in helium droplets is largely quenched,^{19,140} careful examinations of small rare gas^{113,141} and $(\text{NO})_n$ clusters¹⁴² demonstrated later that considerable fragmentation can indeed occur. In the case of $(\text{NO})_2$ subclusters in helium droplets the fragmentation to NO^+ occurs with unit probability for certain droplet sizes and thus can even be more likely than in free clusters.¹⁴³ Spectroscopic investigations, on the other hand, can specifically address an individual k -mer and thus do not suffer from those ambiguities. The subcluster size corresponding to an observed resonance is readily identified from the dependence of the signal on the scattering cell pressure. This requires, however, that resonances of different k -mers do not overlap spectrally.

2.4.3 Evaporation of helium atoms subsequent to a pick-up process

Following a sticking collision between a foreign molecule and a helium droplet, the kinetic energy of the collision, the molecule's internal energy E_{int} as well as the binding energy E_{bind} of the impurity to the droplet will be dissipated to the droplet. This energy release $E_{\text{pick-up}}$ hence can be written as

$$E_{\text{pick-up}} = \frac{1}{2} \frac{m_S m_D}{m_S + m_D} (\mathbf{v}_S - \mathbf{v}_D)^2 + E_{\text{int}} + E_{\text{bind}}, \quad (2.32)$$

where m_D is the mass of the droplet, and \mathbf{v}_D and \mathbf{v}_S are the velocity vectors of the droplet and the scattering partner in the laboratory frame, respectively. Making use of the geometries and mass ratios involved, the kinetic term in this equation can be simplified considerably.¹⁹ We note first that the droplet mass usually is much larger than the mass of the scattering gas particle. Moreover, the mean energy release $\langle E_{\text{pick-up}} \rangle$ is obtained by averaging the right hand side of equation (2.32) over all velocities \mathbf{v}_S . We obtain therefore

$$\langle E_{\text{pick-up}} \rangle = \frac{m_S}{2} \langle (\mathbf{v}_S - \mathbf{v}_D)^2 \rangle + E_{\text{int}} + E_{\text{bind}} \quad (2.33a)$$

$$= \frac{m_S}{2} (\langle v_S^2 \rangle + \langle v_D^2 \rangle - 2 \langle v_S v_D \cos \vartheta \rangle) + E_{\text{int}} + E_{\text{bind}}, \quad (2.33b)$$

where we have expressed the scalar product $\mathbf{v}_S \cdot \mathbf{v}_D$ using the angle ϑ between the two velocity vectors. The averaging conveniently is performed in a coordinate system aligned with the droplet velocity vector \mathbf{v}_D . In a scattering cell filled with gas the velocity vectors \mathbf{v}_S are distributed according to an isotropic Maxwell-Boltzmann distribution. For an isotropic velocity distribution the last term in the parenthesis involves the integral $\int_0^\pi \sin \vartheta \cos \vartheta d\vartheta = 0$ and therefore vanishes. As the term $\langle v_S^2 \rangle$ simply equals the mean squared velocity of the Maxwell-Boltzmann distribution we find

$$\langle E_{\text{pick-up}} \rangle_{\text{cell}} = \frac{3k_B T}{2} + \frac{m_S}{2} v_D^2 + E_{\text{int}} + E_{\text{bind}}, \quad (2.34)$$

where we assume that there is no significant spread in the speed distribution of the droplet beam.

Instead of passing the droplet beam through a scattering cell uniformly filled with gas it can be beneficial to cross the droplet jet with an effusive beam of dopant species. This alternative method to introduce impurities into helium droplets permits a much more efficient use of the scattering species as high densities are produced locally. Moreover, the flux of chromophores from the scattering cell into the detection chamber is significantly reduced as a directed flow towards a pump can be established. In our apparatus the effusive beam from a slit nozzle intersects the droplet beam at right angles. For this particular geometry the collision energy takes on a similar form as in equation (2.34). However, the velocity vectors of the scattering particle are roughly parallel so that mean squared velocity $\langle v_S^2 \rangle$ has to be evaluated one-dimensionally. Hence, we obtain

$$\langle E_{\text{pick-up}} \rangle_{\text{eff}} = \frac{k_B T}{2} + \frac{m_S}{2} v_D^2 + E_{\text{int}} + E_{\text{bind}}. \quad (2.35)$$

Collisions with a purely effusive beam therefore are gentler than collisions with a particle in a scattering cell as the average available energy is reduced by $k_B T$.

Molecule	Vibrational constants [cm^{-1}]						Rot. constants [cm^{-1}]	
	ν_1	ν_2	ν_3	ν_4	ν_5	ν_6	A_o	B_o
CH ₃ I	2971	1254	528	3060	1436	883	5.11	0.250217
CF ₃ I	1075	743	286	1187	540	262	0.1910	0.050808

TABLE 2.4: Molecular constants of CH₃I and CF₃I. The vibrational constants for CF₃I are from reference [144], while those for CH₃I are from the compilation in [145]. The rotational constants are taken from [146].

The mean rovibrational internal energies E_{int} of the chromophores CH₃I and CF₃I at room temperature have been estimated on the basis of the rigid rotor and harmonic oscillator approximations using the vibrational and rotational constants shown in Table 2.4. The resulting values for E_{int} as well as $\langle E_{\text{pick-up}} \rangle_{\text{cell}}$ are given in Table 2.5 without, however, taking into account the unknown binding energy E_{bind} of the impurity. Based on the bulk binding energy of $7.2 \text{ K} = 5.0 \text{ cm}^{-1}$ per ⁴He atom the ensuing loss of helium atoms by evaporation can readily be estimated. Depending on the speed of the droplet beam we find a mean loss $\langle \Delta N \rangle_{\text{cell}}$ of about 230–330 ⁴He atoms for CH₃I and of 330–475 atoms for CF₃I using the scattering cell. If an effusive beam is employed instead, the evaporation of ⁴He atoms is expected to be reduced by about 40 atoms. Binding energies of molecular species to helium droplets have been calculated for SF₆¹⁴⁷ and are found to be of the order of 500 cm^{-1} . We therefore expect the release of the binding energy E_{bind} to cause the additional evaporation of some 100 atoms.

These estimates indicate that following the absorption of a single CH₃I or CF₃I molecule the helium cluster will loose some 300–600 atoms by evaporation. The cross section for capturing a second impurity will therefore be somewhat smaller, an effect which has been neglected when deriving the Poisson distributions in equations (2.30). In this work, however, special care was taken to make sure that the vast majority of helium droplets contain either no or only a single impurity when their properties are interrogated experimentally. Therefore, the reduced cross section for capturing a second or third particle are of minor relevance here.

Molecule	$\langle E_{\text{rot}} \rangle$ [cm^{-1}]	$\langle E_{\text{vib}} \rangle$ [cm^{-1}]	$\langle E_{\text{int}} \rangle$ [cm^{-1}]	$\frac{m_{\text{s}}}{2} v_{\text{D}}^2$ [cm^{-1}]	$\langle E_{\text{pick-up}} \rangle_{\text{cell}}$ [cm^{-1}]	$\langle \Delta N \rangle_{\text{cell}}$
CH ₃ I	307	73	381	[452] [974]	[1140] [1662]	[228] [332]
CF ₃ I	308	414	721	[624] [1344]	[1653] [2373]	[331] [475]

TABLE 2.5: Available energy following a collision between a helium droplet and a CH₃I or CF₃I molecule at room temperature (295 K). Values depending on the speed v_{D} of the droplet beam are given for the smallest and largest experimental speed of 276 m/s ([...]) and 405 m/s ([...]), respectively. The mean values $\langle E_{\text{pick-up}} \rangle_{\text{eff}}$ for pick-up processes using the effusive beam can be obtained by subtracting $k_{\text{B}}T = 205 \text{ cm}^{-1}$ from $\langle E_{\text{pick-up}} \rangle_{\text{cell}}$. The contribution of the binding energy E_{bind} is neglected in this table.

2.5 Photodissociation of CF_3I and CH_3I in the gas phase

2.5.1 Introduction

In a typical photodissociation experiment an ensemble of isotropically oriented species is excited to a repulsive electronic state which subsequently causes the molecules to fragment. When a linearly polarized photolysis laser is used, a direction in the laboratory frame is singled out by its electric field vector \mathbf{E} . The polarization direction defines an important frame of reference as several vector quantities characteristic of the dissociation may be correlated to \mathbf{E} . These vector quantities include the electronic and rotational angular momentum of the photofragments and, most notably, their velocity \mathbf{v} . The latter encompasses the angular distribution of the fragments from which many details of the dissociation dynamics can be deduced. For a one-photon transition the center-of-mass angular distribution $I(\theta)$ of the photofragments with respect to the polarization direction \mathbf{E} is given by¹⁴⁸

$$I(\theta) = \frac{1}{4\pi} [1 + \beta \cdot P_2(\cos \theta)] , \quad (2.36)$$

where θ is the angle between \mathbf{v} and \mathbf{E} , β denotes the so-called recoil anisotropy parameter, and P_2 is the second-order Legendre polynomial, *i.e.* $P_2(x) = (3x^2 - 1)/2$.

Equation (2.36) gives evidence of an $\mathbf{E}-\boldsymbol{\mu}-\mathbf{v}$ correlation, where $\boldsymbol{\mu}$ stands for the electronic transition dipole moment of the parent molecule. The relative orientation of \mathbf{E} and $\boldsymbol{\mu}$ determines the absorption probability which is proportional to $(\boldsymbol{\mu} \cdot \mathbf{E})^2$. The $\boldsymbol{\mu}-\mathbf{v}$ correlation is measured by the anisotropy parameter β . It is defined as the expectation value

$$\beta = 2 \langle P_2(\cos \chi) \rangle , \quad (2.37)$$

where χ is the angle between $\boldsymbol{\mu}$ and the observed fragment velocity \mathbf{v} , and P_2 is the second-order Legendre polynomial given above. Accordingly, β can take on the values $-1 \leq \beta \leq 2$.

At this point it is instructive to introduce the approximation of *axial recoil*, where the photofragment trajectories are assumed to follow the direction of the chemical bond at the moment of photoexcitation. In other words, the observed velocity vector \mathbf{v} is taken to be parallel to the initial direction of the breaking bond. The inspection of equation (2.37) in the axial recoil limit shows that a purely *parallel* dissociative transition corresponds to $\beta = 2$, whereas a purely *perpendicular* transition leads to $\beta = -1$. In this approximation, the angular distributions $I(\theta)$ are proportional to $\cos^2 \theta$ in the case of a parallel transition, while a perpendicular transition yields $I(\theta) \propto \sin^2 \theta$.

The axial recoil approximation breaks down if the dissociative life time becomes comparable to the rotational period of the excited parent molecule or if the shape of the excited state potential energy surface leads to off-axis nuclear motion. In both cases β can take on values other than -1 and 2 . There are, however, further mechanisms that may bring about intermediate values of β . For instance, both parallel and perpendicular dissociative transitions may be excited simultaneously and contribute to the outcome of the monitored photodissociation process. In this case, β may be written as the sum¹⁴⁹

$$\beta = a\beta_{\parallel} + b\beta_{\perp} , \quad (2.38)$$

where a and b denote the relative intensities of the parallel and the perpendicular contributions, respectively. Furthermore, in polyatomic molecules dissociative transitions with neither parallel nor perpendicular character may be allowed.

Measuring angular distributions thus may not only shed light on the relative time scales of the parent rotation and dissociation process but can also reveal the symmetry of the ground and excited electronic states involved.

We now proceed to consider the energy balance of the model photodissociation reaction of CX_3I into the fragments I and CX_3 , where X denotes an H or F atom. This energy balance can be written as

$$E_{\text{int}}(CX_3I) + h\nu = D_0 + T_{\text{tot}} + E_{\text{int}}(I) + E_{\text{int}}(CX_3) , \quad (2.39)$$

where E_{int} denotes the internal energy of the designated molecule or photofragment, $h\nu$ is the energy of the photolysis photon, D_0 stands for the dissociation energy of the parent molecule, and T_{tot} is the total kinetic energy release of the dissociation reaction. In view of the cooling provided by a supersonic expansion or, as in our case, by the helium environment, the internal energy of the parent molecule can be neglected. One consequently may write the total kinetic energy release as

$$T_{\text{tot}} = h\nu - D_0 - E_{\text{int}}(I) - E_{\text{int}}(CX_3) . \quad (2.40)$$

The partitioning of the total translational energy T_{tot} among the fragments is obtained from momentum conservation which yields

$$T(I) = \left(\frac{m(CX_3)}{m(I) + m(CX_3)} \right) T_{\text{tot}} , \quad (2.41a)$$

and

$$T(CX_3) = \left(\frac{m(I)}{m(I) + m(CX_3)} \right) T_{\text{tot}} , \quad (2.41b)$$

where m denotes the mass of the designated molecule or fragment. The ratio of the kinetic energies thus is the inverse of the fragments' mass ratio.

2.5.2 Photodissociation in the A band

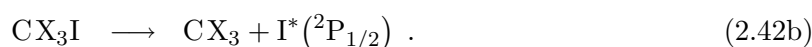
The dissociation of CH_3I and, to lesser extent, of its fluorinated analogue CF_3I by near ultraviolet (UV) radiation rank among the most extensively studied photochemical reactions and have become model systems for understanding the photodissociation dynamics of polyatomic molecules. The extensive and continuously expanding body of literature on these reactions has been reviewed regularly.^{145, 150, 151}

The first UV absorption band is known as ‘‘A band’’. Centered around 265 nm it broadly covers the wavelength range from about 210 nm to 330 nm. An excitation to the A band promotes a nonbonding electron from the iodine atom to the antibonding σ^* molecular orbital associated with the C–I bond ($n \rightarrow \sigma^*$ transition) and thereby initiates the disintegration of the molecule. The photodissociation lifetime of CH_3I has been measured by pump-probe experiments^{152, 153} and was found to be of the order of 100 fs, in agreement with earlier estimates.¹⁵⁴ Since this time scale is short compared to a rotational period of the parent molecule,

the A band dissociation of CH₃I is thought of as a fast and direct process where a rotational smearing of the angular distributions is not expected. Analogous arguments apply to the dissociation of CF₃I which is taken to proceed on a similar time scale.¹⁵⁵ Following an electronic excitation in the A band these molecules therefore promptly dissociate to produce (fluorinated) alkyl radicals and either ground state (²P_{3/2}) or spin-orbit excited (²P_{1/2}) iodine atoms. The spin-orbit coupling¹⁵⁶ of 7603 cm⁻¹ in iodine is much larger than the width of the rovibrational energy distributions of the alkyl fragments and thus gives rise to two energetically distinct decay channels,



and



The dissociation dynamics of this reaction are closely related to the electronic structure of the A band. Mulliken¹⁵⁷ was the first to point out that the broad A band arises from a superposition of optically allowed transitions from the ground state *X* to three repulsive electronic states, which he termed ³Q₁, ³Q₀ and ¹Q₁ in order of increasing energy. Based on magnetic circular dichroism measurements Gedanken and co-workers disentangled the contributions of these three transitions for various alkyl iodides including CH₃I¹⁵⁸ and CF₃I.¹⁵⁹ They found that the ³Q₀ ← *X* transition is dominant and accounts for about 80% of the total absorption across the A band. The absorption maxima of the transitions to ³Q₁, ³Q₀ and ¹Q₁ in CH₃I (CF₃I) were located at 299.9 (301.8), 261.1 (264.1) and 239.8 (237.9) nm, respectively. As the weaker transitions ³Q₁ ← *X* and ¹Q₁ ← *X* are located in the low- and high-energy wings of the spectrum, respectively, the preferential excitation shifts from ³Q₁ and ³Q₀ to ³Q₀ and ¹Q₁ as the photolysis laser is tuned from longer to shorter wavelengths.

Figure 2.19 schematically shows the potential energy curves of the three electronically excited states along the C–I reaction coordinate. In the *C*_{3*v*} notation the ³Q₀ state has *A*₁ symmetry and correlates diabatically to the CX₃ + I* product channel (2.42b), whereas both the ³Q₁ and the ¹Q₁ have *E* symmetry and correlate diabatically to CX₃ + I (2.42a). On account of the *A*₁ symmetry of the electronic ground state the ³Q₀ ← *X* transition has a transition moment parallel to the *C*₃ axis of the parent molecule, while the ³Q₁ ← *X* and ¹Q₁ ← *X* transitions are perpendicular. In the limit of diabatic behaviour and axial recoil the CX₃ + I* channel should therefore yield fragments with an anisotropy parameter of β* = 2, whereas the CX₃ + I channel should give β = -1. However, the experimentally observed angular distributions from A band dissociation of both CH₃I¹⁶⁰ and CF₃I^{155,161,162} generally exhibit β* values somewhat less than 2 and β values considerably greater than -1. The interpretation of these data begins with a closer inspection of the potential energy curves in Figure 2.19. The ³Q₁ curve is isolated from the other electronic states and produces only fragments with β = -1 in the axial recoil limit. The curves associated with the ³Q₀ and ¹Q₁ states, however, reveal a crossing point. Whereas parent molecules prepared in ³Q₀ dissociate diabatically to CX₃ + I*, non-adiabatic population transfer to the ¹Q₁ surface at the crossing point produces CX₃ + I with an anisotropy parameter β = 2. Similarly, an excitation to the ¹Q₁ state, followed by a non-adiabatic transition to the ³Q₀ surface yields CX₃ + I* with β* = -1. The ³Q₀ → ¹Q₁ curve crossing thus gives a contribution to the CX₃ + I product channel that explains the observation of β > -1, while ¹Q₁ → ³Q₀ population transfer is thought to make the anisotropy

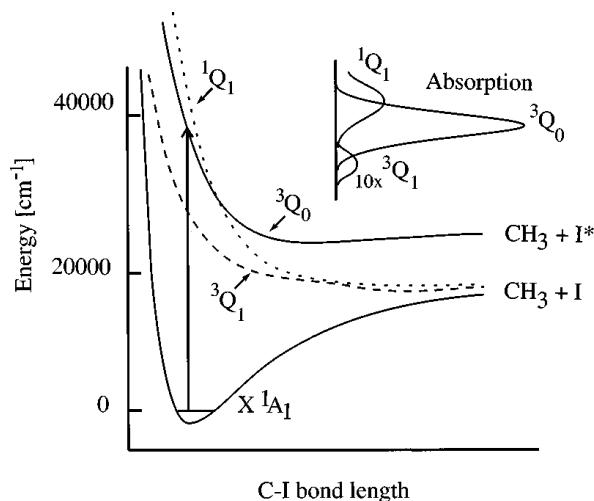


FIGURE 2.19: Schematic illustration of the potential energy surfaces relevant to the photodissociation of CH_3I . The inset shows the deconvoluted absorption spectra from Gedanken and Rowe.¹⁵⁸ Similar considerations apply to CF_3I . The figure is reproduced from reference [160].

parameter β^* deviate from 2. In the red wing of the A band an excitation to the high-energy 1Q_1 surface may be neglected. The simultaneous excitation of the 3Q_1 and 3Q_0 states then leads to a mixed anisotropy in the I channel via $^3Q_0 \rightarrow ^1Q_1$ curve crossing that can be unraveled according to equation (2.38). In the far red wing of the A band an excitation to the 3Q_0 state becomes less likely and the I channel therefore is expected to show an increasingly pure perpendicular character with anisotropy parameters approaching $\beta = -1$.

Initial attempts to explain observed quantum yields for alkyl and substituted-alkyl iodides were made on the basis of a one-dimensional Landau-Zener model,¹⁶³ which, however, failed to predict differences in I channel quantum yield from CH_3I and CD_3I . As the transfer of population between the repulsive surfaces 1Q_1 and 3Q_0 requires a distortion of the C_{3v} symmetry of the dissociating molecule, Person *et al.*¹⁶⁴ have linked the coupling to an excitation of the e symmetry vibrations of the parent molecule. Considering the $^3Q_0 \rightarrow ^1Q_1$ curve crossing process they predicted stronger coupling for wave functions on the 3Q_0 surface that extend deeper into regions of reduced (C_S) symmetry. This qualitative model then was successfully applied to explain the quantum yields from CH_3I and CD_3I at 248 nm. They argued that CH_3I , having a larger zero-point motion, is more likely to sample regions of C_S symmetry on the 3Q_0 surface and therefore has a higher probability of finally producing ground-state iodine. The authors also controlled the thermal excitation of the low frequency e symmetry vibration (ν_6 , see Table 2.4) of CF_3I in a molecular beam by varying the nozzle temperature and found an enhanced I channel quantum yield for thermally excited CF_3I in agreement with their predictions. Deviations from the C_{3v} symmetry in the dissociation process also are indicated by classical trajectory calculations on *ab initio* potential energy surfaces carried out by Amatatsu *et al.*^{165,166} These authors predict the $\text{CH}_3\text{-I}$ axis to bend slightly by about 5° as the C-I distance increases resulting in a rotational excitation of the free CH_3 fragment about an axis perpendicular to its C_3 axis. Vibrational excitation has been found mainly in

$\lambda = 266.1 \text{ nm}$	$D_0 = 19440 \pm 160 \text{ cm}^{-1}$	$h\nu - D_0 = 18140 \text{ cm}^{-1}$			
Product channel	$E_{\text{int}}(\text{I})$ [cm^{-1}]	$\langle E_{\text{int}}(\text{CH}_3) \rangle$ [cm^{-1}]	$\langle T_{\text{tot}} \rangle$ [cm^{-1}]	$\langle T(\text{CH}_3) \rangle$ [cm^{-1}]	$\langle T(\text{I}) \rangle$ [cm^{-1}]
$\text{CH}_3 + \text{I}^*$ $\phi^* = 0.73, \beta^* = 1.9$	7603	390	10150	9080	1070
$\text{CH}_3 + \text{I}$ $\phi = 0.27, \beta = 1.8$	0	1500	16640	14880	1760

TABLE 2.6: Quantum yields, anisotropy parameters and energy partitioning in the 266 nm photodissociation of CH_3I . The shown data is a compilation of published results (see text). The bond energy D_0 is taken from reference [145].

the umbrella mode ν_2 of the CX_3 fragments, whose frequency is 606 cm^{-1} and $\approx 700 \text{ cm}^{-1}$ in CH_3 ¹⁶⁷ and CF_3 ,¹⁶² respectively. For CH_3I this result comes unsurprisingly as the geometry of the alkyl group changes from pyramidal in the parent molecule to near-planar^{167,168} in the free radical. In contrast to the methyl radical the free CF_3 group retains a pyramidal structure¹⁶⁸ thus rendering an umbrella mode excitation is less obvious. Nevertheless, as will be shown below, the internal excitation of the CF_3 fragment is on average even larger than for CH_3 .

In order to establish the initial conditions for the 266 nm dissociation experiments inside helium droplets we proceed to discuss available data on the gas phase dissociation of both CH_3I and CF_3I . Of particular interest are rovibrationally averaged quantum yields, anisotropy parameters and the initial kinetic energy of the fragments for which we give recommended values. Missing data is obtained from linear interpolation.

266 nm photolysis of CH_3I

The overall quantum yield ϕ^* in the I^* channel may be determined from a weighted average of the quantum yields for each populated vibrational state of the nascent methyl fragments. More straightforward experimental methods for determining ϕ^* are, however, based upon non-state-selective techniques such as electron-impact time-of-flight mass spectrometry.¹⁶⁹ Quantum yield measurements prior to 1998 have recently been summarized.¹⁶⁰ Unfortunately, some of these and later experiments at 266 nm were carried out on room temperature samples^{170,171} and should be taken with care as temperature effects on the quantum yield cannot be ruled out completely. Nevertheless results from molecular beam experiments are very similar^{169,172} and were shown to scale like the room temperature data when the wavelength of the photolysis laser is varied.¹⁶⁰ We therefore adopt the commonly accepted^{160,171} value of $\phi^* = 0.73$.

Recoil anisotropy parameters β and β^* for the I and I^* channel, respectively, are most conveniently obtained from ion imaging studies. Complications due to alignment effects in the CH_3 products may be avoided by monitoring the I and I^* products, images of which can be obtained separately. We use the results from a recent velocity map imaging study by Eppink and Parker¹⁶⁰ on jet-cooled molecules, who obtained values of $\beta^* = 1.90 \pm 0.05$ and $\beta = 1.8 \pm 0.05$

at 266 nm.

The energy partitioning following photodissociation has also been investigated by Eppink and Parker.¹⁴⁵ As expected, most of the vibrational energy disposed in the CH_3 fragment was found in the umbrella mode¹⁶⁷ ν_2 (606 cm^{-1}). Additionally, photolysis in the blue wing of the A band was shown to result in a significant excitation of the C–H symmetric stretch mode¹⁷³ ν_1 (3004 cm^{-1}). Using the velocity map imaging technique the authors recorded kinetic energy distributions for both the I and I* products, as well as CH_3 in the vibrational ground and the ($\nu_1 = 0, \nu_2 = 1, 2, 3$) and ($\nu_1 = 1, \nu_2 = 0$) vibrationally excited states. The CH_3 distributions were subsequently scaled and summed to match the iodine curves that each comprise all corresponding CH_3 rovibrational product states. In the I* channel no ν_1 excitation was observed and based and relative yields of [0.63, 0.28, 0.065, 0.02] were obtained for $\nu_2 = [0, 1, 2, 3]$. From these values we extract a mean vibrational energy disposal of 290 cm^{-1} in this channel.

Due to considerable excitation of the ν_1 mode in CH_3 , the I channel was found to display a weakly bimodal kinetic energy distribution at 266 nm. For $\nu_1 = 0$ the described summation gave relative yields [0.19, 0.29, 0.22] for $\nu_2 = [0, 1, 2]$, thus indicating a population inversion in agreement with many theoretical studies.^{150, 174–176} The experimentally found values are particularly consistent with classical trajectory calculations by Huang *et al.*¹⁷⁴ We use their theoretical values to complete the relative yields and obtain [0.19, 0.29, 0.22, 0.17, 0.05] for $\nu_2 = [0, 1, 2, 3, 4]$. Eppink and Parker estimated the fraction of ν_1 excited CH_3 molecules to be 0.19 ± 0.06 . Using these values and assuming that a ν_1 excitation occurs for $\nu_2 = 0$ only, one obtains a mean vibrational energy disposal of 1400 cm^{-1} in the I channel.

The rotational excitation of the CH_3 fragments at 266 nm has been measured by Houston and co-workers¹⁷⁷ and Chandler *et al.*¹⁷⁸ They obtained a mean rotational energy of $83 \pm 21\text{ cm}^{-1}$ and 114 cm^{-1} , respectively. We therefore adopt an estimated mean rotational excitation of 100 cm^{-1} in each product channel. The energy balance in equation (2.40) can then be used to obtain estimates for the mean kinetic energy of both products and in each channel. A summary of the analysis is given in Table 2.6.

With respect to the state-selective detection of methyl fragments carried out in this work we also note the ϕ^* quantum yield for specific vibrational states of this fragment. For the dissociation wavelength of 266 nm these quantum yields have recently been determined by Eppink and Parker.¹⁶⁰ For further reference we note their values for the vibrational ground state and for the first umbrella mode excited state which were given as $\phi^*(v = 0) = 0.94$ and $\phi^*(\nu_2 = 1) = 0.83$.¹⁶⁰

266 nm photolysis of CF_3I

Kavita *et al.*¹⁷⁹ have measured the the overall quantum yield of I and I* production from the photodissociation of CF_3I in the center and red wing of the A band. Using a room temperature sample and a two-photon laser-induced VUV fluorescence scheme they measured $\phi^* = 0.89$ at 266 nm. This value is in very good agreement with the results found for jet-cooled molecules by Kim *et al.*¹⁸¹ for 277 nm ($\phi^* = 0.87$) as well as with those of Felder¹⁶¹ ($\phi^* = 0.88$) and van Veen *et al.*¹⁴⁹ ($\phi^* = 0.92$) for 248 nm. We therefore adopt $\phi^* = 0.89$. A compilation¹⁷⁹ of quantum yields ϕ^* for perfluoroalkyl iodides across the A band illustrates that consistently

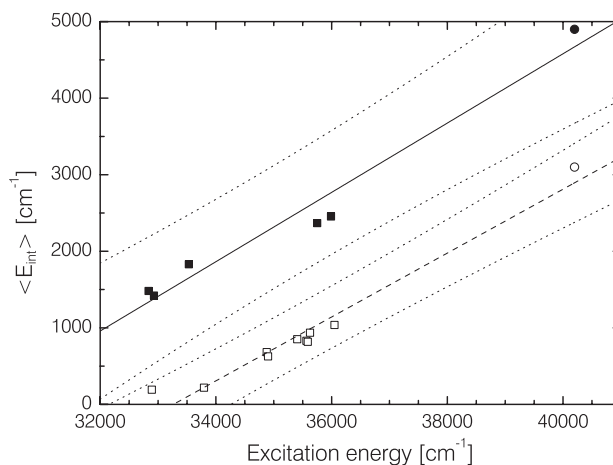


FIGURE 2.20: Mean internal energy of the CF_3 fragments as measured in the red wing of the A band by Aguirre and Pratt¹⁶² (squares) and at 248 nm by Felder¹⁸⁰ (circles). Open symbols correspond to the $\text{CF}_3 + \text{I}^*$ product channel, while filled symbols show data from the $\text{CF}_3 + \text{I}$ channel. The solid and dashed lines show linear fits to the data, while the dotted curves illustrate the 95% prediction bands of the fits.

higher yields ϕ^* can be expected than for their non-fluorinated analogues.

Measurements of the the recoil anisotropy parameters β and β^* in the red wing of the A band have been carried out by Furlan *et al.*¹⁵⁵ and very recently by Aguirre and Pratt.¹⁶² Both groups produced cool parent molecules in supersonic expansions and found β to increase from $\beta \approx -0.5$ at 300 nm to $\beta = 1.1$ around 275 nm in the I product channel. The values observed in the I^* channel disagree considerably at longer wavelength. However, with wavelengths approaching the center of the A band increasingly consistent values were observed. At the shortest wavelength under study values of $\beta^* = 1.91$ ¹⁵⁵ (275 nm) and $\beta^* = 1.90$ ¹⁶² (277.4 nm) were found. These results can be compared to earlier molecular beam studies by van Veen *et al.*¹⁴⁹, Felder¹⁶¹ and Person *et al.*¹⁶⁴ at 248 nm. They found $\beta^* = 1.42$ ¹⁴⁹ and $\beta^* = 1.6$ ^{161,164} in the I^* channel and almost isotropic angular distribution in the I channel with anisotropy parameters of $\beta = 0.64$,¹⁴⁹ $\beta = -0.2$ ¹⁶¹ and $\beta = 0.05$.¹⁶⁴ As a result we adopt an interpolated value of $\beta^* = 1.8$ in the I^* channel at 266 nm. In view of the substantial discrepancy between the literature values of β at the photolysis wavelength of 248 nm, we base our estimation of the anisotropy parameter in the I channel at 266 nm solely on the recent and more consistent measurements at 275 nm and adopt the value $\beta = 1.1$.

The energy partitioning into internal and translational contributions as a function of excitation energy has been studied by Furlan *et al.*¹⁵⁵ and very recently by Aguirre and Pratt¹⁶² in the red wing of the A band using pulsed molecular beams. The average internal energies $\langle E_{\text{int}} \rangle$ found by these two groups agree reasonably well and can be compared to the results of Felder¹⁸⁰ who studied the photodissociation of jet-cooled CF_3I at 248 nm. Figure 2.20 shows a plot of the tabulated results of Aguirre and Pratt as well as those of Felder. Linear interpolation yields mean internal energies at 266 nm of 3490 cm^{-1} and 1800 cm^{-1} in the I and I^* channel, respectively. A compilation of all adopted values for the 266 nm photodissociation of CF_3I is

$\lambda = 266.1 \text{ nm}$	$D_0 = 18780 \pm 105 \text{ cm}^{-1}$	$h\nu - D_0 = 18800 \text{ cm}^{-1}$			
Product channel	$E_{\text{int}}(\text{I})$ [cm^{-1}]	$\langle E_{\text{int}}(\text{CF}_3) \rangle$ [cm^{-1}]	$\langle T_{\text{tot}} \rangle$ [cm^{-1}]	$\langle T(\text{CF}_3) \rangle$ [cm^{-1}]	$\langle T(\text{I}) \rangle$ [cm^{-1}]
$\text{CF}_3 + \text{I}^*$ $\phi^* = 0.89, \beta^* = 1.8$	7603	1800	9400	6090	3310
$\text{CF}_3 + \text{I}$ $\phi = 0.11, \beta = 1.1$	0	3490	15310	9920	5390

TABLE 2.7: Quantum yields, anisotropy parameters and energy partitioning in the 266 nm photodissociation of CF_3I . The shown data is a compilation of results from the literature. Missing values have been interpolated or estimated (see text). The bond energy D_0 is taken from reference [182].

given in Table 2.7.

Chapter 3

Experimental Setup

3.1 Droplet Beam Apparatus

As part of this work a new helium droplet beam machine has been conceived, built and made operational. The apparatus has been specifically designed to study photoionization and -dissociation events inside or at the surface of helium clusters by ion and electron imaging techniques. Particular effort was made to ensure excellent vacuum in the detection region of the apparatus and to place this region at the shortest possible distance from the droplet source. The vacuum quality is crucial to successfully carrying out the experiments since the presence of residual gas chromophores in the detection region of the setup will in many cases lead to unacceptable levels of background signal in both electron and ion imaging studies. As the use of diffusion pumps unavoidably causes some hydrocarbon contamination, we alternatively chose to evacuate all vacuum stages of the machine exclusively by turbomolecular drag pumps. All of these pumps are backed by compact, dry membrane pumps (*MD 4, Vacuubrand*) which eliminate the risk of accidentally contaminating the vacuum system with high vapor pressure roughing pump oil. The short flight path to the detection region ascertains high droplet flux densities and, together with the low background pressure in the detection region, allows us to potentially achieve high signal-to-noise ratios.

Figure 3.1 shows a vertical section of the apparatus. It accommodates three differentially pumped vacuum chambers which are referred to as “source chamber”, “doping chamber” and “detection chamber”, respectively. All chambers are custom-designed and were manufactured by *Kurt J. Lesker Company* from AISI 304L (DIN 1.4306) stainless steel. They are electropolished in order to significantly reduce both the surface area and the chemical activity of the chamber walls and hence to obtain low outgassing rates.

Source and doping chamber form a mechanical and functional unit that is able to produce a high-intensity collimated beam of doped helium droplets with widely adjustable mean sizes. This unit and the detection chamber are mounted onto separate support frames. This way the chambers can more easily be transported, e.g. in order to be linked up to other experiments. The mechanical manipulation of the vacuum system is further facilitated by a ball rail system of 1200 mm travel, fixed to the support frame of the source unit (see Figure 3.2). This device allows one to readily slide back the source unit from the detection chamber and hence gain

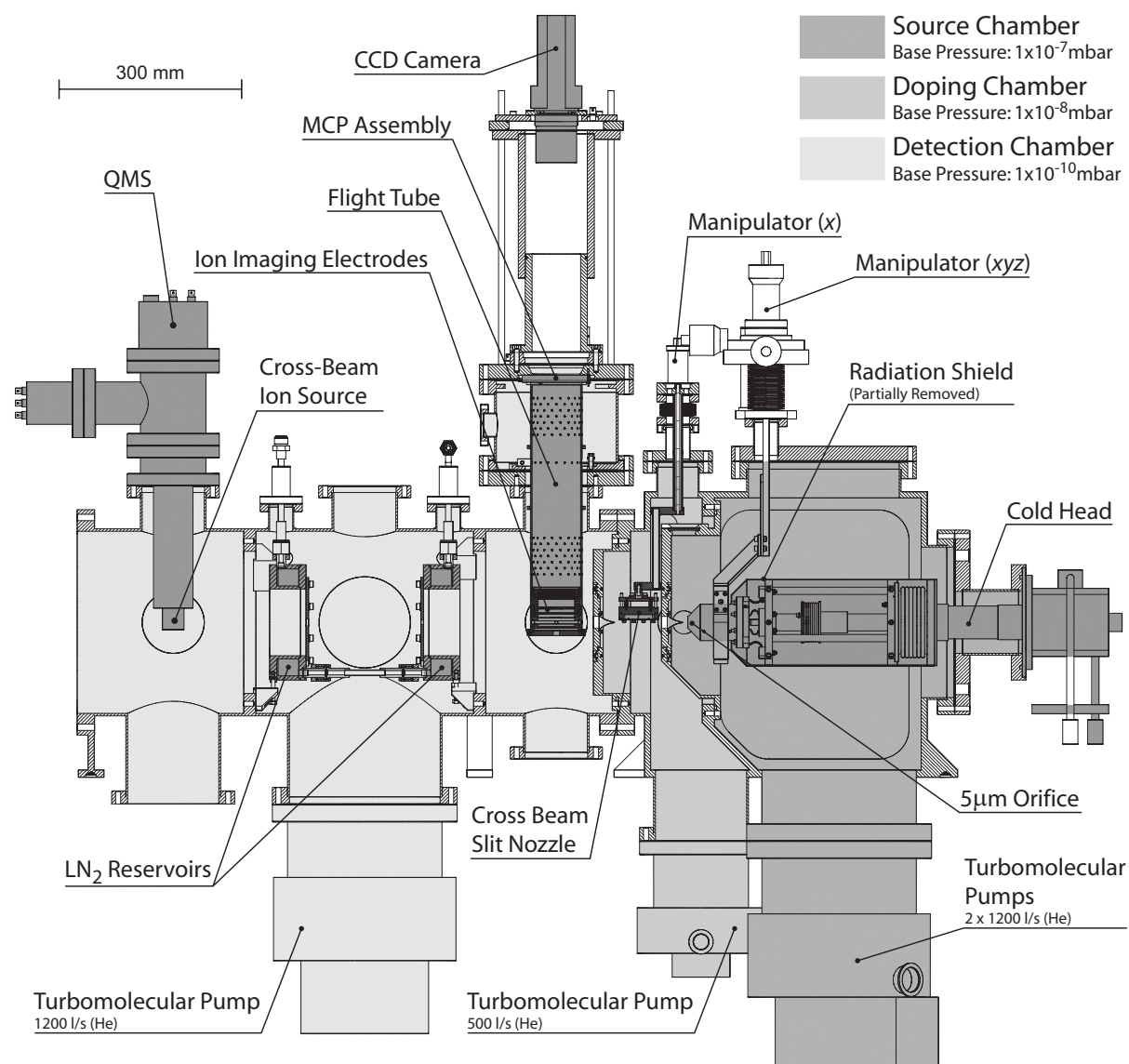


FIGURE 3.1: Accurate scale vertical cross section of the helium droplet machine through the axis of the molecular beam. The droplet beam propagates horizontally from right to left. The geometries of the three principal vacuum stages are highlighted by different gray shades. Some vacuum components, e.g. the bakeout lamps, are not shown.

access to the interior of the chambers through the connecting 14" Conflat flange.

The source chamber houses the continuous cluster source (see Section 3.3) and is equipped with two large turbomolecular drag pumps (*TMU 1601 P*, *Pfeiffer Vacuum*) with a nominal helium pumping speed of 2×1200 l/s to deal with the high particle flux entering this vacuum stage. The mainly o-ring sealed chamber offers easy access to the cryogenic components through two large 310 mm \times 410 mm openings on its sides and reaches a base pressure below

$1 \cdot 10^{-7}$ mbar. The pressure in the source chamber is measured by a combined Pirani and cold-cathode gauge (*PKR 251, Pfeiffer Vacuum*) that covers the full pressure range from $5 \cdot 10^{-9}$ mbar to 1 bar.

In the doping chamber the traversing droplets pick-up impurities via collisions. For this purpose the chamber is equipped with both a leak valve (*UDV 235, Balzers*) as well as a $50 \text{ mm} \times 50 \text{ }\mu\text{m}$ slit nozzle situated vertically above the droplet beam. The valve allows adjusting the leak rate such that a constant scattering gas pressure is obtained. Alternatively, a cross beam emerging from the slit nozzle can be used to make the droplets pick-up the desired foreign species. The slit nozzle is mechanically connected to a one-dimensional translation stage which allows us to vary the distance between the droplet beam and the slit nozzle in order to optimize the pick-up conditions. The cross beam stagnation pressure is regulated with a second leak valve (*UDV 235, Balzers*) and species-independently monitored in the range of 10^{-4} to 1.1 mbar by a capacitive diaphragm gauge (*CMR 264, Pfeiffer Vacuum*). In contrast to the source chamber, the doping chamber is a fully Conflat sealed vacuum stage. It is separated from both source and detection chamber by o-ring sealed, removable partition walls. The wall towards the source chamber is of rectangular shape and installed into a large $580 \text{ mm} \times 310 \text{ mm}$ opening. The partition wall separating doping and detection chamber is of cylindrical geometry and extends a few centimeters into the detection chamber (see Figure 3.1). These removable walls offer the possibility to adapt the lengths of source and doping chamber, for example to accommodate further or different vacuum components. This design results in a somewhat complex geometry of the doping chamber. Nevertheless a maximum pumping speed in this volume is assured, mainly due to the large width of the source unit. The turbomolecular drag pump (*TMU 521, Pfeiffer Vacuum*) evacuating the chamber has a nominal pumping speed of 500 l/s for both helium and nitrogen and permits attaining base pressures below $1 \cdot 10^{-8}$ mbar. The doping chamber has a geometrical length of 112 mm (measured between the skimmer apertures, for details see Section 3.2) and thus offers enough space to fit in a small oven to bring less volatile dopant species into the gas phase^a. As in the source chamber, the pressure is measured by a full-range gauge (*PKR 251, Pfeiffer Vacuum*).

The detection chamber is of cylindrical shape with an inner diameter of 300 mm. It is connected to the source unit by means of large 14" (DN 300 CF) Conflat flanges^b. This fully Conflat sealed stage is designed to reach base pressures in the ultra-high vacuum (UHV) regime well below $1 \cdot 10^{-10}$ mbar. It is evacuated by an in-series arrangement of two turbomolecular drag pumps. The main pump (*TMU 1601 P, Pfeiffer Vacuum*) provides an elevated pumping speed of 1200 l/s for helium, but has a relatively low compression ratio of only $4 \cdot 10^4$ for molecular hydrogen. Since this molecule is continuously formed by outgassing from the stainless steel chamber walls, partial pressures of hydrogen below $1 \cdot 10^{-8}$ mbar turned out not to be attainable using only the main pump. We therefore chose to back the main pump by another small

^aSuch an oven, capable of sustaining temperatures of up to 1000 °C has been built as a part of this work. The experiments presented in this thesis were however carried out on species that, under ambient conditions, form liquids of relatively high vapor pressure. The oven therefore was of no use here.

^bIt is important to note that there is no common standard for Conflat flanges larger than DN 200 CF. Flanges from different vendors therefore are not necessarily identical. The DN 250 CF flanges on our machine are of *Pfeiffer Vacuum* type in order to be compatible with the turbomolecular pumps. The 14" (DN 300 CF) flanges, however, are from *Kurt J. Lesker Company*.

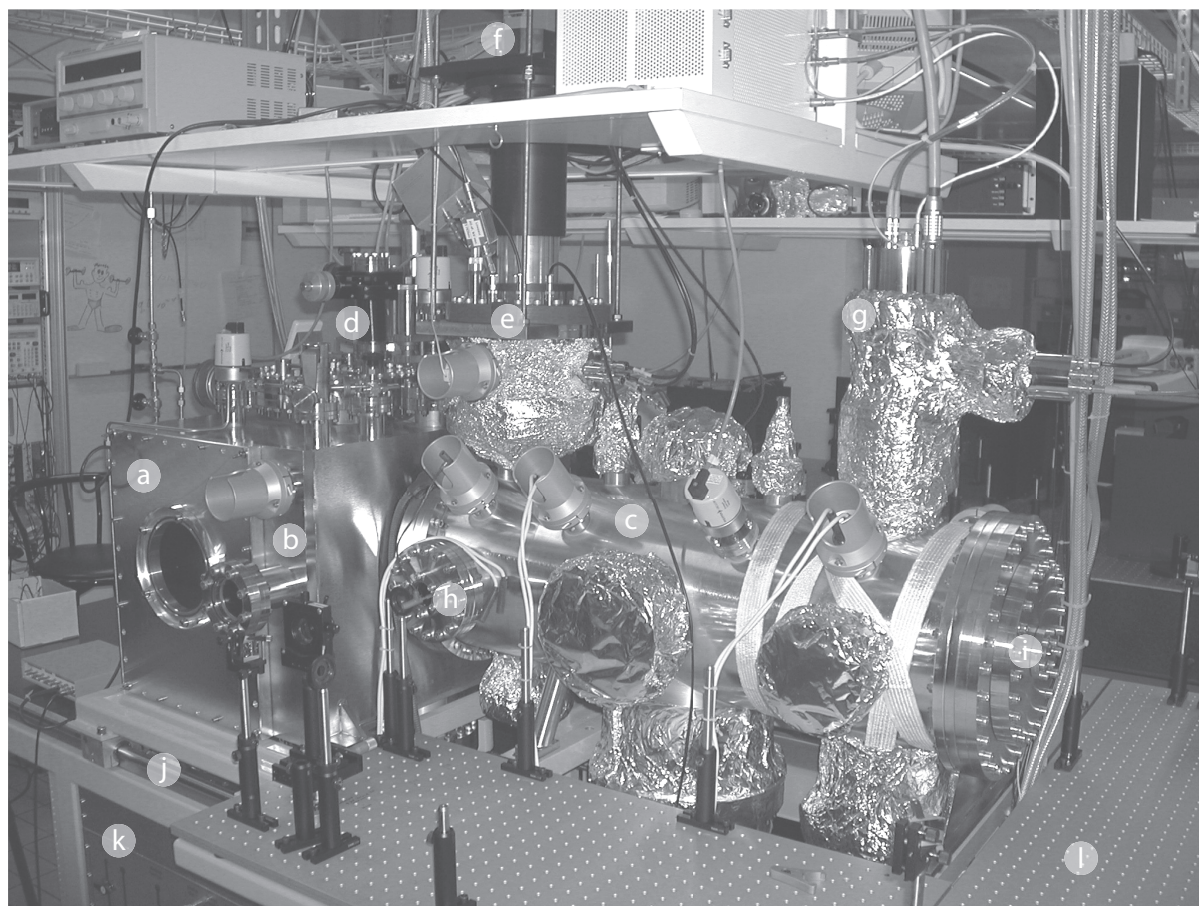


FIGURE 3.2: Photograph of the helium droplet machine. The helium droplet beam is formed in the source chamber (a) (rectangular shape, on the left), passes through the doping chamber (b), and enters the UHV detection chamber (c) (cylindrical shape, on the right). Other visible components include: (d) xyz-manipulator for the cryogenic orifice assembly, (e) ion imaging setup with MCP detector, (f) CCD camera, (g) quadrupole mass spectrometer, optical viewports for lasers propagating (h) perpendicular and (i) parallel to the droplet beam, (j) ball rail system, (k) gas manifold, and (l) optical tables attached to the support frame of the detection chamber.

turbomolecular drag pump (*TMH 071 P, Pfeiffer Vacuum*) which enhances the compression ratio by a factor of $1 \cdot 10^5$. The pumping speed for species sticking to cold surfaces at liquid nitrogen temperature is further increased by two communicating liquid nitrogen reservoirs (see Figure 3.1). These reservoirs in the shape of hollow cylinders have a volume of 470 ml each and are made of UHV-compatible oxygen-free (OF) copper. Together they currently have a geometrical surface area of 1900 cm^2 which can easily be increased by attaching further pieces to the reservoirs. With an inner diameter of 110 mm they in particular offer the possibility to install a cryogenic flight tube into the detection chamber. The liquid nitrogen reservoirs are sealed by silver solder in order to obtain a leak tight and bakeable system. Once cooled down, one filling every 3–4 hours is needed to maintain the minimum temperature. Since the reservoirs

are well insulated and have a large heat capacity, they remain reasonably cool over night and can be cooled down entirely within minutes on the next day. A base pressure in the UHV regime can however only be attained in a reasonable time if the walls of the vessel are heated in order to more rapidly desorb water and other compounds of high vapor pressure (“bakeout”). For this reason the detection chamber is equipped with three pairs of infrared lamps (*KRS 500 KW, Heraeus*) that in total can set free a heating power of 3 kW on the inside of the vessel. The lamps were stripped of all high vapor pressure components to finally expose only the quartz bulb and nickel wires to the vacuum. The infrared heaters as well as some additional heating strips and jackets are powered by a home-built programmable bakeout controller. Rather than raising the temperature of the vacuum system as a whole, this more economical bakeout method allows us to directly heat the surfaces where the adsorbates reside. This results in more rapid bakeout cycles, but may put more thermal stress on certain components of the vacuum system. Since some of the home-built devices in the detection chamber contain PTFE and *Viton* components, the bakeout temperature of the chamber should not exceed 150 °C in order to avoid a decomposition of the material. After a single 24 h bakeout the detection chamber typically reaches a base pressure of $1 \cdot 10^{-10}$ mbar.

Equipped with a home-built ion imaging setup (see Section 3.5) and a commercial quadrupole mass spectrometer (QMS) system (*QMG 422, Balzers*), the detection chamber holds two instruments capable of analyzing the droplet beam. The detection regions of the ion imaging setup and the QMS are located at a distance of 216 mm and 846 mm downstream of the orifice, respectively. The axes of both devices are oriented vertically and hence perpendicularly to the droplet beam, an arrangement that allows the simultaneous investigation of droplet beam properties using both instruments. *Suprasil* fused silica viewports permit the introduction of UV laser beams propagating both perpendicular and parallel to the droplet beam. The principal components of the QMS are a *QMA 410* mass analyzer with a rod diameter of 16 mm, a cross-beam ion source, and a *QMH 410-3* high frequency generator that gives access to a mass range from 0.3 to 341.33 amu. Ion currents can be recorded using either a Faraday cup or a secondary electron multiplier (SEM). For all experiments presented in this work the electron energy of the electron impact ionizer was set to 70 eV at a fixed electron current of 1 mA.

Figure 3.3 shows a typical mass spectrum of the residual gas in the detection chamber after bakeout. Hydrogen is by far the major constituent of the residual gas. Other components include CO₂, CO, H₂O, and some hydrocarbons. The partial pressure of the latter two components can efficiently be reduced by cooling down the liquid nitrogen reservoirs in the detection chamber.

3.2 Geometry and fluxes of the droplet beam

The droplet jet is skimmed and collimated by two molecular beam skimmers (*Model 2, Beam Dynamics*) mounted to the vacuum partition walls that separate the three vacuum stages of the machine (see Figure 3.1). We accurately align skimmers and apertures using an optical telescope (*NA720, Leica*). The first skimmer with a diameter of 0.3 mm is placed at a nominal distance of 9 mm from the orifice. Its diameter was chosen relatively small in order to reduce the gas load on the doping chamber. The distance between orifice and first skimmer can be varied by ± 7 mm by means of the xyz-manipulator rigidly connected to the orifice assembly which

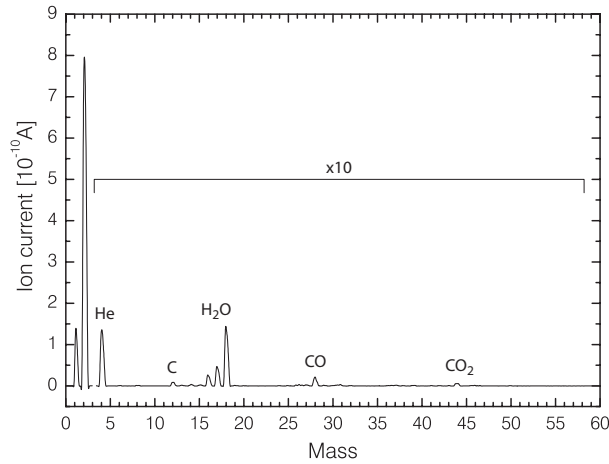


FIGURE 3.3: Mass spectrum of the residual gas in the baked detection chamber recorded with the SEM at a pressure of $1 \cdot 10^{-10}$ mbar. Ion currents corresponding to masses larger than 3 amu are shown amplified by a factor of 10 to make them visible. Some helium leaks in from a misaligned atomic beam in the source chamber. If helium is disregarded, hydrogen is found to account for more than 95 % of the residual gas. Cooling down the liquid nitrogen reservoirs further suppresses the remaining water and hydrocarbon components.

permits some optimization of the droplet beam intensity. The second skimmer with a diameter of 1.0 mm is placed at the doping chamber exit about 121 mm downstream of the orifice and thus defines a solid angle of $5.4 \cdot 10^{-5}$ sterad. The resulting geometry of the droplet beam in doping and detection chamber is illustrated in Figure 3.4. At the position of experimental interrogation by laser light the molecular beam attains a width of 1.8 mm which is well matched to the velocity mapping properties of the ion imaging setup (see Section 3.5).

If chromophores are introduced into the doping chamber in order to be picked-up by the helium droplets, some of the molecules will unavoidably pass through the aperture of the second skimmer and enter the detection chamber. The presence of unsolvated dopant molecules in the detection region of the ion imaging setup is, however, highly undesirable since the resulting images will be a superposition of both gas-phase and droplet signals. The region of the detection chamber accessible to those molecules is shown in Figure 3.4 as lightly shaded area. We use an additional aperture (AP) to partially block the flow of gas-phase chromophores into the flight tube of the ion imaging setup. With a diameter of 1.7 mm the aperture does not interfere with the droplet beam.

Table 3.1 shows the base and typical operating pressures of the three vacuum stages. Note that the helium pressure in the doping chamber is kept inferior to $1 \cdot 10^{-5}$ mbar. In this pressure range the droplet beam attenuation caused by collisions with helium atoms is small. This can be inferred from Figure 3.5 which illustrates the effect of elevated helium pressures in the doping chamber. In this experiment, carried out at a stagnation pressure $p_o = 20$ bar and a stagnation temperature $T_o = 15$ K, helium was deliberately introduced into the vacuum chamber using the leak valve. Simultaneously, the ion signals of various helium droplet fragments produced by electron-impact ionization were recorded using the QMS. It becomes clear that significant

Vacuum Stage	Base Pressure [mbar]	Typical Operating Pressure [mbar He]			
		$T_o = 8$ K	11 K	15 K	19 K
Source Chamber	$1 \cdot 10^{-7}$	$1.6 \cdot 10^{-3}$	$1.3 \cdot 10^{-3}$	$9.8 \cdot 10^{-4}$	$8.3 \cdot 10^{-4}$
Doping Chamber	$1 \cdot 10^{-8}$	$4.0 \cdot 10^{-6}$	$4.3 \cdot 10^{-6}$	$4.2 \cdot 10^{-6}$	$3.8 \cdot 10^{-6}$
Detection Chamber	$1 \cdot 10^{-10}$	$1.1 \cdot 10^{-7}$	$4.2 \cdot 10^{-8}$	$1.6 \cdot 10^{-8}$	$5.1 \cdot 10^{-9}$

TABLE 3.1: Base and typical operating pressures of the three differentially pumped vacuum stages of the helium droplet machine. The operating pressures are partial pressures of helium and are given for a backing pressure of $p_o = 30$ bar and some selected stagnation temperatures T_o . At this stagnation pressure the temperature $T_o = 8$ K can only be maintained temporarily (see Figure 3.20).

intensity losses occur if the chamber pressure is raised above some 10^{-5} mbar which justifies the choice of the first skimmer. However, the influence of edge effects on the gas flow through a skimmer grows as the diameter of the skimmer aperture gets smaller. In the source chamber helium atoms scattered back from the skimmer edges or the vacuum partition wall may interfere with the expanding helium and thereby significantly alter the characteristics of the droplet beam. It is therefore important to determine expansion conditions where these undesirable destructive effects are minimal.

Figure 3.6 and Figure 3.7 illustrate the partial pressures of helium in source and detection chamber for some selected backing pressures p_o and for stagnation temperatures T_o up to 40 K. From the measured helium pressures p_{He} the net particle flux ϕ_{He} into a particular chamber can be calculated according to

$$\phi_{\text{He}} = \frac{s}{k_{\text{B}}T} \cdot p_{\text{He}} \quad (3.1)$$

if the pumping speed s of the vacuum stage is known. Here $T \cong 295$ K denotes the temperature of the helium gas in the chamber. Based on the nominal pumping speeds of 2400 l/s in the source and 1200 l/s in the detection chamber we obtain the particle fluxes shown on the right vertical axis in both Figure 3.6 and Figure 3.7. In the case of the source chamber the flux scale is however not entirely correct as the pumping speed of the turbomolecular pumps for helium drops from $2 \cdot 1200$ l/s at $1 \cdot 10^{-4}$ mbar to $2 \cdot 1100$ l/s at $1 \cdot 10^{-3}$ mbar and eventually to $2 \cdot 600$ l/s at $1 \cdot 10^{-2}$ mbar.

The pressure in the source chamber is found to grow regularly with the stagnation pressure p_o and to increase smoothly as the stagnation temperature T_o is lowered. This behaviour can be deduced from the relation¹¹⁹

$$\phi_{\text{He}} = p_o A \left[\frac{\gamma}{m_4 k_{\text{B}} T_o} \left(\frac{2}{\gamma + 1} \right)^{(\gamma+1)(\gamma-1)} \right]^{1/2} \quad (3.2)$$

which describes the particle flux through an orifice of area A in the approximation of ideal gas behaviour. Here, m_4 denotes the mass of a ^4He atom and γ is the ratio of the specific heats. Equation (3.2) is a good description for the high temperature part of Figure 3.6.

The dependence of detection chamber pressure on both p_o and T_o is far more complex. We attribute this to changes in the beam divergence as clustering occurs. For stagnation pressures

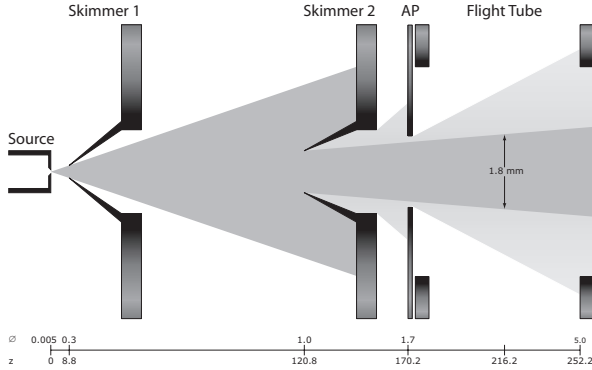


FIGURE 3.4: Arrangement of apertures and resulting beam geometry shown schematically in a horizontal cross section of the machine. At the point of intersection with a perpendicularly propagating laser pulse the droplet beam has a width of 1.8 mm. The lightly shaded area shows the region of the machine accessible to chromophores emerging with random direction from the doping chamber. An additional aperture (AP) with a diameter of 1.7 mm keeps most of those molecules from directly entering the flight tube of the ion imaging setup.

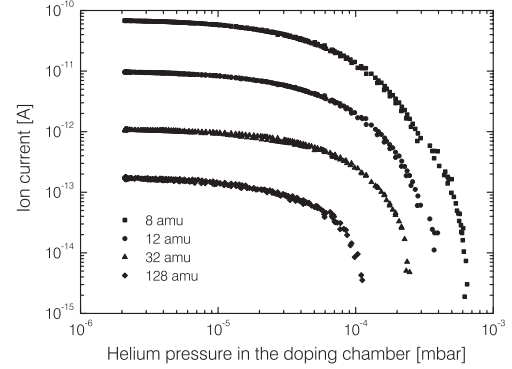


FIGURE 3.5: Attenuation of a helium droplet beam as a function of helium pressure in the doping chamber. The attenuation is measured mass-spectrometrically for various fragment masses. At a stagnation pressure $p_o = 20$ bar and a stagnation temperature $T_o = 15$ K the doping chamber attains an operating pressure of $2 \cdot 10^{-6}$ mbar helium. Additional helium is introduced by means of a leak valve.

in excess of 30 bar the increase of detection chamber pressure with stagnation pressure becomes irregular. For $p_o = 50$ bar and for $T_o \gtrsim 23$ K the fluxes fall short of the values observed at $p_o = 30$ bar, indicating destructive processes in the source chamber. For the dissociation experiments presented in this work we therefore chose a stagnation pressure of 30 bar where no signature of destructive processes is seen. This ensures that the cluster size scaling law discussed in Section 2.3 can be applied to estimate the mean cluster size produced. At this stagnation pressure we obtain high fluxes of the order of 10^{14} atoms s^{-1} into the detection chamber.

Based on the estimated mean droplet sizes shown in Table 2.2 the atom fluxes into the detection chamber may be converted into droplet fluxes. Such a conversion obviously neglects the monoatomic component of the beam and therefore has to be taken with care. The resulting droplet fluxes and flux densities are illustrated in Figure 3.8 as a function of stagnation temperature T_o . It becomes clear that the maximum droplet fluxes and therefore the highest signal levels can be expected at stagnation temperatures around 16 K. For the standard expansion conditions of $p_o = 30$ bar and $T_o = 15$ K this crude estimation predicts a droplet flux of $8.0 \cdot 10^{10}$ droplets s^{-1} or a flux density of $1.5 \cdot 10^{15}$ droplets s^{-1} sterad $^{-1}$. However, many details of the plot, such as the droplet flux minima at $T_o = 12$ K and 19 K, are not significant. This is due to the large uncertainties involved, e.g. regarding the mean cluster sizes \overline{N} .

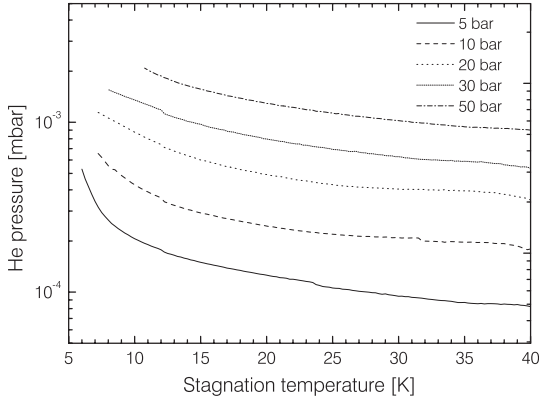


FIGURE 3.6: Partial helium pressure and particle flux into the source chamber as a function of stagnation pressure and temperature. The flux scale is calculated using equation (3.1) and based on a constant pumping speed of $2 \cdot 1200$ l/s.

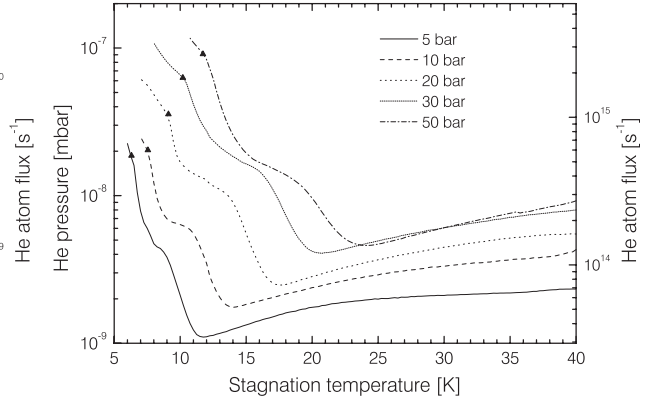


FIGURE 3.7: Partial helium pressure and particle flux into the detection chamber as a function of stagnation pressure and temperature. The solid triangles indicate the transition from the subcritical to the supercritical expansion regime.

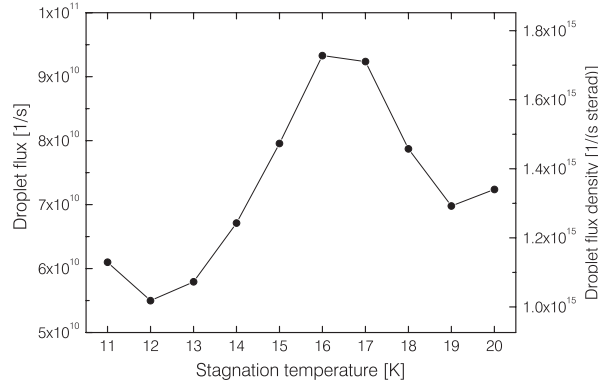


FIGURE 3.8: Estimated droplet flux into the detection chamber as a function of stagnation temperature T_0 .

3.3 Cluster Source

3.3.1 Construction

In order to form helium clusters in the expansion the helium gas has to be cooled to cryogenic stagnation temperatures well below 50 K. In our machine the cooling is achieved by a closed-cycle refrigerator system comprising a cold head (*RDK-205D*, *Sumitomo Heavy Industries*) and a compressor unit (*CKW-21A*, *Sumitomo Heavy Industries*). This refrigeration method eliminates the need for liquid cryogenics and provides continuous and reliable cooling. Our particular system has been calibrated to deliver a cooling power of 4 W at 37.6 K on the first and 0.5 W at 4.12 K on the second stage, both measured at an electric power frequency of 60 Hz and in vertical position. The cooling power at 50 Hz and in horizontal position as chosen in our

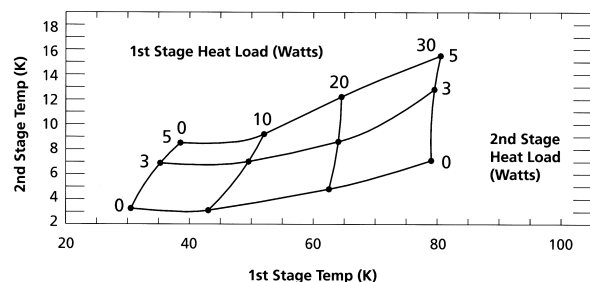


FIGURE 3.9: Typical load map of the *RDK-205D* cold head for a wide range of thermal loads. The map is given for a power frequency of 60 Hz and a vertical (head down) position. Any other orientation of the cold head may result in a power loss of up to 20 %. The figure is reproduced from a *Janis* brochure [183].

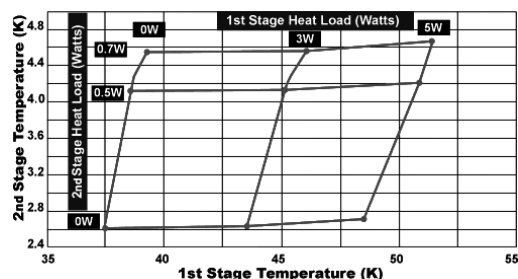


FIGURE 3.10: Typical load map of the *RDK-205D* cold head at 50 Hz power frequency and for moderate thermal loads. Again, the map applies to a vertical (head down) position. The figure is taken from the *Sumitomo Heavy Industries* internet pages [184].

setup is somewhat reduced, but the system is still able to reach minimal temperatures inferior to 4 K. Typical load maps of the cold head are shown in Figure 3.9 and Figure 3.10. They illustrate the available cooling power in a wide range of thermal loads on both first and second stage.

Before discussing the components of the cryogenic setup it is useful to become familiar with the materials involved. In contrast to the bakeable UHV chamber where substances of extremely low vapor pressure and high-temperature compatibility must be used, the vacuum in the source chamber is much less demanding and allows us to build components from a much larger variety of materials. The inhouse-built droplet source mainly is constructed from standard electrolytic tough pitch (ETP) copper which is readily available in many shapes, inexpensive and has a high thermal conductivity. Frequently, a good thermal contact between two surfaces is crucial to avoid cooling power loss and undesirable temperature gradients. For this purpose we use indium washers or *Apiezon H* grease which both substantially enhance the contact area and hence the thermal conductance.¹⁸⁵ Permanent thermal contact is established by soldering or by using *Stycast* (*Lake Shore Cryotronics*), a self-hardening epoxy resin for cryogenic use. If heat flow between two mechanically joint parts of different temperature is undesirable the connecting piece has to have a low thermal conductivity. Often, G-10 (also known as HGW 2372) is a good choice. This glass fiber reinforced epoxy resin not only has a exceptionally low thermal conductivity but also is light and strong, has good vacuum characteristics, and can easily be machined. A metallic material of relatively low thermal conductivity is stainless steel. It is used in the form of thin walled tubing to set up gas line connections of small thermal conductance. Brass shows a thermal contraction/expansion very similar to copper but is mechanically much stronger. In order to establish a reliable thermal contact between two mechanically joint copper components over a wide range of temperatures we therefore use brass fasteners. In particular, brass screws are used to mount the temperature sensors. Electrical connections are made using phosphor bronze wires of small gauges, *i.e.* 32 or 36 AWG (*Lake Shore Cryotronics*). These cryogenic wires have a low thermal conductivity and a relatively high electrical resistivity. Heat

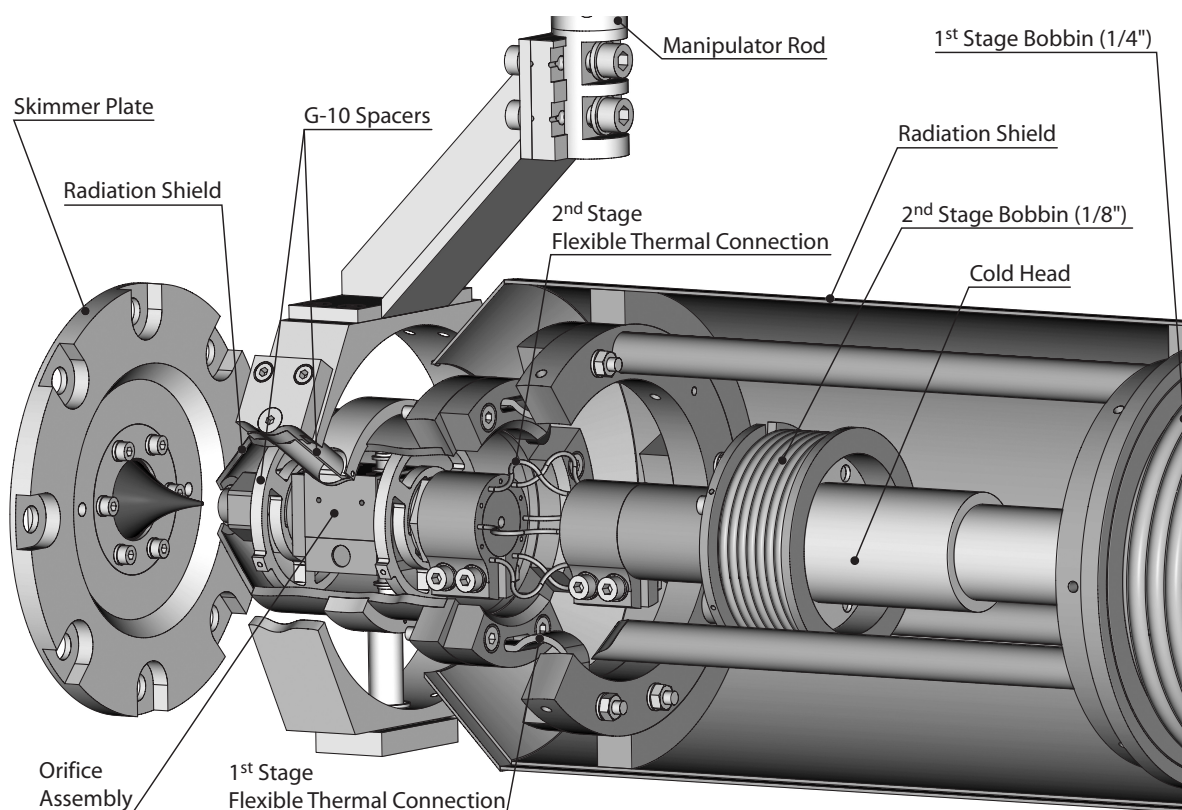


FIGURE 3.11: Details of the cryogenic cluster source. A radiation shield thermally connected to the first stage of the cold head forms the outer layer of the setup. The orifice assembly is accurately positioned by means of a micrometer driven xyz-manipulator (not shown). Flexible thermal connections to the stationary cold head are established by copper wires (see text). Note the special shape of the G-10 spacers mechanically connecting room temperature to first stage and first stage to second stage components. The gas lines interconnecting the two bobbins and the orifice assembly are not shown.

flow along the wires can potentially cause temperature misreadings if the wires connect to a temperature sensor. The wires therefore are carefully wrapped around the cold head to increase the wire length between two refrigerator stages. They are readily secured in place using dental floss made from *Dacron* fibers.

Figure 3.11 shows details of the cryogenic components mounted to the horizontally installed cold head. The setup consists of a fixed part rigidly attached to the cold head and a second, movable part that includes the orifice assembly and is mechanically connected to a micrometer driven xyz-manipulator (*E-PSM-1502, Caburn-MDC*). This way the orifice position can be varied by ± 7 mm in the direction of the droplet beam and by ± 5 mm perpendicular to it. Since the heavy cold head remains stationary, a translation of the orifice is carried out with little force and using compact mechanics. The design thus permits an easy, rapid and accurate

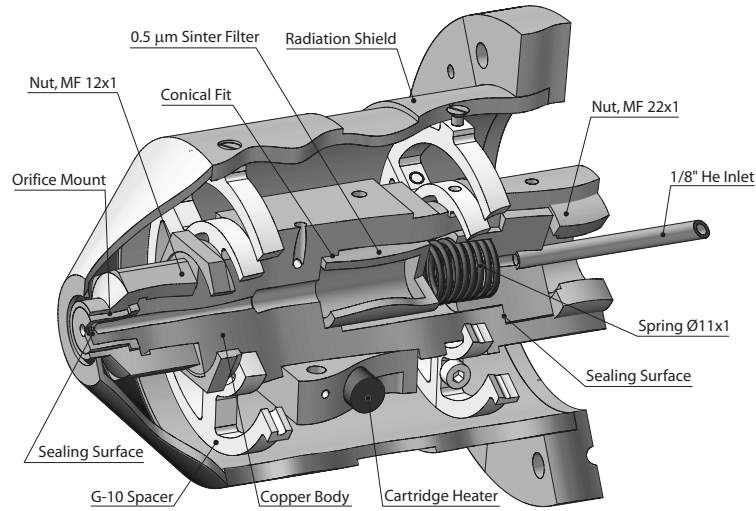


FIGURE 3.12: Details of the orifice assembly. The $5\ \mu\text{m}$ orifice (*A0200P*, *Frey*) is attached to the end of the bore through the copper body by means of a screw-on copper fitting. A $0.5\ \mu\text{m}$ sinter filter (*SS-4F-K4-05*, *Swagelok*) prevents microparticles immersed in the helium flow from reaching and blocking the orifice. The marked surfaces are sealed with indium gaskets.

in-situ positioning of the orifice with respect to the first skimmer.

As illustrated in Figure 3.11 the orifice assembly is fully enclosed by a cylindrically symmetric copper radiation shield that is thermally connected to the first stage of the cold head. The surfaces facing room temperature are hand-polished to reduce the emissivity and to minimize the radiative heat load on the first stage of the cold head (see Section 3.3.2). Movable and fixed part of the setup have separate shields that are thermally interconnected by means of flexible copper braids made of wires with a diameter of $0.2\ \text{mm}$, a free length of $35\ \text{mm}$ and a total cross section of $15\ \text{mm}^2$. From the temperature dependent thermal conductivity of copper¹⁸⁶ the braids are estimated to have a minimum heat conductance of $0.17\ \text{W/K}$. We use G-10 spacers to mechanically connect the radiation shield of the movable part of the setup to the manipulator. The spacers have a hollow cylinder geometry to reduce their cross section and hence the thermal conduction. An uncalibrated silicon diode (*DT-70-CU-13*, *Lake Shore Cryotronics*) is used to measure the temperature on the movable part of the radiation shield with an accuracy of $\pm 1\ \text{K}$. In order to be able to warm up the system more rapidly a $25\ \text{W}$ cartridge heater (*HTR-25*, *Lake Shore Cryotronics*) is permanently anchored to the first stage components using *Stycast*.

The helium gas flowing towards the orifice cools in two steps by making thermal contact with the first and, later, with the second stage of the cold head. For this purpose each stage is equipped with a bobbin consisting of about 7 windings of copper tubing ($1/4''$ O.D. on first and $1/8''$ O.D. on second stage) soft-soldered to a copper support piece. Indium washers are used to ensure a good thermal conductance between the cold head and the bobbins mounted to each of its stages. We use thin walled stainless steel tubing to avoid conduction losses along the gas lines that interconnect the two bobbins and link the first stage bobbin to the room temperature

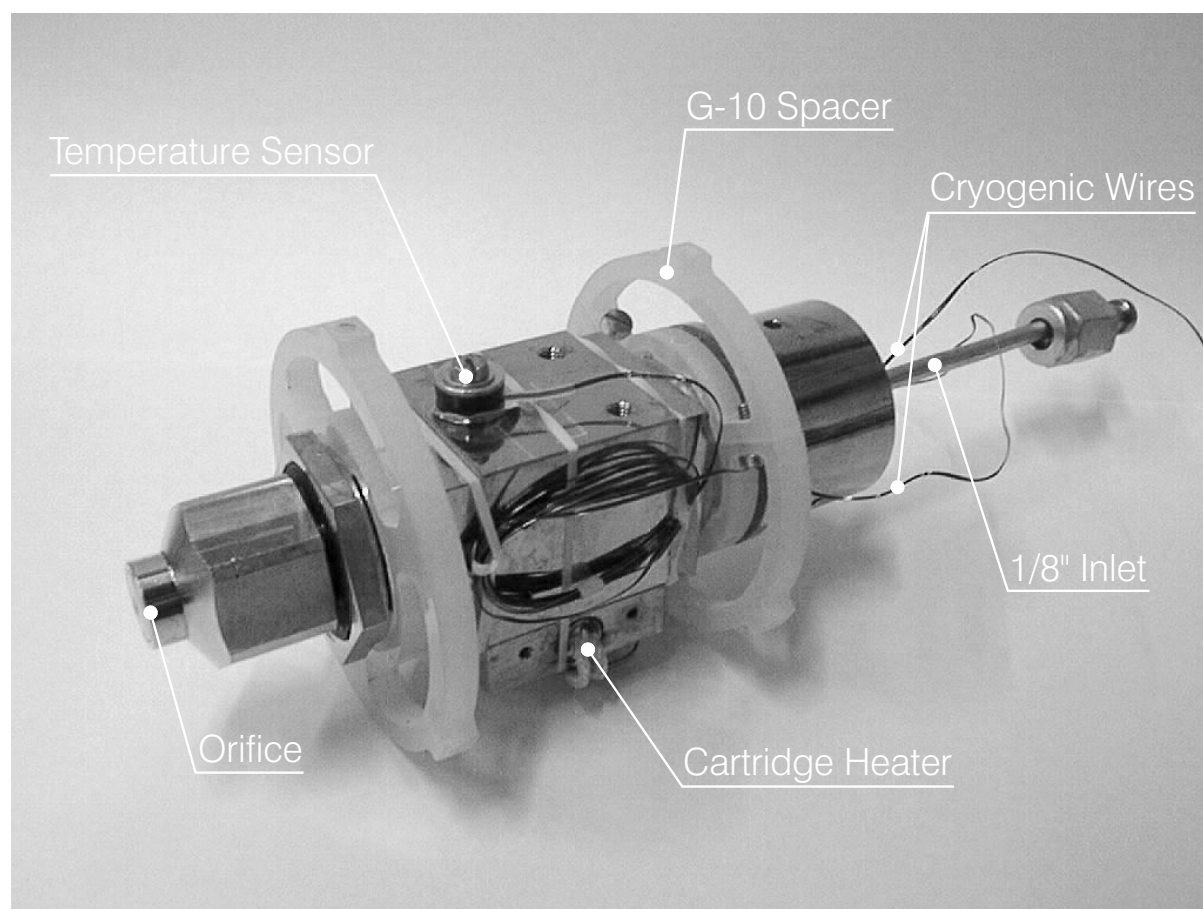


FIGURE 3.13: Photograph of the orifice assembly made mainly of electrolytic tough pitch (ETP) copper. The assembly is thermally coupled to the second stage of the cold head using a set of high-purity copper wires (not shown). Two specially designed G-10 spacers mechanically attach the assembly to the radiation shield (not shown) and provide excellent thermal insulation. The temperature sensor is a silicon diode (*DT-470-CU-13, Lake Shore Cryotronics*) calibrated to 30 mK accuracy in the temperature range from 4 to 325 K. A 25 W cartridge heater (*HTR-25, Lake Shore Cryotronics*) is permanently anchored in a removable copper block using an electrically nonconductive cryogenic epoxy resin (*Stycast, Lake Shore Cryotronics*). The thermal contact area to the heating block and to the temperature sensor is increased by washers made of 0.127 mm thick indium foil. Brass screws show a thermal contraction/expansion similar to copper and therefore are used to reliably mount both heating block and temperature sensor. The cryogenic wires are fastened by dental floss made from *Dacron* fibers.

vacuum feedthrough. The former connection consist of 1/8" tubing and has a length of 150 cm, while the latter connection (1/4") is 70 cm long.

A 1/8" flexible copper gas line links the second stage bobbin to the orifice assembly shown in Figure 3.12 and in Figure 3.13. The assembly holds the 5 μm orifice (*A0200P, Frey*), which is sold as an aperture for electron microscopes. The orifice is laser-drilled into a platinum-iridium disk measuring 0.52 mm in height and 2 mm in diameter (see Figure 3.14). Figure 3.15 shows

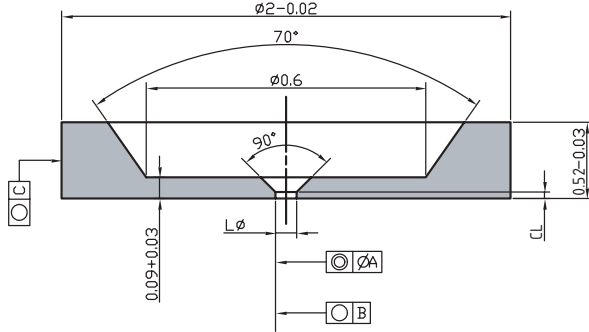


FIGURE 3.14: Cross section of the platinum-iridium disk into which the orifice is drilled. The disk is mounted such that the bottom of the shown section is facing vacuum. The dimensions are $L = 5 \mu\text{m}$, $CL \approx 5 \mu\text{m}$, $A = 0.02 \text{ mm}$, $B = 1 \mu\text{m}$, and $C = 0.02 \text{ mm}$.

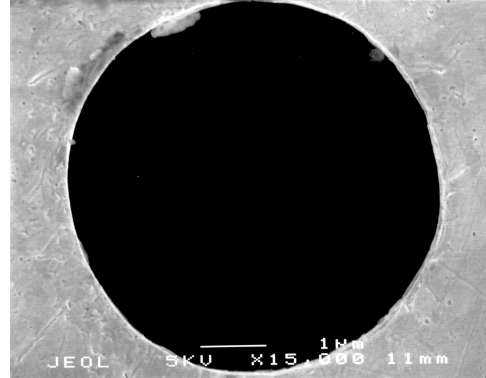


FIGURE 3.15: Scanning electron microscope image of a typical $5 \mu\text{m}$ orifice. The picture shows the downstream exit of the orifice. From the ruler at the bottom of the image one calculates a diameter of approximately $5.5 \mu\text{m}$. The effective diameter of the orifice may however be smaller since the interior of the orifice channel is not resolved.

a scanning electron microscope image of a typical $5 \mu\text{m}$ orifice. As can be seen from the image, the orifice is round and shows little edge deformations. Orifices of the same type have been used in the Toennies group in Göttingen,¹⁸⁷ where the reference data for our estimation of mean droplet sizes were measured (see Section 2.3). This increases our confidence that the droplet size distributions produced in our machine are similar to the ones predicted.

Inside the copper body of the assembly a stainless steel sinter filter (*SS-4F-K4-05*, *Swagelok*) with a nominal pore size of $0.5 \mu\text{m}$ removes small particles from the helium flow that otherwise may block the orifice. A calibrated silicon diode (*DT-70-CU-13*, *Lake Shore Cryotronics*) is mounted on top of the copper body to measure the local temperature with an accuracy of 30 mK (see Figure 3.13). The temperature is adjusted by means of a 25 W cartridge heater (*HTR-25*, *Lake Shore Cryotronics*) mounted to the bottom of the copper body. Copper body and radiation shield of the orifice assembly are thermally well insulated and mechanically connected by specially shaped G-10 spacers. The spacers have been machined such that a heat flow can only occur along paths much longer than the radial distance between first and second stage components (see Figure 3.12).

Thermally, the orifice assembly is connected to the second stage of the cold head. Similar to the first stage the thermal connection is established by means of flexible copper wires. Since typical stagnation temperatures T_o are between 5 K and 25 K, it is advantageous to exploit the superior thermal conductivity of high purity copper in this temperature range. Compared to standard ETP copper the thermal conductivity can thus be enhanced by more than one order of magnitude.¹⁸⁶ In our case the connection is made using 90 high purity copper wires (99.9999 %, *Alfa Aesar*) with a diameter of 0.25 mm each and a free length of 45 mm. This solution results in a thermal conductance better than 0.6 W/K and ensures a low mechanical resistance to any translation of the orifice assembly.

3.3.2 Heat loads

Under experimental conditions the heat loads on the two stages of the cold head are a result of various physical processes which can be summarized as

- Cooling the helium gas to cryogenic temperatures (P_{cooling}),
- Radiative heat transfer (P_{rad}),
- Solid conduction (P_{solid}), and
- Gas conduction (P_{gas}).

In the following paragraphs we will give estimates of all four contributions to the heat load on each of the two stages of the cold head.

Cooling the helium gas

The heat load resulting from the refrigeration of helium from an initial temperature T_i to a final temperature T_f depends on the particle flux ϕ_{He} through the gas line, *i.e.* into the source chamber. As the pressure p_o in the gas line stays constant during the refrigeration process we are interested in the isobaric molar heat capacity C_p of helium-4. The substance behaves like an ideal gas over a vast range of temperatures and pressures and C_p consequently varies little until temperatures below approximately 10 K are reached.¹¹¹ For the degree of approximation required here it is therefore safe to assume a temperature independent value $C_p = 20.8 \text{ J K}^{-1} \text{ mol}^{-1}$. The heat load P_{cooling} then is simply given by

$$P_{\text{cooling}} = \frac{C_p}{N_A} (T_i - T_f) \phi_{\text{He}} , \quad (3.3)$$

where $N_A = 6.022 \cdot 10^{23} \text{ mol}^{-1}$ denotes the Avogadro constant. For the standard stagnation pressure $p_o = 30 \text{ bar}$ an upper limit to the typical particle flux is given by $\phi_{\text{He}} \lesssim 1 \cdot 10^{20} \text{ s}^{-1}$ (see Figure 3.6). Typical first stage temperatures are 40–70 K. Upper estimates for P_{cooling} hence are obtained assuming the first and second stage to cool helium from 295 K to 40 K and from 70 K to 5 K, respectively. As a result one finds a heat load of

$$P_{\text{cooling}}^{\text{1st}} \leq 880 \text{ mW}$$

on first and of

$$P_{\text{cooling}}^{\text{2nd}} \leq 220 \text{ mW}$$

on second stage.

Radiative heat transfer

According to the Stefan-Boltzmann and Kirchhoff laws a surface of area A and temperature T emits thermal radiation with a total power

$$P = \epsilon \sigma A T^4 , \quad (3.4)$$

where $\sigma = 5.67 \cdot 10^{-8} \text{ W m}^{-2} \text{ K}^{-4}$ is constant and $\epsilon \leq 1$ denotes the temperature dependent total emissivity of the surface.

The energy balance of a cold surface A_1 at temperature T_1 in radiative exchange with a warm surface A_2 at temperature T_2 is given by

$$P_{\text{rad}} = \epsilon \sigma A_1 (T_2^4 - T_1^4) , \quad (3.5)$$

where ϵ is a geometry dependent factor that involves the emissivities ϵ_1 and ϵ_2 of the two surfaces.¹⁸⁶ For long coaxial cylinders and diffuse^c reflection the relation

$$\epsilon = \frac{\epsilon_1 \epsilon_2}{\epsilon_2 + \frac{A_1}{A_2} (1 - \epsilon_2) \epsilon_1} \quad (3.6)$$

holds¹⁸⁶ which will serve as an approximation for our system. For the exchange of radiative energy between the walls of the vacuum chamber and the copper radiation shield connected to the first stage of the cold head we use the values $T_1 = 40 \text{ K}$, $T_2 = 295 \text{ K}$, $A_1 = 1500 \text{ cm}^2$, $A_2 = 14000 \text{ cm}^2$, $\epsilon_1 = 0.019$ (polished copper¹⁸⁶), and $\epsilon_2 = 0.08$ (stainless steel¹⁸⁶) which yields $\epsilon = 0.0186$ and

$$P_{\text{rad}}^{\text{1st}} \leq 1.2 \text{ W} .$$

Compared to using oxidized, unpolished copper ($\epsilon_1 \approx 0.7$) this value represents a reduction of radiative heat load by a factor of approximately 20. The radiative energy exchange between the copper radiation shield and the inner second stage assembly ($A \approx 500 \text{ cm}^2$) can be estimated similarly. One obtains a very small heat load

$$P_{\text{rad}}^{\text{2nd}} \leq 10 \text{ mW} .$$

The radiation shield hence efficiently removes the radiative heat load from the second stage of the cold head.

Solid conduction

Head loads caused by solid conduction are due to mechanical connections between first and second stage as well as between second stage and the room temperature components. In our setup such connections are established by the G-10 spacers, the cryogenic wires, and the stainless steel gas lines. In the limit of thermal equilibrium and one-dimensional conduction the heat transfer along a connecting piece of uniform cross section A , length L and thermal conductivity $K(T)$ can be written as

$$P_{\text{solid}} = \frac{A}{L} (\theta_2 - \theta_1) , \quad (3.7)$$

where

$$\theta_i = \int_0^{T_i} K(T) dT \quad (3.8)$$

is the so-called thermal conductivity integral and the indices 1 and 2 refer to the cold and the warm surface, respectively.¹⁸⁵ For many materials relevant to cryogenic engineering the

^cCompared to specular reflection this approximation results in slightly higher heat loads. Since we are interested in upper estimates of the radiative heat transfer, all calculations are based on diffuse reflection.

integrals θ_i have been tabulated (see for example [185]). For the geometries of our setup one finds in total

$$P_{\text{solid}}^{\text{1st}} \leq 250 \text{ mW}$$

on first and

$$P_{\text{solid}}^{\text{2nd}} \leq 60 \text{ mW}$$

on second stage. In deriving these values a perfect contact to the insulator was assumed. The values represent upper limits to the real solid conduction losses since the real contact surface is generally much lower.¹⁸⁵

Gas conduction

The residual pressure in a vacuum chamber leads to heat transfer from warm to cold surfaces. If the mean free path of the gas particles is small compared to the distance between the surfaces a pressure drop reduces the number of particles carrying heat, but at the same time increases their mean free path. These two counteracting effects cause the heat flux to be independent of pressure in this pressure range. A different behaviour is found if the pressure is lowered such that the mean free path largely exceeds the distance between the surfaces. In this so-called free molecular flow regime collisions between the gas particles themselves are rare compared to collisions with either of the surfaces. The heat flux thus only depends on the number of gas particles hitting a surface per unit time and hence is proportional to the gas pressure p . For two long coaxial cylinders of areas A_1 and A_2 and temperatures T_1 (cold) and T_2 (warm) the heat transfer to the cold surface in the free molecular flow regime can be estimated by¹⁸⁶

$$P_{\text{gas}} = 0.021 \cdot A_1 \alpha p (T_2 - T_1) \frac{\text{W}}{\text{cm}^2 \text{ mbar K}}, \quad (3.9a)$$

where

$$\alpha = \frac{\alpha_1 \alpha_2}{\alpha_2 + \frac{A_1}{A_2} (1 - \alpha_2) \alpha_1} \quad (3.9b)$$

is the so-called overall accommodation coefficient. For helium approximate values are $\alpha = 0.6$ (20 K), $\alpha = 0.4$ (76 K) and $\alpha = 0.3$ (300 K).¹⁸⁶ Using same surface areas as in our estimation for the radiative heat load one finds

$$P_{\text{gas}}^{\text{1st}} \approx 2.9 \text{ W}$$

and

$$P_{\text{gas}}^{\text{2nd}} \approx 320 \text{ mW}$$

for $p = 1 \cdot 10^{-3}$ mbar. This pressure corresponds to mean free paths of approximately 20.0 cm, 4.3 cm and 0.90 cm for helium at kinetic temperatures of 300 K, 76 K and 20 K,¹⁸⁶ respectively. In view of the dimensions of the cryogenic setup this pressure roughly defines the upper limit for the free molecular flow regime. At the same time $p = 1 \cdot 10^{-3}$ mbar is a typical source chamber pressure for the standard backing pressure of 30 bar (see Figure 3.6).

	P_{cooling} [W]	P_{rad} [W]	P_{solid} [W]	P_{gas} [W]	P_{total} [W]
First stage	0.88	1.20	0.25	2.90	5.20
Second stage	0.22	0.01	0.06	0.32	0.60

TABLE 3.2: Estimated contributions of the different heat transport mechanisms to the total heat load P_{total} on first and second stage of the cold head. The contributions arising from the cooling of the helium gas and from gas conduction are given specifically for the typical stagnation pressure of 30 bar.

Summary

The estimated heat loads resulting from the various heat transport mechanisms discussed above are summarized in Table 3.2. In deriving these values we made relatively crude assumptions concerning the geometry of our setup. Moreover many of the values are based on empirical parameters such as emissivities and accommodation coefficients which may or may not accurately describe the actual behaviour of our system. In spite of these uncertainties it becomes clear that gas conduction constitutes the most important heat load on both stages of the cold head. Solid conduction, on the other hand, turns out not to contribute significantly to the thermal load of the system.

The significance of the gas conduction mechanism is ultimately a consequence of our choice to pump the entire vacuum apparatus with turbomolecular drag pumps (see Section 3.1). A powerful diffusion pump could deliver a pumping speed a factor of 5–10 more elevated than the pair of turbomolecular pumps chosen here and reduce the gas conduction heat loads accordingly. Smaller heat loads would allow us to reach and sustain lower stagnation temperatures or, alternatively, to produce more intense droplet beams using higher stagnation pressures. As we will point out below the droplet source nevertheless allows us to produce helium droplets from a wide range of expansion conditions including the supercritical expansion regime and expansions from the critical point (see Figure 3.20). The limitations imposed by the gas conduction heat load therefore are practically of minor importance.

3.3.3 Stagnation temperature

The temperature of the orifice assembly is stabilized by a commercial temperature controller (*Model 331, Lake Shore Cryotronics*) to better than 100 mK tolerance. The spatial proximity of cartridge heater and temperature sensor (see Figure 3.13) ensures a prompt response of the sensor to any change in heating power. In practice, any arbitrary temperature change in the region between 10 K and 20 K any can be completed within less than 15 s.

In contrast to the stagnation pressure p_o , which is readily read off from a manometer connected to the helium gas line on the outside of the vacuum chamber, the stagnation temperature T_o is potentially more difficult to determine. In particular, the question has to be answered whether the temperature measured by the sensor on the orifice assembly corresponds to the stagnation temperature at the orifice some 35 mm away. Potential reasons for erroneous temperature measurements are for example an improper thermal anchoring of the silicon diode or an imperfect cooling of the orifice disk which is partially exposed to room temperature

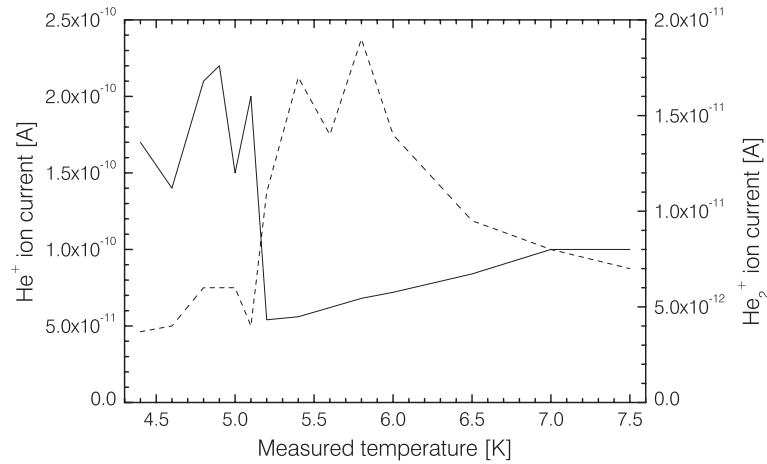


FIGURE 3.16: Ion currents for the droplet fragment ions He^+ (solid line, left scale) and He_2^+ (dashed line, right scale) for expansion conditions in the vicinity of the critical point of ^4He . The ion currents were measured by the Faraday cup on the mass spectrometer as a function of the temperature read by the silicon diode mounted to the orifice assembly. The stagnation pressure was maintained constant at $p_o = 2.2$ bar.

thermal radiation.

In order to shed light on this issue mass-spectrometric calibration measurements have been carried out. They exploit the fact that the average droplet size increases dramatically when the expansion regime is changed from subcritical to supercritical (see Section 2.1). The isentrope dividing these regimes is well known¹¹¹ and shown in Figure 2.1. Changes in droplet sizes have been shown to affect the fragmentation pattern resulting from electron impact ionization.¹⁸⁸ Consequently, we look for signatures of the expansion regime change in the ion currents of the most prominent, small fragment ions, *i.e.* He^+ or He_2^+ .

Figure 3.16 illustrates the measured currents for the two above-mentioned fragment ions in the vicinity of the critical point. During the experiment the stagnation temperature was slowly lowered from 7.5 K to 4.4 K, while the stagnation pressures was kept at $p_o = 2.2$ bar, *i.e.* very close to the critical pressure of 2.275 bar. Both ion signals show a sharp change around the critical temperature of 5.2 K which is taken as evidence that measured temperature and stagnation temperature agree within a tolerance of ± 0.1 K.

In principle, more calibration points at higher temperatures can be obtained by carrying out similar experiments for more elevated stagnation pressures. However, above the critical point the changes in fragmentation pattern are less pronounced and do not permit the direct derivation of a well-defined transition temperature. In Figure 3.17 we therefore plot the *first derivative* of the He_2^+ ion currents with respect to the measured temperature for various stagnation pressures p_o . The maxima of the plotted curves indicate the most rapid change of ion current with respect to the measured temperature. In spite of the more gradual change of fragmentation pattern at elevated stagnation pressures the temperatures of the maxima are rather well defined and may approximately be identified as the temperatures of expansion regime change. In Figure 3.18 the temperatures obtained this way are plotted against the nominal temperature

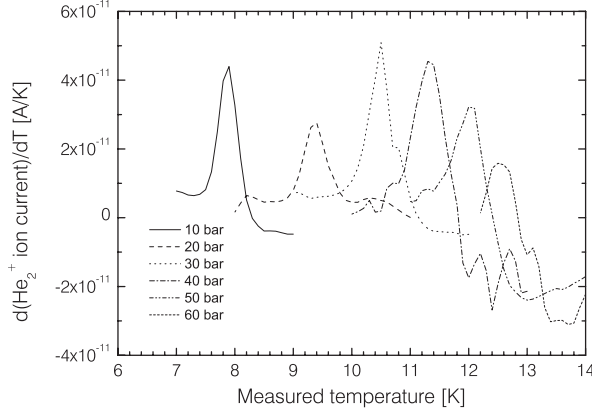


FIGURE 3.17: First derivative of the He_2^+ ion currents with respect to the temperature measured on the orifice assembly. The curves shown correspond to various stagnation pressures p_o ranging from 10 to 60 bar.

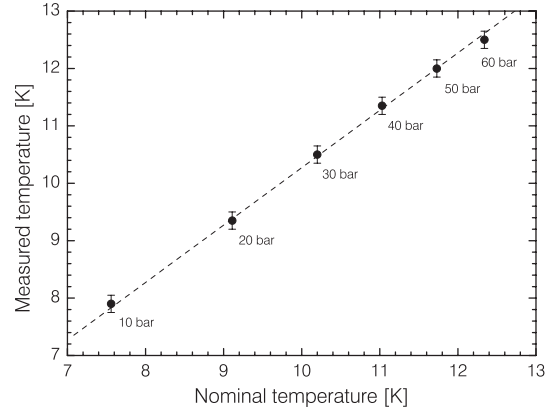


FIGURE 3.18: Temperatures of the maxima shown in Figure 3.17 versus nominal temperatures given by the isentrope through the critical point. The dashed line has unity slope.

given by the isentrope through the critical point. The values have been fitted with a straight line of unity slope. The fit indicates that the temperatures corresponding to the maxima in Figure 3.17 are systematically about 0.27 K higher than the nominal values. In view of the much more accurate temperature measurement around 5 K we believe that this shift, rather than being a systematic error in the stagnation temperature measurements, is a consequence of the imprecise way by which we define the temperature of expansion regime change. The fact that the 0.3 K shift is rather constant over a wide range of temperatures while not being observed at all at 5 K adds weight to this argument.

As a result we are convinced that the measured temperature does indeed accurately correspond to the stagnation temperature of the expansion. Based on the discussion above the maximum uncertainty of the readings can be given as $-0.3/+0.1$ K.

3.3.4 Performance

Figure 3.19 and Figure 3.20 illustrate two important aspects of the performance of the refrigeration system. Due to the heat capacity of the copper components mounted to the cold head both cooling down and warming up the system take a considerable amount of time. The time constant for cooling down the source can be inferred from Figure 3.19. The system reaches the fully cooled state about 10 hours after switching on the closed-cycle refrigerator system. In order to save compressor time at night and on weekends and yet to find an operational source in the mornings the compressor unit is coupled to a programmable timer that timely deactivates and activates the refrigeration system.

Figure 3.20 shows typical minimum stagnation temperatures T_o the system can maintain as a function of stagnation pressure p_o . Clearly, the system gives access to both the supercritical and subcritical expansion regimes. Temperatures below the critical temperature of 5.2 K can be maintained if the stagnation pressure is kept below about 4 bar.

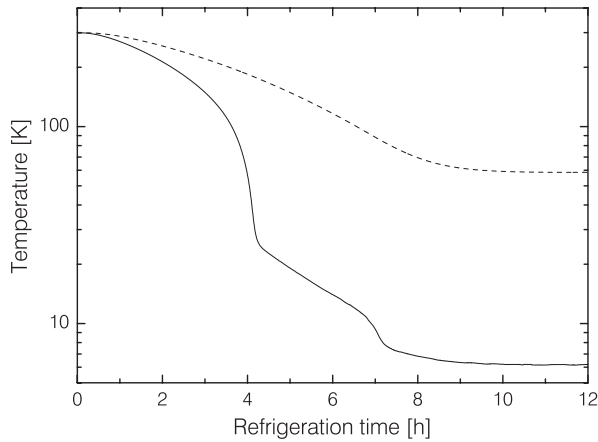


FIGURE 3.19: Typical refrigeration behaviour of the helium droplet source. The plot shows the temperature measured on the first (dashed line) and second stage (solid line) of the cold head. The data was taken for a $5 \mu\text{m}$ orifice and a stagnation pressure of 10 bar.

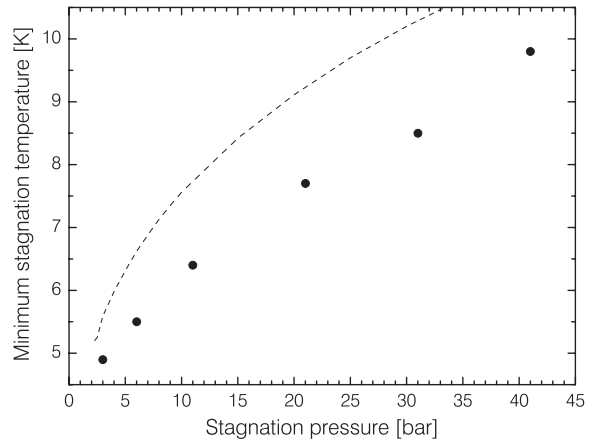


FIGURE 3.20: Typical minimum *sustainable* stagnation temperatures (dots) for a $5 \mu\text{m}$ orifice as a function of stagnation pressure. The dashed line illustrates the critical isentrope in bulk ^4He .

3.4 Cross beam doping

3.4.1 Introduction

As pointed out in Section 2.4 helium clusters readily pick-up foreign molecules by collisions. The most straightforward way to dope helium droplets with single or multiple impurities hence is to simply fill the doping chamber of our machine with an appropriate pressure p_S of the species to be introduced. Since the velocity vectors of the the gas phase molecules are in this case randomly oriented, some of the molecules inevitably will pass through the skimmer at the downstream end of the doping chamber and may subsequently enter the detection region of the ion imaging setup (see Section 3.2). The presence of both doped helium droplets and unsolvated dopant molecules in the detection region will however generally yield signals composed of two contributions that can be difficult to disentangle. It is therefore of great importance to minimize the density of gas phase dopant molecules in the detection region of the imaging setup.

The total effusive flux of scattering molecules ϕ_S into the detection chamber can easily be estimated from kinetic gas theory. Graham's law of effusion¹⁸⁹ states

$$\phi_S = \frac{A_{\text{sk}} p_S}{(2\pi m_S k_B T_S)^{1/2}}, \quad (3.10)$$

where m_S and T_S are the mass and the kinetic temperature of the scattering molecules, A_{sk} is the area of the skimmer aperture, and p_S is the partial pressure of the scattering gas in the doping chamber. We recall that under typical expansion conditions of $p_o = 30$ bar and $T_o = 15$ K the estimated average droplet size is $\bar{N} = 6080$ atoms (see Table 2.2). In order to dope 10 % of these droplets with a single foreign molecules, the pressure in the scattering cell

has to be set to about $p_S = 4.8 \cdot 10^{-7}$ mbar (see Figure 2.18).

The evaluation of equation (3.10) based on this pressure, the actual skimmer diameter of 1 mm, a kinetic temperature $T_S = 295$ K, and a dopant mass $m_S = 142$ amu (CH_3I) yields an effusive flux of $\phi_S = 4.9 \cdot 10^{11}$ s⁻¹. This compares to a flux of *doped* droplets of $\tilde{\phi}_D = 8.0 \cdot 10^9$ droplets s⁻¹ as estimated in Section 3.2. Under these typical conditions the doped droplets thus account for less than 2 % of the total flux of dopant molecules into the detection chamber. Instead, this flux is almost exclusively due to effusion from the doping chamber. The *direct* flux of unsolvated dopant molecules into the detection region of the ion imaging setup is however greatly reduced by an aperture of 1.7 mm diameter installed at the entrance of the flight tube (see Figure 3.4). Considering the solid angle defined by the aperture and the cosine angular distribution¹⁹⁰ of the beam emerging from the doping chamber, the direct effusive flux into the detection region can be estimated as $1.4 \cdot 10^8$ s⁻¹, which is roughly 50 times smaller than the flux of doped droplets.

These estimations highlight the importance of the effusive transport of dopant molecules into the detection chamber. In particular, it becomes clear that the partial pressure of the dopant species in the detection chamber is almost entirely determined by this transport mechanism. Although the dopant molecules are not likely to enter the detection region of the imaging setup directly, they may appear there after a few collisions with the walls or the vacuum components of the detection chamber. It therefore is instructive to compare the expected densities of singly doped droplets \tilde{n}_D and dopant species in the residual gas n_S at the point of interrogation with laser light, *i.e.* in the detection center of the ion imaging setup. These densities may be calculated using

$$\tilde{n}_D = \frac{\tilde{\phi}_D}{v_D A_D} \quad (3.11a)$$

and

$$n_S = \frac{\phi_S + \tilde{\phi}_D}{s_S}, \quad (3.11b)$$

where v_D denotes the droplet beam speed, A_D is the cross section of the droplet beam in the detection zone, and s_S is the pumping speed for the dopant molecules in the detection chamber. Taking the pumping speed for molecular nitrogen $s_S = 1400$ l/s and a droplet beam diameter of 1.8 mm one can proceed to evaluate these equations for the typical expansion conditions of $p_o = 30$ bar and $T_o = 15$ K already used above. For these conditions the droplet beam speed is given by $v_D = 355$ m/s (see Section 4.7.1) and one finds $\tilde{n}_D = 8.9 \cdot 10^{12}$ m⁻³ and $n_S = 3.6 \cdot 10^{11}$ m⁻³. However, the effective interaction length of the laser beams with the residual gas may well be an order of magnitude longer than with the molecular beam. The introduction of impurities by means of a gas-filled doping chamber therefore is expected to result in roughly comparable signals from solvated and unsolvated dopant molecules.

In order to reduce the density n_S of unsolvated dopant molecules in the detection region both active and passive measures are taken. Passively, the residual gas density n_S can be lowered by increasing the pumping speed s_S in the chamber. In our apparatus this can be accomplished by cooling down the liquid nitrogen reservoirs installed in the interior of the detection chamber. A more active measure is to suppress the effusive transport of dopant

species into the detection chamber. For this reason the doping chamber is equipped with a nozzle to intersect the droplet beam at right angles with a beam of dopant molecules. This method of introducing impurities into the helium droplets has the advantage of establishing a *directed flow* of dopant molecules towards the turbomolecular pump located at the bottom of the doping chamber. This way many of the molecules either undergo sticking collisions with droplets or are immediately removed from the doping chamber by the pump. Therefore less molecules remain that, after some collisions with the chamber walls, have the right velocity vectors to pass through the skimmer aperture into the detection chamber^d. An additional benefit of this doping method lies in a more economical use of the sample since the required gas densities are created locally.

3.4.2 Setup

The beam of dopant molecules emerges from a $50 \text{ mm} \times 50 \text{ }\mu\text{m}$ slit which is laser-machined into a stainless steel plate of 0.5 mm thickness. The nozzle is situated above the droplet beam and mounted to a one-dimensional translation stage. This way the distance between the droplet beam and the slit nozzle can be varied. For all experiments presented below the nozzle exit was positioned 5 mm above the droplet beam center. In order to obtain a maximum overlap of the two beams, great care was taken to align the slit parallel to the droplet beam.

A flexible *Teflon* hose links the nozzle to a small vacuum compartment which is connected to the doping chamber by means of a right-angle valve. The valve is used to either pump or isolate the volume from the doping chamber. When isolated the compartment can be filled with the desired gas using a leak valve (*UDV 235, Balzers*). The pressure in the volume, *i.e.* the backing pressure of the slit nozzle, is species independently monitored by means of a diaphragm gauge (*CMR 264, Pfeiffer Vacuum*).

3.4.3 Calibration

In this section we describe a calibration of the cross beam doping setup. The calibration will relate the backing pressure of the slit nozzle p_{cross} to a scattering pressure p_S in the doping chamber that produces equally doped helium droplets. This calibration is essential to the photodissociation experiments presented in this work since the droplet beam must be prepared such that the vast majority of droplets contain either none or only a single impurity. Otherwise the signal may be affected by photodissociation processes of dopant clusters that are expected to exhibit very different dissociation dynamics.^{191,192}

Towards this goal we first recall properties of the “normal” pick-up process in a scattering cell. As shown in Section 2.4.2 this process can be described approximately by Poisson statistics. From the equational form (2.30) it becomes obvious that each scattering cell pressure p_S is uniquely related to the intensity ratio P_2/P_1 of doubly to singly doped helium droplets according

^dIn the future an additional differential pumping stage will be installed between doping and detection chamber. This will eventually reduce the effusive flux into the detection chamber by roughly three orders of magnitude. However, the additional vacuum chamber will add to the distance between orifice and detection region and will therefore somewhat reduce the absolute droplet signal.

to

$$\frac{P_2(p_S)}{P_1(p_S)} = \frac{1}{2}\beta p_S, \quad (3.12)$$

where the factor β is essentially a function of the mean capture cross section $\bar{\sigma}_{\text{cap}}(\bar{N})$ (see equations (2.30)). One therefore may write

$$\frac{P_2(p_S)}{P_1(p_S)} \propto \bar{\sigma}_{\text{cap}}(\bar{N}) p_S. \quad (3.13)$$

Since multiple impurities inside a helium droplet are expected to coagulate quickly to form oligomers, the relative intensities P_1 and P_2 may be deduced from the bare monomer and dimer ion signals as measured by the mass spectrometer downstream of the scattering cell. These measurements are however not straightforward since the electron impact ionization involved leads to a number of complications. We note for example that the ionization cross sections of the helium droplets are roughly proportional to their geometric cross sections^{100,193} and hence depend on the droplet size. Moreover, the probability of producing bare impurity ions decreases with cluster size¹⁴² and approaches zero for very large droplets.¹¹⁴ Additionally, the ionization process may lead to fragmentation of molecules and oligomers inside the droplet. Compared to monitoring the monomer and dimer parent ions, higher signal levels may thus be obtained by detecting their most prominent fragment ions.

In order to greatly simplify the mathematical treatment we make the crude assumption that all helium clusters in the droplet beam have a uniform size \bar{N} independent of how many impurities they may contain. Additionally, we will neglect any fragmentation of higher to lower order oligomers in the ionization process. We furthermore assume that the electron impact ionization yields characteristic fragment ions for both monomer and dimer doped helium droplets. For a given droplet size the ratio $R_{2,1}$ of the corresponding ion currents will then be proportional to the ratio of the real intensities P_2/P_1 of doubly and singly doped droplets. We therefore note

$$R_{2,1}(p_S) = \chi(\bar{N}) \frac{P_2(p_S)}{P_1(p_S)}, \quad (3.14)$$

where the factor $\chi(\bar{N})$ accounts for the different overall system and droplet size dependent detection efficiencies of monomer and dimer doped droplets. Putting equations (3.13) and (3.14) together and introducing a new size dependent factor $\alpha(\bar{N})$ one may write

$$R_{2,1}(p_S) = \alpha(\bar{N}) \bar{\sigma}_{\text{cap}}(\bar{N}) p_S. \quad (3.15)$$

Hence, the ratio of the ion currents $R_{2,1}$ and the pressure p_S of scattering particles in the doping chamber are proportional for any given droplet size \bar{N} .

For cross beam doping a similar picture emerges. Assuming that the particle density created by the cross beam in the region of overlap with the droplet beam is uniform and proportional to the backing pressure p_{cross} we may write

$$\tilde{R}_{2,1}(p_{\text{cross}}) = \tilde{\alpha}(\bar{N}) \bar{\sigma}_{\text{cap}}(\bar{N}) p_{\text{cross}} \quad (3.16)$$

similar to (3.15). Here, $\tilde{R}_{2,1}$ denotes the ratio of the ion currents measured for cross beam doping. Since the interaction length of the cross beam with the droplet beam is smaller than

the geometrical length of the doping chamber it is evident that the cross beam has to produce somewhat higher densities to achieve the same level of doping as the gas filled chamber^e. Since the doping method has no influence on the detection efficiencies we note that

$$\tilde{R}_{2,1}(p_{\text{cross}}) = \chi(\bar{N}) \frac{\tilde{P}_2(p_{\text{cross}})}{\tilde{P}_1(p_{\text{cross}})}, \quad (3.17)$$

where, obviously, \tilde{P}_2/\tilde{P}_1 is the intensity ratio of doubly and singly doped helium droplets produced by the cross beam doping method.

Both doping methods yield equal results if the condition

$$\frac{P_2(p_S)}{P_1(p_S)} = \frac{\tilde{P}_2(p_{\text{cross}})}{\tilde{P}_1(p_{\text{cross}})} \quad (3.18)$$

is fulfilled. Using equations (3.14) and (3.17) this condition reduces to

$$R_{2,1}(p_S) = \tilde{R}_{2,1}(p_{\text{cross}}). \quad (3.19)$$

With the aid of equations (3.15) and (3.16) we then find the equivalent condition

$$p_S = \frac{\tilde{\alpha}(\bar{N})}{\alpha(\bar{N})} p_{\text{cross}}. \quad (3.20)$$

The latter equation provides the desired relation between p_S and p_{cross} and therefore constitutes the basis of the calibration. It is important to note that in equation (3.20) the capture cross section $\bar{\sigma}_{\text{cap}}$ has dropped out. Apart from possible higher order effects due to the speed of the scattering particles the calibration thus is independent of the dopant species.

Experimentally, the calibration was carried for a fixed helium stagnation pressure of $p_o = 30$ bar and various stagnation temperatures T_o in the range from 12 K to 18 K. CH_3I was used as a dopant molecule. The electron impact conditions during the experiment were a kinetic energy of 70 eV and an electron current of 1 mA. Under these conditions we observe a characteristic fragmentation pattern of both the CH_3I monomer and dimer. The most prominent fragment ion of the monomer is I^+ (127 amu), while the dimer fragments preferentially to CH_3I_2^+ (269 amu). The calibration therefore is based on the ion currents for those two masses as measured by the Faraday cup of the quadrupole mass spectrometer.

In Figure 3.21 we plot the ratio $R_{2,1}$ of the ion currents at 269 amu and at 127 amu as a function of the scattering gas pressure p_S in the doping chamber. The scattering gas pressure is obtained by subtracting a previously determined background pressure (mainly helium) from the total pressure in the doping chamber. The doping chamber pressure is measured by a cold cathode gauge that is calibrated for molecular nitrogen. Since the gauge sensitivity depends on the species monitored one has to use proper correction factors to convert measured into real pressures for all gases other than N_2 . These correction factors can be estimated by comparing

^eAlthough a minor effect it is worth mentioning that equation (3.16) holds only if there is no effect of the backing pressure p_{cross} on the speed of the dopant molecules emerging from the slit nozzle which is true for a purely effusive beam.

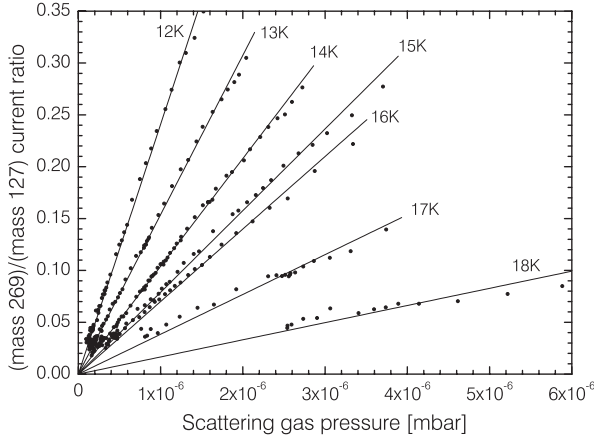


FIGURE 3.21: Plot of the ion current ratio $R_{2,1}(p_S)$ as a function of the scattering gas pressure p_S in the doping chamber. The graph shows results obtained for a fixed helium stagnation pressure $p_o = 30$ bar and various stagnation temperatures T_o in the range from 12 K to 18 K.

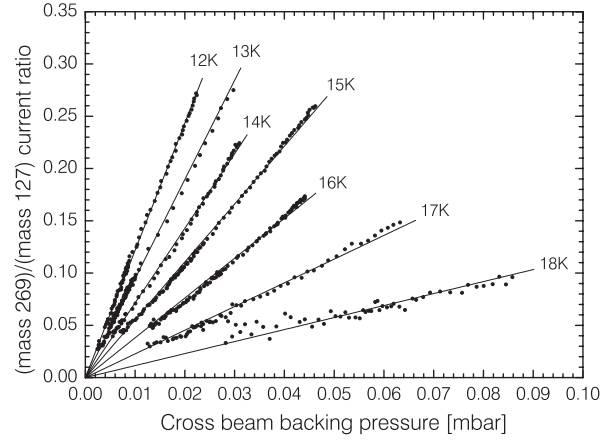


FIGURE 3.22: Plot of the ion current ratio $\tilde{R}_{2,1}(p_{\text{cross}})$ as a function of the cross beam backing pressure p_{cross} . The graph shows results obtained for a fixed helium stagnation pressure $p_o = 30$ bar and various stagnation temperatures T_o in the range from 12 K to 18 K.

the maximum absolute electron impact ionization cross sections of the species of interest to the maximum cross section of molecular nitrogen. Taking the maximum cross sections for CH_3I ,¹⁹⁴ CF_3I ,^{195,196} and N_2 ¹⁹⁷ from the literature one obtains the factors given in Table 3.3. The errors of the shown values can be estimated by comparing correction factors obtained with the same method for other gases to correction factors supplied by the gauge manufacturer. Such an analysis was carried out for seven other gases and lead to a maximum deviation of $\pm 22\%$.

Molecule	Correction factor
CH_3I	0.245
CF_3I	0.281

TABLE 3.3: Cold-cathode gauge correction factors for CH_3I and CF_3I . The relative error of the given values is estimated as $\pm 22\%$.

Figure 3.22 illustrates the results of the complementary experiment where the ratio $\tilde{R}_{2,1}$ of ion currents was recorded as a function of the backing pressure p_{cross} of the cross beam slit nozzle. In this case no correction factors are needed as the pressure measurement by the diaphragm gauge is species independent.

In both cases the recorded curves confirm the linear behaviour suggested by equations (3.15) and (3.16). For each set of expansion conditions (p_o, T_o) we obtained the slopes $\alpha(\bar{N}) \bar{\sigma}_{\text{cap}}(\bar{N})$ and $\tilde{\alpha}(\bar{N}) \bar{\sigma}_{\text{cap}}(\bar{N})$ by linear regression through the origin. Figure 3.23 shows the resulting ratios $\tilde{\alpha}(\bar{N}) / \alpha(\bar{N})$ for each helium stagnation temperature T_o under investigation. Since the ratio is reasonably constant over a wide range of stagnation temperatures, *i.e.* droplet sizes, it

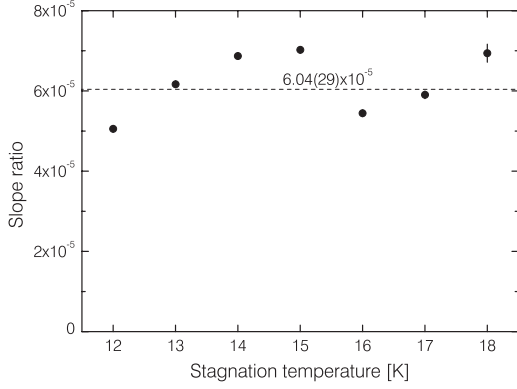


FIGURE 3.23: Ratio of the slopes $\tilde{\alpha}(\bar{N}) \bar{\sigma}_{\text{cap}}(\bar{N})$ and $\alpha(\bar{N}) \bar{\sigma}_{\text{cap}}(\bar{N})$ for CH_3I as dopant molecule. The mean value $6.04(29) \cdot 10^{-5}$ allows one to relate a cross beam backing pressure p_{cross} to an equivalent scattering gas pressure p_{S} .

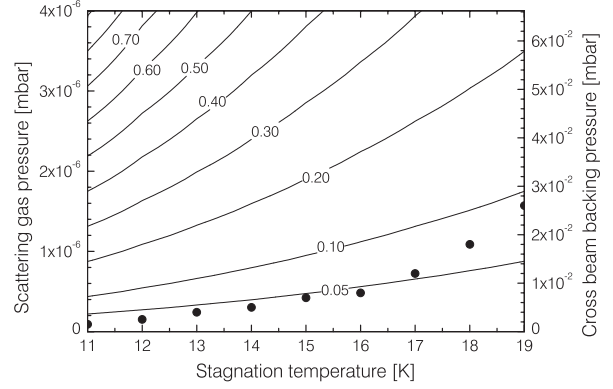


FIGURE 3.24: Contour plot of the intensity ratio P_2/P_1 of dimer and monomer doped helium droplets as a function of stagnation temperature T_o and scattering gas pressure p_{S} (left scale). The sticking coefficient is assumed to be unity. Using the calibration result equivalent backing pressures for the cross beam were calculated (right scale). The solid dots indicate typical cross beam backing pressures as given in Table 3.4.

is useful to work with the mean value

$$\langle \tilde{\alpha}/\alpha \rangle = 6.04(29) \cdot 10^{-5} .$$

The error given here is the statistical error only. However, systematic errors arise which mainly are due the uncertainty of the pressure measurement by the cold-cathode gauge. The accuracy of the gauge is given as $\pm 30\%$ which adds to the uncertainty of the correction factors found above. Together these effects lead to a systematical error of $\pm 38\%$. We therefore write

$$p_{\text{S}} = 6.0(23) \cdot 10^{-5} \cdot p_{\text{cross}} , \quad (3.21)$$

a relation which will be used for both CH_3I and CF_3I . This can be safely done as CH_3I and CF_3I have comparable masses and therefore will have similar speeds and almost identical collision probabilities with the droplets.

Based on this calibration the intensity ratio P_2/P_1 of doubly to singly doped helium droplets can be predicted for any given backing pressure p_{cross} of the cross beam. This is illustrated in Figure 3.24 for the standard helium stagnation pressure $p_o = 30$ bar. The contour lines correspond to intensity ratios $P_2(p_{\text{S}})/P_1(p_{\text{S}})$ as calculated from equations (2.30) using the predicted droplet sizes (see Table 2.2) and realistic factors F_{a_0} ^f. The mean capture cross sections are calculated using a sticking coefficient $S = 1$ and mean integral scattering cross sections as given by equation (2.16). The right scale in Figure 3.24 shows the backing pressures p_{cross} that, according to equation (3.21), correspond to the scattering gas pressures p_{S} shown on the left.

^fThe graph was computed for CH_3I but applies to a very good degree of approximation also to CF_3I whose factor F_{a_0} is by less than 6% different (see Section 2.4.2).

T_o [K]	11	12	13	14	15	16	17	18	19
p_{cross} [10^{-4} mbar]	15	25	40	50	70	80	120	180	260

TABLE 3.4: Typical cross beam backing pressures for helium droplets produced at a stagnation pressure p_o of 30 bar. The pressures apply to both CH_3I and CF_3I .

The solid dots illustrate the typical backing pressures for the dissociation experiments as given in Table 3.4^g. As illustrated these backing pressures p_{cross} lead to predicted ratios P_2/P_1 of $\approx 1/40$ for 11 K and $\approx 1/11$ for 19 K. These predictions suffer however from the uncertainties associated with both the cluster sizes (see Figure 2.8) and the conversion between p_S and p_{cross} given by equation (3.21). Moreover, the dimer to monomer ratio is systematically overestimated since a maximal sticking coefficient was assumed and because the evaporative loss of helium atoms following the pick-up of the first impurity is neglected in the Poisson description of the pick-up processes. The latter effect is particularly relevant to the smaller droplets produced at 17, 18, and 19 K, and would decrease the P_2/P_1 ratio compared to the values shown in the graph. In spite of the uncertainties involved it becomes clear that for backing pressures p_{cross} as given in Table 3.4 monomer doped helium droplets will by far outweigh the doubly doped clusters.

3.5 Ion Imaging

3.5.1 Introduction

Two-dimensional ion imaging is a powerful technique for studying molecular reaction dynamics and has become increasingly popular over the recent years.^{198–200} The significance of this method arises from the fact that the full three-dimensional velocity distribution of a state-selected product may be recovered from a single recorded image. The possibility to measure simultaneously the product’s internal energy as well as its kinetic energy distribution and angular distribution sets this technique apart from conventional time-of-flight methods and permits shedding light on important details of the reaction mechanism.

Owing to these advantages ion imaging has become a standard method for elucidating the dynamics of unimolecular photodissociation reactions as well as bimolecular reactive scattering. Moreover, the technique allows one to study the photoionization of atomic and molecular species since photoelectrons can be imaged with with the very same setup simply by changing the polarity of the voltages applied to the ion optics.

We use an ion imaging setup to monitor the outcome of photon induced reactions inside or at the surface of helium clusters. In case of a dissociation event inside a helium droplet we can learn with which speed, in which direction, and in which quantum state a particular fragment eventually leaves the cluster. This information allows us to gain detailed insight into the translational dynamics of neutral photofragments inside the helium droplets.

^gThese pressures were originally derived from an ion current ratio $\tilde{R}_{2,1}$ of $\approx 1/40$ (see Figure 3.22).

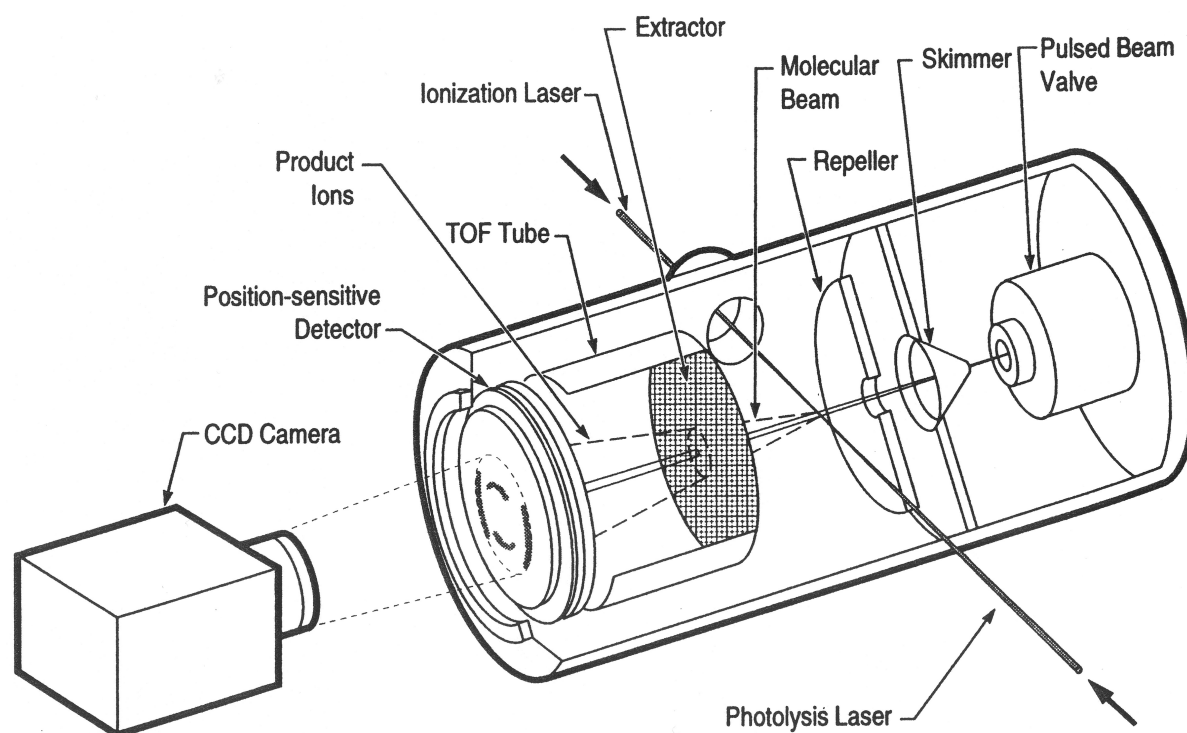


FIGURE 3.25: Conventional single-grid ion imaging apparatus as developed by Chandler and Houston. The figure is reproduced from reference [198].

3.5.2 Conventional ion imaging

The imaging of reaction products based on two-dimensional charge-sensitive detectors was introduced by Chandler and Houston in 1987.²⁰¹ Using a microchannel plate (MCP) and phosphor screen assembly linked to a charge-coupled-device (CCD) camera they recorded images of photofragments which had been state-selectively ionized using a REMPI scheme. We will use a schematic illustration of their original apparatus, shown in Figure 3.25, to discuss the technique in more detail.

A collimated beam of cold parent molecules is prepared by skimming the supersonic expansion emerging from a pulsed valve. Further downstream the beam enters the detection region where a homogeneous electric field is maintained between the positively charged repeller plate and the extractor grid that is kept at ground. Here, the molecular beam is sequentially irradiated by two linearly polarized laser pulses that propagate perpendicular with respect to the axis of the supersonic jet. The photolysis pulse dissociates the parent molecule and creates a cloud of neutral fragments that expands due to the kinetic energy release. Using a REMPI scheme a specific fragment species subsequently is state-selectively ionized by the second laser pulse. By virtue of its small mass the photoelectron takes away virtually all the kinetic energy available in an ionization event and the positive ions thus are created with nearly no change in velocity. Once formed, the ions find themselves in the electric field and are accelerated towards

the detector. After passing the extractor grid they move through the field-free drift zone of the apparatus while constantly continuing to expand. Ultimately, the ions hit the front MCP and are detected as light pulses on the phosphor screen. The ion images eventually are obtained by accumulating the light signals on the camera over a certain number of laser shots.

Although highly inhomogeneous electric fields are present in the close vicinity of the wires of a grid electrode, the electric fields in conventional imaging setups can macroscopically be described as homogeneous and with flat equipotential surfaces parallel to the detector surface. The radius at which a particular fragment ion eventually hits the detector hence is solely determined by the unaffected fragment's velocity component parallel to the detector surface as well as its time-of-flight. In order for the ion images to represent true projections of the fragment cloud it therefore is crucial that all ions of the same species experience the same time-of-flight regardless of their initial distance to the detector ("space resolution") and their initial velocity vector ("energy resolution"). Under these conditions the imaging properties are similar to an ideal experiment where the ionized fragments expand in a field-free environment and, once macroscopic size is reached, are accelerated towards the detector by an instantaneously activated and infinitely high electric field. The requirement of equal time-of-flight commonly is referred to as "pancaking" because the electric field has to flatten the expanding ion cloud in the dimension perpendicular to the ion detector.

Good space and energy resolution are obtained simultaneously in two-grid setups as introduced by Wiley and McLaren.²⁰² Using focused lasers, however, the differences in initial distance to the detector are readily minimized. Under these conditions space resolution is no longer a requirement and it becomes beneficial to employ the simpler and more transmissive single-grid setup as discussed above and as shown in Figure 3.25. Here, "pancaking" simply is achieved if the kinetic energy acquired by the ions in the electric field between the repeller and extractor electrodes is high compared to the initial kinetic energy of the nascent fragments, which usually is the case.

For both single and two-grid instruments the ion time-of-flight is linearly related to the square root of the ion mass. If the spread in time-of-flight of a particular species is small, the ions therefore arrive at the detector as pancake shaped bunches which are separated in time according to their mass. By applying a short negative high voltage pulse to the front plate of the MCP assembly, the detection sensitivity can be tailored to match a single mass only. Under "pancaking" conditions the imaging of molecular or atomic reaction products thus can most easily be coupled with mass selection. Moreover, ions of the same mass arrive at the detector with an almost identical terminal speed which results in a uniform detection sensitivity regardless of the initial velocity of the products.

However, a major drawback arises from the homogeneous fields used in the grid setups. Since no electric forces occur in the plane parallel to the detector surface the image resolution is always limited by the dimensions of the ionization volume in this plane. In order to achieve images of high spatial resolution it thus may become necessary to reduce the diameter of the molecular beam at the price of signal loss. We will show in the following section how that limitation can be overcome.

3.5.3 Velocity map imaging

A considerable leap in the resolution of ion and electron imaging was brought about in 1997 by Eppink and Parker.^{203,204} They realized that open electrodes can shape the electrostatic potential in such a way that particles emerging from different source positions but with identical velocity vectors hit the same spot on the ion detector. The technique therefore was termed “velocity map imaging”. Transmission losses and substantial trajectory deflections associated with the presence of grids in conventional apparatus are thus elegantly avoided. Most importantly, however, this technique eliminates the blurring caused by the finite size of the source volume.

While drastically enhancing the resolution of the recorded ion or electron images the technique preserves the essential properties of conventional imaging based on flat equipotential surfaces. Most notably, the time-of-flight τ still is linearly related to the square root of the the ion mass, while the spread in time-of-flight $\Delta\tau$ is small and found to obey $\Delta\tau/\tau \lesssim 1\%$.²⁰³ Like in conventional imaging, this “pancaking” property of the velocity map imaging setup permits easy mass selection and results in a uniform detection sensitivity.

The ion optics of the instrument consist of a repeller plate and two open electrodes that together form a so-called asymmetric immersion lens. Voltages are applied to the repeller plate (V_R) and the extractor electrode (V_E) in the center of the equally spaced assembly, while the second open electrode is kept at ground. In order to elucidate the behaviour of this lens it is instructive to examine some general properties associated with the trajectories of non-relativistic charged particles in cylindrically symmetric ion optics. It can be shown²⁰⁵ that the focal plane of a particular setup depends only on the ratio of the applied voltages, whereas the absolute voltages can be chosen freely. Moreover, the shape of the trajectories is independent of the mass-to-charge ratio q/m . Any two particles born into the same point in space with identical kinetic energy and a velocity vector that points into the same direction will therefore follow a trajectory of identical shape in space, although the time-of-flight will be different if the two masses are dissimilar. It is for this reason that both ions and electrons may be velocity mapped by using voltages of the same magnitude but opposite polarity. Moreover, for a fixed set of voltages one may assign an energy scale to the image radii which is independent of the particle mass. Once carried out for a particular species such a calibration then applies equally well to all other masses.

For the three-electrode velocity mapping optics these considerations imply that focusing only can be accomplished for a fixed and geometry dependent ratio V_E/V_R which has to be determined experimentally. With V_E and V_R locked to another only the repeller voltage V_R can be chosen freely. This degree of freedom may be used to adjust the time-of-flight of the particles and, at the same time, the size of the obtained image. Particles created with little kinetic energy release can therefore only be observed with reasonable spatial resolution on the detector if the repeller voltage is kept low. This has consequences for the detection sensitivity since the repeller voltage determines the kinetic energy with which the charged particles impinge on the front plate of the MCP detector. As illustrated in in Figure 3.26 the detection sensitivity drops dramatically with decreasing repeller voltage. With respect to monitoring the kinetic and angular distribution of reaction products with little kinetic energy release it therefore becomes desirable to find a means to operate the ion optics with high repeller voltages while maintaining a large image diameter. We will present a solution to this dilemma in the next section.

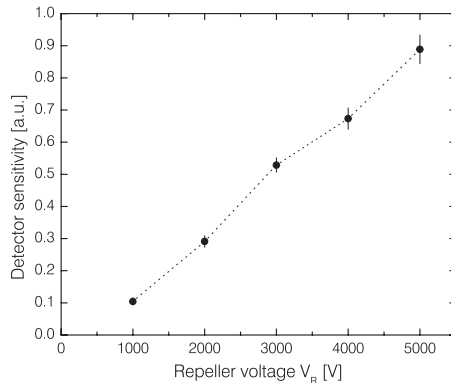


FIGURE 3.26: Sensitivity of the MCP detector used in our imaging setup as a function of repeller voltage V_R . Focusing conditions were maintained by adjusting the extractor voltage V_E accordingly. The sensitivity refers to the electrical signal obtained by operating the phosphor screen as an anode. A potential difference of 650 V was applied across each of the two MCPs of the chevron assembly.

3.5.4 Image magnification by an einzel lens

Offerhaus *et al.*²⁰⁶ demonstrated that a simple einzel lens can be employed to considerably magnify velocity map images. The lens is mounted in between the asymmetric immersion lens composed of repeller, extractor, and ground electrode and the charge-sensitive detector. It consists of three identical and equally spaced open electrodes. Only the voltage V_{lens} on the center electrode is varied, while the two outer electrodes are kept at ground. The asymmetric immersion lens then is operated such that a velocity map image is created in a plane in front of the einzel lens which then images this plane magnified onto the detector. Analogous to light optics the lens *inverts* the velocity map image. Since the electrostatic potential in front of and behind the einzel lens is identical, no net effect on the kinetic energy of the traversing particles results. The einzel lens thus provides a means to magnify an ion or electron image without having to reduce the voltages on the repeller electrode. Highly magnified images of products with low kinetic energy release can thus be obtained without loss in detection sensitivity.

Velocity map imaging with einzel lens requires three electrode voltages to be set precisely. These voltages are the repeller voltage V_R , the extractor voltage V_E and the voltage on the center electrode of the einzel lens V_{lens} . Unlike in imaging without einzel lens the ratios of these three voltages are not locked to one another. This follows from the fact that changing the voltage V_{lens} results in a different focal length of the einzel lens. In order to obtain sharp images on the MCP detector the focal plane of the repeller/extractor optics thus has to be adapted accordingly. Each einzel lens voltage thus corresponds to a particular set of focusing conditions for which the characteristic voltage ratio has to be determined individually.

It is useful to note that the inverting effect of the einzel lens can be exploited to reveal the origin of the ion images, *i.e.* the point (or the pixel) onto which particles of zero kinetic energy in the laboratory frame are mapped. This is especially valuable if the propagation direction of the molecular beam under study is perpendicular to the axis of the instrument. In this case the velocity components of the molecular beam parallel to the detector surface cause a displacement of any velocity-mapped fragment cloud and make it difficult to accurately

determine the origin. In the absence of lens errors the origin position is, however, insensitive to the voltage on the einzel lens. Two images, recorded with and without the einzel lens, will therefore exhibit displacements in opposite directions from which the position of the origin can be derived. Knowing the image origin then allows identifying absolute velocities in the laboratory frame, which, for example, can be used to measure the speed distribution of the molecular beam under study.

3.5.5 Properties

Under velocity mapping conditions a monochromatic and spherically symmetric ion or electron cloud of expansion speed v will give rise to a ring structure on the detector. The radius R of the ring is related to the ion time-of-flight τ by the empirical relation²⁰³

$$R = \mathcal{N}v\tau, \quad (3.22)$$

where \mathcal{N} , often termed magnification factor, depends on the apparatus geometry and the voltage settings of the einzel lens^h.

Similar to conventional grid setups, the time-of-flight τ in a velocity map imaging setup is determined by the potential energy gained in the initial acceleration. Thus, a standard time-of-flight dependence of the form

$$\tau \propto \sqrt{m/(qV_R)}, \quad (3.23)$$

holds, where V_R denotes the repeller voltage and m and q stand for the particle's mass and charge, respectively.

Introducing the kinetic energy release $T = mv^2/2$ and combining equations (3.22) and (3.23), one finds the mass independent relation

$$R \propto \mathcal{N}\sqrt{T/(qV_R)} \quad (3.24)$$

which forms the basis for the calibration process described in Section 3.5.8.

3.5.6 Setup

The ion optics assembly of the inhouse-built velocity map imaging setup with einzel lens is illustrated in Figure 3.27. All materials involved were carefully selected in order not to compromise the ultra high vacuum in the detection chamber. The grounded flight tube (85 mm O.D., 80 mm I.D.) is made of oxygen-free high conductivity (OFHC) copper and holds a bore of 82 mm diameter into which the electrode assembly is inserted. All electrodes were machined from a zinc-free bronze alloy and were manually polished to remove surface imperfections that could potentially lead to discharges. The electrodes also received a platinum coating that substantially increased the work function of the surfaces to about 5.65 eV.²⁰⁷ This way the risk of accidentally creating photoelectrons by stray UV radiation from the lasers is considerably reduced. Electrical insulation and mechanical alignment of the electrodes is provided by PTFE

^hNote that $\mathcal{N} = 1$ for flat equipotential surfaces as used in conventional grid imaging setups.

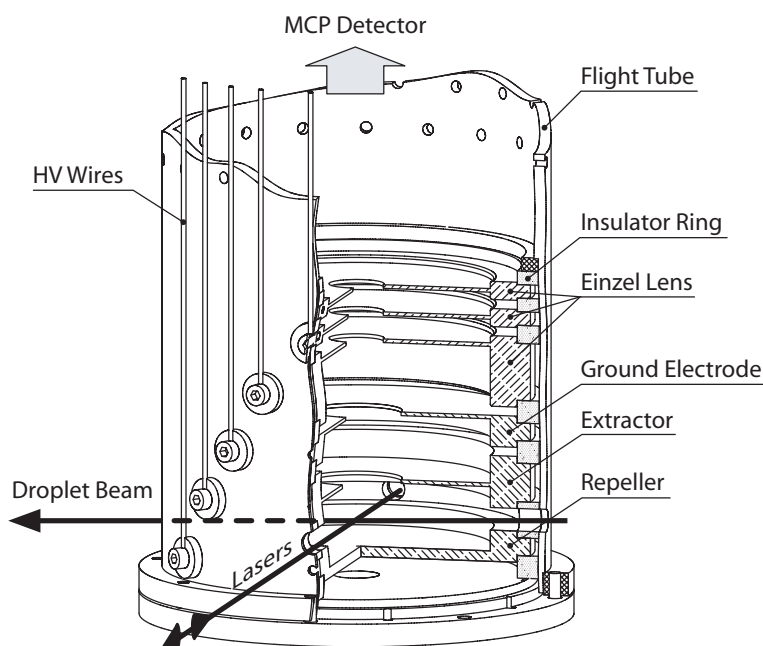


FIGURE 3.27: Ion optics assembly of the velocity map imaging setup with einzel lens. The open extractor and ground electrodes have circular holes of 20 mm diameter, while holes of 12 mm diameter were machined into the electrodes of the einzel lens. The central part of all open plate electrodes has a thickness of 0.8 mm. The electrode spacing is 15 mm in the asymmetric immersion lens and 6 mm in the einzel lens.

spacers in the shape of hollow cylinders. Since these insulators may collect charges, all electrodes were given a relatively thick 9 mm brim that effectively shields the interior of the ion optics from any fields potentially emerging from the spacers.

The axes of the flight tube, the droplet beam, and the lasers are mutually perpendicular. The resolution of any fragment velocity map image thus is limited by the spread of the molecular beam speed. Moreover, the center of any fragment image will be displaced with respect to the origin of the imaging setup due to the parent molecule speed parallel to the detector surface.

Figure 3.1 illustrates how the ion imaging setup is incorporated into the helium droplet machine. The center of the detection region, *i.e.* the region where the droplet and laser beams overlap, is located about 216 mm downstream of the orifice of the droplet source and at a distance of 395 mm from the front surface of the charge- and position-sensitive detector. In order to be able to image photoelectrons the field-free part of the flight tube is shielded from stray magnetic fields by a high permeability foil (*CO-NETIC AA, Detakta*) of 0.1 mm thickness.

The detector consists of a 75 mm diameter chevron MCP assembly and a P-20 phosphor screen (*S-3075-25-I-PS, Galileo*). This phosphor is characterized by a long phosphorescence lifetime and an emission maximum in the green. The MCP assembly is equipped with a center tab that allows us to separately control the voltages across the first and the second plate of the assembly. A fast high voltage switch (*HTS 31-GSM, Behlke*) with a nominal minimum pulse width of 80 ns is used to gate the gain of the front MCP and thereby to record velocity map

images in a mass-selective way. Additionally, the phosphor screen can be operated as an anode in order to obtain an electrical time-of-flight signal. From this signal a mass spectrum can be acquired by either displaying the signal on an oscilloscope or by counting individual events in an multi-channel scaler.

The images are recorded using a $f = 50$ mm objective (*50mm f/1.2, Nikon*) and a 1024×1024 pixel CCD camera (*DU 434-BV, Andor*), whose spectral sensitivity matches well with the emission characteristics of the phosphor screen. The camera is reproducibly positioned at a fixed distance to the phosphor screen. A telescope shield protects the space between camera and detector from ambient light. The camera chip is cooled to below -70 °C by a Peltier element in order to reduce the background noise from thermal electrons. After a given accumulation period the images are transferred to a personal computer (PC) for further processing.

3.5.7 Data analysis

Many important dynamical properties of the process under study are revealed directly by the raw projection images. The outer radius of the image as well as of any distinct ring structure can be converted to the maximum expansion speed associated with a particular product channel. Moreover, the angular distribution of the products can be inferred qualitatively from the projection. For a more quantitative analysis it is, however, indispensable to have a knowledge of the three-dimensional speed and angular distribution that gave rise to the observed projection.

As pointed out in Section 2.5 prompt photodissociation via a one-photon transition results in a fragment cloud of cylindrical symmetry with respect to the polarization axis of the photolysis laser. If the subsequent ionization of the fragments is not affected by alignment effects, the ion cloud will conserve the same symmetry. Under the condition that the symmetry axis of the ion cloud is *parallel* to the detector surface, no information is lost when projecting the ions onto the detector. In this case, the full three-dimensional (3D) velocity distribution of the ions (and the neutral fragments) can be recovered from the two-dimensional image. The unique transformation relating the two-dimensional velocity map image and the 3D velocity distribution of cylindrical symmetry is the so-called (inverse) Abel transform. The properties and the numerical implementation of this transform are discussed in more detail in Appendix B.

The Abel inversion software created as part of this work is essentially based on an algorithm by Vrakking²⁰⁸ and provides a discrete, full 3D velocity distribution in *spherical* coordinates (v, θ) . In the particular case of a photodissociation reaction the polar angle θ is given as the angle between the velocity vector of the fragment and the polarization vector \mathbf{E} of the photolysis laser defining the symmetry axis of the fragment cloud. Due to the cylindrical symmetry of the 3D distribution no dependence on the azimuthal angle φ occurs. Following the treatment by Vrakking²⁰⁸ the 3D velocity distribution is written as a product of a one-dimensional “velocity distribution” $P_v(v)$ and a two-dimensional, speed dependent angular distribution $P_\theta(v, \theta)$. The normalization of these distributions is carried out such that

$$\pi \int_0^\infty \int_0^{2\pi} P_v(v) P_\theta(v, \theta) v^2 |\sin \theta| dv d\theta = 1 \quad (3.25a)$$

which is achieved by choosing

$$\pi \int_0^{2\pi} P_\theta(v, \theta) |\sin \theta| d\theta = 1 \quad (3.25b)$$

for all v , and consequently

$$\int_0^{\infty} v^2 P_v(v) dv = 1. \quad (3.25c)$$

The polar angle is chosen to run formally from 0 to 2π since the inversion procedure analyzes individually the “left” and “right” half of the recorded image corresponding to $\theta \in [0, \pi[$ and $\theta \in [\pi, 2\pi]$, respectively.

The one-dimensional “velocity distribution” $P_v(v)$ represents the distribution of speeds for particles moving into a *particular* direction in space. Physically more relevant is the *speed distribution* $P_s(v)$ which includes the volume element proportional to v^2 and is given as

$$P_s(v) = v^2 P_v(v). \quad (3.26)$$

For a particular mass m the speed distribution may be transformed into a *kinetic energy distribution* $P_e(T)$. From particle conservation $P_s(v) dv = P_e(T) dT$ it follows that

$$P_e(T) = \frac{1}{mv} P_s(v) = \frac{v}{m} P_v(v), \quad (3.27)$$

where T and v are related via $T = mv^2/2$.

The two-dimensional function $P_\theta(v, \theta)$ provides information about the angular distribution of products for any given expansion speed v . Using equation (2.36) one can extract $\beta(v)$, *i.e.* the speed dependence of the anisotropy parameter β . This is achieved conveniently by computing a linear regression for each individual expansion speed v since

$$P_\theta(v, \theta) = \frac{1}{4\pi} + \beta(v) \cdot \frac{1}{8\pi} (3 \cos^2 \theta - 1) \quad (3.28)$$

for all angles θ .

Correcting for homogeneous image background

Experimentally acquired velocity map images may be affected by detector noise or by contributions to the ion or electron signals from minority processes. If these background signals are distributed homogeneously across the image they can conveniently be corrected for *after* carrying out the Abel inversion of the image. This can be seen considering the resulting speed distribution $P_s(v)$ as calculated by the Abel inversion software. Due to the additive property²⁰⁹ of the Abel transform this normalized speed distribution can be written as

$$P_s(v) = P_s^S(v) + P_s^B(v), \quad (3.29)$$

where the contributions of the principal signal and the homogeneous background to the total speed distribution $P_s(v)$ are denoted $P_s^S(v)$ and $P_s^B(v)$, respectively. Based on the equivalent one-dimensional Abel transform pair²⁰⁹ the latter contribution can be shown to take on the form

$$P_s^B(v) = B \cdot \frac{v^2}{\sqrt{v_0^2 - v^2}}, \quad (3.30)$$

where B is a constant that is linearly related to the background level in the image. The parameter v_0 denotes the upper limit for the speeds v considered in the 3D representation of the velocity distribution in spherical coordinates. This parameter can be chosen freely in our Abel inversion software. Note that in order for the description (3.30) to be valid, v_0 has to be set such that *all* speeds $0 \leq v \leq v_0$ are fully represented in the velocity map image the Abel inversion is performed on.

From the functional form of $P_s^B(v)$ it becomes clear that a homogeneous background signal in the ion or electron image affects the calculated speed distribution in particular for large speeds close to v_0 . The constant B therefore is generally found easily by fitting the high-speed part of the calculated speed distribution $P_s(v)$ by equation (3.30). Subsequently the desired speed distribution $P_s^S(v)$ is obtained by subtracting the distribution $P_s^B(v)$ from $P_s(v)$ according to equation (3.29).

If the background contribution $P_s^B(v)$ to the total speed distribution is known, the calculated anisotropy parameters may be corrected in a similar way. Consider the full 3D velocity distribution given by the product $P_v(v) P_\theta(v, \theta)$. Its decomposition into the contributions from the primary signal (superscript “S”) and the background (superscript “B”) yields

$$P_v(v) P_\theta(v, \theta) = P_v^S(v) P_\theta^S(v, \theta) + P_v^B(v) P_\theta^B(v, \theta) . \quad (3.31)$$

Multiplying this expression by v^2 and using equations (3.26), (3.28) and (3.29) one finds

$$P_s(v) \beta(v) = P_s^S(v) \beta^S(v) + P_s^B(v) \beta^B(v) , \quad (3.32)$$

where $\beta(v)$ denotes the anisotropy parameters as obtained from the Abel inversion. Since a homogeneous background signal requires $\beta^B(v) = 0$, one can use equation (3.29) to write

$$\beta^S(v) = \beta(v) \cdot \frac{P_s(v)}{P_s(v) - P_s^B(v)} , \quad (3.33)$$

which leads to corrected anisotropy parameters $\beta^S(v)$ with systematically larger absolute values.

3.5.8 Calibration

In order to calibrate the imaging setup, we rewrite equation (3.24) in the form

$$T = \mathcal{C} \cdot qV_R R^2 , \quad (3.34)$$

where \mathcal{C} is the factor to be determined. Experimentally, two alternative calibration methods, termed “external” and “internal”, can be used. In an external calibration \mathcal{C} is obtained from the image radius corresponding to a product whose kinetic energy is known. An internal calibration relies on a photochemical process with multiple product channels. While it is vital to know the energy *spacing* between the channels, it is not required to know the absolute kinetic energy of the various products. Plotting the square of the measured radii versus the difference in kinetic energy allows one to determine \mathcal{C} simply from the slope of a linear fit to the data.

In order to find the optimal voltage settings and to subsequently calibrate the imaging setup, well-collimated molecular beams were produced by coexpanding a suitable species together with

a carrier gas. The same 5 μm orifice that normally is operated at cryogenic temperatures to produce the droplet beam was used for these room-temperature expansions. Beam skimming and collimation were accomplished by the usual set of skimmers of 0.3 mm and 1.0 mm diameter. A convenient method to find the optimal focusing voltages is to monitor an ion signal without kinetic energy release. In our laboratory such a signal is obtained by REMPI-ionizing the species in the molecular beam using dye lasers or by non-resonant ionization²¹⁰ using 800 nm ultrashort laser pulses. The narrow speed distribution perpendicular to its axis gives the molecular beam a one-dimensional shape in velocity space which greatly facilitates the optimization of the electrode voltages since under- or overfocusing are readily recognized. However, all product images recorded with our detection geometry suffer from a resolution loss due to the velocity spread in the molecular beam. An otherwise straightforward calibration based on the speeds of atomic fragments from the photodissociation of a diatomic molecule thus becomes inaccurate since the ratio between fragment speed and the uncertainty in parent speed is typically of the order of ten. For calibration purposes we therefore image *photoelectrons* that can readily be created with speeds exceeding 10^5 m/s and hence are much faster than any spread in parent speed.

The calibration of our imaging setup was carried out in two steps. In a first step we only used the repeller and the extractor electrodes, while all other electrodes of the setup were kept at ground. This configuration corresponds to the original velocity map imaging setup as introduced by Eppink and Parker.²⁰³ The results of this calibration step then served as a basis for the calibration of the setup with einzel lens. In this second step of the calibration process we applied various voltages V_{lens} to the middle electrode of the einzel lens, while keeping a fixed voltage V_{R} at the repeller plate. The magnification effect of the einzel lens then was quantified by comparing the image radii obtained with the einzel lens to those measured with all einzel lens electrodes at ground.

It is important to note that the calibration as well as the voltage settings are only valid for a particular position of the ionization volume with respect to the ion optics. Therefore, great care was taken to align the laser beams such that the center of this source volume is located exactly half way between the repeller and extractor electrodes and on the symmetry axis of the instrument.

Calibration of the setup without einzel lens

The geometry dependent ratio $V_{\text{E}}/V_{\text{R}}$ between the extractor and repeller voltage was determined by imaging jet-cooled CH_3I molecules using non-resonant ionization by 800 nm femtosecond light pulses. The molecular beam was produced by expanding a room-temperature CH_3I -helium mixture through the 5 μm orifice at a stagnation pressure of approximately 3 bar. The femtosecond laser beam was focused with an $f = 400$ mm lens and carefully aligned. Each pulse of the femtosecond laser had an energy of 1 mJ and a width of about 150 fs at the point of interaction with the molecular beam.

Figure 3.28 illustrates the result of the voltage optimization process. For a given repeller voltage V_{R} the extractor voltage V_{E} was varied until sharp ion images with a FWHM of less than 1 pixel were obtained, which corresponds to a distance of less than 80 μm on the detector. This way the extractor voltage V_{E} could be determined accurately with uncertainties below

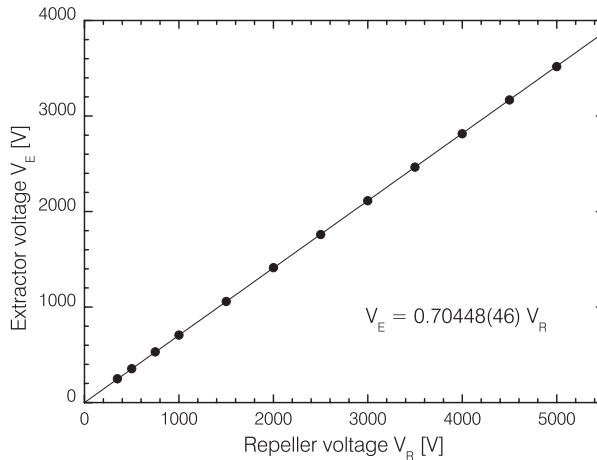


FIGURE 3.28: Experimentally found optimal extractor voltages V_E for various repeller voltages V_R . The error bars on the extractor voltages are smaller than the solid dots.

0.3 %. The linear fit of the data yields the relation

$$V_E = 0.70448(46) \cdot V_R \quad (3.35)$$

between the voltages. For all imaging experiments without einzel lens we will therefore generally note only the repeller voltage V_R . It is understood that the extractor voltage V_E is set to the value given by equation (3.35).

Subsequently an internal calibration of the setup was carried out by imaging the photoelectrons from a two color $[1 + 1']$ REMPI process in jet-cooled aniline. We expanded an aniline–helium mixture at room temperature using a stagnation pressure of 5 bar. The mixture was prepared by passing the carrier gas through liquid aniline contained in a stainless steel bubbler. We used the frequency-doubled output of two dye lasers pumped by separate, synchronized pulsed Nd:YAG lasers. The laser beams were collimated to a diameter of 1 mm and carefully aligned through the detection region of the imaging setup. The time delay between the two unfocussed and counterpropagating laser beams at the point of interaction with the molecular beam was set to zero. In order to avoid one-color ionization, the pulse energy of the excitation laser was reduced to below 100 μJ . The photoelectrons were imaged using negative voltages on the repeller and extractor electrodes. The quality of the images obtained turned out to improve considerably upon insertion of the magnetic shield inside the flight tube.

The calibration is based on zero kinetic energy (ZEKE) photoelectron spectra recorded and assigned by Takahashi *et al.*²¹¹ and Song *et al.*²¹² One dye laser was tuned to a frequency of 34029 cm^{-1} to resonantly excite the intermediate S_1 state via the $S_1 \leftarrow S_0 0_0^0$ transition. The frequency of the ionization dye laser was set to about 29770 cm^{-1} which provides an energy of 1528 cm^{-1} in excess of the ionization potential ($62271 \pm 2 \text{ cm}^{-1}$, reference [212]). However, the frequency of the ionization laser does not need to be known exactly. Instead, the internal calibration relies on the difference in kinetic energy between photoelectrons created via numerous vibronic transitions from the intermediate S_1 state to the respective cationic states.

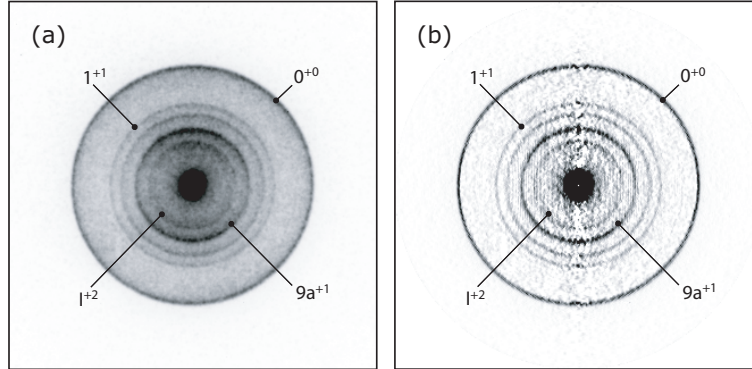


FIGURE 3.29: Raw image (a) of aniline photoelectrons created by $[1 + 1']$ REMPI for a repeller voltage $V_R = -1000$ V, and cut through the 3D velocity distribution (b) obtained by Abel inversion of the raw image. The raw image was obtained by averaging over 18000 laser shots. The laser polarization vectors are parallel to the vertical image axis. The boundary boxes corresponds to an image size of 325×325 pixels. Intensities are shown in a linear gray scale.

Figure 3.29 shows a raw and an Abel inverted image of photoelectrons ejected from aniline via the discussed $[1 + 1']$ REMPI transition. The depicted image was recorded for a repeller voltage $V_R = -1000$ V and clearly reveals a series of sharp ring structures which can be attributed to vibrational excitations in the aniline cation. The assignment of the vibrational levels in the cation follows reference [212]. The unassigned third ring structure is likely to correspond to two unresolved vibronic transitions of similar intensity and is therefore not considered in our analysis. A list of vibrational energy levels used for the calibration is displayed in Table 3.5. The energies presented therein were obtained by averaging the slightly different literature values.^{211,212}

Images similar to the one depicted in Figure 3.29 were recorded for different repeller voltages V_R in the range from 125 V to 5000 V. For lower repeller voltages the images grow in size as the electron cloud is given a longer time to expand. The velocity distributions obtained from the Abel inversions of the images were transformed into energy distributions (see equation (3.27)) for comparison with the ZEKE spectra. The positions R of the four assigned peaks measured in units of pixels is related by equation (3.34) to the kinetic energy T of the photoelectrons given in Table 3.5. For each repeller voltage V_R a calibration constant \mathcal{C} can thus be found by linear regression in a plot of $qV_R R^2$ versus T . The result of this analysis is shown in Figure 3.30. The

Assignment	Energy [cm^{-1}]
0^{+0}	0
1^{+1}	815.5
$9a^{+1}$	1190.5
I^{+2}	1328

TABLE 3.5: Vibrational energy levels in the aniline cation used for the internal calibration of the velocity map imaging setup without einzel lens.^{211,212}

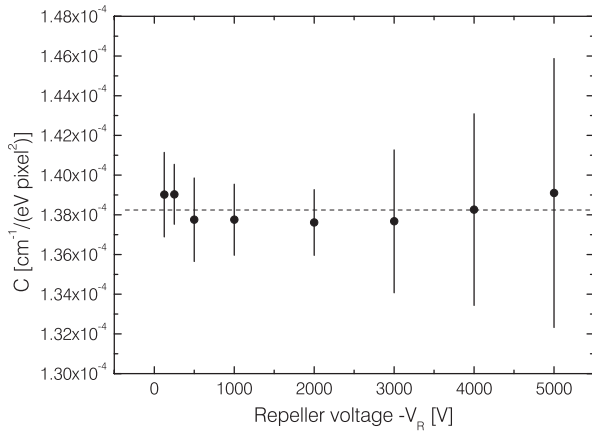


FIGURE 3.30: Internal calibration of the imaging setup without einzel lens. The factor \mathcal{C} is measured for various repeller voltages V_R . The dashed line shows the weighted mean.

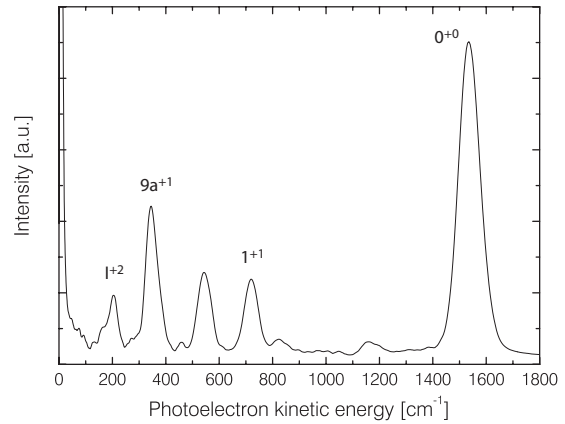


FIGURE 3.31: Kinetic energy distribution of photoelectrons created via $[1 + 1]'$ REMPI in jet-cooled aniline.

weighted mean of the independently obtained factors can be given as

$$\mathcal{C} = 1.3824(77) \cdot 10^{-4} \text{ cm}^{-1}/(\text{eV pixel}^2) \quad (3.36)$$

and is shown in Figure 3.30 as a dashed horizontal line. With this calibration constant at hand any measured image radius R can be converted to a kinetic energy T , irrespective of the mass of the imaged particle. As an example we present in Figure 3.31 the photoelectron kinetic energy distribution corresponding to the image shown in Figure 3.29.

Calibration of the setup with einzel lens

If the velocity map imaging setup is operated with einzel lens, one has to find new focusing voltage ratios for each einzel lens voltage V_{lens} . Like in the case without einzel lens the optimal voltages are determined by velocity mapping a well collimated molecular beam onto the detector. In order to be able to calibrate large magnification factors we produced a *slow* molecular beam by coexpansion aniline with argon instead of helium. Ions with no kinetic energy release were created in $[1 + 1]$ REMPI processes using the $S_1 \leftarrow S_0 0_0^0$ transition.²¹² In this one-color experiment the molecular beam was irradiated by 293.87 nm light pulses of 5 mJ energy. The laser beam was well aligned through the center of the detection region and focussed with a $f = 500$ mm lens. With the repeller voltage fixed at $V_R = 4000$ V the voltage V_{lens} on the einzel lens was varied systematically from 5400 V to 6800 V in steps of 100 V. For each voltage setting the optimal extractor voltage V_E was determined experimentally. Figure 3.32 illustrates the result. Again, the method allowed us to find the optimal extractor voltages with a relatively high accuracy of better than 0.3 %. For the optimal voltage settings the measured FWHM of the velocity map image perpendicular to the direction of the molecular beam was in all cases smaller than 3 pixels on the CCD chip.

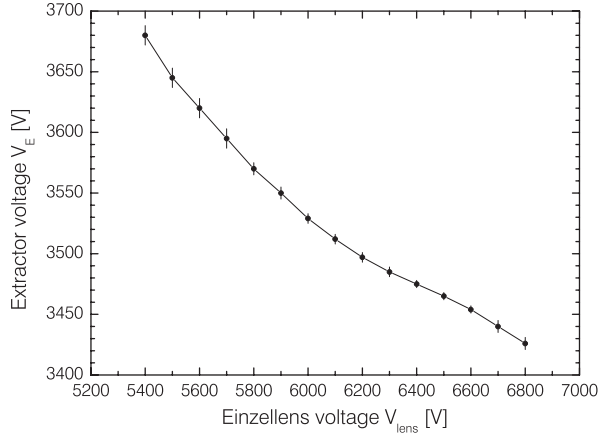


FIGURE 3.32: Experimentally determined optimal extractor voltages V_E for various einzel lens voltages V_{lens} and a fixed repeller voltage of $V_R = 4000$ V.

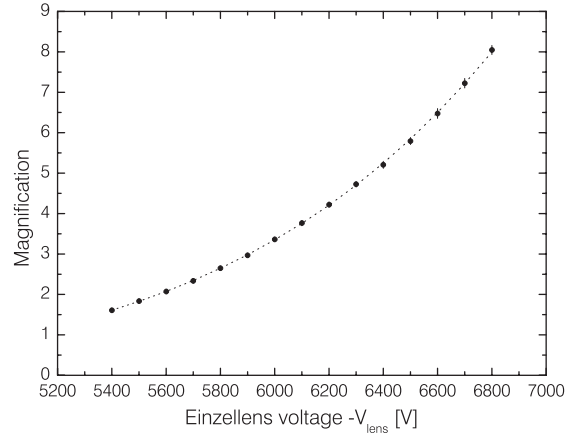


FIGURE 3.33: Magnification of the einzel lens at a repeller voltage of $V_R = -4000$ V and various einzel lens voltages V_{lens} . The magnification is given with respect to a velocity map image recorded with the same repeller voltage and $V_{\text{lens}} = 0$ V. The dotted curve represents a fit by a power law (see text).

The calibration of the the setup with einzel lens is again based on the previously described [1 + 1] two-color REMPI process in jet-cooled aniline. The molecular beam was produced by expanding an argon–aniline mixture at a stagnation pressure of 5 bar. The lasers were set up in the same way as in the experimental calibration of the imaging setup without einzel lens. The magnifying effect of the einzel lens was measured by comparing the radii associated with the strong 0^{+0} transition from the intermediate S_1 to the cationic state. The radii were taken from the maxima in the one-dimensional distribution $P_v(v)$ obtained by Abel inversion of the recorded images. In Figure 3.33 we report the measured magnification of the einzel lens with respect to an image without einzel lens taken with the same repeller voltage $V_R = -4000$ V.

For the studied einzel lens voltages $|V_{\text{lens}}|$ in the range from 5400 V to 6800 V the measured magnification \mathcal{M} could be fitted with a power law

$$\mathcal{M}(V_{\text{lens}}) = 1.816(16) \cdot 10^{-26} \cdot (|V_{\text{lens}}|/\text{V})^{6.9521} . \quad (3.37)$$

The uncertainty reported here is determined by the residuals of this fit which are smaller than 0.9 % for all einzel lens voltages.

Based on equation (3.34) the radii observed with the einzel lens may be written as

$$R = \mathcal{M}(V_{\text{lens}}) \cdot \left(\frac{1}{C} \frac{T}{qV_R} \right)^{\frac{1}{2}} , \quad (3.38)$$

where the repeller voltage is fixed to $V_R = \pm 4000$ V depending on whether positively or negatively charged particles are monitored. With $T = mv^2/2$ one finds the useful relation

$$v = \frac{\sqrt{2CqV_R}}{\mathcal{M}(V_{\text{lens}})} \cdot \frac{R}{\sqrt{m}} \quad (3.39)$$

$ V_R $ [V]	T_{\max} [cm^{-1}]
4000	144960
2000	72480
1000	36240
500	18120
250	9060
125	4530

TABLE 3.6: Maximum laboratory frame kinetic energies observable with the velocity map imaging setup *without* einzel lens. The energies are given for singly charged particles.

$ V_{\text{lens}} $ [V]	T_{\max} [cm^{-1}]
6700	2780
6600	3430
6500	4240
6400	5260
6300	6550
6200	8180

TABLE 3.7: Maximum laboratory frame kinetic energies observable with the velocity map imaging setup *with* einzel lens ($|V_R| = 4000$ V). The energies are given for singly charged particles.

for the speed of the imaged particles. A partial evaluation for singly charged particles yields

$$v = 6.334(59) \cdot 10^{27} \cdot (|V_{\text{lens}}|/\text{V})^{-6.9521} \cdot \frac{R/\text{pixel}}{\sqrt{m/\text{amu}}} \frac{\text{m}}{\text{s}}, \quad (3.40)$$

where the given uncertainty was found by Gaussian error propagation.

3.5.9 Observable kinetic energies

When carrying out imaging or ion time-of-flight measurements it is important to be aware of what kinetic energies are actually mapped onto the charge-sensitive detector. Upper limits to the detected laboratory frame kinetic energies are given in Tables 3.6 and 3.7 for selected voltages on the ion optics. In case of product channels with a particularly distinct kinetic energy release this knowledge can be used to obtain both energy and mass selectivity in the detection. This can be achieved by setting the voltages on the ion optics such that a product with high kinetic energy release is largely imaged to points outside the detector surface. However, ions born with velocity vectors parallel or close to parallel to the axis of the imaging setup will nevertheless reach the detector which in practice limits the attainable energy selectivity.

3.6 Lasers

For the experiments presented in this work two Nd:YAG-pumped dye lasers and a Ti:Sa femtosecond laser system were at our disposal. The output of the two identical dye lasers (*TDL 50*, *Quantel*) can be characterized by a linewidth smaller than 0.1 cm^{-1} . Both the output power and the pulse duration of these lasers are largely determined by the characteristics of the pump lasers. The two Nd:YAG lasers are different models (*YG681C-20*, *Quantel* and *Powerlite 7020*, *Continuum*) which both have a repetition rate of 20 Hz and a pulsewidth of 5–6 ns at 532 nm. Typical pulse energies at 532 nm are 300 mJ for the *Powerlite 7020* and 450 mJ for the *YG681C-20* laser.

The femtosecond laser system consists of a mode-locked oscillator (*NJA-5*, *Clark-MXR*) and a chirped pulse amplifier (*CPA-1000*, *Clark-MXR*). The self-locking oscillator is pumped by a

continuous argon ion laser (*Innova 300, Coherent*) and delivers a train of 60 fs pulses with a time-averaged power of 0.5 W at 800 nm. These pulses subsequently seed the chirped pulse amplifier which includes a pulse stretcher, a regenerative amplifier and a compressor. The regenerative amplifier is pumped by the frequency-doubled output of a Q -switched Nd:YAG laser (*ORC-1000, Clark-MXR*) and can be operated up to a repetition rate of 1000 Hz. After recompression typical pulses have a width (FWHM) of 150–200 fs and an energy of 1.0–1.5 mJ.

3.6.1 Photolysis

All dissociation experiments presented here are carried out at a photolysis wavelength of 266 nm and at a repetition rate of 20 Hz. The 266 nm radiation can conveniently be obtained from the fourth harmonic of a Nd:YAG laser. In our experiments the 532 nm output of one of the lasers is externally frequency-doubled in a KPD crystal and focused with a $f = 500$ mm lens onto the beam of doped droplets. The energy of a single 266 nm photolysis pulse is usually 5 mJ.

3.6.2 Ionization

The fragments CH_3 and iodine can be detected by well-known $[2 + 1]$ REMPI schemes. Using the $3p_z \ ^2A_2''$ Rydberg state as an intermediate, CH_3 radicals in the vibrational ground state may be ionized via the 0_0^0 band around 333.5 nm, while an excitation of the umbrella mode ν_2 can be probed via the 2_1^1 band around 329.4 nm.^{213,214} In both cases we tune the REMPI laser to the unresolved Q branches which are thought to be least sensitive to alignment effects.^{160,215} Iodine in both spin-orbit states $^2P_{3/2}$ and $^2P_{1/2}$ can be state-selectively ionized via $[2 + 1]$ REMPI transitions around 305 nm.^{160,216}

For the REMPI detection of fragments we pump one of the dye lasers by the output of the second Nd:YAG laser. Operating on a mixture of *LDS 698* and *DCM* dyes for the resonant ionization of CH_3 , and *Rhodamin 610* for state-selective iodine detection, the dye laser generates light in the red region of the visible spectrum which subsequently is frequency-doubled in an external KDP crystal. The resulting UV laser light typically has a pulse energy of 3–8 mJ and is focused with a $f = 400$ mm lens onto the droplet beam.

Unfortunately, to the best of our knowledge, no assigned REMPI schemes are available for the trifluoromethyl radical (for unassigned $[3 + 1]$ REMPI spectra in the region from 415–490 nm see reference [217]). In order to image CF_3 fragments from the photolysis of CF_3I as well as other reaction products we alternatively induce ionization by intense 800 nm laser pulses from the Ti:Sa femtosecond laser system. With peak intensities around 10^{14} – 10^{15} W cm^{-2} these ultrashort laser pulses can ionize atomic and molecular species in a non-resonant process²¹⁰ which is thought to result in comparatively little fragmentation.²¹⁸ It is important to note that any direct ionization of helium atoms or pure droplets by these intense IR pulses was not observed in our experiments. This can be attributed to the high helium ionization threshold of 24.56 eV which corresponds to the simultaneous absorption of more than 15 IR photons and effectively impedes non-resonant multi-photon ionization for the laser pulse intensities used here.²¹⁹

Experimentally, we synchronize the photolysis and femtosecond detection lasers by running the regenerative amplifier at the reduced frequency of 20 Hz. The compressor of the chirped

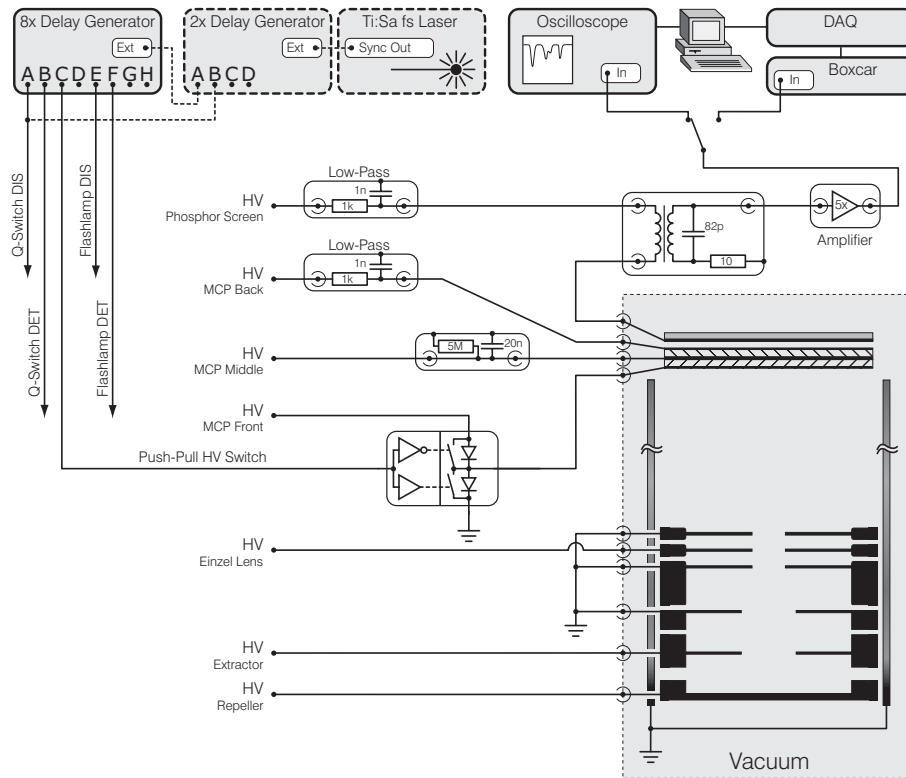


FIGURE 3.34: Electronic schematics for the ion and electron imaging experiments. The components with a solid boundary indicate the configuration used for dissociation (DIS) and detection (DET) by nanosecond laser pulses. Imaging experiments based on fragment ionization by 800 nm femtosecond laser pulses are carried out using a slightly different electronic configuration including the components with a dashed boundary (see text).

amplifier is adjusted such that the dispersion occurring at the optics transmitting the pulses from the laser system to the vacuum chamber is precompensated for. The 800 nm femtosecond pulses are focused with a $f = 400$ mm lens onto a spot of about $10 \mu\text{m}$ diameter in the detection region of the ion imaging setup. At this point the IR pulses have an energy of about 1 mJ and a typical width (FWHM) of 150–200 fs.

3.7 Electronics

3.7.1 Imaging experiments

The electronic schematics for the imaging experiments are shown in Figure 3.34. The central element of the experiments is the velocity map imaging setup which includes the electrodes of the ion optics as well as the MCP and phosphor screen assembly. These components are located in vacuum and all electrical connections thus have to be established via high voltage vacuum feedthroughs. Three out of six electrodes composing the ion optics are permanently grounded. These include the top and bottom electrode of the einzel lens, and the ground

Component	Model	Manufacturer	Max. Voltage [V]	Ripple [mV]
Repeller	<i>PS350</i>	<i>Stanford Research Systems</i>	± 5000	100^\dagger
Extractor	<i>PS350</i>	<i>Stanford Research Systems</i>	± 5000	100^\dagger
Einzel Lens	<i>205B-10R</i>	<i>Bertan</i>	± 10000	100^\dagger
MCP Front	<i>PM28RA</i>	<i>Thorn EMI</i>	± 2800	2^\ddagger
MCP Middle	<i>PS350</i>	<i>Stanford Research Systems</i>	± 5000	100^\dagger
MCP Back	<i>PS350</i>	<i>Stanford Research Systems</i>	± 5000	100^\dagger
Phosphor Screen	<i>PS350</i>	<i>Stanford Research Systems</i>	± 5000	100^\dagger

TABLE 3.8: List of HV power supplies used in the imaging experiments. The output ripple is given either as root mean squared (\dagger) or as peak-to-peak value (\ddagger).

electrode of the velocity map imaging ion optics. Each of the three remaining electrodes, the repeller, the extractor, and the center electrode of the einzel lens, are individually connected to commercial high voltage power supplies as listed in Table 3.8. The findings of the calibration process indicate that the electrode voltages should be stabilized to better than about 0.1 % in order for the calibration to hold and to avoid a loss of image resolution. As shown by the low output ripple in Table 3.8, the commercial high voltage power supplies used in the experiment easily meet this accuracy requirement.

We use another four HV supplies to apply the desired voltages to the MCP and phosphor screen assembly. Typical values for the detector voltages are given in Table 3.9. A fast push-pull solid-state high voltage switch (*HTS 31-GSM, Behlke*) with a nominal minimum pulse width of 80 ns is used to gate the gain of the front MCP in order to obtain mass-selective images. This is achieved by switching the voltage on the front surface of the MCP from ground to a negative voltage preset on the HV power supply during the arrival time of the desired ions. We use the center tab of the assembly to individually control the voltage across each MCP. A 5 M Ω bridge to ground permits stabilizing the voltage on the center tab at 200 V. With the voltages on the front and back surfaces of the assembly typically set to 0 V and 900 V, the voltage on the center tab would otherwise adjust to 450 V since each MCP has an equal electrical resistance of approximately 20M Ω . The electrical connections to the phosphor screen and to the back surface of the chevron assembly are equipped with low-pass filters that strongly

Contact	Voltage [V]
MCP Front	-500/0
MCP Middle	200
MCP Back	900
Phosphor Screen	3200

TABLE 3.9: Typical voltages applied to the MCP and phosphor screen assembly for imaging experiments. Ion mass selection is achieved by applying a negative voltage pulse to the MCP front surface during the arrival of the desired species at the detector.

damp short electrical signals traveling along the cables. This way we minimize reflections that potentially can deteriorate the electrical signal on the detector. The fast electrical pulses on the phosphor screen are separated from the high voltage DC background by means of inductive coupling. The resulting signals are amplified in a preamplifier (*SR445, Stanford Research Systems*) with 300 MHz bandwidth and can subsequently be monitored on an fast (2GSa/s) oscilloscope (*54540C, Hewlett-Packard*). For data acquisition purposes the oscilloscope can be programmed and read by a personal computer (PC). Additionally, the signals can be integrated in a boxcar integrator (*SR250, Stanford Research Systems*) and be read by the PC using a data acquisition card (*6025E, National Instruments*).

The timing of the experiment is controlled in two different ways depending on whether fragments are state-selectively ionized with a dye laser or whether non-resonant ionization by femtosecond pulses is used. The two electronic schemes are illustrated in Figure 3.34. In the former case (components with solid boundary only) the experiment is controlled by the 8-channel delay generator (*Model 551, BNC*) shown in the upper left corner of Figure 3.34. The delay generator is internally triggered at a frequency of 20 Hz and controls the flash lamps and the Q-switches of the Nd:YAG lasers as well as the the high voltage switch connected to the front surface of the MCP detector. In this case the jitter between the pulses emitted by the two Nd:YAG lasers is less than 1 ns.

If femtosecond laser pulses are used to ionize the reaction products, a slightly different electronic scheme, including the components with dashed boundary in Figure 3.34, is used. In this case the femtosecond laser controls the experiment. We use an output from the regenerative amplifier to trigger an additional, more precise delay generator (*DG535, Stanford Research Systems*). One of its outputs then serves as an input for the 8-channel delay generator, while the other output is used to directly trigger the Q-switch of the dissociation laser. This way the jitter between the nano- and femtosecond laser pulses could be reduced to less than 500 ps.

3.7.2 Time-of-flight measurements

If the electrical pulses from the detector are coupled out inductively, the resolution of the time-of-flight mass spectra is limited to about 100 ns. Transients with higher time resolution can however be obtained if the phosphor screen is coupled galvanically to the oscilloscope or, alternatively, a multi-channel scaler. In this case no voltage is applied to the phosphor screen, whereas the front MCP is operated at a negative voltage. For an optimal pulse shape and pulse height distribution we typically use voltages of -1700 V, -950 V, and -200 V on front, center tab, and back of the MCP assembly, respectively. This way pulse widths (FWHM) of about 40 ns are achieved. This mode of operation is however not suitable for imaging experiments, since the end of the flight tube is no longer field free and substantial distortions to the ion or electron images occur.

Low-background time-of-flight mass spectra can conveniently be recorded by galvanically coupling the phosphor screen to a photon counter (*SR400, Stanford Research Systems*). Using the discriminator output of the photon counter as an input to a multi-channel scaler (*T914, EG&G Ortec*) the electrical signals can be counted in bins of widths as small as 5 ns. Since the time-of-flight spread of the ions usually is smaller than or comparable to the electrical pulse width, only one ion can reliably be counted per laser shot and species. Time-of-flight spectra

recorded with the multi-channel scaler therefore only reveal true ion intensities if the count rate is kept sufficiently low. This can be achieved by reducing the laser power, the doping pressure or the detection sensitivity. In order to maintain a favorable pulse height distribution the detection sensitivity is usually decreased by reducing the repeller voltage (compare Figure 3.26), whereas the detector voltages are kept constant.

In case of moderately high count rates the real ion intensities may be estimated from the recorded number of counts using Poisson statistics. If *exactly* one event is counted upon arrival of one or more ions of the same species in a particular laser shot, the correction can be written as

$$c' = -p \cdot \ln \left(1 - \frac{c}{p} \right), \quad (3.41)$$

which can be shown straightforwardly. Here p stands for the number of laser shots, while c and c' are the recorded and corrected number of counts, respectively. For the purpose of quantitative analysis the time-of-flight spectra recorded with the counting method were corrected accordingly.

Chapter 4

Photodissociation in ^4He droplets

4.1 Introduction

In this chapter we will present and discuss results of experiments where CH_3I and CF_3I molecules in ^4He droplets were photolyzed with linearly polarized 266 nm light. Before showing our experimental data, however, it is useful to cast more light on the initial conditions as well as the anticipated outcomes of these photodissociation experiments. One of the central aspects associated with the former issue is the localization of the CH_3I and CF_3I dopant species. Like most closed shell systems these parent molecules are believed to reside *inside* the droplets. The question of whether a particular impurity solvates or binds to the surface of a liquid cluster has been addressed by Ancilotto *et al.*²²⁰ Qualitatively, a single impurity is predicted to localize inside a droplet if the energy cost of creating a cavity accommodating the impurity is smaller than the energy gain due to the attractive interaction with the neighboring helium atoms in the solvated state. This argument led to the development of a dimensionless parameter which can be calculated on the basis of the pair potential between an helium atom and the impurity of interest. If this parameter significantly exceeds a critical value, the impurity is predicted to localize in the droplet interior. Consistent with experiments^{221–223} this approach predicts alkali atoms to reside on the surface of helium droplets. This is essentially a consequence of the only weakly attractive alkali–helium interaction characterized by a much shallower potential well²²⁴ than the helium–helium potential with a well depth of about 7.6 cm^{-1} .²²⁵ Alkali–helium potentials furthermore show a comparatively extended repulsive core which is related to Pauli repulsion. Accordingly, alkali atoms push away the helium atoms to high internuclear distances and thus would require the creation of a relatively large and energetically costly cavity in a solvated state.¹⁴⁷ Closed shell molecules as well as many atoms, however, are characterized by a much stronger binding to helium and have been shown theoretically to attract helium atoms into high density solvation shells around the impurity.^{28, 30, 32, 33, 78, 147, 226–230} This accumulation of helium density at radial distances close to the minimum of the pair potential ensures a large energy gain in solution and at the same time requires a comparatively little cavity to accommodate the impurity. Virtually all molecular species except alkali and alkaline earth clusters therefore are thought to localize inside the helium droplets.

Note that helium solvation shells are expected not only in the intimate vicinity of the parent

molecules but may also form around photolytically created radicals in the droplet interior. Such a shell structure should have consequences for the translational dynamics of photofragments traveling through the helium environment. In particular, this effect ought to modify both the effective mass and the collision cross section of the photofragments and can be expected to appreciably affect the helium flow around the translationally excited radicals. We will come back to this point when discussing our results later on in this chapter.

Having established that our parent molecules CF_3I and CH_3I localize in the droplet interior, we proceed to discuss possible outcomes of an individual photodissociation reaction in a helium droplet. Firstly, we will consider fragment *escape* processes. Obviously, a particular photofragment may travel through the finite-size liquid simply by pushing away helium atoms, reach the droplet surface and escape into the gas phase. Since the speeds of the nascent photofragments studied here largely exceed the Landau critical velocity of ≈ 58 m/s in He II, an escaping particle should definitely experience friction and therefore lose kinetic energy to the environment before departing from the helium cluster it was born into. We will henceforth use the term “*direct*” to designate such an escape process. Based on a rather large droplet radius of 6 nm (compare Figure 2.10) and a rather low fragment speed of 60 m/s, a reasonably safe upper limit for the time scale of a “direct” escape process in our experiments may be specified as ≈ 100 ps. Given that the mean initial speeds of the photofragments studied in this work are at least one order of magnitude higher, *typical* “direct” escape times should be of the order of 10 ps. Recent calculations by Takayanagi *et al.*¹⁰² on the photodissociation of Cl_2 in much smaller $^4\text{He}_{200}$ clusters yielded typical escape times of ≈ 1 ps and therefore are in line with our estimate. These simulations indicate furthermore that “direct” escape accounts in virtually all cases for the fate of the chlorine photofragments. In larger clusters, however, other possibilities must open up. In such systems an individual photofragment may transfer all excess kinetic energy to the cluster and thermalize with the environment. At this point the ultimate fate of such a fragment presumably is still uncertain, since the helium cluster will respond by evaporative cooling to the heat input generated by the fragment pair (see Section 2.2). Neglecting any internal cooling of the fragments, this heat release is limited by the total kinetic energy release of the photolysis reaction which, in our case, is on average of the order of 10000 cm^{-1} (compare Tables 2.6 and 2.7). A rapid energy input of this magnitude is expected to heat typical helium droplets studied in this work to temperatures of roughly 10^0 – 10^1 K (see Section 2.2). With a typical time scale of 10^{-9} – 10^{-7} s evaporation from the droplet surface should be slow compared to “direct” escape processes. A fragment thermalized in a thermally excited helium cluster may therefore still escape into the gas phase, either by departing from the droplet surface in the course of the evaporative cooling, or as a consequence of a complete evaporation of the droplet. In addition to “direct” escape, a fragment thus may enter the gas phase due to *thermal* processes which, as pointed out above, should be characterized by a comparatively long escape time scale.

Another possible outcome of a photodissociation event inside a helium cluster is *recombination*. In principle, recombination may immediately follow the photolysis reaction if one or both of the fragments do not break through the solvent cage intimately surrounding the parent molecule. In view of the relatively heavy fragments studied in this work and given the results of the simulations by Takayanagi *et al.*,¹⁰² such a recombination mechanism is highly unlikely to

be of relevance here. In other cases, where fragments lighter than ${}^4\text{He}$, e.g. hydrogen atoms, are involved, this recombination mechanism may, however, play an important role. An alternative and, as far as this work is concerned, more probable mechanism that may ultimately result in recombination requires *both* fragments to thermalize inside the droplet. Subsequently, the fragments are expected to mutually approach due to attractive dispersion forces, similar to the coagulation of impurities as a consequence of multiple pick-up processes (see Section 2.4). As pointed out above, this approach process presumably takes place in competition with evaporative cooling, the latter of which may still cause the thermal escape of one or both fragments. If recombination eventually occurs nonetheless, the internal cooling of the recombined molecule is expected to cause an additional heat release into the remainder of the droplet. In certain cases this extra heat input may completely evaporate the surrounding helium atoms and produce unsolvated parent molecules. Evidence for such processes will be provided in Section 4.5.

We will analyze the dissociation experiments based on the assumption that the angular and kinetic energy distributions of the nascent fragments in helium droplets is similar to the gas phase distributions discussed in Section 2.5. This frequently made approach^{107,231,232} is, in case of helium droplets, substantiated by the observed infrared spectra of embedded species. Compared to the gas phase values, the vibrational frequencies generally exhibit only small shifts²⁰ of the order of a few cm^{-1} . With the exception of large internuclear distances, the neighboring helium atoms therefore are expected to have little effect on the shape of the intramolecular electronic potential energy surfaces of a solvated impurity. As a consequence, the largest part of the photodissociation dynamics of an embedded parent molecule should occur on potential energy surfaces very similar to those of a free species. With respect to the alkyl iodide molecules studied here it is particularly relevant to note that the crossing of the 1Q_1 and 3Q_0 electronic surfaces (compare Figure 2.19), which plays an essential role in determining the final I^*/I branching ratio, occurs at relatively small C–I bond lengths and therefore should not be affected by the solvent cage.

It is important to bear in mind that the wide *distribution* of initial conditions is expected to substantially broaden any observable of our dissociation experiments. These initial conditions include the droplet size as well as the position and orientation of the dissociating parent molecule inside the droplet. The distribution of droplet sizes has been discussed in Section 2.3. The uncertainty in the position of the parent molecule has been addressed theoretically by Lehmann.⁸² In his model the motion of a neutral dopant molecule inside a helium droplet is confined by a potential which arises from the dispersion interaction of the impurity with the surrounding helium. To a first approximation this interaction is described by the potential of a three-dimensional harmonic oscillator. This leads to numerous low-energy states which may be labeled by a radial and an angular quantum number.²³³ Based on a thermal population of these states at the well-known ${}^4\text{He}$ droplet temperature of 0.38 K, the root mean squared (RMS) radial displacement $\sqrt{\langle a^2 \rangle}$ of an impurity from the droplet center can be computed and has been shown to amount to about 1 nm in the case of SF_6 in a droplet with a radius of 3 nm.⁸² At a particular moment the shortest and longest distance from the parent molecule to the droplet surface may therefore well differ by a factor of two. The orientation of the parent molecules in the droplets is assumed to follow an isotropic distribution. A recent study by



FIGURE 4.1: (Color) Color scale used to display two-dimensional intensity distributions. The color varies in a black-blue-cyan-green-yellow-red-white sequence from low to high intensities.

Pörtner *et al.*²³⁴ on tetracene in ^4He droplets suggests, however, that impurities may exhibit some alignment with respect to the droplet angular momentum acquired in the pick-up process. Since a quantitative description of the coupling mechanism is presently not available, we will neglect this possible effect in the interpretation of our data. The presence of droplet angular momenta has, however, another consequence, since droplet and laboratory frames rotate in this case with respect to one another. A fast rotation of the droplet frame could in particular cause a smearing in the angular product distributions observed with the stationary ion imaging setup. In the course of this chapter we will therefore make some effort to largely rule out this effect for “directly” escaping products.

Experimentally, all results presented in this chapter were obtained under reproducible conditions. We expanded high-purity helium (99.9999 %, *Carbagas*) at cryogenic temperatures through a particular orifice with a nominal diameter of $5\ \mu\text{m}$ which remained in place for the entire experimental period. At all times the helium stagnation pressure was set to $p_o = 30\ \text{bar}$. For a specific data set we will therefore generally only indicate the stagnation temperature T_o for which the estimated mean droplet size \bar{N} produced in the expansion can be inferred from Figure 2.8 or, equivalently, Table 2.2. We generally used the cross beam to introduce impurities into the droplets. If not indicated otherwise the backing pressures given in Table 3.4 apply.

In general, the polarization axes of all lasers were set parallel to the propagation direction of the droplet beam and therefore parallel to the detector surface. This way, the original three-dimensional velocity distribution could be reconstructed using the Abel inversion algorithms described in Section 3.5.7. The only image transformation carried out prior to the numerical Abel inversions was the removal of cosmic ray signatures in the ion images. In particular, no smoothing was applied.

The two-dimensional intensity distributions of the ion images are displayed using the color scale illustrated in Figure 4.1. The images are printed such that the vertical page axis corresponds to the polarization axis of the photolysis laser as well as the propagation direction of the droplet beam. If not indicated otherwise the orientation of the images is such that the velocity vector of the droplet beam points to the page top.

Structure of this chapter

The material in this chapter is ordered according to the various *products* formed by dissociating the two molecules CF_3I and CH_3I in the interior of ^4He droplets. Firstly, results related to the iodine fragments of both parent molecules are presented and discussed. By means of this fragment, many important aspects of our experimental approach can conveniently be illustrated at the start. As it will turn out, the variety of products associated with the iodine radical furthermore allows us to already shape a microscopic picture of the translational motion of neutral photofragments inside the quantum liquid. These concepts then facilitate the discussion

of results obtained for other reaction products which are presented afterwards.

4.2 Iodine fragments

4.2.1 Time-of-flight mass spectra

We begin the presentation of results by showing the time-of-flight mass spectra displayed in Figures 4.2 and 4.3. The transients were obtained by exposing CF_3I - and CH_3I -doped helium droplets to various sequences of laser pulses which involved 266 nm ns pulses from the Nd:YAG laser and ultrashort 800 nm pulses from the femtosecond laser system. The spectra cover the mass region from 120 to 205 and from 245 to 260 amu and illustrate in particular the creation of iodine fragments via different photochemical processes. Each spectrum shows raw data as recorded with the multi-channel scaler and represents a sum over 15000 laser shots. The stagnation temperature was fixed at $T_o = 15$ K which corresponds to an estimated mean droplet size of 6080 atoms in the supersonic expansion (see Table 2.2). We used a relatively small repeller voltage $V_R = 500$ V and no einzel lens. As shown in Table 3.6, this voltage setting maps all ions with laboratory frame kinetic energies below about 18000 cm^{-1} onto the detector. Since the mean kinetic energy release associated with the 266 nm A band dissociation of any parent molecule is smaller than this value (compare Tables 2.6 and 2.7), virtually all fragment ions from this process could be detected. In particular, dissociation products from unsolvated parent molecules present in the gas phase were also monitored.

As can easily be seen, Figures 4.2 and 4.3 share many common features. Most notably, an intense progression of fragment peaks emerges on the heavy-mass side of the iodine peak if the ns UV pulse is *followed* some 120 ns later by the femtosecond IR pulse (traces (d)). This progression, which can be identified as IHe_n with $n = 0, 1, 2, \dots$, is significantly more intense than in all other recorded traces (a)–(c). In order to clarify the processes involved we proceed to discuss the other traces in alphabetical order before coming back to the most relevant traces (d).

The traces (a) in both figures were recorded by irradiating the detection volume of the ion imaging setup solely with 266 nm pulses. The only discernible ion signals in the displayed mass range are I^+ and $(\text{IHe})^+$. These signals are thought to arise as consequence of A band dissociation followed by 266 nm non-resonant multi-photon ionization (MPI) of the neutral I fragments within the same laser pulse which is a well-known process in the gas-phase.²³⁵ In case of a dissociation event inside a helium droplet the unknown time delay between dissociation and ionization, which is only limited by the length of the UV pulse, makes it impossible to determine whether the ensuing I fragment is ionized in- or outside the helium environment. Any cation inside the helium environment is however expected to attract helium atoms forming a so-called “snowball”^{12,236} which could give rise to the observed IHe^+ signal. Alternatively, the fragment may leave the helium environment by virtue of the kinetic energy release of the dissociation reaction before ionization occurs. In this case ionization will result in a pure I^+ signal, unless the escaping neutral fragment forms a van der Waals complex with one or more helium atoms. Below we will more firmly establish that the latter process does indeed occur. It is important to note that the traces (a) do not show any signal at the I_2^+ ion mass. Although the exact

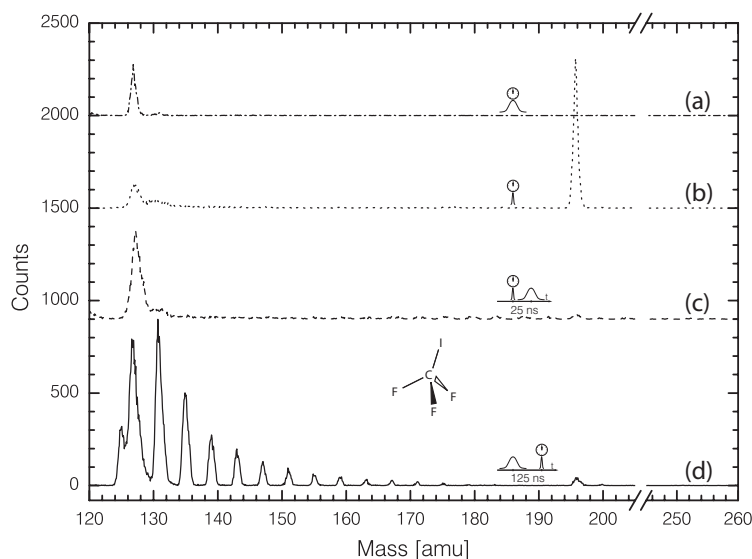


FIGURE 4.2: Time-of-flight mass spectra of ions produced by irradiating CF_3I -doped helium droplets with various laser pulse sequences. The transients were recorded for (a) a single 266 nm ns pulse, (b) a single 800 nm fs pulse, (c) a fs pulse followed by a 266 nm pulse 25 ns later, and (d) a 266 nm pulse followed 125 ns later by a 800 nm fs pulse. The mass scale refers to the time-of-flight measured with respect to the center of a particular pulse which is indicated by the clock symbol in the graph. The helium stagnation temperature T_o was 15 K.

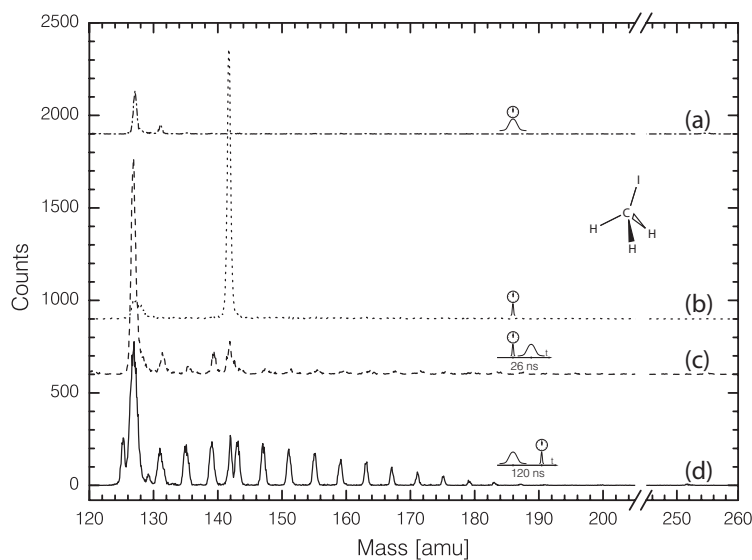


FIGURE 4.3: Time-of-flight mass spectra of ions produced by irradiating CH_3I -doped helium droplets with various laser pulse sequences. The transients were recorded for (a) a single 266 nm ns pulse, (b) a single 800 nm fs pulse, (c) a fs pulse followed by a 266 nm pulse 26 ns later, and (d) a 266 nm pulse followed 120 ns later by a 800 nm fs pulse. The mass scale refers to the time-of-flight measured with respect to the center of a particular pulse which is indicated by the clock symbol in the graph. The helium stagnation temperature T_o was 15 K.

mechanism is not yet fully understood, it is well known that I_2^+ is a prominent product of a UV-induced photochemical reaction in methyl iodide clusters $(CH_3I)_n$.^{237,238} Experiments with considerably higher doping pressures do indeed reveal a substantial I_2^+ signal. We therefore take the absence of this signal as further evidence that undesirable doubly doped clusters are indeed rare under our experimental conditions.

Irradiating the detection volume with single 800 nm fs pulses results in the traces (b). The most prominent signals in the mass spectra clearly are the parent ions $(CF_3I)^+$ and $(CH_3I)^+$ at masses of 196 and 142 amu, respectively. A comparison to mass spectra recorded with a deliberately misaligned droplet beam reveals that these ion signals are almost exclusively due to non-resonant ionization of *unsolvated* parent molecules in the gas phase. The ionization process causes some fragmentation that leads to the relatively weak I^+ ion signals observed for both parent molecules. Note that these findings do not rule out the possibility of ionizing parent molecules located inside the helium droplets by intense 800 nm pulses. However, due to the wide distribution of droplet sizes, such a process is likely to cause ion signals spread out over an enormous mass range. The ion signal on any particular $(CF_3IHe_n)^+$ or $(CH_3IHe_n)^+$ ion mass therefore is expected to be very weak.

The traces (c) show the result of an “inverted” pulse sequence. The detection region of the ion imaging setup is first irradiated with a fs pulse which is followed by a 266 nm UV pulse some 20 ns later. For both systems this leads to a strong depletion of the parent ion signals in favor of I^+ as well as some $(IHe_n)^+$ cations, the latter of which are more prominent in case of CH_3I -doped droplets. We attribute the I^+ signal largely to the 266 nm dissociation of unsolvated parent *ions* in the gas phase. In the interior of helium droplets the same process could lead to the dissociation of “snowball” structures. Alternatively, quenched ionization by the femtosecond laser pulse may prepare the solvated parent molecules in an electronically excited state from which the molecule subsequently is excited to a dissociative ionic state by the UV laser pulse. Both these processes could explain the creation of $(IHe_n)^+$ cations by attachment of helium atoms to the *ionic* I^+ fragments moving through the helium environment.

The traces (d) finally correspond to the typical conditions chosen for many of the experiments presented in this chapter, including the velocity map imaging studies. Here, the femtosecond laser arrives *after* the 266 nm photolysis pulse at the position of the droplet beam. For the traces shown in Figures 4.2 and 4.3 the time delay between the laser pulses was set to about 120 ns. It is readily recognized that the parent ion signal observed in traces (b) is strongly depleted by the preceding 266 nm UV pulse, ensuring that the femtosecond IR pulse interacts mostly with *products* of the A band dissociation. While the depletion is virtually complete for CF_3I , some parent signal still is present in case of CH_3I . We will demonstrate in Section 4.5 that this signal is partially due to recombination processes following the A band dissociation of CH_3I in helium droplets.

Setting the time delay Δt between the UV and the IR pulse to some tens of nanoseconds has two important consequences concerning the IHe_n -progression under study. Firstly, the arrival of ions created by multi-photon processes during the preceding UV laser pulse can be separated in time with respect to ions of the same species produced by the femtosecond laser.

By appropriately gating the gain of the front MCP it thus becomes possible to record images of reaction products ionized exclusively by the femtosecond IR pulses. Secondly, such a time delay is much larger than the typical time scale of “direct” escape from the helium droplets which has been estimated to be of the order of 10 ps. It is also larger than or comparable to the presumable escape times of thermally escaping fragments. For this reason the ionization of all departing products occurs most certainly *outside* the helium droplets. Together these two consequences of the time delay make sure that we probe in virtually all cases the *entire* translational dynamics of *neutral* fragments in helium droplets. The helium atoms of the IHe_n -progression observed here therefore are believed to attach to the *neutral* iodine fragments *before* leaving the droplet environment. Further evidence for this picture will arise from the imaging experiments discussed later in this chapter.

The effect of the delay Δt between ns and fs laser pulse on the time-of-flight mass spectra is illustrated in Figure 4.4 for CH_3I in helium droplets. For delays of 120 ns or longer^a the I^+ and $(\text{IHe})^+$ ion signals arising from the preceding UV pulse clearly separate in time from the corresponding signals arising from non-resonant ionization by the fs pulse. Outside the region of temporal overlap between the two laser pulses the mass spectrum shows little change and thus allows one to freely choose a delay Δt of up to roughly 250 ns without any signal loss. At very long delays the laboratory frame speeds of the atoms and molecules in the dissociation volume become significant. While undissociated and unsolvated molecules from the gas phase move into the detection region and appear mainly on the parent mass, the products of dissociation events inside the droplets leave gradually the detection volume. The fact that at the longest delay $\Delta t = 1500$ ns preferentially IHe_n products with $n = 1, 2, 3$ are detected suggests that the speed of these particular products can approximately compensate the droplet beam speed v_D of roughly 350 m/s (compare Figure 2.2). This is the first evidence that some of the neutral IHe_n fragments leave the droplets with a considerable amount of kinetic energy. The imaging experiments presented below will confirm this finding.

Product intensities

By integrating the counts associated with each peak in the IHe_n progression of the mass spectra accurate relative intensities of the various photolysis products can be derived. In particular, it becomes possible to study the change of the intensity pattern in the IHe_n progression as a function of the mean droplet size \bar{N} , the principal experimental parameter. In order to associate the intensities of neutral products and ions one must however make the assumption that the efficiency of the non-resonant ionization of the IHe_n complexes does not vary substantially with the number n of helium atoms attached. Secondly, it is assumed that the ionization process does not significantly fragment the IHe_n products. This is supported by the very different *shape* of the IHe_n progression for CF_3I and CH_3I parents shown in the traces (d) of Figures 4.2 and 4.3. If the IHe_n product complexes were in both cases formed mainly by fragmentation of a much larger iodine–helium structure, the resulting product pattern should not exhibit such striking dissimilarities. Further evidence for this picture will come from the ion images discussed below.

^aThis value applies of course only to the particular repeller voltage $V_R = 500$ V chosen here. Higher repeller voltages result in smaller flight times and shorter delays therefore are sufficient to completely separate the signals of the two lasers in time.

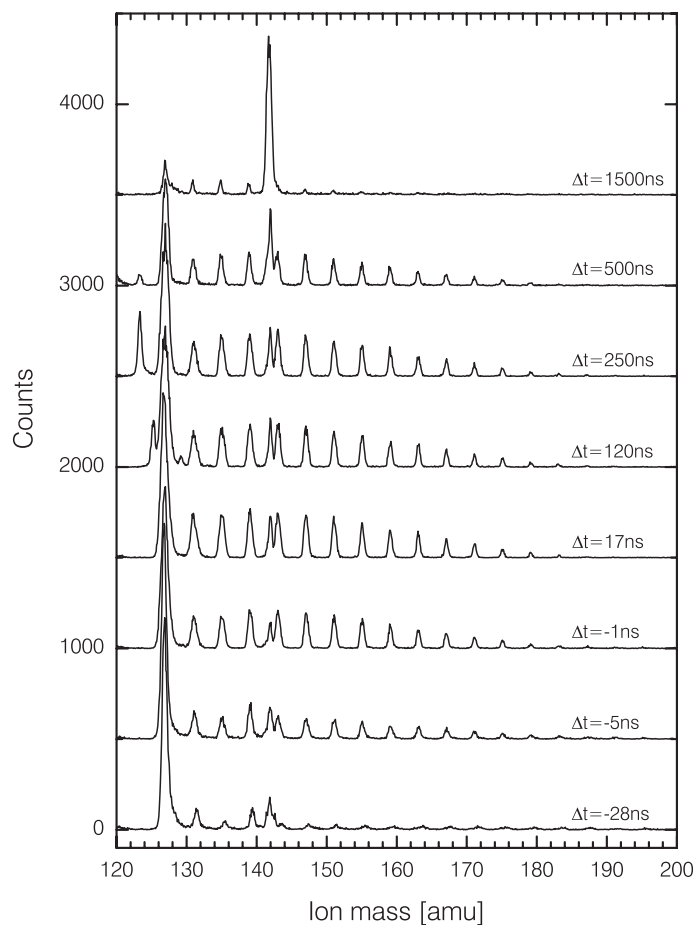


FIGURE 4.4: Effect of the time delay Δt between ns and fs laser pulses on the time-of-flight mass spectrum of products created by the A band photolysis of CH_3I in the interior of ^4He droplets. Each mass spectrum was obtained by accumulating the counts of 15000 laser shots. The helium stagnation temperature T_o was 15 K. The given delays refer to the center of the two pulses with negative delays indicating a preceding femtosecond pulse. Masses are calculated from the time-of-flight with respect to the femtosecond pulses.

The result of this analysis for various helium stagnation temperatures T_o is illustrated in Figure 4.5 for CF_3I and in Figure 4.6 for CH_3I in helium droplets. The data was measured by averaging over at least 15000 laser shots. For CH_3I we report the relative signals for IHe_1 , IHe_2 , \dots , IHe_{16} which could be derived directly from the time-of-flight mass spectra recorded with the multi-channel scaler. In the case of CF_3I the products I , IHe_1 and IHe_2 exhibit particularly high signal levels which could be acquired more accurately using the oscilloscope. The shown signals therefore constitute a carefully matched composition of integrated time-of-flight signals from both the oscilloscope and the multi-channel scaler. The signal of bare iodine atoms escaping from doped droplets is derived by thoroughly comparing signals with and without the droplet beam present. For CF_3I -doped droplets therefore a comprehensive intensity series covering the product range from I to IHe_{14} is available for the selected stagnation temperatures $T_o = 12$,

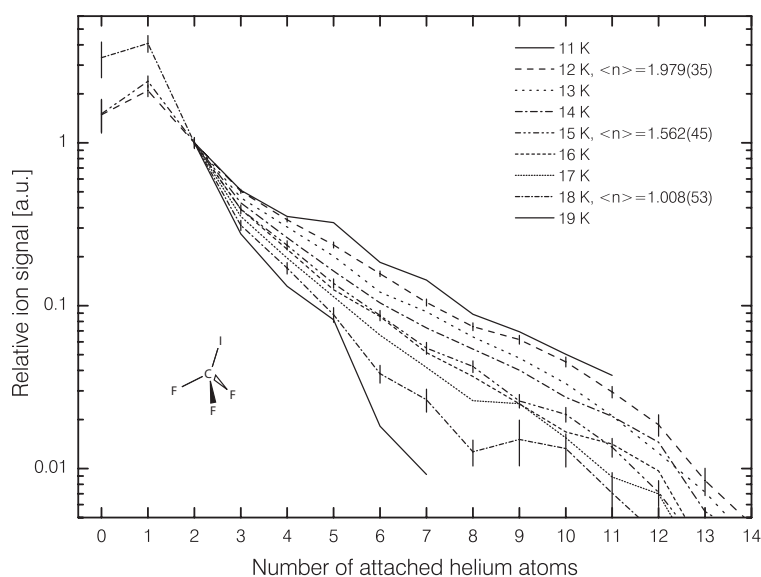


FIGURE 4.5: Droplet size effect on the relative signals of the IHe_n products created by the 266 nm photodissociation of CF_3I in helium droplets. The relative signals for different mean droplet sizes are made comparable by arbitrarily setting the integrated $(\text{IHe}_2)^+$ ion signal to unity. Error bars are given for $T_o = 12, 15,$ and 18 K. The indicated temperatures denote the helium stagnation temperature T_o , and $\langle n \rangle$ is the mean size of the detected complexes.

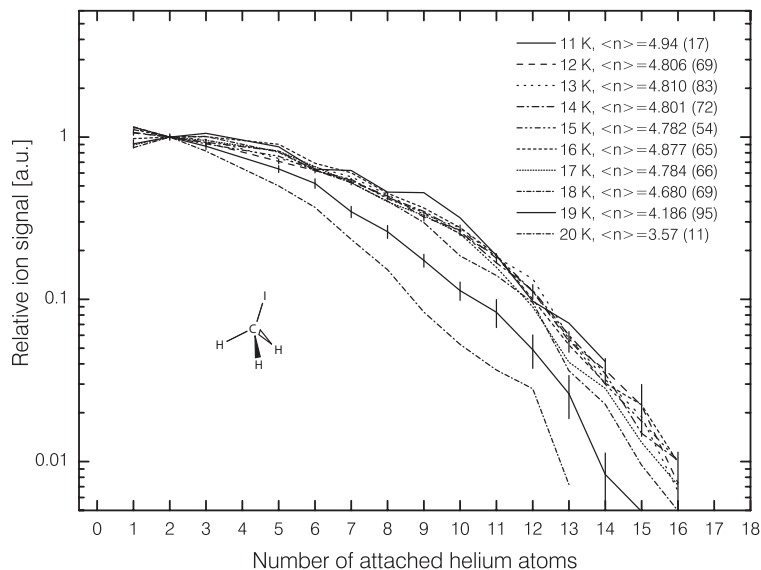


FIGURE 4.6: Droplet size effect on the relative signals of the IHe_n products created by the 266 nm photodissociation of CH_3I in helium droplets. The relative signals for different mean droplet sizes are made comparable by arbitrarily setting the integrated $(\text{IHe}_2)^+$ ion signal to unity. Error bars are given for $T_o = 15$ and 19 K. The indicated temperatures denote the helium stagnation temperature T_o , and $\langle n \rangle$ is the mean size of the detected complexes. Note that $\langle n \rangle$ is calculated assuming that bare iodine atoms are not created by the photodissociation process (compare text on page 109).

15, and 18 K.

As can be seen from the figures, the intensity distribution among the IHe_n products reveals substantial differences between the two model systems CF_3I and CH_3I . For CF_3I -doped ^4He droplets the IHe_n progression peaks at IHe_1 and drops off approximately exponentially with increasing size n of the heterogeneous product complexes. Varying the helium stagnation temperature T_o , *i.e.* the mean droplet size, results in a systematic change of the intensity pattern for *all* droplet sizes \bar{N} under study. For smaller mean droplet sizes \bar{N} relatively fewer large product complexes are produced which leads to a steady shrinking of the average product size $\langle n \rangle$ with decreasing \bar{N} (see the annotations in Figures 4.5 and 4.6 for actual values of $\langle n \rangle$). Note that the effect is consistently observed over an intensity range covering about two orders of magnitude.

For the IHe_n products from CH_3I in helium droplets a different picture emerges. Compared to the photolysis of CF_3I , the larger product complexes $\text{IHe}_3, \text{IHe}_4, \dots, \text{IHe}_{16}$ carry relatively much more intensity which results in a substantially larger average product size $\langle n \rangle$ for all mean droplet sizes \bar{N} investigated. In stark contrast to CF_3I , no significant droplet size effect on the intensity pattern is observable unless the helium stagnation temperature is raised above $T_o \approx 18$ K. Only for the elevated stagnation temperatures $T_o = 19$ and 20 K, *i.e.* for relatively small mean droplet sizes \bar{N} , the average size $\langle n \rangle$ of the product clusters is found to shrink systematically with decreasing mean droplet size, similar to the CF_3I system. We will discuss possible reasons for the different behaviour of the two systems in Section 4.5 on the grounds of more data.

4.2.2 Imaging the IHe_n product complexes

A wealth of information complementing the time-of-flight data can be obtained by velocity map imaging the products of the photolysis reaction in the interior of helium droplets. In particular, one can recover the three-dimensional angular and speed distribution of the escaping products. As discussed before, setting the delay Δt between UV photolysis and femtosecond ionization pulse to some tens of nanoseconds ensures that the products most certainly are detected after leaving the helium droplets. In the experiments presented here Δt was typically set to 50 ns. Mass selectivity is achieved by gating the gain of the front MCP of the detector assembly. At a repeller voltage of $V_R = 4000$ V the difference in time-of-flight between the neighboring products in the IHe_n progression is roughly 90 ns, a time span sufficiently long to permit an easy product selection using our HV switch.

We introduce the velocity map images by presenting in Figure 4.7 results for bare iodine fragments from the 266 nm photolysis of both CF_3I and CH_3I . In spite of the efforts made to reduce the partial pressure of unsolvated parent molecules in the detection region of the imaging setup, the prominent signal due to the dissociation of thermalized gas phase molecules is easily recognized. In order to illustrate its shape we have highlighted the lower half of the background signal by the dashed curves. As a consequence of the dissimilar partitioning of the total kinetic energy in the photodissociation of the two parent molecules (see Tables 2.6 and 2.7), iodine fragments from the 266 nm photolysis of CF_3I are faster and therefore lead to a structure with a larger radius in the velocity map image. In both cases the background signal is centered about the origin of the imaging setup since the randomly propagating molecules of the residual gas have on average no net velocity in the laboratory frame. Due to the droplet beam speed, any

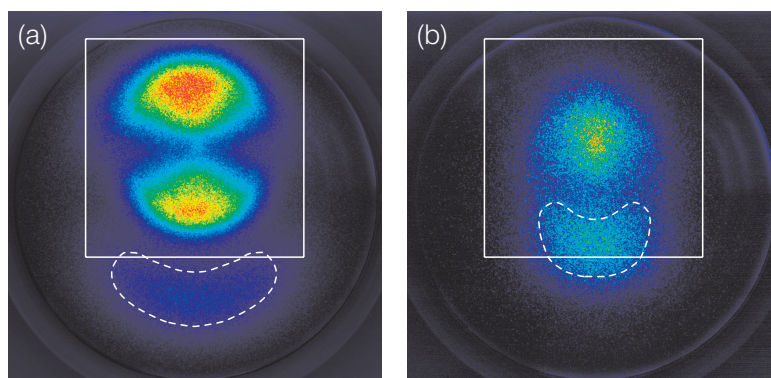


FIGURE 4.7: (Color) Velocity map images of escaping bare iodine fragments from the 266 nm photolysis of CF_3I (a) and CH_3I (b) in the interior of helium droplets. The images were recorded for an einzel lens voltage of $V_{\text{lens}} = 6200$ V and using integration times of 3 hours (a) and 1 hour (b). The helium stagnation temperature T_o was 15 K. Note the substantial gas phase background in both images indicated by the dashed curves. The illustrations show the full 1024×1024 pixel images as acquired by the camera. The squares designate a representative 600×600 pixel sector containing the ion signal from doped droplets. The contours of the circular detector become visible due to stray light from the detector edges.

ion image of products from dissociation events in the helium droplets will however exhibit a finite displacement. This becomes obvious in the case of CF_3I where the iodine emerging from the helium droplets leads to a clear ring structure superimposed on the gas phase background. The radius associated with this ring structure is considerably smaller than the radius of the gas phase background which qualitatively indicates a significantly lower kinetic energy for iodine fragments emerging from the helium environment. In the case of CH_3I hardly any iodine signal from the droplets is discernible. In particular, no ring structure becomes apparent, although a thorough analysis of this particular image is strongly impaired by the substantial gas phase background. Nevertheless we will later on present reasons why bare iodine is not a likely product of the the 266 nm A band dissociation of CH_3I in the medium size helium droplets studied here.

Having shed some light on the general features of the ion images obtained with our setup we proceed to present velocity map images of the other products in the IHe_n progression. Figure 4.8 and Figure 4.9 show ion images of the helium-containing product complexes $\text{IHe}_1, \text{IHe}_2, \dots, \text{IHe}_{12}$ from CF_3I - and CH_3I -doped helium droplets, respectively. All images were recorded using the standard stagnation temperature $T_o = 15$ K and a constant einzel lens voltage V_{lens} of 6200 V, and show the 600×600 pixel sector defined in Figure 4.7. A few general properties of the data become obvious immediately. Firstly, and in contrast to bare iodine, the images of IHe_n with $n = 1, 2, \dots, 12$ are characterized by the absence of gas phase background. Neutral or cationic iodine fragments from the photolysis of unsolvated parent molecules therefore do *not* pick-up further helium atoms for example by collisions with helium droplets, the atomic component of the molecular beam or helium atoms in the background gas. An important consequence of this finding is that the helium atoms incorporated into any particular IHe_n product complex must indeed stem from the *very same helium droplet* the parent molecule was solvated in. Secondly, a qualitative inspection of the radial intensity distribution clearly reveals

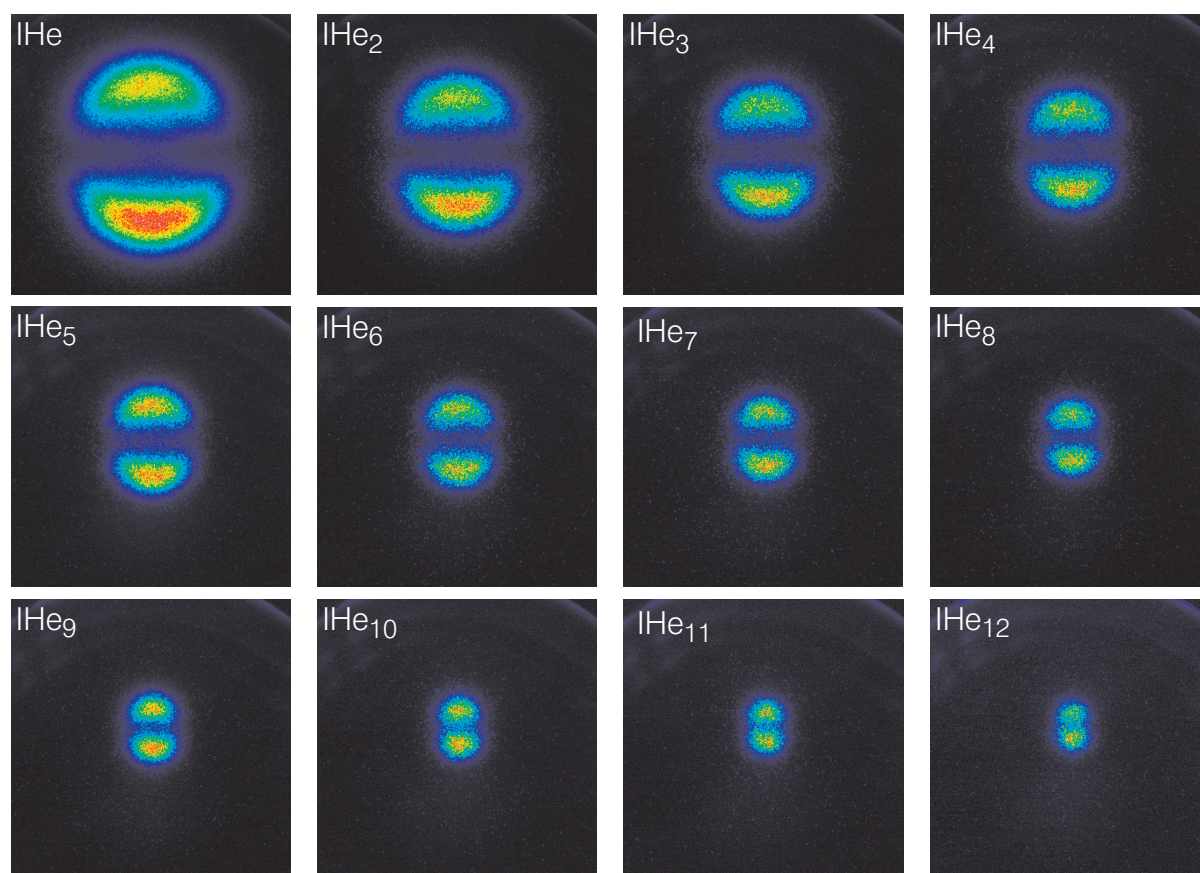


FIGURE 4.8: (Color) Velocity map images of departing IHe_n products ($n = 1, 2, \dots, 12$) from the 266 nm photodissociation of CF_3I in helium droplets. The images show the sector of 600×600 pixels defined in Figure 4.7. We used a helium stagnation temperature T_o of 15 K and an einzel lens voltage V_{lens} of 6200 V. The images typically were obtained using an integration time of 1 hour.

a correlation between the size n and the terminal speed of the product clusters: The larger the IHe_n complex size the smaller the speed the product leaves the helium droplet with. Thirdly, the ion images show a remarkable similarity in the angular distribution across all product cluster sizes studied. This strongly suggests that the formation and escape of *all* IHe_n products is based on the *same* mechanisms, the nature of which will be discussed in more detail below. Prior to this discussion we will however present a more quantitative analysis of the ion images.

Speed distributions

The inverse Abel transform of the velocity map images provides us directly with both the three-dimensional speed and angular distribution of the products (see Section 3.5.7). For both parent molecules the speed distributions of the escaping IHe_n complexes exhibit a single peak structure

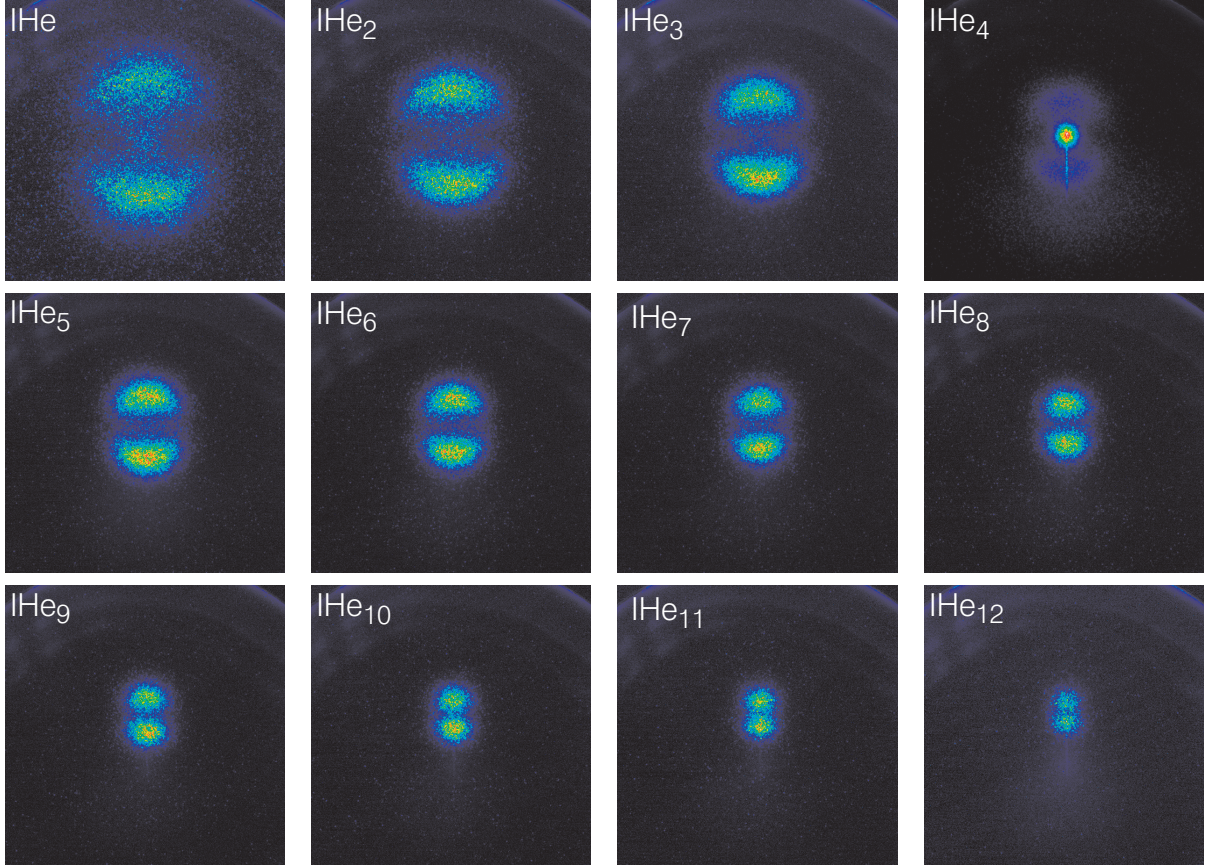


FIGURE 4.9: (Color) Velocity map images of departing IHe_n products ($n = 1, 2, \dots, 12$) from the 266 nm photodissociation of CH_3I in helium droplets. The images show the sector of 600×600 pixels defined in Figure 4.7. We used a helium stagnation temperature T_o of 15 K and an einzel lens voltage V_{lens} of 6200 V. The images typically were obtained using an integration time of 1 hour. Note that the IHe_4 ion image includes signal from $(\text{CH}_3\text{I})^+$ parent ions since the mass difference is only 1 amu.

which in all cases could be fitted to a satisfactory extent with the purely empirical fit function

$$P_s(v) = \frac{A}{\sqrt{2\pi}\sigma} v^2 \exp\left[-\frac{1}{2}\left(\frac{v-v_c}{\sigma}\right)^2\right] / N(v_c, \sigma), \quad (4.1a)$$

using

$$N(v_c, \sigma) = \frac{v_c\sigma}{\sqrt{2\pi}} \exp\left(-\frac{v_c^2}{2\sigma^2}\right) + \frac{1}{2}(v_c^2 + \sigma^2) \left\{1 + \text{erf}\left(\frac{v_c}{\sqrt{2}\sigma}\right)\right\} \quad (4.1b)$$

as a normalization factor. Here A , v_c and σ are parameters to the distribution. As an example we illustrate the best fits to two typical experimental speed distributions in Figures 4.10 and 4.11. The depicted experimental speed distributions were slightly corrected for homogeneous background in the velocity map images using the procedure described in Section 3.5.7. From the figures it becomes clear that the fit function provides an excellent description of the

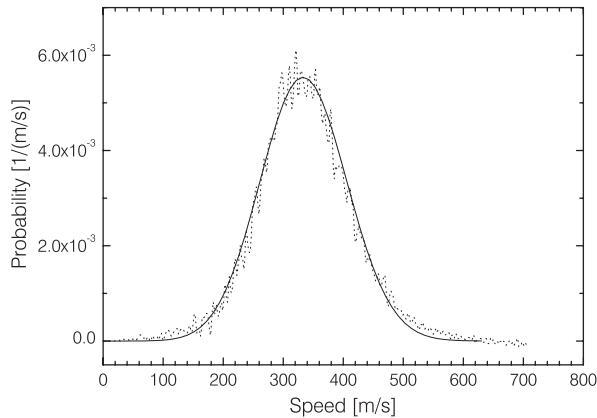


FIGURE 4.10: Measured speed distribution of departing IHe_2 complexes from the photolysis of CF_3I in helium droplets produced under the expansion conditions $p_o = 30$ bar and $T_o = 15$ K (dotted curve). The solid line is a fit to the experimental speed distribution using equations (4.1).

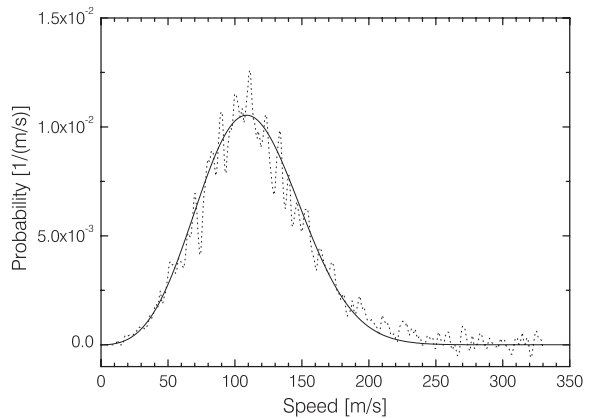


FIGURE 4.11: Measured speed distribution of departing IHe_9 complexes from the photolysis of CH_3I in helium droplets produced under the expansion conditions $p_o = 30$ bar and $T_o = 15$ K (dotted curve). The solid line is a fit to the experimental speed distribution using equations (4.1).

real speed distributions over the full range of speeds, despite some minor uncertainties regarding the *exact* shape of the high speed tail of the distributions. The empirical fit function therefore permits a very accurate and methodical estimation of both the most probable speed

$$\hat{v} = \frac{1}{2} \left(v_c + \sqrt{v_c^2 + 8\sigma^2} \right) \quad (4.2)$$

as well as the FWHM of the speed distributions, the latter of which can readily be computed numerically.

The most probable speeds \hat{v} and the widths (FWHM) of the speed distributions obtained directly from this analysis are shown in Figures 4.12 and 4.13 for a variety of IHe_n products and helium stagnation temperatures, *i.e.* mean droplet sizes. Due to the dominant gas phase background in the I^+ ion image from CH_3I -doped helium droplets (see Figure 4.7), however, no data could be obtained for this particular product (for an estimate of the product intensity see text on page 109).

As can be seen from Figure 4.12, the most probable speeds \hat{v} of the IHe_n products decrease dramatically with increasing size n of the complexes, an effect that already became obvious from the ion images shown in Figures 4.8 and 4.9. With the exception of very small product complexes with $n = 0, 1,$ and 2 , the drop of \hat{v} with growing cluster size n follows to a good degree of approximation an exponential behaviour with very similar decay constants for all parent molecules and all mean helium droplet sizes under study. The most probable speeds observed can be as high as 530 m/s for bare iodine and reach values below 65 m/s for the largest complexes studied. Using the expression

$$\hat{v} = \sqrt{2k_{\text{B}}T/m} \quad (4.3)$$

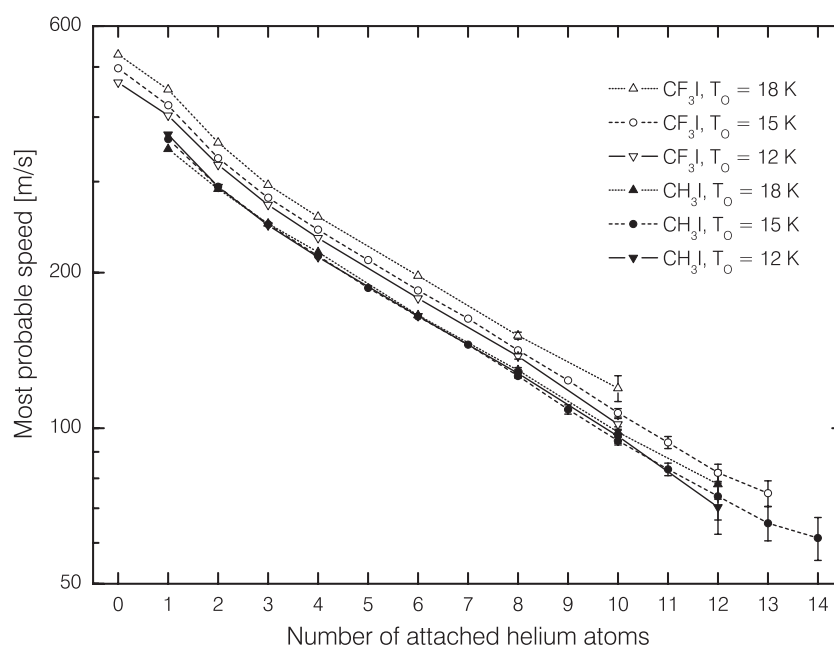


FIGURE 4.12: Most probable speeds of the departing IHe_n products from the 266 nm photolysis of CF_3I and CH_3I in helium droplets produced at the stagnation temperatures $T_0 = 12, 15,$ and 18 K . Error bars are given only if larger than the plot symbols.

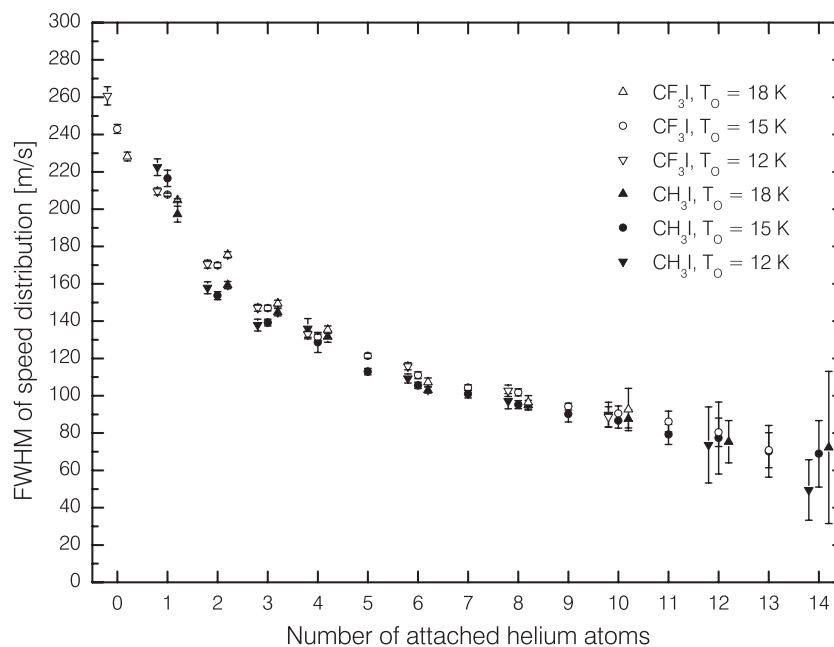


FIGURE 4.13: Widths (FWHM) of the speed distributions of departing IHe_n products from the 266 nm photolysis of CF_3I and CH_3I in helium droplets produced at the stagnation temperatures $T_0 = 12, 15,$ and 18 K . The data points for 12 and 18 K are displaced horizontally by ± 0.2 for the benefit of clarity.

for the most probable speed of a Maxwell-Boltzmann distribution, the experimental results for \hat{v} may tentatively be converted into translational temperatures T . IHe₁ complexes escaping with a most probable speed of 350 m/s, for instance, hence are easily shown to exhibit a translational temperature of ≈ 965 K in this approximation. Even the particularly slow IHe₁₄ complexes with a mass $m = 183$ amu still have translational temperatures well in excess of 30 K. These high temperatures clearly point to a non-thermal escape of the IHe_{*n*} complexes from the droplets which consequently is characterized as “direct”. A more detailed discussion of the escape process will be given at the end of this section.

An important consequence of the sharp drop of most probable speeds with product size concerns the possibility of complex fragmentation during or in the aftermath of the non-resonant ionization by ultrashort infrared pulses. If the various detected IHe_{*n*}⁺ ions were members of a broad fragmentation pattern starting from larger iodine–helium complexes, the speed distribution of all monitored products should be virtually identical. Clearly, the observed speed distributions are not washed out to such an extent. Instead, Figure 4.12 illustrates that the size n of a product can be identified on the basis of the measured most probable speed \hat{v} with an uncertainty of only about ± 1 helium atom. We therefore are convinced that fragmentation due to the ionization process is not a dominant effect. The particular shape of the velocity map image of bare iodine from the dissociation of CF₃I in helium clusters shown in Figure 4.7 suggests however a very *minor* contribution of fragmentation processes to the I⁺ ion signal. In contrast to the ion images of all IHe_{*n*} product complexes from CF₃I with $n \geq 1$, the image of bare iodine fragments exhibits a wedge shaped structure with ion intensity at unusually low speeds. This particular structure may indeed be related to the fragmentation of departed IHe_{*n*} product complexes induced by the ultrashort IR ionization laser pulses. Since larger IHe_{*n*} complexes can generally be characterized by a similar angular distribution but lower speeds in the droplet frame, contributions from those products to the I⁺ ion image may add up to give the observed wedge shape. Moreover, preliminary ion images of escaping spin-orbit excited bare iodine fragments recorded using a REMPI scheme and nanosecond laser pulses^b do not exhibit this particular shape but structures fully analogous to those of the IHe_{*n*} complexes. The non-resonant ionization by 800 nm femtosecond laser pulses therefore is believed to cause some fragmentation of the irradiated IHe_{*n*} complexes with bare iodine as a favored product. Nevertheless, the total contribution of fragmentation processes to the iodine signal is weak since the ion intensities at low speeds have to be weighted by a rather small volume element. In spite of the noticeable contribution of fragmentation processes, the resulting speed distributions of bare iodine therefore are still very well approximated by the fit function given in equation (4.1). As a consequence we will neglect laser-induced complex fragmentation in the further discussion of the results.

^bAlthough a qualitative result of these experiments is used in this line of reasoning, our initial attempts to state-specifically detect escaping bare iodine fragments by REMPI can be characterized as unsuccessful. The failure of these experiments can be attributed to the large background from unsolvated gas phase molecules relative to the small number of iodine atoms that escape from the droplets without any helium atoms attached (see Figure 4.7). In particular, these experiments did not permit the extraction of any quantitative angular or speed distributions from the velocity map images. With an improved experimental setup including an additional vacuum stage (see also Section 5.2), an experimental assessment of the spin-orbit state of the escaping fragments will, however, be possible in the future.

Parent molecule	$\langle\langle T(\text{I}) \rangle\rangle$ [cm $^{-1}$]	$\langle\langle v(\text{I}) \rangle\rangle$ [m/s]
CH $_3$ I	1260	487
CF $_3$ I	3540	817

TABLE 4.1: Spin-orbit state averaged kinetic energies $\langle\langle T(\text{I}) \rangle\rangle$ and estimated mean speeds $\langle\langle v(\text{I}) \rangle\rangle$ of iodine fragments from the 266 nm A band dissociation of free CH $_3$ I and CF $_3$ I molecules in the gas phase. The energies are based on the values given in Tables 2.6 and 2.7. The corresponding speeds are estimated using the simplistic relation $\langle\langle T(\text{I}) \rangle\rangle = m(\text{I}) \langle\langle v(\text{I}) \rangle\rangle^2/2$.

Figure 4.12 furthermore permits one to study the influence of the mean helium droplet size \overline{N} on the most probable speeds \hat{v} of the IHe $_n$ fragments. This droplet size effect is clearly observable for CF $_3$ I where the most probable speed systematically is highest for the smallest mean droplet size investigated. However, within the present experimental accuracy and for helium stagnation temperatures of 12, 15 and 18 K, no such droplet size effect could be established for CH $_3$ I-doped helium droplets. This behaviour is strikingly similar to the droplet size effect on the *intensities* of the IHe $_n$ products presented earlier which for CH $_3$ I only becomes significant for relatively small mean droplet sizes produced at stagnation temperatures above 18 K, while being very prominent for the CF $_3$ I-doped system over the full range of mean droplet sizes investigated. The different response of the two model systems to a change of the mean droplet size \overline{N} will be discussed in Section 4.5.

The widths (FWHM) of the speed distributions estimated from the best fits is shown in Figure 4.13. Compared to the most probable speeds \hat{v} shown in Figure 4.12 the data is considerably noisier and hardly exhibits any systematic differences between the two parent molecules or consistent droplet size effects. The data can however globally be described by a sharp initial drop of the FWHM with product size n , that gradually levels out as the complex size n increases. In spite of the noise on the data points we note that the observed widths generally show little variation, *i.e.* only a few m/s, if the mean droplet size \overline{N} or the parent molecule are changed.

The role of the initial kinetic energy

One of the most striking aspects of these results is the apparent lack of sensitivity of both the most probable speed \hat{v} and the width of each individual IHe $_n$ speed distribution to the dramatic change in initial kinetic energy of the iodine fragments imposed by a substitution of the CH $_3$ I parents by CF $_3$ I. We will therefore proceed to more quantitatively analyze this effect. Since we do not use a state-selective ionization scheme, it is useful to note the initial spin-orbit state averaged mean kinetic energy $\langle\langle T_i(\text{I}) \rangle\rangle$ and mean speed $\langle\langle v_i(\text{I}) \rangle\rangle$ of the iodine fragments. Following our argument in the introduction to this chapter, we estimate these values from the gas phase mean kinetic energy $\langle\langle T(\text{I}) \rangle\rangle$ and speed $\langle\langle v(\text{I}) \rangle\rangle$ which are summarized in Table 4.1 for both parent molecules under study. On average a nascent iodine fragment from the photolysis of CF $_3$ I carries therefore about three times the kinetic energy of iodine from CH $_3$ I, or, in other words, is about 70 % faster.

These values should be contrasted with the changes in speed distribution and kinetic energy

observed for individual IHe_n products upon interchange of the parent molecule in helium droplets of equal mean size \bar{N} . The effect on the speed distributions is illustrated in Figure 4.14 for droplets produced at the standard stagnation temperature $T_o = 15$ K. The graph shows *both* the most probable speeds \hat{v} and the widths (FWHM) of the IHe_n speed distributions. In contrast to Figures 4.12 and Figure 4.13 we use a linear speed scale that permits one to read the plotted data more precisely. The graph highlights again how little the speed distribution width of any particular IHe_n product is affected by the substitution of the parent molecule. The most probable speeds \hat{v} of the IHe_n products from CF_3I are, however, systematically by about 15 % higher than from the CH_3I parent. Nevertheless this difference is in all cases small compared to the width of the speed distribution. For any particular IHe_n product complex the two speed distributions recorded from solvated CF_3I and CH_3I therefore do exhibit a small shift in peak speed but overall are characterized by a large *overlap* in speed space.

The lacking signature of the initial kinetic energy in the speed distributions of the IHe_n products may also be examined in energy space. Based on the assumption that the fit function (4.1) provides a valid description of the real speed distributions and taking into account the masses of the different complexes, we have calculated the corresponding kinetic energy distributions (see equation 3.27). From these distributions the mean kinetic energies of the individual IHe_n products are derived easily. The results of these calculations are plotted in Figure 4.15. As can be seen from the graph, the largest differences between the two parent molecules occur for the smallest mean droplet sizes under study, *i.e.* at a helium stagnation temperature of 18 K. Even at this high stagnation temperature, however, the mean kinetic energies of the various products from CF_3I are in all cases (with the exception of IHe_1) less than 50 % higher than the energies found for the CH_3I parent. Similar to the most probable speeds, the differences in kinetic energy therefore are drastically smaller than in the gas phase.

These results establish a high degree of correlation between size and terminal speed of the IHe_n product complexes which is little affected by an interchange of the parent molecules CF_3I and CH_3I or a varying mean droplet size \bar{N} . This strongly suggests that the terminal speed of any individual IHe_n product ($n = 1, 2, \dots$) escaping from the helium droplet is to a first degree of approximation *not* determined by the initial kinetic energy of the iodine fragment. Instead, the mechanisms governing the motion in and the escape from the helium droplets seem to allow only specific terminal speeds for a given complex size n . Equivalently one may state that for a given terminal speed only certain complex sizes are allowed to form. Processes that could give rise to this selection will be discussed at the end of this section.

Based on this reasoning we can discuss the possibility of creating bare iodine fragments from the 266 nm photodissociation of CH_3I in the interior of the medium size ^4He droplets studied here. As can be seen from an extrapolation of the curves in Figure 4.15 to $n = 0$, bare iodine correlates to mean kinetic energies of the order of 1000 cm^{-1} or higher. A comparison with Table 4.1 reveals that this requires the iodine fragments to leave the cluster with kinetic energies close to the mean gas phase value. Since we expect considerable energy losses to occur, such terminal kinetic energies are highly unlikely. Although we are currently not able to accurately measure the relative intensity of bare iodine fragments from solvated CH_3I due to the high gas phase background (see Figure 4.7) we therefore estimate this intensity to be close to zero.

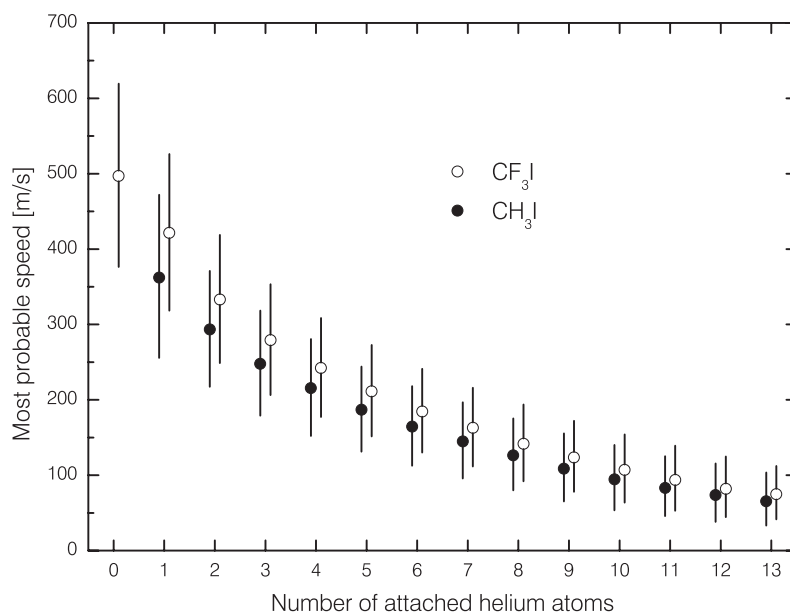


FIGURE 4.14: Comparison of the speed distributions of departing IHe_n products from the 266 nm A band dissociation of CF_3I and CH_3I embedded in helium droplets, measured at a helium stagnation temperature of 15 K. The dots indicate the most probable speed, while the bars illustrate the FWHM of the distributions. For the benefit of clarity the points have been displaced horizontally by ± 0.1 with respect to the correct number of helium atoms attached to the iodine fragment.

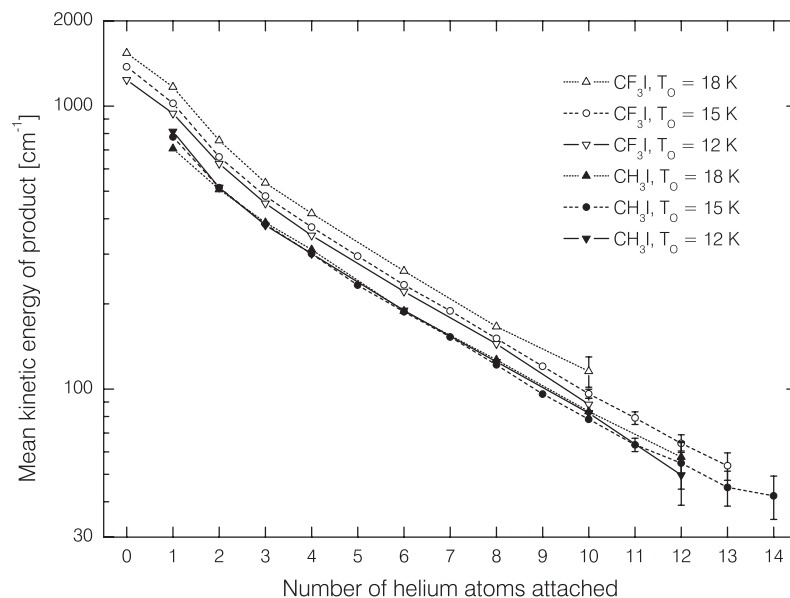


FIGURE 4.15: Mean kinetic energy of individual departing IHe_n products from the 266 nm A band dissociation of CF_3I and CH_3I in helium droplets produced at the stagnation temperatures $T_0 = 12, 15,$ and 18 K. The energies are calculated from the best fits to the speed distributions by function (4.1). Error bars are given only if larger than the plot symbols.

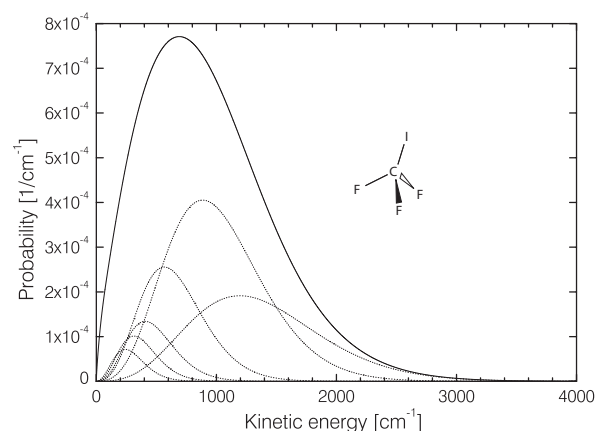


FIGURE 4.16: Overall kinetic energy distribution (solid line) of all IHe_n product complexes escaping from CF_3I -doped ^4He droplets produced at the stagnation temperature $T_o = 15$ K. The contributions of the most prominent products I , IHe_1 , \dots , IHe_5 are indicated by the dotted lines.

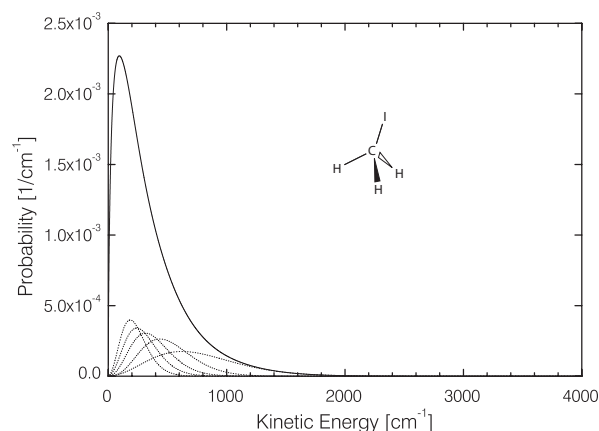


FIGURE 4.17: Overall kinetic energy distribution (solid line) of all IHe_n product complexes escaping from CH_3I -doped ^4He droplets produced at the stagnation temperature $T_o = 15$ K. The contributions of the most prominent products IHe_1 , IHe_2 , \dots , IHe_5 are indicated by the dotted lines.

In agreement with the explanation provided above for the irregular shape of the I^+ ion image obtained for CF_3I parents we attribute any droplet signal in the I^+ image for CH_3I parents to fragmentation processes accompanying the non-resonant femtosecond ionization of escaping IHe_n product complexes.

Overall mean kinetic energy of the products

An important consequence of the speed-size correlation of the IHe_n products concerns the droplet size effect on the *overall* mean kinetic energy of the escaping IHe_n complexes. From the picture developed above it follows that a change in mean droplet size \overline{N} will affect the *intensity distribution* of the IHe_n products rather than the individual mean kinetic energy of each escaping IHe_n complex. Qualitatively, the higher kinetic energy losses expected for fragments escaping “directly” from larger droplets should favor the production of slower and, as a consequence of the speed-size correlation, also larger IHe_n complexes. This is exactly the behaviour found in the case of CF_3I -doped helium droplets shown in Figure 4.5: The mean product size $\langle n \rangle$ steadily increases with mean droplet size \overline{N} . As stated before, in case of CH_3I this effect appears only for relatively high stagnation temperatures above about 18 K, *i.e.* small mean droplet sizes (see Figure 4.6). Possible reasons for this behaviour will be discussed in Section 4.5.

We now proceed to actually evaluate the overall mean kinetic energy $\langle\langle T_f \rangle\rangle$ of all escaping iodine–helium complexes for different mean droplet sizes \overline{N} and for both parent molecules. Towards this goal we transformed the fitted speed distribution of each escaping IHe_n product into energy space and calculated an overall kinetic energy distribution comprising all product sizes n . As an example we illustrate the overall kinetic energy distributions and their decomposition in Figures 4.16 and 4.17 for a stagnation temperature of 15 K. In these distributions the

Parent molecule	T_o [K]	$\langle\langle T_i(\text{I}) \rangle\rangle$ [cm^{-1}]	$\langle\langle T_f(\text{IHe}_n) \rangle\rangle$ [cm^{-1}]	Energy loss [%]
CF_3I	12	3540	807 (74)	77.2 (21)
	15	3540	937 (87)	73.5 (25)
	18	3540	1200 (150)	66.1 (42)
CH_3I	12	1260	350 (12)	72.2 (10)
	15	1260	344 (12)	72.7 (10)
	18	1260	333 (11)	73.6 (9)

TABLE 4.2: Overall mean kinetic energy of the escaping IHe_n products averaged over all complex sizes n and over the internal state distribution of iodine. The mean initial kinetic energy $\langle\langle T_i \rangle\rangle$ is taken from Table 4.1, while the mean final kinetic energy $\langle\langle T_f \rangle\rangle$ is calculated from the relative product intensities and the fits to the speed distributions (see text). The data is given for both parent molecules and for three selected helium stagnation temperatures T_o . The reported errors are based on the uncertainties in the relative intensity of each IHe_n product and in the parameters of the fit function for the speed distributions.

contribution of each product is given by its measured relative intensity (see Figures 4.5 and 4.6). Based on the discussion on page 109 the intensity of bare iodine from CH_3I is assumed to be zero. A few missing intensities or speed distributions were linearly interpolated. The overall mean kinetic energy $\langle\langle T_f \rangle\rangle$ then was computed straightforwardly from the distribution. The results of these calculations are tabulated in Table 4.2 and displayed in Figures 4.18 and 4.19. Note the different energy scale of the latter graphs.

The figures clearly show the different response of the two model systems to a change in mean droplet size \bar{N} . According to Table 2.2 the helium stagnation temperatures 12, 15 and 18 K lead to mean sizes of about 15000, 6000, and 3000 helium atoms, respectively. For an impurity located at the center of an average size droplet these conditions therefore vary the distance to the surface by more than 2 nm (see equation (1.6) and Figure 2.10) and should have a considerable effect on the kinetic energy of the escaping products. This is indeed the case for CF_3I where the overall mean kinetic energy of the escaping products decreases systematically and significantly with increasing mean droplet size \bar{N} . For CH_3I no such droplet size effect is found. This does not come surprisingly as for the stagnation temperatures studied a droplet size effect is absent both in the mean kinetic energy of each individual product *and* in the IHe_n product intensity distributions.

As a principal result of this analysis we note that the relative overall mean kinetic energy loss (see Table 4.2 and Figures 4.18 and 4.19) of the escaping iodine fragments is roughly the same for both parent molecules under study, despite the dramatic difference in initial kinetic energy.

Angular distributions

The analysis of the Abel inverted velocity map images of the escaping IHe_n products provides us also with the anisotropy parameter β as a function of product speed v in the droplet frame. In order to remove experimental noise from this observable and to consistently compare the

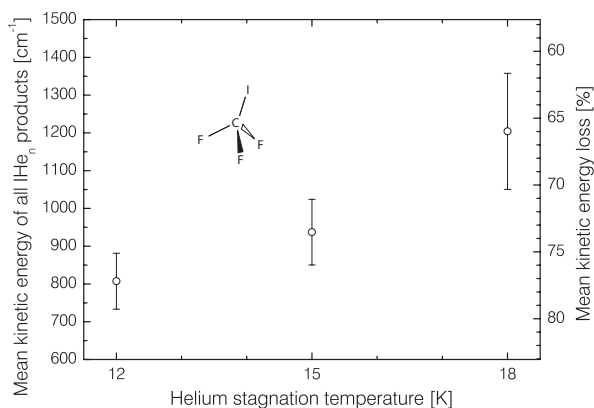


FIGURE 4.18: Overall mean kinetic energy of the IHe_n products escaping from CF₃I-doped ⁴He droplets and the corresponding mean kinetic energy loss as a function of the helium stagnation temperature T_o . The data is given for the selected stagnation temperatures $T_o = 12, 15$ and 18 K.

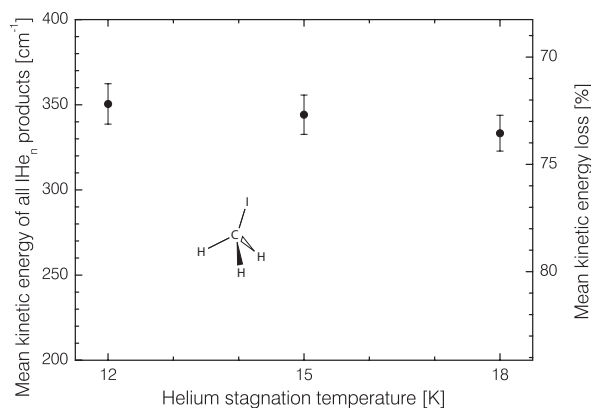


FIGURE 4.19: Overall mean kinetic energy of the IHe_n products escaping from CH₃I-doped ⁴He droplets and the corresponding mean kinetic energy loss as a function of the helium stagnation temperature T_o . The displayed values were obtained assuming that no bare iodine fragments are produced from this system.

anisotropy parameters of different IHe_n products it is advantageous to average the anisotropy parameters over the typical speeds of each escaping product. In Figures 4.20 and 4.21 we report the results of such an analysis for both parent molecules. The mean anisotropy parameter for each escaping IHe_n product complex was obtained by averaging $\beta(v)$ over all speeds within the FWHM of the corresponding speed distribution. Prior to this treatment we corrected the speed dependent anisotropy parameters $\beta(v)$ for homogeneous image background using the procedure described in Section 3.5.7. The displayed data is limited to products for which velocity map images of satisfactory contrast could be obtained within an integration time of one hour. Averaged anisotropy parameters for large IHe_n product complexes with $n > 10$ from CF₃I consequently are scarce since these complexes carry considerably less intensity than the equivalent products from solvated CH₃I (compare Figures 4.5 and 4.6). Note that the comparatively high droplet flux densities associated with the helium stagnation temperature $T_o = 15$ K (see Figure 3.8) allow obtaining anisotropy parameters for larger product complexes than at the other stagnation temperatures $T_o = 12$ K and 18 K studied here.

Similar to the assessment of the overall mean kinetic energy of the escaping products, the experimentally found values may be compared to the spin-orbit state averaged anisotropy parameters $\langle\beta\rangle$ associated with the 266 nm photolysis of free CF₃I and CH₃I molecules in the gas phase. These values are given in Table 4.3 and are indicated in Figures 4.20 and 4.21 by horizontal lines. The figures clearly illustrate that dissociating the parent molecules inside the droplets leads to *reduced* mean anisotropy parameters, i.e. broadened angular structures. For both parent molecules these mean anisotropy parameters are found to follow similar trends: The smaller IHe_n product complexes with $n \lesssim 7$ show comparable mean anisotropy parameters which are only by about 0.2 smaller than in the gas phase. The larger complexes with $n \gtrsim 8$ exhibit mean anisotropy parameters which continuously decrease with increasing product size n and reach

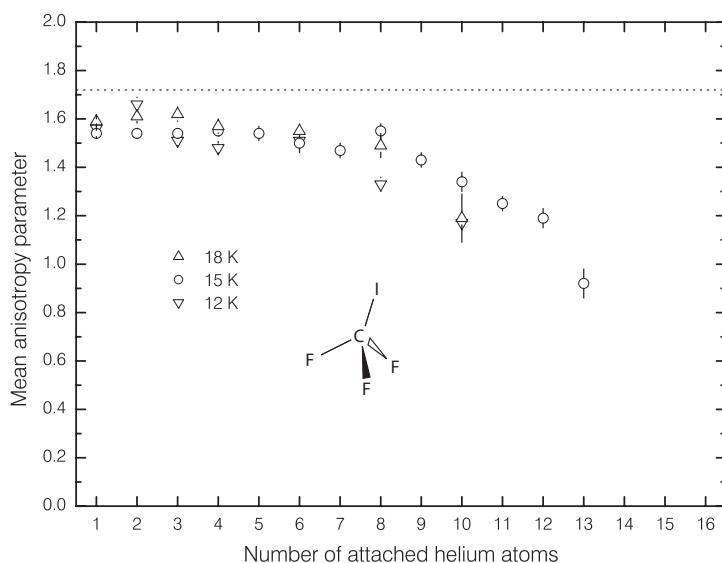


FIGURE 4.20: Mean anisotropy parameters of individual departing IHe_n products from the photolysis of CF_3I in the interior of ^4He droplets at three selected stagnation temperatures T_o . The reported anisotropy parameters were obtained by averaging over the FWHM of the speed distribution of each product (see text). The estimated spin-orbit state averaged anisotropy parameters for the 266 nm photolysis of free CF_3I molecules in the gas phase is indicated by the dotted horizontal line.

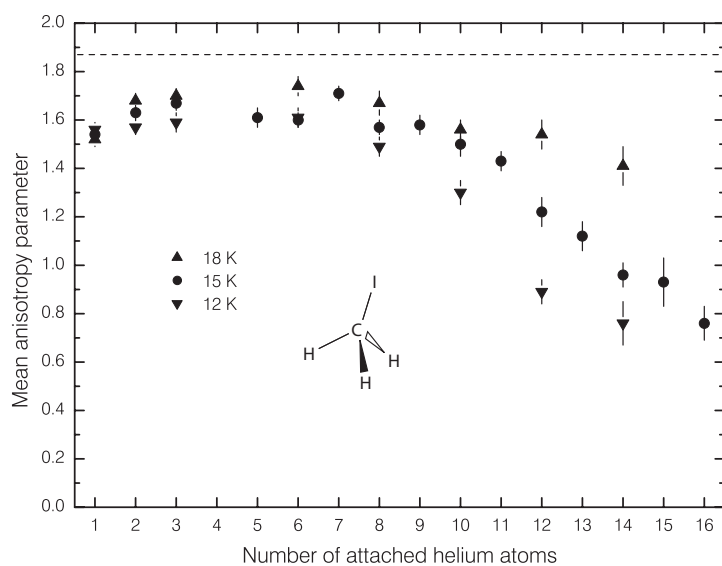


FIGURE 4.21: Mean anisotropy parameters of individual departing IHe_n products from the photolysis of CH_3I in the interior of ^4He droplets at three selected stagnation temperatures T_o . The reported anisotropy parameters were obtained by averaging over the FWHM of the speed distribution of each product (see text). The estimated spin-orbit state averaged anisotropy parameters for the 266 nm photolysis of free CH_3I molecules in the gas phase is indicated by the dashed horizontal line. The contribution of parent ions to the IHe_4 ion image (see Figure 4.9) impairs a precise determination of the anisotropy parameter for this particular product complex.

Parent molecule	$\langle\beta\rangle$
CH ₃ I	1.87
CF ₃ I	1.72

TABLE 4.3: Spin-orbit state averaged mean anisotropy parameters $\langle\beta\rangle$ associated with the 266 nm A band dissociation of free CH₃I and CF₃I molecules in the gas phase. The anisotropy parameters are based on the values given in Tables 2.6 and 2.7.

values as low as 0.76 ± 0.07 for IHe₁₆ from CH₃I at $T_o = 15$ K. In the case of CH₃I, where more experimental results for large product complexes are available, additionally a significant droplet size effect becomes apparent: Larger mean droplet sizes lead to lower mean anisotropy parameters. While this effect is weak for small and rapidly escaping IHe_{*n*} complexes with $n \lesssim 7$, it becomes more and more pronounced with increasing complex sizes n . Due to lack of data it is however not clear whether a similar effect would also become apparent for larger products complexes from solvated CF₃I. Note that the decrease of the anisotropy parameter with product size n is a real effect and *not* a consequence of a decreasing signal-to-noise ratio in the velocity map images. This can be seen by considering the signal levels at the three helium stagnation temperatures T_o under study. Due to the higher droplet flux densities the signal-to-noise ratio at $T_o = 15$ K is systematically higher than at 12 or 18 K (compare Figure 3.8). Nevertheless more elevated anisotropy parameters are found for large product complexes at $T_o = 18$ K which rules out a major influence of the image noise on the displayed mean anisotropy parameters.

4.2.3 Discussion

4.2.3.1 Escape process

Lessons from the speed distributions As shown above, the most probable speeds \hat{v} of individual departing IHe_{*n*} complexes from the photolysis of either parent molecule correspond to very high translational temperatures in the droplet frame. For most complex sizes n these translational temperatures largely exceed 10^2 K and therefore are much higher than the attainable droplet temperatures of roughly 10^0 – 10^1 K which were estimated in the introduction to this chapter on the basis of the total kinetic energy release of the photodissociation reaction (see page 92). The escape process of these IHe_{*n*} complexes from the droplets therefore is clearly of non-thermal origin and, as a consequence, characterized as “direct”. For extremely large complexes with sizes $n \gtrsim 12$ and relatively low translational temperatures of some tens of Kelvin this argument does, however, not fully apply. From the product intensities given in Figures 4.5 and 4.6 we learn, however, that IHe_{*n*} complexes with sizes $n \gtrsim 12$ are by 1–2 orders of magnitude less abundant than the most prominent small IHe_{*n*} products. Accordingly, thermally escaping products could constitute at most a very minor contribution to the ensemble of escaping IHe_{*n*} complexes. Moreover, as mentioned before, the extraordinary similarity of *all* (IHe_{*n*})⁺ ion images in two-dimensional shape, *i.e.* including the angular information, strongly suggests that the escape process of all IHe_{*n*} products, including the large complexes, is identical and does *not* depend on complex size or product speed. As a whole, the evidence presented above thus points convincingly to a “direct” escape of virtually all departing IHe_{*n*} complexes.

Further substantiation of this assessment will come from the separate analysis of the angular distributions carried out below.

Lessons from the angular distributions We have derived mean anisotropy parameters of many escaping IHe_n products from the analysis of mass-selective velocity map images. (see Figures 4.20 and 4.21). The results show that the most prominent smaller IHe_n complexes with $n \lesssim 7$ escape with mean anisotropy parameters only slightly inferior to the estimated mean gas phase values. Accordingly, the vast majority of departing IHe_n complexes exhibit only weakly broadened angular distributions. In the course of the escape process the initial correlation between the velocity vectors of the nascent fragments and the polarization vector of the photolysis laser pulse thus is largely maintained. The data on the larger and much less abundant IHe_n complexes with $n \gtrsim 8$ shows furthermore that the angular broadening increases with the complex size n and, at least for CH_3I parent molecules, also with the mean droplet size \bar{N} .

In order to interpret these data we now suggest and subsequently separately assess three different processes that may account for the observed reduction of the anisotropy parameters compared to the gas phase. Firstly, the interaction of the moving fragment with the helium environment can cause deflections from a straight trajectory and therefore may broaden the angular distributions of “directly” escaping fragments. Secondly, the droplet as a whole may rotate on the time scale of “direct” escape processes which again should wash-out the angular distribution of the products observed in the laboratory frame. As a third process we re-examine a thermally driven escape of the IHe_n products in the light of the observed anisotropy parameters in order to independently rule out this hypothetical possibility.

The broadening effect of the first process, *i.e.* trajectory deflections accompanying the “direct” fragment escape, can be expected to increase with the mean distance from the solvated parent molecules to the droplet surface, since the fragments will on average undergo more collisions with the helium atoms before escaping into the gas phase. Raising the mean cluster size \bar{N} consequently should globally reduce the anisotropy parameters of the escaping products. Moreover, a correlation between product size n and angular smearing emerges if the traveling fragments are assumed to steadily lose kinetic energy to the helium bath. In this picture, larger traveled distances correspond to lower fragment speeds. Due to the established speed-size correlation, larger product complexes escaping with lower speeds from the droplets could thus be associated with larger initial distances to the surface. Consequently, departing complexes containing a greater number n of helium atoms should exhibit increasingly smeared out angular distributions which is in full qualitative agreement with the experimental results. Trajectory deflections in the droplet interior thus can contribute to and, based on the reasoning above, may even solely bring about the experimentally observed broadening in the angular distributions of the escaping IHe_n complexes.

The angular smearing due to the second process, *i.e.* rotation of the helium clusters in the laboratory frame, should increase with both the escape time of the fragments and the rotational frequency of the droplets. Average droplet rotational frequencies $\langle f \rangle = \langle \omega \rangle / (2\pi)$ resulting from single sticking collisions with a typical dopant molecule are estimated in Appendix C as

a function of mean droplet size \overline{N} (see equation(C.12)). Based on classical considerations the frequency $\overline{\langle f \rangle}$ is found to decrease with increasing mean droplet size \overline{N} . While small droplets with $\overline{N} \approx 3000$ are estimated to spin relatively fast with a mean frequency $\overline{\langle f \rangle} \approx 10^9 \text{ s}^{-1}$, large droplets with $\overline{N} \approx 15000$ are predicted to have lower mean rotational frequencies $\overline{\langle f \rangle} \approx 10^8 \text{ s}^{-1}$. This behaviour makes it difficult to predict the consequences of a change in mean droplet size \overline{N} : On the one hand, larger droplets should lead to longer escape times and therefore create enhanced angular smearing. On the other hand, larger droplets spin slower which reduces the broadening effect on the angular distributions. Since presently a *precise* understanding of how both effects vary with \overline{N} is not available, it is beyond our means to predict the net effect of a changing mean droplet size on the angular distribution of the escaping products. As a consequence, a possible correlation between product size n and angular smearing due to droplet rotations can presently not be established neither. A conclusive assessment of the significance of droplet rotations for the broadening seen in the angular distributions of the departing IHe_n complexes is therefore not attempted at this stage.

The observed mean anisotropy parameters and the estimated rotational frequencies of the ^4He droplets provide, however, an independent means to estimate the escape time scale of the IHe_n complexes. Towards this goal we note again that the velocity vectors of the escaping IHe_n complexes exhibit a clear signature of the initial vector correlation with the polarization axis of the photolysis laser, regardless of the complex size n . It therefore can safely be concluded that the escape of the vast majority of IHe_n product complexes from the ^4He droplets is *fast* compared to the mean rotational period of the droplets and, as a consequence of the estimations in Appendix C, should be located in the sub-nanosecond regime. A particularly short escape time scale can be deduced for the smaller IHe_n products with $n \lesssim 7$ which exhibit mean anisotropy parameters close to the gas phase value and, according to the intensity distributions shown in Figures 4.5 and 4.6, account for the vast majority of the departing IHe_n products. This result agrees fully with our previous estimate where a typical time scale of 10 ps was assigned to “directly” escaping products. This value suggests that the mean droplet rotational periods and the average fragment escape times differ by at least two orders of magnitude. If this difference was fully reliable one could certainly neglect angular smearing due to droplet rotations for “directly” escaping products. However, we have to emphasize the uncertainties associated with the estimation of the mean droplet rotational frequencies $\overline{\langle f \rangle}$ as carried out in Appendix C. These calculations do not include any angular momentum loss following the pick-up process, e.g. due to evaporation of helium atoms from the cluster surface. More critically, droplet angular momenta resulting from the cluster formation processes in the subcritical supersonic expansion are entirely disregarded. In the light of the evidence presented so far we thus cannot rule out that droplet rotations *may* contribute to the limited degree of angular smearing, in particular for the larger and slower IHe_n product complexes which are thought to escape on a relatively longer time scale. The line of reasoning presented above illustrates, however, how the significance of droplet rotations can be tested further: If the loss of angular structure compared to the gas phase was mainly caused by droplet rotations, “directly” escaping fragments with a *shorter* mean escape time clearly should exhibit a *lesser* degree of angular broadening. We will therefore discuss this mechanism again in the light of the measured anisotropy parameters of the escaping alkyl fragments in Section 4.4.

The estimation of the droplet rotational frequencies is also valuable in assessing the significance of the third hypothetical broadening mechanism, *i.e.* a thermal product escape. As already pointed out in the introduction to this chapter, such an escape process implies that iodine fragments transfer their entire excess kinetic energy to the medium, thermalize in the droplet interior and later on escape as a consequence of evaporative processes. Evidently, such a process should substantially broaden the angular distributions of the departing products. In particular, one could expect a complete loss of angular structure if the time scale of such a thermal fragment release was to be long compared to the rotational period of the droplets. As shown in Section 2.2, evaporative processes typically take place on a time scale of 10^{-9} – 10^{-7} s which is comparable to the estimated mean rotational periods of helium droplets in the size range studied here (see Appendix C). On the time scale of a thermally driven fragment escape the droplets therefore ought to rotate typically by roughly one period which, as a consequence, should largely wash-out the angular distributions and yield mean anisotropy parameters close to zero. Moreover, evaporation from the droplet surface can be expected to release particles with an appreciable *distribution* of angles with respect to the surface normal and therefore should broaden the angular distributions, even if the droplets were *not* to rotate in the laboratory frame. The observed angular distributions clearly illustrate that such a broadening does not occur. From the observed mean anisotropy parameters it thus can be concluded that the vast majority of IHe_n products are *not* released via evaporative processes. Although a very minor contribution of thermally driven escape processes to the total product signal can not be fully excluded, these findings independently add further substantiation to the general characterization of the IHe_n escape as “direct”.

As a summary we note that out of the three proposed mechanisms only trajectory deflections in the droplets and, possibly, droplet rotations may significantly contribute to the broadening observed in the angular distributions of the escaping IHe_n complexes. Even if only the angular information in the $(\text{IHe}_n)^+$ ion images is considered, we can thus largely rule out a thermally driven escape of the departing IHe_n complexes. Although no quantitative analysis is presented yet, it is shown that trajectory deflections in the droplet interior in the course of a “direct” escape can qualitatively account for all important trends in the observed mean anisotropy parameters of the departing IHe_n complexes. A possible contribution of droplet rotations to the loss of angular structure is predicted to decrease for more rapidly escaping reaction products and will therefore be revisited in Section 4.4 considering the angular distributions of the departing CF_3 and CH_3 fragments.

Conclusion Both the observed speed and angular distributions point independently to a “direct” escape of the departing IHe_n complexes. Accordingly, we have little doubt that virtually all detected IHe_n complexes escape indeed “directly” from the droplets and therefore should have typical escape times of the order of 10 ps as estimated in the introduction to this chapter. This finding is fully in line with the recent calculations by Takayanagi *et al.*¹⁰² on the dissociation of Cl_2 in smaller helium droplets where, similarly, almost exclusively “direct” escape was found. The classical Monte Carlo simulations presented in Section 4.6 will further confirm this assessment.

4.2.3.2 A possible model

The analysis of the overall kinetic energy distributions of escaping IHe_n complexes has provided us with another important result. Regardless of the absolute value of their initial kinetic energy, the departing iodine fragments are found to transfer on average about 70 % of this energy to typical droplets with a mean size of ≈ 6000 atoms produced at our standard stagnation temperature of 15 K (see Table 4.2). Assuming “direct” escape, this behaviour indicates an energy transfer mechanism where the relative kinetic energy loss of a moving fragment per unit distance is, to a first approximation, independent of its absolute kinetic energy. A simple viscous fluid description based on Stokes flow past a sphere should consequently fail, since the predicted relative kinetic energy loss per traveled distance *is* a function of the fragment’s instantaneous translational energy (see Appendix D.1). Alternatively, one may therefore consider a statistical sequence of independent binary hard-sphere collisions with helium atoms as a starting point for a model of the fragment motion inside the helium droplets. Such a description has been successfully employed to simulate the speed and angular relaxation of translationally exited molecular and atomic fragments in various bath gases. Indeed, this billiard-ball type model has been found to predict particularly well the relaxation by collisions with rare gas and especially helium atoms in the gas phase (see for example references [239–242]). Using such a description for the photofragment relaxation in the condensed phase certainly oversimplifies the fragment and solvent dynamics, as the many-body character of the liquid state is entirely disregarded. On the other hand, it is already evident that such a model could, at least qualitatively, account for many important aspects of the experimental data. From the mathematical expressions given in Appendix D.2 for a statistical distribution of impact parameters it becomes clear that the mean relative kinetic energy loss of the traveling particles is solely determined by the number of collisions with helium atoms. As the hard-sphere collision cross section is independent of the relative speed of the collision partners, it follows that the mean relative kinetic energy loss per unit distance is independent of the fragment’s absolute kinetic energy, in accord with the experimental results for the IHe_n complexes. Moreover, such a description allows one to predict trajectory deflections occurring in the course of a “direct” fragment escape (see Table D.1 for a calculation of the average scattering angle per collision). In the case of iodine, the large mass ratio between this particular fragment and a ^4He atom furthermore ensures that trajectory deflections are small as observed. In Section 4.6 we will therefore use this simple description to simulate the motion and “direct” escape of some of the fragments by means of classical Monte Carlo calculations, taking into account the specific distribution of initial conditions for photolysis reactions in helium droplets.

4.2.3.3 Complex formation

Having established that the departing iodine fragments leave the helium droplets in virtually all cases via “direct” escape processes we proceed to examine possible origins for the observed fragment– He_n complex formation. The ionization some tens of nanoseconds after the “direct” departure from the droplets reveals that most of the released iodine atoms form van der Waals complexes with a varying number of helium atoms that can be larger than 15. Most remarkably, we find a high degree of correlation between the droplet frame speed and the size of these IHe_n

complexes: The faster the iodine atoms, the lower the number of helium atoms they bind to. Although we have shown that the helium atoms attached to the iodine atoms must come from the same helium droplet the parent molecule was embedded in, it is at this stage not fully clear *where* the product complexes form and *how* the speed-size correlation comes about.

One may propose that *bare* iodine atoms escape from the ^4He clusters and subsequently collide and coagulate with individual helium atoms that were released from the *same* droplet into the gas phase. Such ^4He atoms could originate from evaporation processes accompanying the energy transfer from the translationally relaxing fragment pair to the droplet. Depending on the droplet temperature thermally released ^4He atoms may reach RMS velocities of a few hundred m/s in the droplet frame which is comparable to the speeds found for the departing IHe_n complexes. Since the velocity vectors of a “directly” escaping fragment and evaporating helium atoms in its neighborhood can be expected to point into crudely similar directions, one could argue that the largest product complexes can form if the “directly” escaping iodine atoms have speeds similar to the majority of thermally released ^4He atoms. Such a process could potentially explain the observed speed-size correlation in the IHe_n products. A closer inspection of this model reveals, however, that the formation of complexes in the gas phase is highly unlikely. On the typical escape time scale of “directly” departing products of ≈ 10 ps, for example, only a few helium atoms will evaporate from an average size droplet which does not provide the necessary densities for colliding and coagulating with multiple helium atoms. This can be seen by looking at our standard expansion conditions of $p_o = 30$ bar and $T_o = 15$ K. From the estimates made in Section 2.3 we learn that the mean droplet size produced in such an expansion is roughly $\bar{N} \approx 6000$. Neglecting the internal cooling of the fragments, the possible heat release into a helium droplet prior to the fragment departure is limited by the total kinetic energy release of the photolysis reaction. Averaged over the two decay channels of the photolysis reaction this total kinetic energy release is with $\langle\langle T_{\text{tot}} \rangle\rangle = 11900 \text{ cm}^{-1}$ largest in case of CH_3I (compare Tables 2.6 and 2.7). From the values given in Table 2.1 the resulting maximum temperature of an average size droplet can be estimated to be lower than 3.5 K. The evaporation rates arising as a consequence of the thermal excitation can be taken from Figure 2.6. For the mean size $\bar{N} \approx 6000$ discussed here, the initial evaporation rate of less than $1 \cdot 10^{13} \text{ s}^{-1}$ results in a maximum of 100 ^4He atoms evaporating on the typical time scale of the fragment escape. The recent calculations for the dissociation of Cl_2 in small ^4He clusters at a finite temperature of 4 K predict this evaporation to follow approximately an isotropic distribution¹⁰² as the dissipation of heat inside the quantum fluid is extremely effective. With a bulk density droplet radius of about 40 Å the average size droplet has a surface area of roughly 5100 Å². On average only one helium atom is therefore expected to be released per 50 Å² of surface area. Even if the collisions were to occur relatively close to the surface, a “directly” departing iodine atom thus is not likely to encounter more than one evaporated helium atom. The implausibility of the model described above is further substantiated by considering that energy and momentum conservation most certainly require three-body collisions to actually bind a helium atom to a bare iodine atom. With the helium atom densities as low as estimated above, the creation of the IHe_n product complexes in the gas phase can thus be ruled out.

We therefore are convinced that the IHe_n complexes form *in the droplet interior*. This picture can be further refined by considering the strength of the iodine–helium interaction. Although to the best of our knowledge no iodine–helium pair potential is available yet, one may

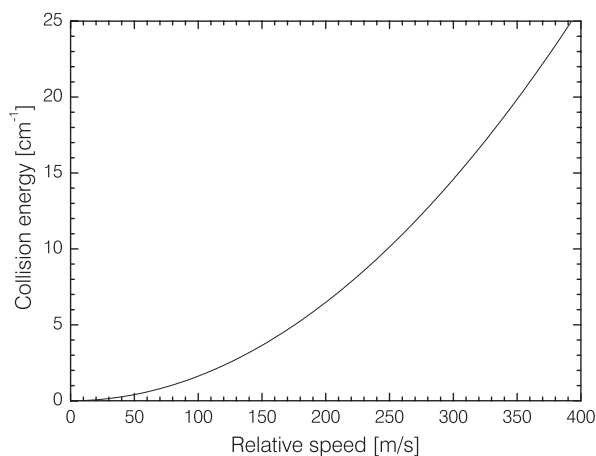


FIGURE 4.22: Energy available in a two-body I–He collision as a function of relative speed.

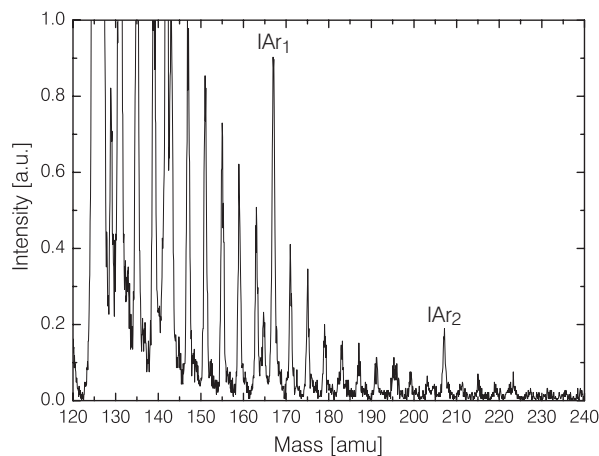


FIGURE 4.23: Outcome of the 266 nm A band photolysis of CH_3I in ^4He droplets additionally doped with on average two extra Ar atoms. The helium stagnation temperature was $T_o = 15$ K.

roughly estimate the well depth by comparison with other helium–halogen potentials. Such potentials have been calculated for He–Br,^{243,244} He–Cl,^{243,245} and He–F²⁴³ and indicate a well depth of the order of 20 cm^{-1} for the interaction of both ground state and spin-orbit excited iodine with helium. This should be contrasted with the energy available in a two-body iodine-helium collision at typical relative speeds. A plot of this energy based on the reduced mass of 3.88 amu is shown in Figure 4.22 as a function of relative speed. As we presently lack a microscopic picture of how the complexes form it is advantageous not to consider complex *formation*, but complex *destruction* in the following discussion. Let us therefore assume that an I–He complex has already formed inside the droplet and is traveling with a relative speed of 200 m/s through the helium environment. As can be inferred from Figure 4.22, the available energy associated with a collision at this relative speed is only about 5 cm^{-1} which is likely *not* to destroy an existing I–He complex. Accordingly, complexes composed of an iodine atom and one or more helium atoms formed in the droplet interior may very well survive a “direct” escape process and appear as small radical-doped helium clusters in the gas phase. Note, however, that the typical speeds associated with escaping IHe_1 products are with $\approx 400\text{ m/s}$ (see Figure 4.12) substantially higher than the speed of 200 m/s used in our example. This may be accounted for considering that the available energy of a He–IHe collision will typically not be fully transferred into an excitation of the existing I–He bond, as other channels, e.g. rotational excitation, are open. The characteristic speeds of escaping IHe_1 complexes can therefore well be higher than the value obtained from a direct conversion of the binding energy into a relative speed.

Another indication that helium atoms may permanently bind to translationally excited iodine radicals even at elevated speeds and under the relatively high collision rates associated with the bulk density in the central region of the droplet (compare Figure 2.11) comes from an experiment where on average two argon atoms were added to the CH_3I -doped droplets prior to the 266 nm photolysis reaction. The argon atoms are known to migrate to the drop-

let interior¹⁴⁷ and will localize near the CH_3I chromophore due to the dipole-induced dipole dispersion interaction.¹⁹ The mass-spectrum of the dissociation products as recorded by non-resonant femtosecond ionization is depicted in Figure 4.23. It becomes clear that some of the argon atoms attach to the nascent iodine fragments and are dragged out of the helium cluster into the gas phase. Consequently, a van der Waals bond formed between iodine and argon can indeed survive the *entire* translational motion of the fragment through the finite-size helium environment. Due to the much stronger interaction between iodine and argon it is however not fully clear whether a similar picture applies to the formation of IHe_n complexes. Taking the results of Br-Ar scattering experiments²⁴⁶ as an approximation, we expect a well depth of the order of 100 cm^{-1} for the I-Ar pair potential, which is about five times as much as for I-He . On the other hand, the statistics governing the survival of a traveling IAr_n complex in liquid helium are very different from the formation of IHe_n . While any argon atom detaching in the course of the escape process is irretrievably lost, ^4He atoms from the droplet environment may at any point attach to an IHe_n structure and thus increase the complex size. Even though the initial speed of an iodine atom may be too high to allow the formation of even a small IHe_1 complex, such a dynamical complex growth may therefore well occur in a later phase of the “direct” escape process when the fragment speed relative to the medium is lower.

Based on these considerations we propose that the formation of IHe_n complexes in the droplet interior should be viewed as the dynamical development of helium solvation shells around the fragment under the destructive influence of the impinging helium flow. Such a picture may also explain the observed correlation between size and terminal speed of the escaping IHe_n products: Slower fragments experience gentler collisions with the helium atoms of the surrounding medium and therefore should allow the formation of larger complex structures.

An important consequence of this basic model is that the interaction strength between a fragment X and helium should strongly influence the characteristic speeds of the escaping XHe_n product complexes. Qualitatively, a stronger attractive interaction should increase these speeds, as higher collision energies are required to achieve a similar dynamical equilibrium between complex formation and destruction. These considerations should, in principle, particularly well apply to small XHe_n complexes whose binding energies are expected to be more strongly determined by the nature of the fragment-helium interaction. In the limit of very large XHe_n complexes, however, the influence of the fragment X on the binding energy of yet another helium atom to the preexisting structure should diminish. The fragment species X therefore is expected to have little effect on the characteristic speeds of these large structures.

A *small* difference between the most probable speeds of complexes formed around two fragments does however not necessarily imply a dissimilar interaction strength with helium. Given the finite widths of the speed distributions as shown in Figure 4.13, a particular complex size is likely to form for a certain *range* of relative speeds rather than for a particular speed only. Due to the finite width of such an “acceptance interval” the most probable speed associated with a particular complex size should somewhat depend on the *distribution* of terminal fragment speeds. If the weight of the slower fragments within the acceptance interval of a XHe_n complex is increased, the most probable speed of this particular product should decrease, although the selection mechanism is entirely identical. The observed differences in the most probable speeds of the IHe_n product complexes from CF_3I and CH_3I shown, for example, in Figure 4.12

are thought to arise primarily from this second order effect, and not for example from the different degree of spin-orbit excitation of the iodine fragments. In this context we note that a significant electronic relaxation of spin-orbit excited iodine fragments in the course of the escape process is not expected. This conviction is based on the extremely weak efficiency of the collisional quenching of the iodine $^2P_{1/2}$ state by helium atoms in the gas phase, which, at room temperature, is characterized by a probability inferior to 10^{-8} per collision.^{247,248} We furthermore stress that a comprehensive interpretation of the observed speed distribution *widths* (see Figure 4.13) is presently beyond our understanding. As we will point out in more detail in Chapter 5, more research is needed to shape a clearer picture of the microscopic processes governing the complex formation inside the helium clusters.

As a result we emphasize that the data presented in this section points to a formation of the IHe_n complexes in the interior of the helium droplets. The proposed mechanism involves a dynamical development of solvation shells around the traveling radicals and may account for many observed effects including the correlation between speed and size of the escaping product complexes. Due to the dynamical character of this mechanism it remains unclear where exactly individual helium atoms attach permanently to a traveling photofragment. In view of the estimated collision energies, particularly favorable conditions for complex growth are predicted for the last part of the “direct” escape process where fragment speeds should be lowest. In this respect, a special role of the surface layer with its characteristic density drop could be possible.

4.3 Alkyl fragments

In this section we investigate the translational dynamics of methyl (CH_3) and fluorinated methyl (CF_3) radicals in liquid helium droplets by means of velocity map imaging. These studies serve as a complement to the experiments on the iodine fragments from the photolysis of solvated CF_3I and CH_3I which were presented and discussed in the previous section. Among other implications, the analysis of the alkyl ion images will permit us to illuminate the influence of the fragment mass on both the mean kinetic energy transfer to the finite-size liquid and the loss of correlation between the velocity vector of the photofragments and the polarization vector of the photolysis laser pulse.

4.3.1 The CF_3 radical

As pointed out in Section 3.6, we are not aware of a well-characterized REMPI scheme that would allow a state-selective ionization of this particular reaction product. Similar to the detection of the IHe_n complexes we therefore utilized intense ultrashort 800 nm laser pulses to non-resonantly ionize bare CF_3 radicals as well as possible CF_3He_n complexes escaping from the liquid helium environment in the aftermath of the 266 nm photolysis of droplet-solvated CF_3I . In contrast to the iodine fragments, which typically leave the droplets with a considerable number of 4He atoms attached, no evidence of CF_3He_n complexes was found in these experiments.

We therefore present data only on *bare* CF_3 radicals. Typical velocity map images of this product are illustrated in Figure 4.24. The pictures were recorded at the helium stagnation temperatures $T_o = 12, 15$ and 18 K (indicated in the upper left corner of each panel) which

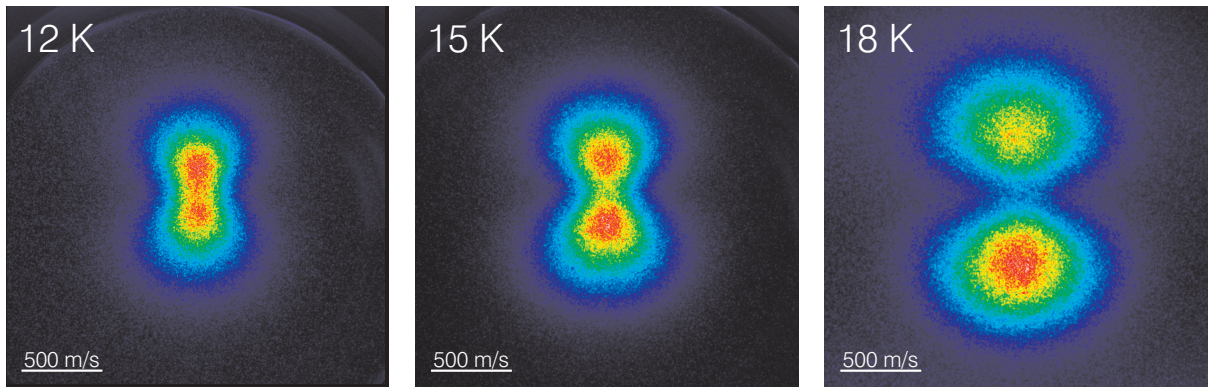


FIGURE 4.24: (Color) Typical velocity map images of escaping bare CF_3 photofragments. The fragments were created by dissociating CF_3I in the interior of ^4He droplets of three selected mean sizes. The temperature in the upper left corner of each panel indicates the helium stagnation temperature T_o . Originally recorded using different einzel lens voltages V_{lens} , the images have been scaled such that the speed scale shown in the lower left corner of each image is identical. The fragments were ionized in a non-state-selective way using intense ultrashort 800 nm laser pulses. The time delay Δt between UV photolysis and IR ionization laser pulses was set to 18 ns. The images were recorded using a total integration time of typically four hours.

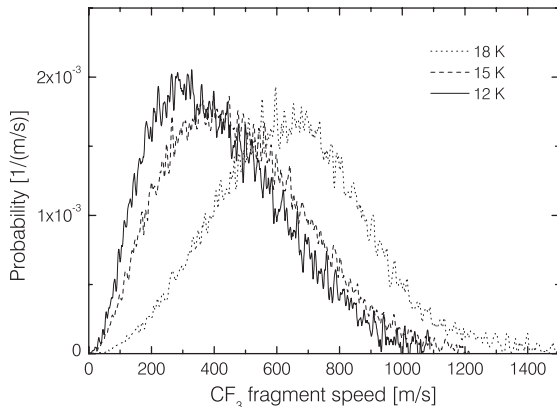


FIGURE 4.25: Speed distributions of bare CF_3 fragments escaping from ^4He droplets produced at the stagnation temperatures $T_o = 12, 15$ and 18 K. The displayed speed distributions were obtained by performing numerical Abel inversions on the two-dimensional intensity distributions shown in Figure 4.24.

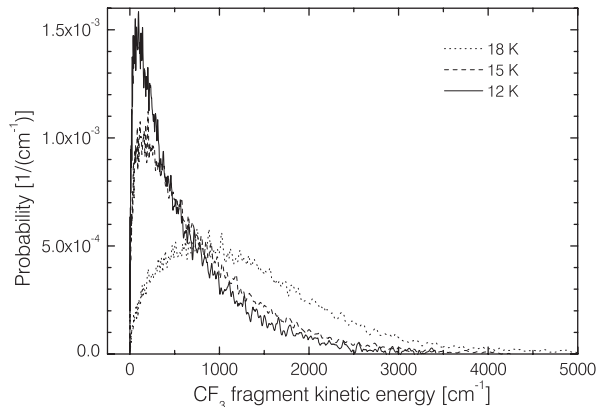


FIGURE 4.26: Kinetic energy distributions of bare CF_3 fragments escaping from ^4He droplets produced at the stagnation temperatures $T_o = 12, 15$ and 18 K. The energy distributions were found by transforming the speed distributions shown in Figure 4.25 into energy space using equation (3.27).

correspond to estimated mean droplet sizes \bar{N} of approximately 15000, 6000 and 3000 ^4He atoms, respectively (see Table 2.2). The images clearly reveal that a change in the mean size \bar{N} has a pronounced effect on both the speed and the angular distributions of the escaping CF_3 fragments. Qualitatively, CF_3 radicals escaping from bigger droplets are on average slower and

Parent molecule	$\langle\langle T(\text{CF}_3)\rangle\rangle$ [cm ⁻¹]	$\langle\langle v(\text{CF}_3)\rangle\rangle$ [m/s]
CF ₃ I	6510	1500

TABLE 4.4: Dissociation channel averaged mean kinetic energy $\langle\langle T(\text{CF}_3)\rangle\rangle$ and estimated mean speed $\langle\langle v(\text{CF}_3)\rangle\rangle$ of trifluoromethyl fragments from the 266 nm A band dissociation of free CF₃I molecules in the gas phase. The energy is based on the values given in Table 2.7. The corresponding mean speed is roughly estimated using the simplistic relation $\langle\langle T(\text{CF}_3)\rangle\rangle = m(\text{CF}_3)\langle\langle v(\text{CF}_3)\rangle\rangle^2/2$.

exhibit a more washed-out angular distribution. In order to discuss this effect in more detail, we examine the observed speed and angular distributions in a more quantitative manner in the following paragraphs.

Kinetic energy distributions

The speed and corresponding kinetic energy distributions of departing bare CF₃ radicals were computed by performing numerical Abel inversions on the velocity map images shown in Figure 4.24, and are illustrated in Figures 4.25 and 4.26. As usually, the speed distributions were corrected for a homogeneous image background ^c using the procedure described in Section 3.5.7. We note that neither the speed nor the energy distributions exhibit a clear sign of a bimodality that would allow us to separate the two dissociation channels (2.42). The mean kinetic energy $\langle\langle T_f(\text{CF}_3)\rangle\rangle$ of the escaping bare trifluoromethyl radicals thus can only be computed as an average over the decay channels, taking into account the entire experimental energy distribution. As we are interested in the mean energy transfer to the quantum liquid, the resulting values should be compared to the estimated decay channel averaged mean kinetic energy $\langle\langle T(\text{CF}_3)\rangle\rangle$ of these fragments from the photolysis of free parent molecules in the gas phase which are given in Table 4.4.

The result of such an analysis is illustrated in Figure 4.27 for a comprehensive set of stagnation conditions ranging from $T_o = 12$ K to $T_o = 18$ K. It becomes clear that a droplet size effect on the kinetic energy of the departing CF₃ products is present over the full range of mean droplet sizes \bar{N} investigated here. The mean kinetic energy losses amount to 80–90 % and therefore are significantly *larger* than those found on average for the escaping iodine fragments (compare Figures 4.18 and 4.19). For further reference we give the experimental values for the mean kinetic energy $\langle\langle T_f(\text{CF}_3)\rangle\rangle$ at the selected stagnation temperatures $T_o = 12, 15,$ and 18 K in Table 4.5. Together with the mean kinetic energies observed for iodine fragments

^cSimilar to the images of bare iodine shown in Figure 4.7, (CF₃)⁺ ion images are potentially affected by signal from the photolysis of unsolvated parent molecules in the residual gas. As a consequence of their high speeds (see Table 4.4) most of the CF₃ fragments from gas phase parent molecules are however not mapped onto the surface of the position-sensitive detector and therefore do not appear in the ion images. It is important to note that the spatial separation between gas phase and droplet signal is particularly good for CF₃ fragments escaping from the helium clusters with low speeds in the laboratory frame. This is the case for the lower lobe in the ion images depicted here, as fragments mapped there have droplet frame velocity vectors that partially compensate the droplet beam speed. In order to most efficiently eliminate contributions from gas phase photolysis events we typically report speed and angular distributions for this single lobe only.

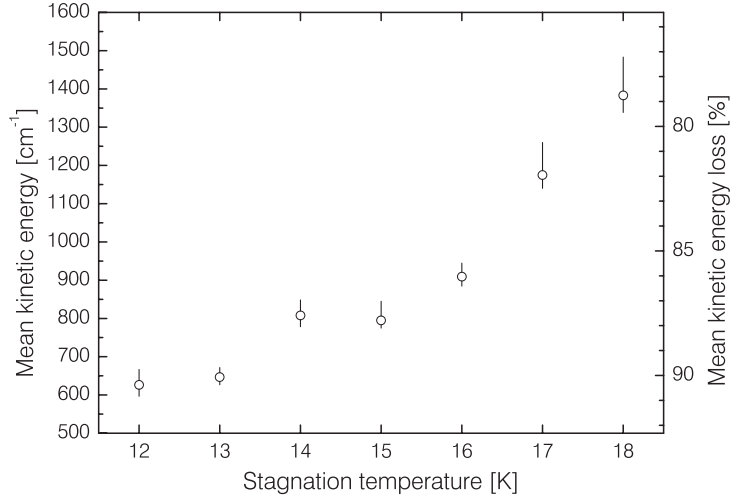


FIGURE 4.27: Mean kinetic energy $\langle\langle T_f(\text{CF}_3) \rangle\rangle$ of escaping bare CF_3 radicals as a function of the helium stagnation temperature T_o . The scale on the right hand side indicates the mean relative kinetic energy loss compared to the average gas phase value given in Table 4.4.

departing from the same system, these results will allow us to assess the average total kinetic energy transfer to helium droplets of various mean sizes (see Section 4.4).

Angular distributions

The anisotropy parameter β of the escaping CF_3 radicals depends strongly on the fragment speed v . This can be seen from Figure 4.28 which illustrates the function $\beta(v)$ together with the corresponding speed distribution for the selected stagnation temperature $T_o = 15$ K. It seems appropriate to describe the behaviour of $\beta(v)$ by introducing three different speed regions. At low speeds (here $v \lesssim 50$ m/s) the angular distributions are practically isotropic with anisotropy parameters oscillating about $\beta = 0$. In the region of intermediate speeds $\beta(v)$ increases approximately linearly. All higher speeds (here $v \gtrsim 350$ m/s) that carry an appreciable ion signal exhibit an approximately constant anisotropy parameter which will be referred to as “limiting” value β_{lim} . For the example shown in Figure 4.28 we estimate a value of $\beta_{\text{lim}} = 1.61 \pm 0.07$.

Parent molecule	T_o [K]	$\langle\langle T_i(\text{CF}_3) \rangle\rangle$ [cm ⁻¹]	$\langle\langle T_f(\text{CF}_3) \rangle\rangle$ [cm ⁻¹]	Energy loss [%]
CF_3I	12	6510	627 (40)	90.4 (6)
	15	6510	795 (50)	87.8 (8)
	18	6510	1383 (100)	78.8 (15)

TABLE 4.5: Mean kinetic energy $\langle\langle T_f \rangle\rangle$ of bare CF_3 radicals departing from droplets produced at selected stagnation temperatures T_o . The mean initial kinetic energy $\langle\langle T_i \rangle\rangle$ is taken from Table 4.4, whereas $\langle\langle T_f \rangle\rangle$ is extracted from the energy distributions shown in Figure 4.26. The reported errors arise mainly from the uncertainty in the background intensity of the ion images.

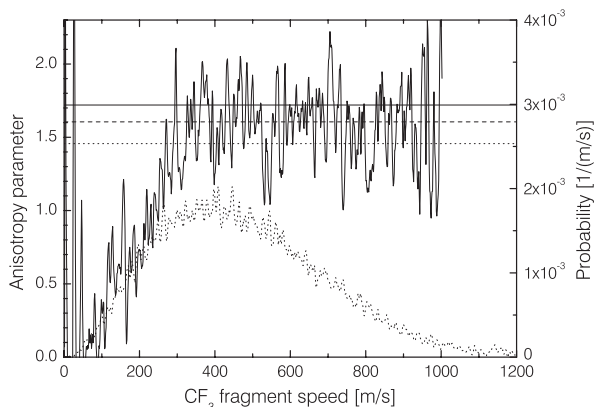


FIGURE 4.28: Anisotropy parameter β as a function of fragment speed v (solid line, left scale) and the speed distribution (dotted line, right scale) of CF_3 fragments escaping from ^4He droplets produced at $T_o = 15$ K. The horizontal lines illustrate the averaged (dotted line) and limiting anisotropy (dashed line) parameters as well as the gas phase value (solid line). See text for details.

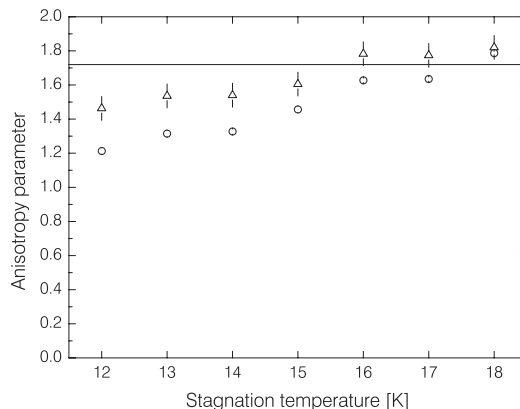


FIGURE 4.29: Averaged (circles) and limiting (triangles) anisotropy parameters of bare CF_3 radicals from the 266 nm dissociation of CF_3I molecules in the interior of ^4He droplets produced at various stagnation temperatures. The horizontal line indicates the estimated anisotropy parameter in the gas phase (compare Table 4.3).

Although the onset of the three regions varies slightly with mean droplet size \overline{N} , they are characteristic for *all* velocity map images of escaping bare CF_3 radicals recorded in this work.

In contrast to the departing IHe_n complexes studied before, the function $\beta(v)$ varies considerably *across* the FWHM of the CF_3 speed distribution, *i.e.* at speeds that are associated with the highest signal levels. In order to evaluate this effect we report both the limiting anisotropy parameter β_{lim} and an averaged value for each stagnation temperature T_o . Similar to the treatment of the IHe_n complexes the mean value is obtained by averaging $\beta(v)$ over all speeds v within the FWHM of the product speed distribution. The result of this analysis is illustrated in Figure 4.29 which shows the two values as a function of stagnation temperature T_o . As can be seen from this plot, both the limiting and the averaged anisotropy parameters depend on the mean droplet size \overline{N} . Whereas both anisotropy parameters reach the gas phase limit^d for $T_o = 18$ K, they drop continuously with decreasing stagnation temperature. At $T_o = 12$ K an averaged anisotropy parameter of only 1.21 ± 0.02 is found. This decrease of the anisotropy parameters is much more pronounced than in the case of the IHe_n products, where the averaged anisotropy parameters of the most prominent small complexes change by less than 0.2 when the stagnation temperature is lowered from $T_o = 18$ to 12 K. As we will show below, an even more dramatic decrease of the anisotropy parameters occurs for the lighter CH_3 fragments. We will therefore discuss this effect more profoundly in Section 4.4 and proceed to present the data for the methyl radical.

^dIt is not clear why the limiting anisotropy parameters slightly exceed the estimated gas phase value at $T_o = 16, 17,$ and 18 K.

4.3.2 The CH_3 radical

Unlike the CF_3 fragments, bare CH_3 radicals may be state-selectively ionized using the previously described, well-known $[2 + 1]$ REMPI schemes in the near UV around 330 nm (see Section 3.6.2). This enabled us to carry out dissociation experiments where either vibrational ground state or umbrella mode excited methyl radicals were probed with the aid of a dye laser^e.

As a starting point we show in Figure 4.30 typical ion images of escaping bare CH_3 fragments in the vibrational ground state. The stagnation temperatures that determine the mean size \bar{N} of the helium droplets (compare Table 2.2) are indicated in the upper left corner of each panel. A brief examination of these images reveals a droplet size effect on both the speed and the angular distributions which is qualitatively similar to the effect previously seen for the heavier CF_3 fragments: The larger droplets produced at lower stagnation temperatures T_o cause the fragments to escape with lower speeds and with less and less structure in the angular coordinate. Similar to the treatment of the CF_3 images we proceed to separately examine the observed speed, *i.e.* kinetic energy distributions, and the angular distributions in more detail.

Kinetic energy distributions

The numerical Abel inversion of the velocity map images of vibrational ground state methyl fragments shown in Figure 4.30 leads to the speed distributions depicted in Figure 4.31. Small corrections to the speed distributions were applied in order to account for background signals in the ion images. As usually, we used the correction method described in Section 3.5.7 which assumes a uniform background level in the images. With the aid of transform (3.27) we subsequently obtained the corresponding kinetic energy distributions as illustrated in Figure 4.32. Similar to the CF_3 fragments, neither the speed nor the energy distributions of the departing vibrational ground state CH_3 fragments exhibit a clear signature of the two decay channels (2.42) associated with the two spin-orbit states of iodine. Accordingly, the decay channel averaged mean kinetic energy $\langle\langle T_f(\text{CH}_3, v = 0) \rangle\rangle$ of the escaping methyl radicals emerges as a principal observable. As a reference, we give in Table 4.6 estimations of decay channel averaged mean kinetic energies $\langle\langle T \rangle\rangle$ and speeds $\langle\langle v \rangle\rangle$ of methyl fragments from the 266 nm photolysis of free CH_3I molecules in the gas phase. These values include an average over all vibrational states (all v) as well as mean kinetic energies for the vibrational ground state ($v = 0$) and the first umbrella mode excited state ($\nu_2 = 1$) whose frequency has previously been specified as 606 cm^{-1} (see Section 2.5). Following our usual approach, the mean gas phase kinetic energy of vibrational ground state methyl fragments $\langle\langle T(\text{CH}_3, v = 0) \rangle\rangle$ will serve as an estimate of the mean initial kinetic energy $\langle\langle T_i(\text{CH}_3, v = 0) \rangle\rangle$ of nascent vibrational ground state CH_3 fragments in the interior of helium droplets.

The mean final kinetic energy $\langle\langle T_f(\text{CH}_3, v = 0) \rangle\rangle$ of methyl fragments leaving the droplet environment in the vibrational ground state is calculated directly from the observed energy

^eIn order to obtain REMPI signal levels similar to those achieved using non-resonant ionization by femtosecond pulses, we increased the backing pressures of the cross beam by about 50 % compared to the values given in Table 3.4. A careful comparison for selected stagnation conditions confirmed that the new doping conditions did not cause any significant change in the properties of the ion images. We therefore are convinced that virtually only monomer-doped helium droplets contributed to the ion signal in these experiments, despite the slightly increased doping pressures.

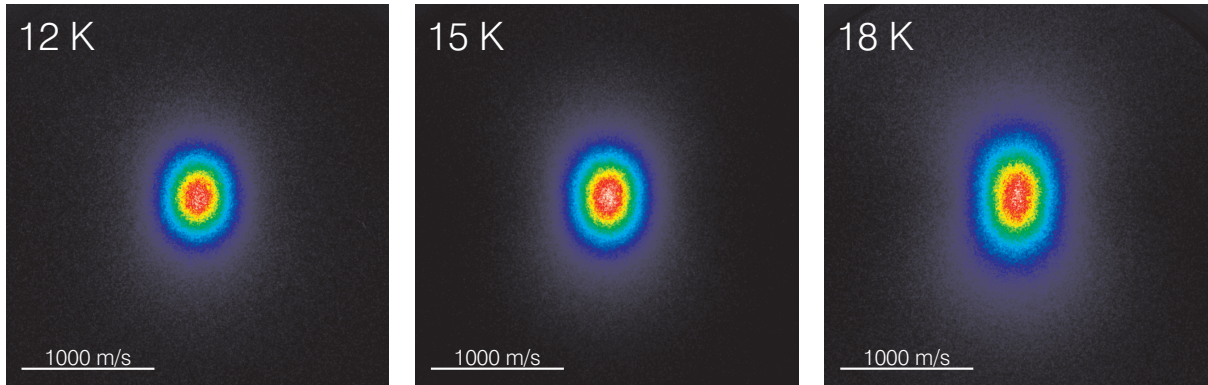


FIGURE 4.30: (Color) Typical velocity map images of escaping bare CH_3 fragments in the vibrational ground state. The fragments were created by dissociating CH_3I in ^4He droplets of three selected mean sizes. State-selective ionization is accomplished using a $[2 + 1]$ REMPI scheme at 333.5 nm. The temperature in the upper left corner of each panel indicates the helium stagnation temperature T_o . All shown velocity map images were recorded using the einzel lens voltage $V_{\text{lens}} = 6700$ V and an integration time of at least four hours. The time delay Δt between the UV photolysis and ionization nanosecond laser pulses was set to 15 ns.

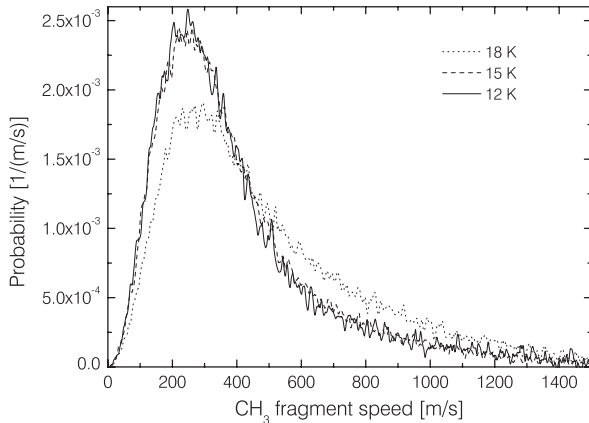


FIGURE 4.31: Speed distributions of escaping bare CH_3 fragments in the vibrational ground state. The fragments were detected after escaping from ^4He droplets produced at the stagnation temperatures $T_o = 12, 15,$ and 18 K. The displayed speed distributions were obtained by performing numerical Abel inversions on the two-dimensional intensity distributions shown in Figure 4.30.

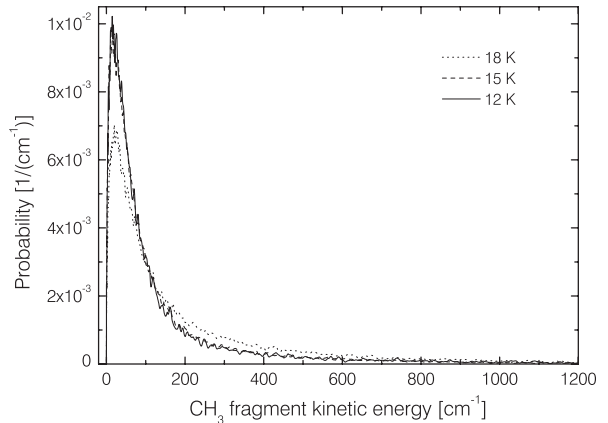


FIGURE 4.32: Kinetic energy distributions of escaping bare CH_3 fragments in the vibrational ground state. The curves correspond to helium clusters produced at the stagnation temperatures $T_o = 12, 15$ and 18 K. The energy distributions were found by transforming the speed distributions shown in Figure 4.31 into energy space using equation (3.27).

distributions and is shown in Figure 4.33 for some selected stagnation temperatures T_o in the range from 12 to 18 K. In contrast to the data on bare CF_3 , a significant droplet size effect on the final kinetic energy emerges only at high stagnation temperatures $T_o = 17$ K and $T_o = 18$ K that are associated with relatively small mean droplet sizes \bar{N} . At lower stagnation temperatures the

Parent molecule	CH_3 vib. state	$\langle\langle T(\text{CH}_3) \rangle\rangle$ [cm^{-1}]	$\langle\langle v(\text{CH}_3) \rangle\rangle$ [m/s]
CH_3I	all v	10650	4120
	$v = 0$	9830	3960
	$\nu_2 = 1$	10040	4000

TABLE 4.6: Dissociation channel averaged mean kinetic energy $\langle\langle T(\text{CH}_3) \rangle\rangle$ and estimated mean speed $\langle\langle v(\text{CH}_3) \rangle\rangle$ of CH_3 fragments in specific vibrational states created by the 266 nm A band dissociation of free CH_3I molecules in the gas phase. The mean kinetic energy considering all vibrational states $\langle\langle T(\text{CH}_3, \text{all } v) \rangle\rangle$ is based on the values given in Table 2.6. The mean energies in the vibrational ground state $\langle\langle T(\text{CH}_3, v = 0) \rangle\rangle$ and in the first umbrella mode excited state $\langle\langle T(\text{CH}_3, \nu_2 = 1) \rangle\rangle$ were calculated neglecting any rotational energy content of the methyl fragments and using the state-specific quantum yields $\phi^*(v = 0) = 0.94$ and $\phi^*(\nu_2 = 1) = 0.83$ specified in Section 2.5. In all cases the corresponding average speed $\langle\langle v(\text{CH}_3) \rangle\rangle$ was estimated using the simplistic relation $\langle\langle T(\text{CH}_3) \rangle\rangle = m(\text{CH}_3) \langle\langle v(\text{CH}_3) \rangle\rangle^2 / 2$.

speed and energy distributions of the methyl fragments undergo little change. Possible reasons for this behaviour will emerge in Section 4.5, where we present evidence for recombination of CH_3I in the medium-size helium clusters studied here.

For later comparison with other photodissociation products we specify in Table 4.7 the mean kinetic energy as well as the mean relative kinetic energy loss of escaping bare CH_3 radicals in the vibrational ground state for the selected helium stagnation temperatures $T_o = 12, 15$ and 18 K. The mean relative kinetic energy losses are with more than 97 % considerably *larger* than for any other departing fragment studied in this work. Note that these values were calculated assuming that vibrational cooling in the course of the fragment escape does not occur. In any case, this should only be a minor approximation since the mean kinetic energies associated with the most populated vibrational states $v = 0$ and $\nu_2 = 1$ in the gas phase differ only slightly. Experimental evidence that vibrational cooling is indeed at least incomplete will be given below.

Parent molecule	T_o [K]	$\langle\langle T_i(\text{CH}_3, v = 0) \rangle\rangle$ [cm^{-1}]	$\langle\langle T_f(\text{CH}_3, v = 0) \rangle\rangle$ [cm^{-1}]	Energy loss [%]
CH_3I	12	9830	141 (16)	98.6 (2)
	15	9830	139 (7)	98.6 (1)
	18	9830	205 (12)	97.9 (1)

TABLE 4.7: Mean kinetic energy $\langle\langle T_f(\text{CH}_3, v = 0) \rangle\rangle$ and mean relative kinetic energy loss of escaping bare CH_3 radicals in the vibrational ground state for selected helium stagnation temperatures T_o . The mean initial kinetic energy $\langle\langle T_i(\text{CH}_3, v = 0) \rangle\rangle$ is taken from Table 4.6, whereas $\langle\langle T_f(\text{CH}_3, v = 0) \rangle\rangle$ is extracted from the kinetic energy distributions shown in Figure 4.32. The reported errors arise mainly from the uncertainty concerning the background intensity in the ion images.

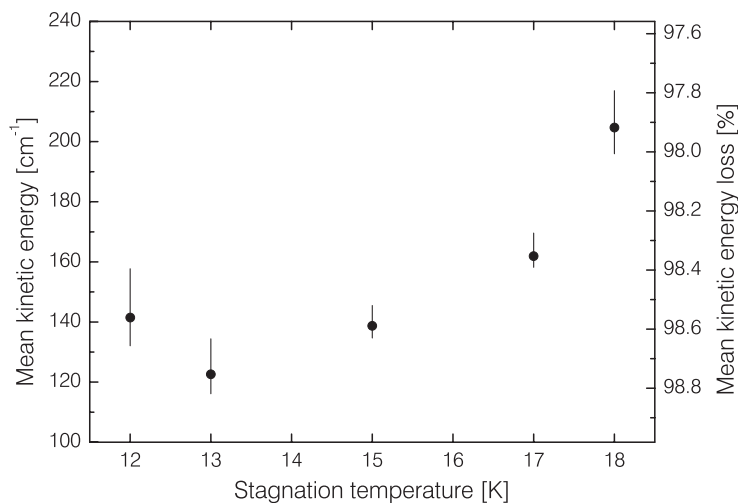


FIGURE 4.33: Mean kinetic energy $\langle\langle T_f(\text{CH}_3, v=0) \rangle\rangle$ of escaping bare vibrational ground state CH_3 radicals as a function of the helium stagnation temperature T_o . The scale on the right hand side indicates the mean relative kinetic energy loss compared to the average gas phase value $\langle\langle T(\text{CH}_3, v=0) \rangle\rangle = 9830 \text{ cm}^{-1}$ given in Table 4.6. In computing this mean relative energy loss, possible contributions to the experimental $v=0$ signal arising from vibrational cooling in the course of the methyl escape were entirely disregarded.

Angular distributions

Similar to the departing CF_3 radicals analyzed previously, escaping bare CH_3 radicals in the vibrational ground state exhibit anisotropy parameters β that vary substantially as a function of fragment speed v in the droplet frame. Qualitatively, the same three characteristic speed regions as for escaping CF_3 are also found here. For vibrational ground state methyl radicals this behaviour is illustrated in Figure 4.34 which shows a similar plot as Figure 4.28 for the non-state-selectively detected trifluoromethyl fragments. At low speeds the angular distributions of the escaping bare CH_3 fragments in the vibrational ground state have no significant structure. At intermediate speeds the anisotropy parameter increases in a roughly linear fashion until a plateau is reached that stretches out towards the highest speeds observed. As before, the anisotropy parameter corresponding to the plateau is referred to as limiting value β_{lim} which, together with an average anisotropy parameter, is reported in Figure 4.35 as a function of stagnation temperature T_o . Again, the mean anisotropy parameter was obtained by averaging the function $\beta(v)$ over all speeds within the FWHM of the corresponding speed distributions.

As can be seen from Figure 4.35, *both* the limiting and the average anisotropy parameters associated with the departing vibrational ground state methyl fragments remain significantly lower than the decay channel averaged gas phase value^f, even for the comparatively small mean

^fRegarding the dissociation of free CH_3I molecules in the gas phase we assume that the dissociation channel averaged anisotropy parameters for methyl fragments in the vibrational ground state and in the first umbrella mode excited state are similar to the overall mean anisotropy parameter $\langle\beta\rangle$ given in Table 4.3. At least for methyl in the vibrational ground state this is fully supported by recent velocity map imaging experiments at the relevant photolysis wavelength of 266 nm which indicate a decay channel averaged value of $\approx 1.9(1)$.¹⁶⁰

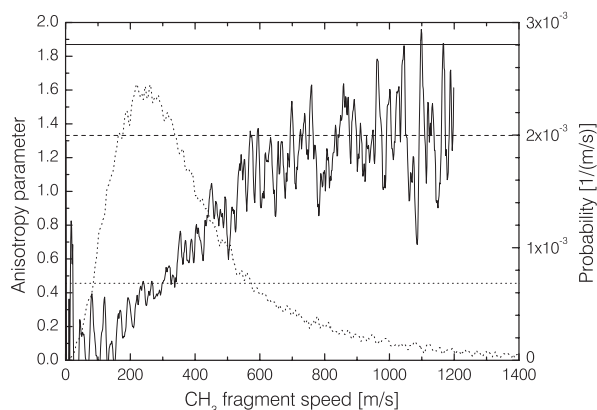


FIGURE 4.34: Anisotropy parameter β of escaping bare CH_3 fragments in the vibrational ground state as a function of fragment speed v (solid line, left scale). The graph also shows the corresponding speed distribution (dotted line, right scale). In this example the helium stagnation temperature T_o was set to 15 K. The horizontal lines illustrate the averaged (dotted line) and limiting anisotropy (dashed line) parameters as well as the estimated gas phase value (solid line). See text for details.

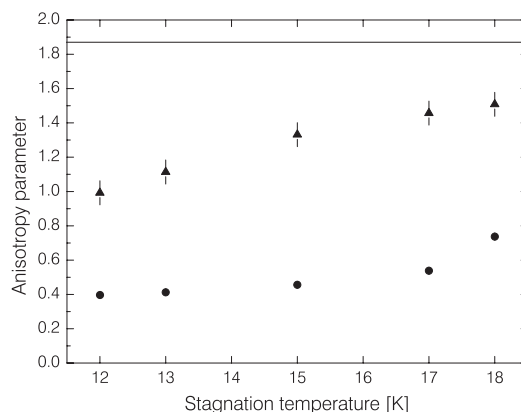


FIGURE 4.35: Averaged (circles) and limiting (triangles) anisotropy parameters of escaping bare CH_3 radicals in the vibrational ground state. The data is given for various helium stagnation temperatures T_o . The horizontal line indicates the estimated mean anisotropy parameter in the gas phase (compare Table 4.3).

droplet sizes produced at high stagnation temperatures of 17 or 18 K. The experimentally observed angular distributions of escaping CH_3 fragments in the vibrational ground state thus are substantially *more broadened* than the angular distributions of the departing CF_3 fragments.

Umbrella mode excited CH_3 fragments

We have employed the previously described $[2 + 1]$ REMPI scheme in the vicinity of 330 nm (see Section 3.6.2) to state-selectively ionize escaping bare CH_3 fragments in the first umbrella mode (ν_2) excited state. Since gas phase studies have shown that a considerable amount of CH_3 fragments are born in this $\nu_2 = 1$ vibrational state (compare Section 2.5), an absence of the corresponding ion signal in our experiments would indicate an efficient vibrational cooling in the course of the fragment escape through the liquid helium environment. Studies of the 266 nm photolysis of free CH_3I molecules in the gas phase have also established that methyl fragments born in the vibrational states $v = 0$ and $\nu_2 = 1$ have decay channel averaged mean kinetic energies that differ by only $\approx 2.1\%$ (see Table 4.6). Furthermore, methyl fragments born in $v = 0$ and $\nu_2 = 1$ presumably have very similar dissociation channel averaged mean anisotropy parameters^f. If all departing methyl fragments were to escape “directly” from the droplets, *prominent* differences between the speed or angular distributions of departing $\nu_2 = 1$ excited and vibrational ground state methyl radicals would thus suggest a dissimilar interaction of the umbrella mode excited fragments with the quantum liquid they are traveling through.

Our experiments reveal, however, a substantial $\nu_2 = 1$ ion signal from which we derived speed and angular distributions that are very similar to the distributions observed for CH_3 in

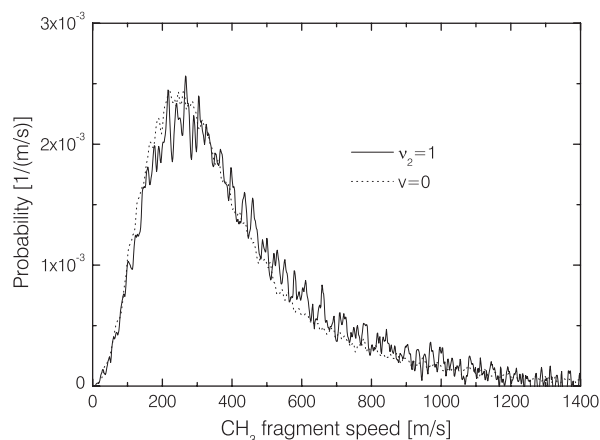


FIGURE 4.36: Speed distributions of umbrella mode excited ($\nu_2 = 1$) CH_3 fragments (solid curve) and methyl fragments in the vibrational ground state (dotted curve) escaping from helium droplets produced at a stagnation temperature of 15 K. Within the experimental error the distributions are indistinguishable.

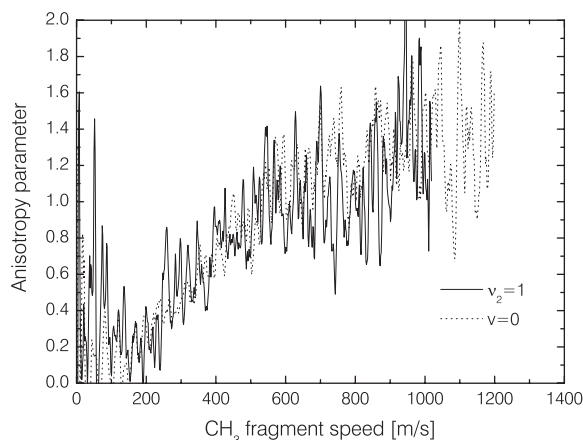


FIGURE 4.37: Plot of the anisotropy parameter β versus fragment speed for umbrella mode excited ($\nu_2 = 1$) CH_3 fragments (solid curve) and methyl fragments in the vibrational ground state (dotted curve) escaping from helium droplets produced at a stagnation temperature of 15 K. In the limits of the experimental resolution the two curves are identical.

the vibrational ground state. This is illustrated in Figures 4.36 and 4.37, where we graphically compare both the speed and the angular distributions observed at our standard helium stagnation temperature $T_o = 15$ K. As no significant differences between these distribution emerge we have no evidence that the motion of vibrational ground state and vibrationally excited methyl fragments through liquid helium should be governed by different interactions. Since, according to gas phase experiments, the majority of methyl fragments from the 266 nm photolysis of CH_3I are born in either the vibrational ground state or the first umbrella mode excited state (see Section 2.5), the speed and angular distributions measured here should constitute a good approximation of those distributions expected for the *ensemble* of vibrational states formed in the dissociation process. In the limit of “direct” escape, the mean relative kinetic energy losses derived for escaping bare methyl fragments in the vibrational ground state should therefore also apply approximately to the said *ensemble* of vibrational states. The appreciable amount of methyl radicals escaping from the droplets in the $\nu_2 = 1$ vibrational state proves furthermore that the vibrational cooling of the ν_2 mode is, at best, incomplete.

CH_3He_n progression

In addition to the detection of escaping methyl fragments in specific vibrational states we have used non-resonant ionization by intense femtosecond laser pulses to investigate the formation of products other than bare methyl. These experiments revealed a CH_3He_n progression in the product mass spectrum which is illustrated in Figure 4.38 for our standard helium stagnation temperature of 15 K. Compared to the IHe_n progressions observed for both parent molecules CH_3I and CF_3I (see Section 4.2), the intensity of the CH_3He_n products ($n = 1, 2, \dots$) is

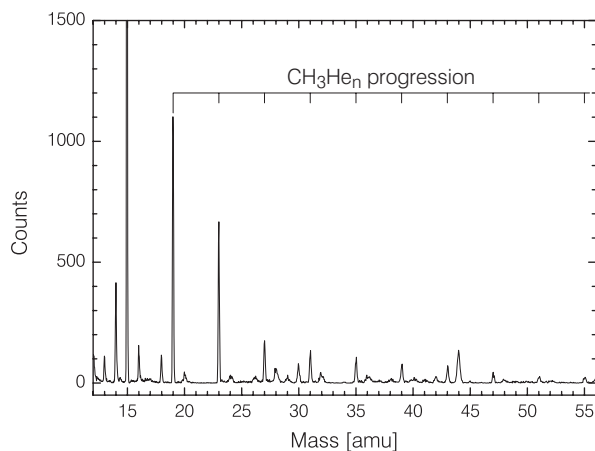


FIGURE 4.38: Time-of-flight mass spectrum of species in the detection volume of the velocity map imaging setup following the 266 nm photolysis of CH_3I molecules in the interior of ^4He droplets. The mass spectrum was obtained by accumulating the counts of 15000 laser shots and illustrates the formation of CH_3He_n complexes in the aftermath of the photolysis of the parent molecule. Other ion signals are mainly due to the presence of background gas species in the detection region. The ionization of the various species was accomplished using intense 800 nm pulses with a duration of about 150–200 fs (FWHM). These pulses were delayed by $\Delta t \approx 120$ ns with respect to the UV dissociation pulses. The helium stagnation temperature T_o was set to 15 K.

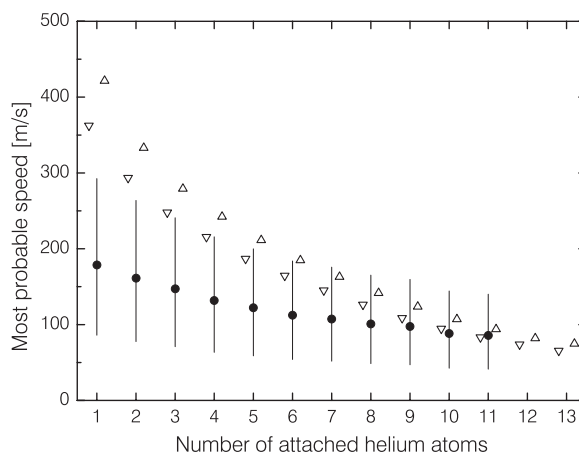


FIGURE 4.39: Most probable speed (dots) and FWHM (bars) of the CH_3He_n speed distributions observed at a helium stagnation temperature of 15 K. For comparison, the graph also shows the most probable speeds of the IHe_n product complexes created by the 266 nm photolysis of CF_3I (Δ) and CH_3I (∇) in helium droplets of identical mean size. In order to increase the clarity of the plot, the latter symbols are displaced horizontally by +0.2 (Δ) and -0.2 (∇) with respect to the correct number of attached helium atoms.

relatively weak, since even the most prominent CH_3He_1 product is, at $T_o = 15$ K, about 2.5 times less abundant than bare CH_3 .

Other characteristics of the CH_3He_n complexes are found to be similar to those of the IHe_n products. The speed distributions of the escaping CH_3He_n products obtained by performing Abel inversions on the velocity map images could well be described by the same empirical fit function (4.1) used before. These fits provided us with the most probable speed \hat{v} as well as the FWHM of the speed distributions, both of which are illustrated in Figure 4.39 together with the most probable speeds of the “directly” escaping IHe_n complexes. As in the case of the IHe_n products, a high degree of correlation between the most probable speed \hat{v} and the size n of the escaping CH_3He_n complexes is observed. However, the speeds associated with any particular CH_3He_n structure are found to be systematically lower than the characteristic speeds of escaping IHe_n complexes of the same size n . Figure 4.39 shows furthermore that the most probable speeds of the IHe_n and the CH_3He_n complexes become increasingly similar with growing complex sizes n .

The angular distributions of the CH_3He_n product complexes departing from the droplets

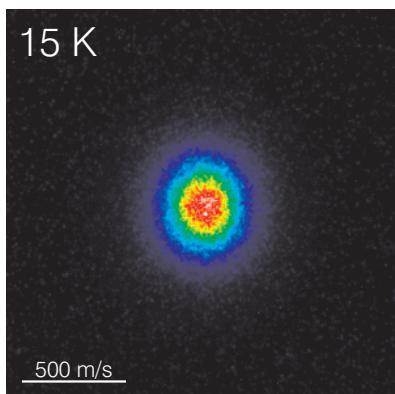


FIGURE 4.40: (Color) Velocity map image of CH_3He_1 products formed by the 266 nm photolysis of CH_3I molecules isolated in the interior of ^4He clusters. The helium stagnation temperature T_o was set to 15 K. The image shows a 300×300 pixel sector and was recorded using an einzel lens voltage $V_{\text{ens}} = 6200$ V and an integration time of one hour. The product complexes were ionized by intense ultrashort 800 nm laser pulses arriving about 50 ns after the UV photolysis pulses in the detection volume.

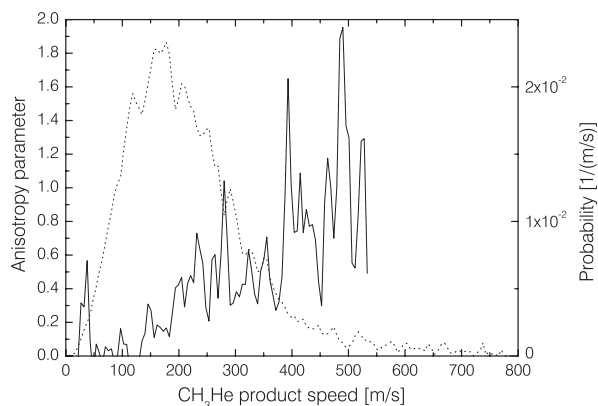


FIGURE 4.41: Anisotropy parameter β of escaping CH_3He_1 complexes as a function of product speed v (solid line, left scale). The graph also shows the corresponding speed distribution (dotted line, right scale). The data was obtained by performing a numerical Abel inversion on the ion image shown in Figure 4.40.

are, similar to those of escaping bare CH_3 , not fully isotropic. As an example we show in Figure 4.40 the recorded velocity map image and in Figure 4.41 the corresponding speed and anisotropy parameter distributions for CH_3He_1 complexes escaping from helium droplets produced at a stagnation temperature of 15 K. Qualitatively, the anisotropy parameter shows a speed dependence similar to those of the bare alkyl fragments analyzed before. While the angular distributions are virtually isotropic at low product speeds, the anisotropy parameter increases in a roughly linear fashion for higher speeds in the droplet frame. Due to the relative low intensity of the $(\text{CH}_3\text{He}_1)^+$ ion image, Figure 4.41 does unfortunately not permit us to verify whether the anisotropy parameter distribution eventually reaches a constant value as observed for the bare alkyl fragments.

4.3.3 Discussion

4.3.3.1 Escape process

Lessons from the speed distributions In order to discuss the nature of the underlying escape process we examine the experimentally observed speed distributions of escaping bare CF_3 , bare CH_3 , and CH_3He_n products in a similar way as the speed distributions of individual departing IHe_n complexes (compare Section 4.2.3.1). Again, it is instructive to use equation (4.3) to crudely convert the most probable speeds \hat{v} of each speed distribution into a translational temperature T . As the said equation may be written as $T = m\hat{v}^2/(2k_B)$, it is

evident that lower translational temperatures T result if the fragment mass m or the most probable speed \hat{v} decrease. Since both bare alkyl fragments as well as the CH_3He_n complexes usually have smaller masses or escape with lower most probable speeds than the most prominent small IHe_n complexes, their translational temperatures T should generally be lower. As a consequence, completely ruling out a thermal escape mechanism should become somewhat more difficult for these products.

In order to carry out a more detailed discussion we focus on our standard helium stagnation temperature $T_o = 15$ K (similar lines of reasoning can be put forward for all other stagnation temperatures studied here). For this typical expansion condition the escaping bare CF_3 fragments exhibit a most probable speed of ≈ 400 m/s (see Figure 4.25) or a translational temperature of ≈ 665 K. For the same mean pure droplet size \bar{N} the escaping bare CH_3 fragments in the vibrational ground state (which in terms of speed and angular distributions is believed to be roughly representative for the *ensemble* of vibrational states formed in the dissociation reaction) exhibit a most probable speed of ≈ 250 m/s (see Figure 4.31) or a translational temperature of ≈ 56 K. With about ≈ 35 K the translational temperature of the departing CH_3He_1 complexes (see Figure 4.41) is even lower. The translational temperatures associated with escaping bare CH_3 radicals in the vibrational ground state as well as with the departing CH_3He_n products thus approach the temperature region of 10^0 – 10^1 K which we believe can be attained by typical ^4He droplets (see page 92). Whereas a thermally driven escape can be ruled out for virtually all departing CF_3 fragments, evaporative processes thus may significantly contribute to the release of bare CH_3 radicals and CH_3He_n complexes from the ^4He droplets. In order to estimate the possible importance of such processes more quantitatively, we examine a thermally excited ^4He droplet at the upper end of the estimated temperature range, *i.e.* at a temperature of 10 K. At this relatively high hypothetical droplet temperature thermally released bare CH_3 fragments should, according to equation (4.3), exhibit most probable droplet frame speeds of about 105 m/s. The inspection of the experimentally observed speed distribution of escaping bare methyl radicals in the vibrational ground state (see Figure 4.31) then clearly shows that a Maxwell-Boltzmann speed distribution with a most probable speed around 100 m/s could potentially account for only some 10 % of the total number of departing fragments. Based on this evidence we conclude that the majority of escaping alkyl fragments must leave the droplets via non-thermal, “direct” escape processes, while a small but significant contribution of thermal processes to the release of CH_3 and CH_3He_n products is possible. From the estimations made above it is evident that the latter processes could only play a major role for particularly slow fragments in the low-speed tail of the CH_3 and CH_3He_n speed distributions.

Lessons from the angular distributions Whereas the high mean anisotropy parameters associated with most of the departing IHe_n complexes enabled us to most certainly rule out thermally driven escape processes, such a global reasoning cannot be made for the escaping bare alkyl fragments and CH_3He_n complexes. As can be seen from the graphs in Figures 4.28, 4.34 and 4.41, a considerable fraction of each of the products considered here escapes with substantially reduced anisotropy parameters close or equal to zero. Unfortunately, the lowest anisotropy parameters occur for the smallest speeds, *i.e.* in a speed region where thermal escape processes may play a role. As a consequence, the anisotropy parameters themselves do not

provide further evidence against a thermal contribution to the release of CH_3 or CH_3He_n products. The strikingly similar *shape* of the $\beta(v)$ function observed for CF_3 , vibrational ground state CH_3 and CH_3He_1 (unfortunately the experimental noise permits only a comparison at relatively low speeds here) suggests however, that the escape of *all* of these products is dominated by the same process which, given the conclusions drawn earlier for the departing CF_3 radicals, should be “direct” escape.

Conclusion Based on the evidence provided by the observed speed distributions we are convinced that the departing bare CF_3 fragments leave the ^4He clusters in virtually all cases via “direct” escape. The experimental evidence for the departing bare CH_3 radicals and CH_3He_n complexes is less conclusive. Both the speed and the angular distributions strongly suggest that the *majority* of each of the latter products leave the droplets via “direct” escape. Nevertheless, thermal, *i.e.* evaporative processes, may possibly cause the departure of some 10 % of these products. The classical Monte Carlo simulations presented in Section 4.6 will confirm the largely “direct” escape of all alkyl radicals.

4.4 Discussion: iodine and alkyl fragments

Having presented the available data on both the iodine and the alkyl fragments we now are in a position to discuss various aspects of the fragment translational dynamics inside liquid helium clusters in conclusion. For the benefit of simplicity we will make the hypothesis that *all* departing reaction products leave the helium droplets via “direct” escape processes. Since possible thermal contributions to the escape of bare CH_3 and the CH_3He_n complexes are estimated to be small, this assumption should constitute a good approximation. Firstly, we will compare the angular distributions of the different escaping reaction products and definitively assess the possibility of angular broadening due to droplet angular momenta. Secondly, we will discuss the influence of the fragment mass on the relaxation of both the kinetic energies and the velocity vectors of the traveling fragments. Thirdly, we will estimate the average *total* kinetic energy transfer ΔE from a particular fragment pair to helium droplets of various mean sizes \bar{N} . This assessment will allow us to answer the question whether the fragments produced from the 266 nm photodissociation of CH_3I or CF_3I in helium droplets are typically traveling through superfluid He II or normal He I above the λ -point. Finally, we will inspect the properties of the escaping CH_3He_n complexes in the light of the simple complex formation model developed in Section 4.2.3.3. Furthermore, we will present possible reasons for the dissimilar intensity of the XHe_n complex progressions associated with different photofragments X.

4.4.1 Angular broadening

We previously suggested three different mechanisms that possibly could explain the loss of structure in the angular distributions of the various departing products studied here (see Section 4.2.3.1). These mechanisms were trajectory deflections inside the droplets, droplet rotation in the laboratory frame and an evaporative fragment release. Having established that thermal escape processes are not likely to play a *major* role in the release of the products studied in

this work, we are left with trajectory deflections and droplet rotations as possible dominant broadening mechanisms and proceed to discuss the likelihood of the latter. Towards this goal let us consider products escaping with a *fixed* speed in the droplet frame, e.g. 200 m/s. Assuming “direct” escape processes, the order of escape times τ of such products should be directly related to their initial speeds. The inspection of the mean initial speeds for which estimates are given in Tables 4.1, 4.4, and 4.6 shows that the relation

$$\tau(\text{CH}_3) < \tau(\text{CF}_3) < \tau(\text{I}) \quad (4.4)$$

should hold. For any given product speed the alkyl fragments thus ought to escape faster than the corresponding iodine products. If droplet rotations were to be primarily responsible for the observed angular broadening, alkyl fragments escaping with 200 m/s should accordingly have angular distributions which are less broadened than those of the corresponding iodine products escaping with identical speed. The anisotropy parameters β at any product speed and for the standard stagnation temperature of 15 K can be inferred from Figures 4.20, 4.21, 4.28, and 4.34 (note that IHe_5 is the most likely product for a speed of 200 m/s). The data shows that for $v = 200$ m/s the relations

$$\beta(\text{CF}_3) < \beta(\text{IHe}_5) \quad (4.5a)$$

and

$$\beta(\text{CH}_3) < \beta(\text{IHe}_5) \quad (4.5b)$$

hold, where equations (4.5a) and (4.5b) refer to CF_3I and CH_3I parent molecules, respectively. Note that similar relations can be established for virtually all other selected speeds v . This finding is the *contrary* of the hypothetical behaviour predicted above. The experimental data therefore is clearly *not* compatible with angular broadening by droplet rotations. As a consequence, *trajectory deflections* in the course of a “direct” product escape from a droplet emerge as the *likely dominant broadening mechanism* for the angular distributions of all products. Further evidence for this finding will come from the simulations presented in Section 4.6.

4.4.2 The role of the fragment mass

The comparison of the results obtained for the three fragments iodine, methyl and fluorinated methyl clearly shows that the fragment mass plays a significant role in determining the loss of kinetic energy and angular structure while moving through the liquid. This is illustrated in Figures 4.42 and 4.43 which show plots of the mean kinetic energies and the mean anisotropy parameters of various escaping products as a function of the product mass. In order to compare the mean kinetic energies and anisotropy parameters, both are displayed as fraction of the dissociation channel averaged mean gas phase values. Both figures show data that was measured at our standard stagnation temperature of 15 K. Note that similar graphs can be established for other mean droplet sizes \bar{N} .

The trends emerging from the figures are evident. A smaller fragment mass leads on average to a larger relative loss of kinetic energy and more smearing in the angular coordinate. As already mentioned in Section 4.2.3.2, the escaping fragments thus show characteristics that in many respects are similar to the predictions of a simple billiard-ball type model. As pointed

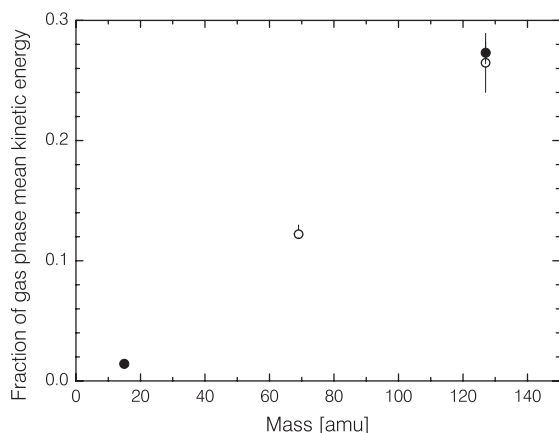


FIGURE 4.42: Mean kinetic energy $\langle\langle T_f \rangle\rangle$ of the escaping products, expressed as fraction of the mean kinetic energy $\langle\langle T_i \rangle\rangle$ associated with the 266 nm photolysis of free parent molecules in the gas phase (compare Tables 4.2, 4.5, and 4.7). The plot shows the ratio $\langle\langle T_f \rangle\rangle / \langle\langle T_i \rangle\rangle$ as a function of fragment mass. Open symbols correspond to products created by the A band photolysis of CF_3I molecules, whereas full symbols indicate products from the 266 nm photodissociation of CH_3I . At the iodine mass of 127 amu we show the mean kinetic energy of *all* IHe_n complexes created. For CH_3 only bare fragments in the vibrational ground state are taken into account as an approximation. The data is given for a stagnation temperature of 15 K.

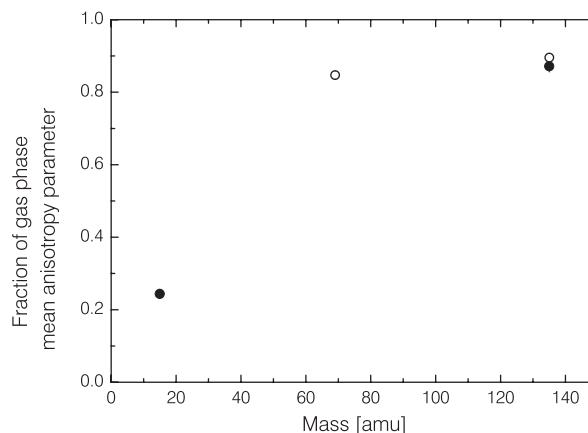


FIGURE 4.43: Ratio of experimentally observed average anisotropy parameters (see Figures 4.20, 4.21, 4.29, and 4.35) to the mean anisotropy parameters $\langle\beta\rangle$ expected for the 266 nm photolysis in the gas phase (see Table 4.3). The anisotropy parameter ratio is shown as a function of the fragment mass. As usually, open symbols denote data obtained from the photodissociation of CF_3I , while full symbols are associated with products from CH_3I parent molecules. Instead of the entire IHe_n progressions we show the data for escaping IHe_2 complexes which are considered to be representative. In case of CH_3 the data refers to bare fragments in the vibrational ground state. The graph shows data recorded at a stagnation temperature of 15 K.

out in Appendix D.2, the mass ratio ϱ of impinging and target particles is a key parameter in such a model. Averaged over the expected distribution of impact parameters both the mean energy loss and the average scattering angle per single collision are exclusively a function of ϱ (see equations (D.10)). The resulting predictions of this hard-sphere scattering model for single collisions of the relevant fragments with initially stationary ^4He atoms are tabulated in Table D.1 and confirm, at least qualitatively, the trends in the experimental data. Encouraged by these findings we have carried out classical Monte Carlo calculations in order to see to what extent quantitative aspects of the experimental data can be reproduced on the basis of such a simplistic description. The results of these calculations are presented in Section 4.6 and will further confirm our characterization of the fragment escape processes as largely “direct”.

4.4.3 Mean total kinetic energy transfer

The average total energy transfer ΔE to droplets of a given mean size may be estimated from the mean kinetic energy $\langle\langle T_f \rangle\rangle$ of the escaping products determined previously (compare Tables 4.2, 4.5 and 4.7). The result of this analysis is given in Table 4.8 for three selected helium stagnation

Parent molecule	T_o [K]	$\langle\langle T_{\text{tot}} \rangle\rangle$ [cm^{-1}]	$\langle\langle T_{\text{f}}(\text{IHe}_n) \rangle\rangle$ [cm^{-1}]	$\langle\langle T_{\text{f}}(\text{CX}_3) \rangle\rangle$ [cm^{-1}]	ΔE [cm^{-1}]	$\Delta E / \langle\langle T_{\text{tot}} \rangle\rangle$ [%]
CF_3I	12	10050	807 (74)	627 (40)	8616 (84)	85.73 (84)
	15	10050	937 (87)	795 (50)	8318 (100)	82.77 (100)
	18	10050	1200 (150)	1383 (100)	7467 (180)	74.30 (180)
CH_3I	12	11900	350 (12)	141 (16)	11409 (20)	95.87 (17)
	15	11900	344 (12)	139 (7)	11417 (14)	95.94 (12)
	18	11900	333 (11)	205 (12)	11362 (16)	95.48 (13)

TABLE 4.8: Mean total kinetic energy transfer ΔE from a pair of created photofragments to helium droplets of selected mean sizes \bar{N} . As always, T_o is the helium stagnation temperature. $\langle\langle T_{\text{tot}} \rangle\rangle$ denotes the total kinetic energy release of the 266 nm photolysis reaction averaged over the two decay channels and is calculated from the values given in Tables 2.6 and 2.7. Depending on the parent molecule, X stands for either a H or a F atom. The mean kinetic energy $\langle\langle T_{\text{f}}(\text{CH}_3) \rangle\rangle$ of escaping CH_3 fragments is approximated by the mean kinetic energy $\langle\langle T_{\text{f}}(\text{CH}_3, v = 0) \rangle\rangle$ of departing vibrational ground state methyl fragments specified in Table 4.7. Moreover, the formation of CH_3He_n complexes is neglected in this analysis.

temperatures T_o and both parent molecules considered in this work. In this approach, fragments that fully transfer their kinetic energy to the droplet and become trapped inside are evidently not taken into account. As we will show in Section 4.5, trapping of fragments does indeed occur, in particular for CH_3I parent molecules. The values ΔE given here represent therefore rather *lower* limits for the actual mean total energy transfer to the liquid. This follows also from the fact that any contribution from the particularly slow CH_3He_n complexes ($n = 1, 2, \dots$) is neglected in our estimations.

It is found that the mean total energy release for CF_3I parent molecules is with ≈ 7500 – 8600 cm^{-1} somewhat smaller than in case of CH_3I parents for which we estimate a mean heat input of $\approx 11400 \text{ cm}^{-1}$. Assuming a rapid dissipation of energy into the droplets, the estimated cluster temperatures in Table 2.1 can be used to show that energy releases of this magnitude should heat the smaller droplets produced at stagnation temperatures of 15 and 18 K on average *above* the λ -point. Only the largest droplets considered here ($T_o = 12 \text{ K}$) should typically remain colder than $T_\lambda \approx 2.18 \text{ K}$ throughout the fragment escape process. For stagnation temperatures $T_o \gtrsim 14 \text{ K}$ escaping fragments thus should typically probe *normal fluid* helium droplets, at least in the last part of a “direct” escape process.

4.4.4 Complex formation

The speed distributions observed for the departing CH_3He_n complexes may be used to further discuss our basic model for complex formation inside the liquid helium droplets which was introduced in Section 4.2.3.3. For this reason we focus again on the plot of the most probable speeds of escaping CH_3He_n and IHe_n complexes shown in Figure 4.39. The plot seems to suggest that the most probable speeds of all fragment– He_n complexes converge to a similar and finite asymptotic value around 50 m/s for large product sizes n . Unfortunately, no conclusive evidence for such a behaviour could be obtained experimentally, since the acquisition of high-quality ion im-

ages for large complexes with sizes $n \gtrsim 10$ is severely impaired by the extremely low intensities associated with those products. We note, however, that only the most probable *speeds* of both the escaping IHe_n and the CH_3He_n products seem to approach a similar asymptotic value. Due to the different masses of the iodine and methyl radicals, a similar convergence occurs neither for the momentum nor for the kinetic energy associated with the complexes unless infinitely large complex sizes are considered.

These results are in qualitative agreement with the predictions of our basic model. We suggested previously that the *interaction* of an additional helium atom with a preexisting complex as well as the *relative speed* of this structure with respect to the helium environment determine to a large extent the actual mean size n of a fragment- He_n complex traveling through the liquid environment. Calculations on the structure and energetics of small doped helium clusters involving both atomic²³⁰ and molecular^{78,228,229} dopant species predict the first solvation shell around an impurity to close once a complex size of more than about $n = 15$ –25 helium atoms is reached. Since the completion of this innermost solvation shell can be expected to largely reduce the effect of the impurity on the binding energy of any additional helium atom, the characteristic speeds should become largely independent of the fragment species in precisely this size range, which is supported by our experimental data. Based on the observed differences in the characteristic speeds of complexes containing the same number n of helium atoms, we note furthermore that our model predicts the CH_3 -He interaction to be appreciably weaker than the I-He interaction. Unfortunately, we are not in a position to cross-check this result, since, to the best of our knowledge, no independent data on these potentials is available yet.

The latter result is, however, to be treated with care since a *molecular* photofragment like CH_3 should introduce a number of complications. Firstly, the internal degrees of freedom of such a species may couple to the vibrational modes of an existing complex structure and could therefore ultimately revoke the attachment of helium atoms. This effect should shift any emerging complex size distribution towards smaller sizes n which, as a consequence, should result in *smaller* most probable speeds for each escaping complex. At this stage it cannot be excluded that such an effect is, at least partially, responsible for the observed most probable speeds of the departing CH_3He_n complexes. We will come back to this point in the next paragraph. Secondly, the geometry of the fragment may, at a given relative speed, influence the probability of permanent binding to a helium atom, since certain binding sites may be particularly protected from or exposed to the impinging helium flow. For instance, a number of binding sites with a strongly attractive fragment-He pair potential may not guarantee high characteristic complex speeds if helium atoms bound to these sites are particularly likely to undergo collisions with helium atoms of the bath liquid. Again, such an effect may play a role in determining the most probable speeds seen for the CH_3He_n complexes.

Another important aspect of the complex formation in the aftermath of photodissociation reactions in helium droplets is the strongly varying *intensity* of the fragment- He_n progressions in the mass spectra. While iodine atoms have been shown to leave the droplets on average with some helium atoms attached, CH_3 fragments display only a relative weak CH_3He_n progression, and CF_3 radicals have only been detected as bare, fully unsolvated particles. We will focus on the difference between CH_3 and CF_3 which is particularly intriguing. This difference may be explained using the simple complex formation model proposed earlier. Assuming that the

interaction of both alkyl fragments with helium is similar, the characteristic speeds found for the CH_3He_n products (see Figure 4.39) should approximately also apply to any hypothetical CF_3He_n complexes. The CF_3 radicals, however, depart from the droplets with speeds that on average are considerably higher than the speeds associated with any of the CH_3He_n structures ($n = 0, 1, \dots$). In particular, the CF_3 speeds are in most cases more elevated than 180 m/s which is approximately the most probable speed for escaping CH_3He_1 products at a stagnation temperature of 15 K. One may therefore argue that CF_3He_1 complexes should be formed with a much lower probability than CH_3He_1 products, and, as a consequence, could not be detected in our experiments.

Alternatively, the observed differences between the CH_3 and CF_3 radicals may also be accounted for considering the internal energy distribution of the nascent fragments. As suggested above, we will assume for this purpose that internally excited fragments inside a previously formed helium solvation shell can relax vibrationally or rotationally and thereby cause the detachment of helium atoms. Such internal relaxation processes may, in principle, occur before or after the complexes leave the finite-size cluster. While in the former case only a temporary destruction of the complex structure is to be expected, the latter process should permanently remove helium atoms from the departed van der Waals complexes. In any case, a non-destructive “direct” complex escape only is ascertained for fragments in the vibrational and rotational ground state. As can be inferred from Tables 2.6 and 2.7, CF_3 fragments produced by the 266 nm A band photolysis reaction are expected to carry, on average, a considerably higher amount of internal energy than CH_3 radicals. More importantly, the probability of creating alkyl fragments in the vibrational ground state by a 266 nm photolysis reaction is considerably lower for CF_3I than for CH_3I .^{145,162} Similarly, rotationally unexcited alkyl fragments are less likely to be formed in the photolysis of CF_3I , as the rotational constants of CF_3 are much lower than those of CH_3 . If non-radiative vibrational or rotational relaxation of these radicals in the interior of small complexes does indeed play a role, non-destructive escape processes should thus be more likely for CH_3 fragments and may hence be responsible for the appearance of the CH_3He_n progression. In case of CF_3 it thus appears possible that some CF_3He_n complexes form *temporarily* and subsequently disintegrate as a consequence of the mentioned internal relaxation processes. As indicated above, the decay of some of such metastable structures could possibly occur *after* departing from the droplets and before the ionization laser pulses arrive in the detection volume, since “direct” escape (≈ 10 ps) and detection (≈ 10 ns) are typically separated by three orders of magnitude in time. In order to elucidate this possibility, it is desirable to carry out pump-probe experiments with higher time resolution. This can be done using the femtosecond laser system in our laboratory, since UV photolysis pulses may readily be obtained by frequency-tripling the 800 nm IR pulses delivered by the system. Work in this direction is currently under way.

4.5 Recombination

In this section we examine the possibility of fragment recombination in the aftermath of the 266 nm photodissociation of CH_3I and CF_3I in the interior of liquid ^4He droplets. Given the high average kinetic energy losses experienced by the escaping photolysis products (see

Tables 4.2, 4.5 and 4.7), some of the fragments can be expected to completely lose their excess kinetic energy and to translationally thermalize inside the cluster they were born into, in particular for the largest mean droplet sizes studied in this work. As already suggested in the introduction to this chapter, one therefore may think about recombination as a process that can follow if *both* photofragments from the same parent molecule transfer virtually all their kinetic energy to the environment *before* they reach the droplet surface and escape into the gas phase.

Let us consider such an entirely “caged” dissociation event in more detail. As specified in Table 4.8, the mean total kinetic energy release $\langle\langle T_{\text{tot}}\rangle\rangle$ of the 266 nm photolysis reaction amounts to 10000–12000 cm^{-1} , depending on the parent molecule. Even if a possible internal cooling of the fragments is neglected, such an energy input should substantially heat-up and may even completely evaporate some ^4He clusters in the size range under study here. If a helium cluster survives this initial heat input, however, the pair of spatially separated photofragments is likely to remain solvated in the same droplet^g. Due to the attractive dispersion interactions the two radical solutes should then approach again and may ultimately recombine, thereby giving rise to an additional heat release which will be discussed more profoundly in the next paragraph. It is important to note that the evaporation of helium atoms ($\approx 10^{-9}$ – 10^{-7} s, see Section 2.2) and the mutual approach of the fragments ($\approx 10^{-10}$ – 10^{-8} s, see reference [19]) presumably take place on similar time scales and therefore should generally *not* be thought of as sequential processes. Moreover, we stress that due to the full translational cooling of the fragment pair, a recombined parent molecule cannot be expected to bear any signature of the original vector correlation between the polarization of the photolysis laser and the fragment velocity.

The recombination dynamics of both molecules studied here are expected to depend strongly on the electronic excitation of the iodine fragments. For spin-orbit excited iodine recombination occurs on the 3Q_0 electronic surface of the parent molecule which is characterized by a shallow potential well (see Figure 2.19) with a depth of about 1700 cm^{-1} .^{166,249} From this electronic surface the recombined molecule may relax to vibrationally excited levels of the electronic ground state via radiative or non-radiative processes. Fluorescence spectra of recombined CH_3I and CD_3I in rare gas matrices²⁴⁹ indicate that the radiative relaxation from the 3Q_0 surface gives rise to a substantial excitation of the C–I stretch vibration around $v = 37$. Although the fluorescence lifetime of this transition is not known exactly, an upper limit of ≈ 5 ns has been established experimentally.²⁴⁹ Spin-orbit unexcited iodine fragments, on the other hand, can recombine with the alkyl fragments directly on the potential energy surface of the electronic ground state. Recombination events involving both spin-orbit states of iodine thus are expected to produce temporarily vibrationally highly excited parent molecules in the electronic ground state which can cool further by transferring vibrational energy to the liquid environment. In any case, the total heat release of a recombination process is limited by the energy of the 266 nm photolysis photon, that is about 37600 cm^{-1} . Any radiative transition involved in the internal relaxation reduces, however, the actual heat input into the droplet.

An inspection of Figure 2.19 and Tables 2.6 and 2.7 shows that the internal cooling of a

^gAnother hypothetical possibility is a thermally driven release of fragments during the evaporative cooling process. The analysis of the data on iodine and alkyl fragments undertaken in Sections 4.2 and 4.3 has shown that such processes certainly are of minor importance compared to the dominant “direct” escape of reaction products. The possibility of an evaporative fragment release could, however, not be fully excluded.

recombined parent molecule leads to a second heat release into the surrounding droplet that can be larger than the preceding heat input due to the complete translational relaxation of the nascent photofragments. As can be seen qualitatively from Table 2.1, a total heat release of this scale will in many cases lead to a complete evaporation of the droplet. Accordingly, recombination events should frequently yield bare, unsolvated parent molecules with isotropic angular distributions and thermal kinetic energies in the droplet frame. Since some droplets may even survive this second heat release, the signal of bare parent molecules can, however, not be expected to fully reflect all recombination events. In this context it is instructive to examine the likely product distribution from recombination processes in ^4He droplets as suggested by the picture described above. While bare recombined molecules R may be produced by *any* heat release exceeding the energy required to completely evaporate all helium atoms in the cluster, product complexes RHe_n of a certain size $n \geq 1$ should only be created for a relatively *specific* heat input. If recombination occurs and the accompanying heat release is sufficiently high to completely evaporate at least some of the droplets, this picture therefore predicts the signal intensity of bare recombined molecules R to vastly exceed the intensity of any individual RHe_n complexes. This reasoning is supported by the velocity map images of IHe_n products from the dissociation of CH_3I in helium droplets shown in Figure 4.9 which give the first evidence for the occurrence of recombination processes. While additional signal from droplet-born CH_3I molecules appears in the IHe_4 image, no evidence for CH_3IHe_n complexes with $n \geq 1$ is found in the IHe_{4+n} images, although the mass difference is identical. Compared to the size distributions of the “directly” escaping IHe_n product complexes presented and discussed in Section 4.2, the size distribution of the recombination products therefore is strikingly different. Whereas the escape of bare iodine fragments from helium clusters is relatively unlikely, recombination processes in droplets seem to favor the formation of unsolvated parent molecules.

Consequently, we have systematically recorded velocity map images of bare parent ions. Experimentally, this is readily accomplished by gating the gain of the MCP detector on the parent mass, *i.e.* 142 amu for CH_3I and 196 amu for CF_3I . Due to their small mass difference, the product ions $(\text{CH}_3\text{I})^+$ and $(\text{IHe}_4)^+$ from the dissociation of solvated CH_3I have a similar time-of-flight and cannot be fully separated without losing signal. For the CH_3I parent we therefore intentionally used a somewhat wider detector gate to record images containing the signal from *both* products. This approach permits a convenient comparison of “direct” escape and recombination signals in a single image and, as it will become clear below, allows us to deduce important properties of the recombination process. Similar to the IHe_n progression studied in Section 4.2 we used intense ultrashort 800 nm laser pulses to non-resonantly ionize the reaction products. As usually, the parent molecules were introduced into the droplets by cross beam scattering using the backing pressures specified in Table 3.4.

4.5.1 Droplet size effects

Velocity map images of the parent ions recorded using a *fixed* time delay $\Delta t = 50$ ns between UV dissociation and IR ionization laser pulses are shown in Figures 4.44 and 4.45. In order to illustrate droplet size effects we present results for various helium stagnation temperatures T_o that, according to Table 2.2, can be associated with different mean droplet sizes \bar{N} .

For both CH_3I and CF_3I the recorded images show background structures which are easily

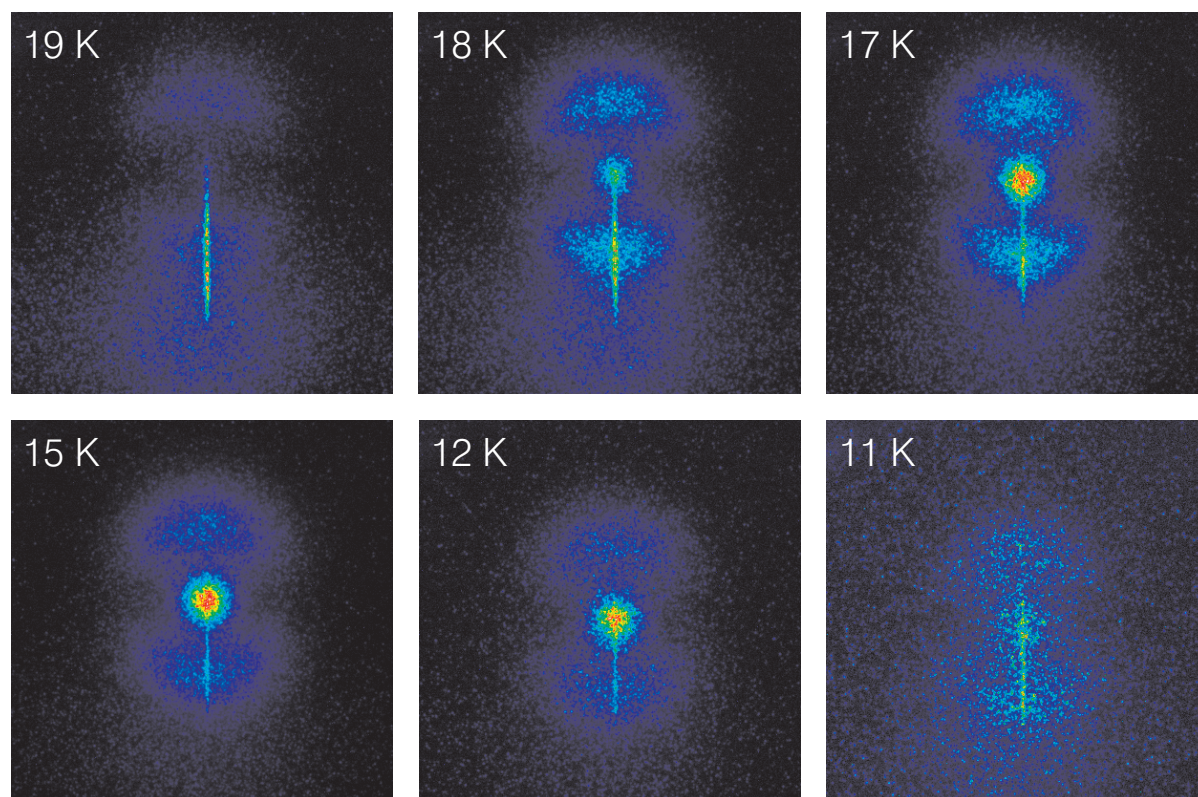


FIGURE 4.44: (Color) Velocity map images of CH_3I molecules in the detection volume of the ion imaging setup. The images were recorded using an einzel lens voltage $V_{\text{lens}} = 6200$ V and an integration time of one hour. The time delay between UV dissociation and femtosecond ionization pulses was set to 50 ns. Each picture shows a 400×400 pixel sector centered about the the same point as the sector defined in Figure 4.7. Note that the images equally contain signal from escaping IHe_4 fragments whose mass differs by only one amu from the mass of CH_3I . The indicated temperatures denote the helium stagnation temperature T_o .

attributed to the ionization of undissociated parent molecules in the background gas as well as in the effusive beam emerging from the doping chamber (compare Section 3.4.1). Since the ionization process is not accompanied by a kinetic energy release, the velocity map images reflect directly the laboratory frame velocities of these neutral alkyl iodide molecules. Randomly propagating residual gas species therefore are imaged as a “blob” without angular structure. This blob is centered about the origin of the imaging setup and appears close to the bottom of the selected sectors illustrated here. The directional flow of the effusive beam, however, is characterized by a highly anisotropic velocity distribution. The ionization of parent molecules in the effusive beam thus gives rise to the easily recognizable vertical streak in the velocity map images, the center of which is substantially displaced with respect to the origin of the setup.

If CH_3I is used as dopant species, an isotropic signal with $\beta = 0 \pm 0.1$ is observed in addition to the background structures described above. Based on the characteristic displacement on the detector this structure is readily identified as a CH_3I recombination signal. As expected, the

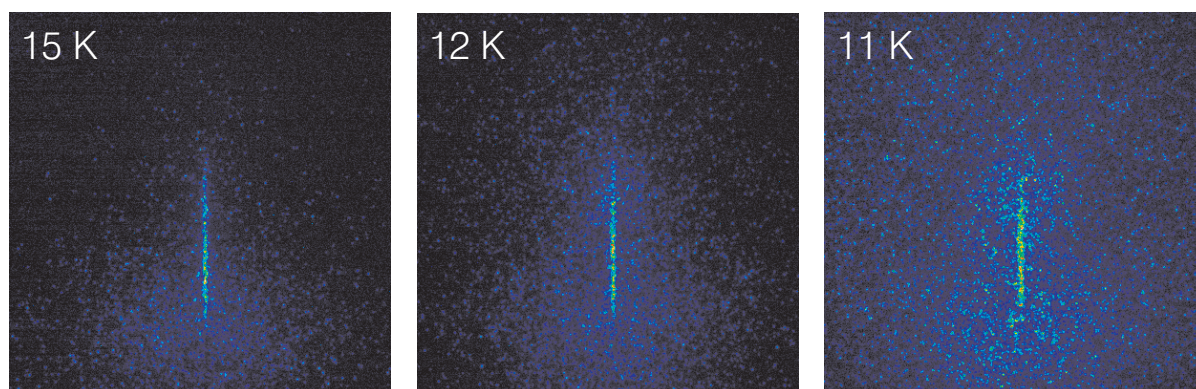


FIGURE 4.45: (Color) Velocity map images of CF_3I molecules in the detection volume of the ion imaging setup. The images were recorded using an einzel lens voltage $V_{\text{ens}} = 6200$ V and an integration time of 15 minutes. The time delay Δt between UV dissociation and femtosecond ionization pulses was set to 50 ns. Each picture shows a 400×400 pixel sector centered about the the same point as the sector defined in Figure 4.7. The indicated temperatures denote the helium stagnation temperature T_o .

structure gives evidence of a finite kinetic energy release and shows no significant angular structure. Although practically absent for the smallest mean droplet size produced at $T_o = 19$ K, the recombination signal grows substantially in strength as the mean droplet size is increased. For large droplets produced at $T_o < 15$ K, however, the signal fades somewhat and is hardly perceivable in the poor-quality image at $T_o = 11$ K.

The inspection of Figure 4.45 reveals that in contrast to CH_3I no significant recombination signal appears in case of CF_3I -doped droplets, regardless of the stagnation temperature. Since recombination only is possible if neither of the two photofragments escape into the gas phase, this result demonstrates vividly that the probability for trapping *both* photofragments from CF_3I inside a ^4He droplet of given size is *significantly lower* than in case of CH_3I parent molecules.

One should however bear in mind that these measurements do *not* permit completely ruling out photofragment recombination for CF_3I parent molecules. Due to the detection technique a recombination signal only results if the accompanying heat release leads to a complete evaporation of the helium droplet. In the limit of very large helium clusters the detection probability therefore should be low, although trapping and recombination are likely for both parent molecules. This interpretation is substantiated by the weak recombination signal seen for CH_3I at the low helium stagnation temperature of 11 K. Similarly, recombination of CF_3I in droplets of comparable mean size \bar{N} may not result in a bare ion signal.

Further details of the CH_3I recombination process can be deduced from the speed distributions. For this reason we performed Abel inversions on the ion images shown in Figure 4.44 and slightly corrected the resulting speed distributions for detector background as described in Section 3.5.7. Since the lower part of the images contains contributions from the background gas and the effusive beam, only the the upper half of the images was processed. As an example we show in Figures 4.46 and 4.47 the resulting speed distributions for the helium

stagnation temperatures T_o of 18 and 15 K, respectively. The simultaneous detection of both $(\text{CH}_3\text{I})^+$ and $(\text{IHe}_4)^+$ ions clearly gives rise to two overlapping contributions in speed space which may be disentangled by means of suitable analytical fit functions. As demonstrated before, the contribution of the “directly” escaping IHe_4 fragments can be fitted to the function (4.1) whose parameters v_c and σ are well known from the analysis in Section 4.2. The speed distribution of the recombined CH_3I molecules, however, is found to follow approximately a Maxwell-Boltzmann distribution

$$P_s(v) = B \sqrt{\frac{2}{\pi}} \left(\frac{m}{k_{\text{B}}T} \right)^{\frac{3}{2}} v^2 \exp \left(-\frac{mv^2}{2k_{\text{B}}T} \right), \quad (4.6)$$

where m denotes the mass of the molecules, while the amplitude B and the translational temperature T are fit parameters. Fitting the total speed distribution as shown in Figures 4.46 and 4.47 therefore requires the optimization of three parameters, namely the amplitudes A and B of the two contributions and the translational temperature T of the recombination signal. Following a successful fitting procedure the relative contribution of the recombination signal to the total ion signal can be retrieved by simply calculating the ratio $B/(A+B)$.

The fit results for various stagnation temperatures T_o are illustrated in Figures 4.48 and 4.49. Figure 4.48 shows the estimated contribution of the recombination signal to the total detected ion signal. As already seen from the images, the recombination signal is small for $T_o = 19$ K, but grows substantially relative to the IHe_4 contribution as the mean droplet size is increased and reaches a peak value at $T_o = 15$ K. For larger helium clusters the relative contribution of the recombination signal decreases slightly. Since, as discussed before, the probability of trapping and recombination should grow if the mean droplet size is increased, this effect is thought to reflect incomplete evaporation in the aftermath of recombination events in those large droplets.

We focus on the data point at $T_o = 15$ K to illustrate the small magnitude of the recombination signal in comparison to the total intensity of all “directly” escaping IHe_n products ($n = 0, 1, 2, \dots$). At this stagnation temperature the IHe_4 complexes are found to account for about 11.6 (4) % of the total intensity in the IHe_n progression (compare Figure 4.6). Accordingly, the recombination signal at $T_o = 15$ K carries only 4.9 (2) % of the integrated intensity of the IHe_n progression from the photodissociation of CH_3I . Since only bare CH_3I molecules are detected, recombination events without complete evaporation of the droplet are, however, not included in this value.

As can be inferred from Figure 4.49, the average translational temperatures of the recombined molecules reach values around 25 K and stay remarkably constant over the full range of helium stagnation temperatures studied. The fact that those temperatures are way above the droplet equilibrium temperature of about 0.4 K strongly suggests that the recombined parent molecules acquire their kinetic energy indeed as a consequence of a complete evaporation of the surrounding helium atoms as suggested above. The insensitivity of the translational temperature to the mean cluster size \bar{N} may be explained as a result of two counteracting effects. Compared to smaller droplets, larger helium clusters are characterized by a higher heat capacity and thus should yield translationally colder recombined molecules in case of complete droplet evaporation. On the other hand, bigger helium clusters are increasingly likely not to evaporate completely which can be expected to reduce the ion signal of molecules with particularly

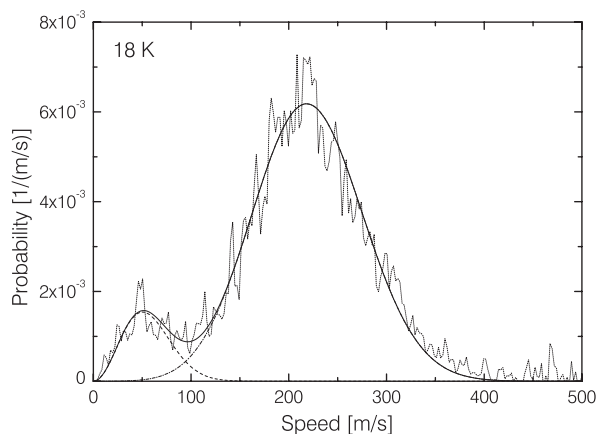


FIGURE 4.46: Experimentally observed speed distributions of both recombined CH_3I molecules and “directly” escaping IHe_4 complexes at the stagnation temperature $T_o = 18$ K. The recombination signal is fitted using a Maxwell-Boltzmann distribution (dashed line). The speed scale has been calculated for the parent mass of 142 amu.

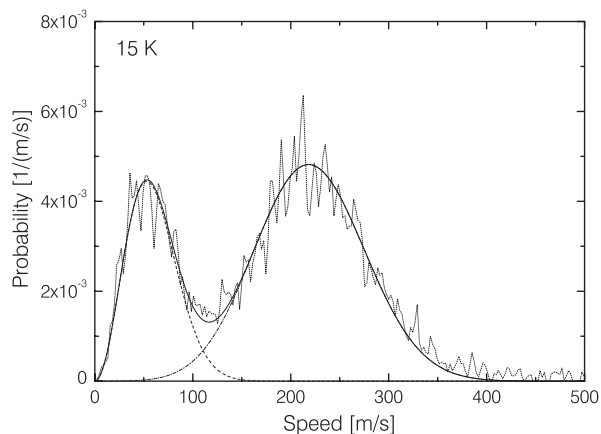


FIGURE 4.47: Experimentally observed speed distributions of both recombined CH_3I molecules and “directly” escaping IHe_4 complexes at the stagnation temperature $T_o = 15$ K. The recombination signal is fitted using a Maxwell-Boltzmann distribution (dashed line). The speed scale has been calculated for the parent mass of 142 amu.

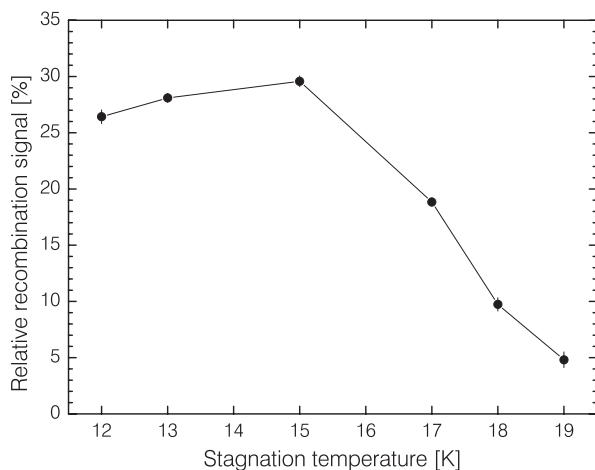


FIGURE 4.48: Contribution of the recombination signal to the total detected ion signal as a function of the stagnation temperature T_o .

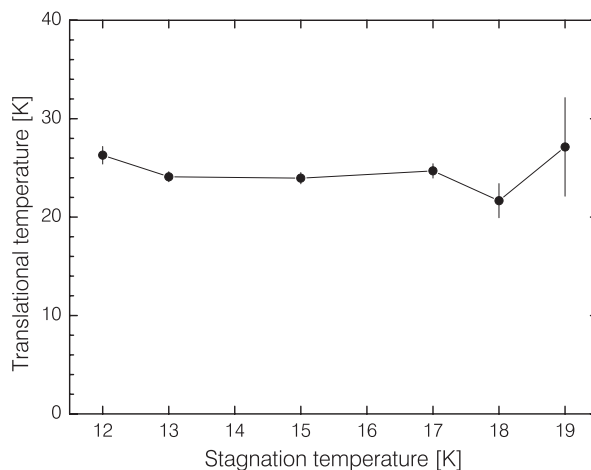


FIGURE 4.49: Translational temperature of the recombination signal as a function of the stagnation temperature T_o .

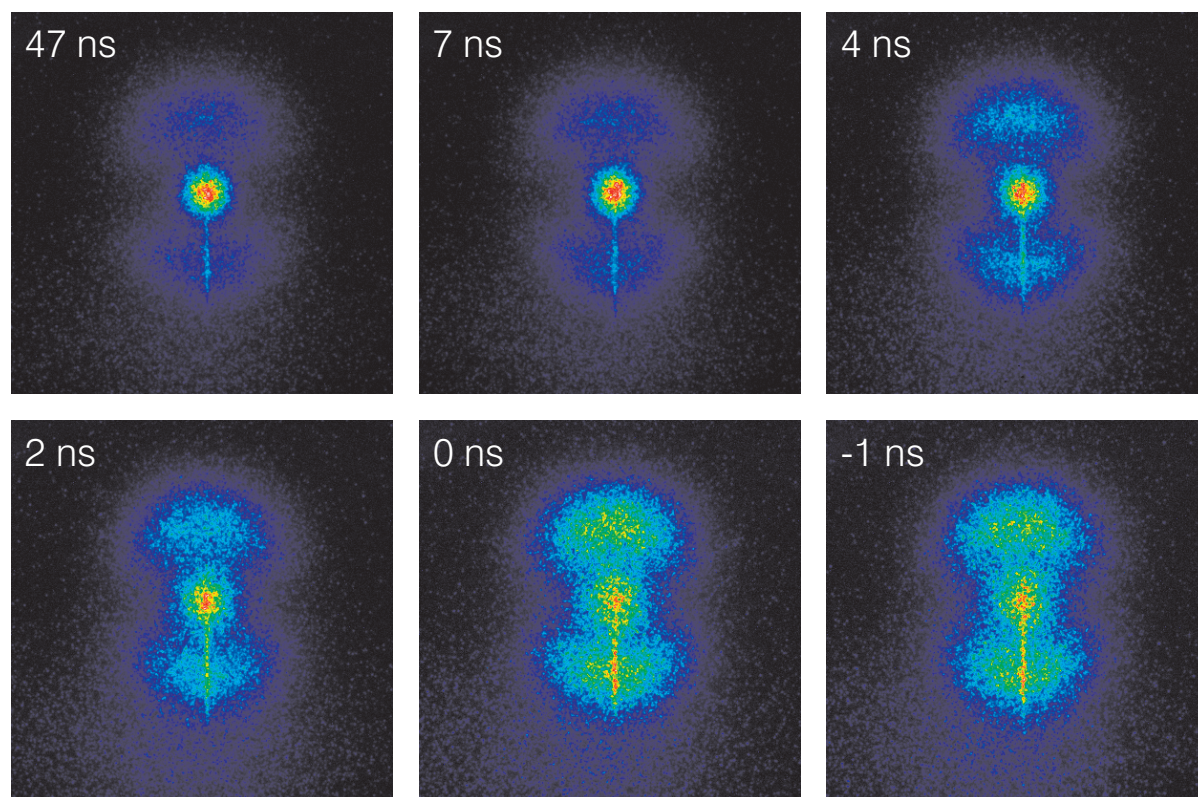


FIGURE 4.50: (Color) Change of the CH_3I recombination signal with the time delay Δt between UV photolysis and femtosecond ionization laser pulses. The images were recorded using an einzel lens voltage $V_{\text{lens}} = 6200$ V and an integration time of one hour. The helium stagnation temperature was fixed at $T_o = 15$ K. Each picture shows a 400×400 pixel sector centered about the the same point as the sector defined in Figure 4.7. The time delay between UV dissociation and femtosecond ionization pulses is indicated in the upper left corner of each image.

low translational temperatures. Together these two effects may cancel out each other to some extent.

4.5.2 Time dependence

As a complement to the droplet size dependence we have studied the dependence of the CH_3I recombination signal on the time delay Δt between nanosecond UV photolysis and femtosecond IR ionization pulses. These studies were carried out at a constant helium stagnation temperature of $T_o = 15$ K, *i.e.* for a fixed mean droplet size \bar{N} . Figure 4.50 illustrates the measured velocity map images for numerous time delays Δt which, as always, refer to the chronological distance between the pulse centers. It can be seen that the ratio between recombination and escape signal changes in favor of the “directly” escaping IHe_4 complexes as the ionization laser is fired earlier. Simultaneously the recombination signal grows broader thereby indicating higher translational temperatures of the formed CH_3I molecules. Naturally, both effects appear also prominently

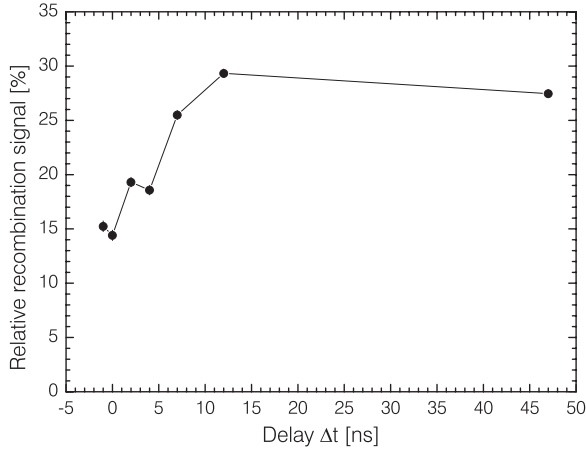


FIGURE 4.51: Contribution of the recombination signal to the total ion signal as a function of the time delay Δt between nanosecond photolysis and femtosecond ionization pulses. The helium stagnation temperature was set to 15 K.

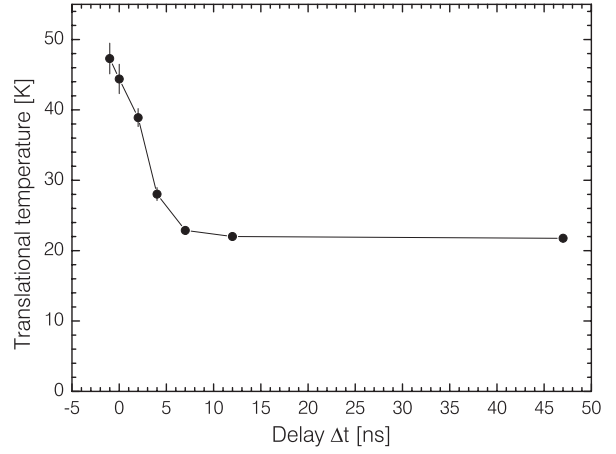


FIGURE 4.52: Translational temperature of the recombination signal as a function of the time delay Δt between nanosecond photolysis and femtosecond ionization pulses. The helium stagnation temperature was kept at $T_o = 15$ K.

in the corresponding speed distributions. These distributions were obtained in the same way as described in the previous section. Again, the relative contribution of the recombination signal and its translational temperature were found by fitting the total speed distribution with the analytical functions introduced above.

The results of this analysis are shown in Figures 4.51 and 4.52. From the plot of the relative recombination signal in Figure 4.51 it becomes obvious that recombined parent molecules and IHe_4 complexes are formed on *different time scales*. Whereas the IHe_n products have previously been estimated to escape typically within about 10 ps from the droplets, the signal of bare parent ions attributed to recombination processes appears with a time constant of about 5 ns. A similar time constant is found for the decrease of the parent molecule translational temperature with increasing time delay Δt depicted in Figure 4.52.

It is important to bear in mind that the time resolution of these experiment is somewhat impaired by the duration of the 266 nm photolysis pulses which typically have a width (FWHM) of 5–6 ns. Compared to the broad UV pulses, the femtosecond ionization laser pulses can be considered as infinitely sharp. Consequently, the delay-dependent ion signals $S_R(\Delta t)$ and $S_E(\Delta t)$ corresponding to the recombined CH_3I molecules and the “directly” escaping IHe_4 complexes, respectively, may both approximately be written as

$$S(\Delta t) = \int_{-\infty}^{\Delta t} d\tau \int_{-\infty}^{+\infty} dt f_{\text{uv}}(\tau - t) \cdot f_{\text{form}}(t) , \quad (4.7)$$

which involves a convolution of the UV laser pulse envelope f_{uv} (centered around the origin) with the distribution of product formation times f_{form} . The latter is, of course, product-specific and can in case of IHe_4 be regarded as the distribution of escape times. Despite the complexity of these signals it becomes obvious that identical distributions f_{form} would inevitably lead to

a *constant* ratio $S_R(\Delta t)/S_E(\Delta t)$, in clear contrast to the experimental results. Calculations based on realistic IHe₄ formation times around 10 ps show furthermore that the observations may only be reproduced if the typical time scale for the production of bare recombined CH₃I molecules is indeed about 5 ns.

In order to explain this time constant it is instructive to elucidate the time scales of the processes involved in producing the translationally excited, bare parent molecules observed in the velocity map images. These processes include parent dissociation, translational relaxation and, subsequently, mutual approach of the fragments, vibrational and, if spin-orbit excited iodine fragments are involved, electronic relaxation of the recombined molecules as well as the evaporation of the surrounding helium atoms.

With about 100 fs^{152,153} the dissociation lifetime of both parents is clearly way too short to be of relevance here. The same holds for the time constant for complete translational relaxation of the fragments. Based on the typical escape time scale of about 10 ps for the IHe_n products we crudely estimate that a fragment definitely becomes trapped on a time scale of about 100 ps which again is too short to be a significant factor for the time dependence discussed here. The other processes mentioned above, however, may take place on time scales of the order of nanoseconds and therefore may all contribute to the time constant of 5 ns. We therefore will discuss the possible effects of these processes in more detail.

As shown in Section 2.2 the *evaporation* of helium atoms from the surface of a droplet occurs typically on a time scale of 10^{-9} to 10^{-7} s and therefore has to be considered here. The complete translational cooling of the fragment pair constitutes a roughly constant energy input to any droplet and generally is fast compared to the evaporation processes. Due to their higher heat capacity (compare Table 2.1) larger droplets thus are heated to lower initial temperatures before evaporation commences significantly. Since the evaporation rates grow with increasing droplet temperature (see equation (2.3)), larger droplets ought to show lower evaporation rates while, compared to small helium droplets, more helium atoms have to be lost in order to entirely evaporate the clusters. Consequently, we expect the bare parent signal from larger droplets to appear with a longer time constant and to show less kinetic energy release. As this is in full qualitative agreement with the time-dependencies shown in Figures 4.51 and 4.52, evaporative processes alone may account for the observations.

Similarly, the time associated with the *mutual approach* of the trapped fragments inside the ⁴He droplets may explain the observed effects. The time scale of this process is expected to be similar to the time scale of coagulation for successively picked-up impurities in a scattering cell. Based on the long range dispersion forces and frictionless motion this time scale can be estimated as 10^{-10} to 10^{-8} s.¹⁹ Since the kinetic energy loss preceding the mutual approach of the fragments will in many cases heat the ⁴He droplets temporarily to temperatures above the λ -point, it is reasonable to include friction effects. Considering the viscosity of normal helium⁸ at 3.5 K of $\eta = 3.5 \cdot 10^{-6}$ kg m⁻¹ s⁻¹ the previously mentioned times are found to increase by more than one order of magnitude,¹⁹ resulting in approach time scales of the order of at least nanoseconds. Since larger droplets permit the fragments to explore greater mutual distances without escaping from the ⁴He clusters, the approach time scale is expected to grow with droplet size. As stated before, larger droplets are expected to yield translationally cooler impurities upon complete evaporation which establishes the required correlation between approach time

and the translational temperature of the released parents. Consequently, the finite approach time may solely give rise to the observed time-dependent phenomena.

Another explanation for the time dependence of the CH_3I recombination signal and its translational temperature is related to the *electronic relaxation* of the recombined parent molecules in the 3Q_0 state. To the best of our knowledge the fluorescence life time of this transition has not yet been determined exactly, but an upper limit of ≈ 5 ns has emerged from dissociation experiments in solid rare gas matrices.²⁴⁹ Given that the 266 nm photolysis of CH_3I yields mostly spin-orbit excited iodine (see Table 2.6), this fluorescence step may well be dominant in determining the overall time scale for the appearance of bare parent molecules. In this context it seems worthwhile to mention again that a significant collisional quenching of the spin-orbit excited $^2P_{1/2}$ state of the iodine radical does not seem likely, as experiments in the gas phase have established a relaxation probability of less than 10^{-8} per collision.^{247,248} As a consequence, the decrease of the translational temperature with increasing time delay between the laser pulses may be explained by the different total heat release associated with recombination events on the 3Q_0 and, alternatively, on the electronic ground state potential energy surface. For an equal degree of vibrational relaxation in the electronic ground state this difference corresponds to the energy of the fluorescence photon²⁴⁹ of about 11000 cm^{-1} . Recombination on the ground state surface therefore should be associated with a substantially higher heat release and more elevated translational temperatures of the unsolvated CH_3I molecules formed in the process. If the fluorescence is indeed the time limiting step, the early ion signal can be expected to stem from ground state recombination and therefore should be translationally warmer. In absence of electronic relaxation of spin-orbit excited iodine fragments in liquid ^4He , ground state recombination is however a minority process and should therefore only give rise to a relatively weak signal. At long delay times the ion signal then should be dominated by recombination on the 3Q_0 surface and therefore is predicted to be translationally colder, which is in agreement with the experimental results. One of the open questions is, however, whether the thermally excited ^4He droplets may allow for a significant degree of non-radiative relaxation of the 3Q_0 state. In any case, the significance of radiative electronic relaxation for the recombination time constant may be tested by performing dissociation experiments with a different photolysis wavelength. As discussed in Section 2.5, using longer photolysis wavelengths should increase the quantum yield ϕ in the CX_3+I product channel (2.42a). As ϕ approaches unity, the observed time-dependencies should gradually disappear.

4.5.3 Discussion

We have investigated photofragment recombination following the 266 nm A band dissociation of alkyl iodides in liquid ^4He clusters by velocity mapping bare parent ions. In the case of CH_3I -doped clusters, these ion images reveal unsolvated parent molecules with an isotropic speed distribution in the droplet frame and a translational temperature of about 25 K. Following the reasoning presented at the beginning of this section, this ion signal is interpreted as a recombination signal resulting from a complete evaporation of the helium solvent. Moderately time-resolved experiments show that this recombination signal appears with a time-constant of ≈ 5 ns.

These imaging experiments shed light on remarkable differences between our two model

systems. While the images of $(\text{CH}_3\text{I})^+$ cations reveal a clear recombination signal once the helium stagnation temperature is lowered to $T_o \lesssim 18$ K, *i.e.* once the mean droplet size \bar{N} becomes larger than about 3000 atoms, no evidence for recombination of CF_3I is found in the whole droplet size range $\bar{N} \approx 2000$ -20000 atoms investigated here. Similar to the relaxation of both the anisotropy and the kinetic energy of the various photofragments, this result may be rationalized in terms of the basic billiard-ball type model suggested earlier and described mathematically in Appendix D.2. Considering both the mean initial kinetic energy $\langle\langle T_i \rangle\rangle$ of the various fragments and their mass ratio ϱ to ^4He atoms^h, one may categorize the fragments into three qualitatively different regimes. Due to their comparable and relatively large masses, both CF_3 and iodine from the 266 nm photodissociation of CF_3I may be regarded as prototypical “large $\langle\langle T_i \rangle\rangle$ –large ϱ ” particles. The high mass ratio ϱ ensures that the average relative kinetic energy loss per collision is small. Moreover, the high initial kinetic energy places these photofragments far away from thermal equilibrium. Together, these two properties should largely impede a complete translational thermalization of either of these fragments in the finite size helium clusters. It therefore seems reasonable to suppose that both photofragments from CF_3I escape mainly “directly” from the nanodroplets while recombination is not likely to occur. The nascent fragments from CH_3I , on the other hand, may be assigned to two further regimes. The CH_3 fragment carries away the largest part of the total kinetic energy release of the dissociation reaction while its mass ratio ϱ is comparatively small. Methyl may therefore be considered as a “large $\langle\langle T_i \rangle\rangle$ –small ϱ ” fragment. Compared to either fragment from CF_3I , the mean initial kinetic energy of CH_3 is by a factor of ≈ 2 –3 higher. Nonetheless, the small mass ratio ensures that a comparatively large portion of the kinetic energy is lost per collision (compare Table D.1). After 10 statistical binary hard-sphere collisions with ^4He atoms, for example, CF_3 still carries ≈ 33 % of its initial kinetic energy, while CH_3 conserves less than 2 %. Therefore, translational thermalization of methyl can be reached after a relative small number of collisions, so that the trapping of an appreciable number of those fragments inside the droplets can be expected. The complementary iodine radical has a large mass ratio, but, on average, starts out with relatively little kinetic energy. Iodine fragments from the 266 nm photodissociation of CH_3I therefore are assigned to a “small $\langle\langle T_i \rangle\rangle$ –large ϱ ” regime. Due to their substantially lower initial kinetic energy, iodine fragments from CH_3I can certainly be predicted to thermalize more readily than iodine fragments from CF_3I . As a result, the significantly higher probability of recombination in CH_3I -doped ^4He droplets can indeed be inferred from simple considerations.

In this context we find it worthwhile to give a brief account of our attempts to dissociate the diatomics HI and DI in the interior of helium nanodroplets with 266 nm light. By virtue of their small masses, the H and D fragments receive virtually the full kinetic energy release in the dissociation reaction. Compared to the methyl radical, these particles should experience a similar or even higher relative kinetic energy loss per collision (compare equation (D.9a)). Moreover, their mass ratio $\varrho < 1$ allows for large laboratory frame scattering angles $\vartheta > \pi/2$ (see equation (D.9b)) and oscillatory motion inside the medium, here simplified as a gas of hard-sphere particles, becomes possible. Since the nascent iodine atoms are endowed with very little kinetic energy, both of the photofragments should be particularly susceptible to translational

^hFor a given fragment mass m we define the mass ratio as $\varrho = m/m_4$, where m_4 is the mass of a ^4He atom.

thermalization and trapping. Indeed, hardly any signal of escaping photofragments was found in the imaging experiments, which, for this reason, were subsequently abandoned.

Having demonstrated the occurrence of recombination, we make the somewhat weaker statement that any given fragment from the 266 nm dissociation of CH_3I in the interior of liquid ^4He clusters may become permanently trapped inside the native droplet. Compared to recombination, trapping of at least one of the two photofragments is necessarily a more frequent phenomenon and a signature of this effect can be expected to appear also in the properties of the *escaping* photodissociation products. We therefore proceed to reexamine previously observed irregularities concerning the droplet size effect on escaping products from CH_3I -doped helium clusters in the light of this reasoning. In contrast to CF_3I , escaping IHe_n complexes from the photolysis of CH_3I were found to have a product size distribution that is largely independent of the mean droplet size \bar{N} (compare Figure 4.6). Only when the helium stagnation temperature T_o was raised above ≈ 18 K, the IHe_n product size distribution changed in a similar way as observed for CF_3I across the full range of mean droplet sizes \bar{N} (compare Figure 4.5). Most remarkably, this temperature threshold coincides exactly with the onset of recombination (see fig 4.44) which strongly suggests that the two phenomena are intimately related. This can be rationalized assuming that the methyl radicals generally can become trapped in droplets of smaller sizes than the complementary iodine fragments from CH_3I . In this case, the onset of CH_3I recombination should roughly coincide with the onset of trapping of the iodine atoms. The trapping of some of the iodine fragments, however, means that particularly slow and, due to the speed-size correlation, also big IHe_n complexes do not escape anymore into the gas phase. Below $T_o \approx 18$ K therefore two counteracting effects should occur in CH_3I -doped clusters. On the one hand, bigger helium droplets should shift the speed distribution and the size distribution of the escaping IHe_n complexes towards lower speeds and larger product sizes, respectively. On the other hand, some of the slower iodine atoms should get trapped which ought to reduce the intensity of the larger complexes among the escaping IHe_n products. Together, these effects thus could cause the missing droplet size effect on the IHe_n product size distribution below $T_o \approx 18$ K. Similarly, the two opposite effects acting upon the speed distribution of the departing iodine fragments may also be responsible for the lacking droplet size effect on the most probable speeds \hat{v} of the individual IHe_n products leaving the helium clusters (see Figure 4.12). The reasoning that the occurrence of trapping should weaken any droplet size effect on the typical speeds and, consequently, the kinetic energies of the escaping product fraction is substantiated by the data on the complementary CH_3 fragments. Compared to the presumably largely untrapped CF_3 radicals from the photodissociation of CF_3I , the droplet size effect on the mean kinetic energy of the escaping methyl radicals is indeed considerably weaker (compare Figures 4.27 and 4.33).

As mentioned above, the experiments seem to indicate that the methyl fragments from CH_3I can become trapped in smaller droplets than the corresponding iodine atoms. Under appropriate experimental conditions the UV dissociation of CH_3I monomers in the interior of helium clusters may yield a considerable number of droplets that contain only a single CH_3 impurity. This finding opens the door towards chemical reactions involving *radical* species at ultra-low temperatures, since a suitable reaction partner could be introduced subsequently. The

in-situ production of these species avoids furthermore the substantial experimental difficulties generally associated with bringing radicals into the gas phase. As first demonstrated by Nauta and Miller,⁹⁷ the virtual absence of thermal excitations in the droplet interior offers the possibility to steer polar molecules into particular approach geometries with the aid of the long-range dipole–dipole interaction. Although CH₃ itself is, due to the missing dipole moment, not a good candidate, other radical species may be used to attempt the assembly of covalently bound species in specific and, possibly, unusual geometries.

As pointed out above, a conclusive interpretation of the observed time-dependencies is somewhat impaired by the finite duration of the UV dissociation laser pulse. A time-resolution in the sub-nanosecond regime should permit more detailed studies, including, for instance, the variation of the recombination time-constant with droplet size. As pointed out before, both the short UV dissociation and the IR ionization pulses can be obtained from our Ti:Sa femtosecond laser system. Such experiments are currently prepared in our laboratory.

4.6 Simulations

The imaging experiments presented in this chapter have provided us with a comprehensive set of data on both the speed and the angular distributions of various products leaving the helium clusters in the aftermath of the 266 nm photolysis of single CH₃I and CF₃I molecules in the droplet interior. The experimental results indicate that the departing alkyl and iodine photofragments, including complexes formed with a varying number of helium atoms, leave the droplets in the majority of the cases via non-thermal processes. This has been taken as evidence for mainly “direct” escape processes where the fragments, endowed with a substantial amount of kinetic energy and generally considerably heavier than the ⁴He atoms, are thought to push away the helium atoms until they eventually reach the droplet surface and escape into the gas phase. Nevertheless, a few uncertainties remained, in particular with respect to the escape process of those bare alkyl fragments and fragment–He_{*n*} complexes that depart from the finite-size helium clusters with particularly low speeds, *i.e.* with kinetic energies that could potentially be of thermal origin. Furthermore, the microscopic origin of the relaxation of fragment kinetic energy and angular distribution could not be fully elucidated. It therefore seemed desirable to find a further means to assess the nature of the fragment escape and to cast light on the microscopic processes governing the fragment motion in helium clusters.

Many of the experimental observations, most notably the mass-dependence of the angular and translational relaxation, could be explained qualitatively by evoking the essential properties of elastic hard-sphere scattering (see Appendix D.2). Encouraged by this finding, we have carried out classical Monte Carlo simulations based on this simple interaction potential, the results of which will be presented and discussed in this section. These calculations treat the particle motion through liquid helium as sequence of independent binary hard-sphere collisions between the traveling fragment and stationary ⁴He atoms. The thermal motion of the helium atoms as well as second-order collisions involving the translationally excited target atom are entirely disregarded. Evaporative cooling is not included in the simulations, neither. As a consequence, all departing fragments escape via “direct” processes. Compared to Stokes’ flow past a sphere, which is described in some detail in Appendix D.1, this approach should provide a

somewhat more realistic description of the fragment motion through the liquid. This arises from the fact that out of the two descriptions only the hard-sphere scattering model predicts a relative kinetic energy loss per collision, *i.e.* per unit distance, that is independent of the actual kinetic energy of the traveling particle. The experimental results on the escaping iodine fragments indicate exactly this kind of behaviour. Furthermore, the simple viscous flow description leads to straight trajectories, so that the experimentally observed broadening of the angular distributions cannot be predicted straightforwardly.

Even though it is clear that the classical Monte Carlo simulations carried out as part of this work are at best a starting point for a quantitative model, we are confident that some useful information can be extracted from the results. In particular, the calculations should answer the question whether the speed distributions of *both* the alkyl and the iodine fragments from the same parent molecule can consistently be reproduced on the basis of the *same* basic model assumptions. Such a result would not only robustly confirm the presumably predominantly “direct” character of the escape of both fragments, but also strongly indicate that the kinetic energy loss of both the alkyl and the iodine fragments in the quantum liquid is dominated by the same mechanism, *i.e.* individual collisions with helium atoms. If an experimentally observed speed distribution can be reproduced, we moreover expect the simulations to yield a reasonable estimate of the escape time distribution of the fragment under study. Additionally, we were interested to see whether the characteristic shape of the anisotropy parameter distribution $\beta(v)$ of the alkyl fragments (see Figures 4.28, 4.34, and (partially) 4.41) would also emerge from the simulations. Similar to the source of kinetic energy loss, such evidence would strongly point towards elastic collisions between the fragment and individual ^4He atoms as the main origin of angular relaxation. Finally, the simulations offer the possibility to shed light on possible correlations between various system properties, *e.g.* between droplet size, escape time, terminal speed, and total scattering angle which experimentally are more difficult to assess.

4.6.1 The model

In order to simulate the outcome of photodissociation reactions in helium droplets, Monte Carlo calculations are extremely useful, since, as pointed out before, the individual photolysis events are characterized by a wide distribution of initial conditions. These initial conditions include most notably the droplet size, the 3D position and orientation of the parent molecule inside the individual droplet, and the energy partitioning of the photolysis reaction. In the following paragraph we give a more quantitative account of the distributions used in our simulations.

For a given helium stagnation temperature T_o , the size distribution of pure droplets $f(N)$ can be calculated on the basis of the parameters given in Section 2.3. In the simulations, however, the atom number distribution of singly *doped* droplets $h(N)$ is required. This size distribution includes the capture cross section as a weighting factor and, as a first approximation, is assumed to follow the functional form given by equation (C.10) in Appendix C. The simulations furthermore estimate the evaporative loss of helium atoms following a sticking collision between a dopant molecule and a pure helium droplet (see Section 2.4.3), an effect that slightly shifts the atom number distribution $h(N)$ towards smaller droplet sizes. The distribution of parent molecule positions inside a particular helium cluster of size N is assumed to be isotropic.

We describe the radial part $p(r/R)$ of this distribution by a Gaussian, *i.e.*

$$p(r/R) = \frac{1}{\sqrt{2\pi}w_r} \exp \left[-\frac{1}{2} \left(\frac{r/R - r_c}{w_r} \right)^2 \right], \quad (4.8)$$

where, as always, R denotes the droplet radius as given by equation (1.6). Evidently, the parameters r_c and w_r are the center and the standard deviation of the distribution, both expressed as fraction of the droplet radius R . Even though the functional form $p(r/R)$ of the radial distribution is purely empirical, this approach roughly follows the concept of Lehmann,⁸² who predicts a neutral impurity to substantially delocalize inside a ^4He droplet at a temperature of 0.38 K. In the case of SF_6 embedded in a droplet containing $N \approx 2500$ ^4He atoms, for instance, the radial distribution has indeed approximately a Gaussian shape.⁸² In this particular example, the radial distribution is predicted to show a maximum around $r/R \approx 1/3$ and to have a standard deviation $w_r \approx 0.13$.⁸² For the benefit of simplicity we use constant parameters r_c and w_r for any given mean droplet size or, equivalently, for any given helium stagnation temperature T_o . The orientations of the parent molecule inside a helium droplet are described by an isotropic distribution. Accordingly, the initial angular distribution of the nascent fragments with respect to the polarization vector of the 266 nm photolysis laser pulse is given by equation (2.36). In order to save computational effort, the distribution of initial kinetic energies of a particular fragment is neglected. Instead, the decay channel averaged kinetic energies $\langle\langle T \rangle\rangle$ as specified in Tables 4.1, 4.4 and 4.6 are used in the simulations. This simplification is supported by the fact that the experimentally observed speed distributions are broad and appear to bear no signature of the different initial kinetic energies associated with the two dissociation channels (2.42). Similarly, we use the mean anisotropy parameter $\langle\beta\rangle$ (see Table 4.3) to describe the initial angular distribution of the fragments from a particular parent molecule.

In the simulations, the helium clusters are stationary in the laboratory frame. Any broadening of the angular distributions emerging from the simulations therefore cannot be due to droplet angular momenta, but must arise exclusively as a consequence of trajectory deflections inside the finite-size liquid. The ^4He droplets are treated as uniform spheres with bulk number density $\rho_{\text{bulk}} = 0.0219 \text{ \AA}^{-3}$, *i.e.* neglecting the density drop in the surface region shown in Figure 2.11. In order to determine the mean free path λ of a fragment moving through the cluster we introduce the collisional cross section σ of a particular species with a ^4He atom. In the approximation of hard-sphere interaction potentials, this cross section is purely geometrical and speed-independent. If the target atoms are stationary, the mean free path λ is constant and can simply be written as

$$\lambda = \frac{1}{\rho_{\text{bulk}} \cdot \sigma}. \quad (4.9)$$

In order to reduce the computational effort, the distribution of free paths is not considered in the simulations. Instead, all fragments are assumed to travel exactly the distance λ in between two successive collisions.

Before a Monte Carlo simulation is started, the parent molecule (mass, translational temperatureⁱ, internal energyⁱ), the fragment of interest (mass, initial kinetic energy, initial anisotropy

ⁱThese parameters refer to properties of the dopant molecules in the gas phase *before* a pick-up collision with a helium droplet.

Parent molecule	\bar{N}	r_c	w_r	$\sigma(\text{CF}_3)$ [\AA^2]	$\sigma(\text{I})$ [\AA^2]
CF_3I	6080	0.48	0.1	28.5	31.0

TABLE 4.9: Parameters used for the classical Monte Carlo simulation of the escape of CF_3 and iodine fragments from helium droplets produced at a stagnation temperature of 15 K.

parameter) and the essential parameters $\{\bar{N}, r_c, w_r, \sigma\}$ have to be chosen^j. The simulation then traces a large number of 3D trajectories with randomly chosen initial conditions and collision geometries. In each collision the latter are determined by the azimuthal angle and the impact parameter. An individual trajectory calculation is terminated once the fragment either escapes into the gas phase or reaches a translational temperature below 0.38 K, in which case the fragment is assumed to be trapped inside the helium cluster. The statistical weight of a particular trajectory is determined by both the probability of the chosen initial conditions and the probability of the particular sequence of collision geometries, *i.e.* impact parameters (see Section D.2). In case of a successful escape process, the appropriate channel of each discrete observable distribution is incremented by this statistical weight.

The simulation software is written in *C* and makes use of a random number generator based on reference [250]. The calculation of 10^9 trajectories takes roughly 24 hours on a personal computer equipped with a 2.6 GHz Pentium IV processor.

4.6.2 Results

We introduce the results of our simulations by focusing on the 266 nm photolysis of CF_3I in the interior of ^4He clusters. As demonstrated in Section 4.5, this system is much less affected by trapping and recombination than droplet-solvated CH_3I . Both fragments, CF_3 and I , therefore are thought to escape in most cases from the clusters in the size range studied here. Since trapping is incorporated only very crudely in our model, we expect the simulations to yield the best results for CF_3I -doped clusters, provided that “direct” escape is indeed the dominant escape process, as expected.

Figures 4.53 and 4.54 show simulated and measured speed distributions of products related to the fragment pair created by the photolysis of CF_3I . The data corresponds to our standard helium stagnation temperature of 15 K, where the experimental signal levels are particularly high. For each of the two Monte Carlo simulations 10^9 trajectories were calculated. The parameters of the simulations that led to the displayed distributions are given in Table 4.9. Prior to the final calculations, the parameters r_c , w_r , $\sigma(\text{CF}_3)$ and $\sigma(\text{I})$ were optimized in order to match the simulated with the observed speed distributions. In a first step, r_c , w_r and $\sigma(\text{CF}_3)$ were determined from the speed distribution of the CF_3 fragment. In a second step simulations for the iodine fragment were carried out. In the latter calculations only a single parameter, the collision cross section $\sigma(\text{I})$, was optimized while the radial distribution of the parent molecules inside the droplets, given by the parameters r_c and w_r , remained unchanged.

^jAs usually, the parameter \bar{N} denotes the mean size of the *pure* droplets produced in the expansion.

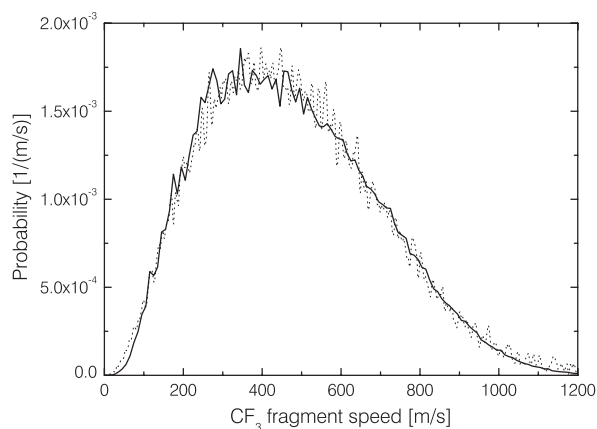


FIGURE 4.53: Measured (dotted curve) and simulated (solid curve) speed distribution of escaping CF_3 radicals from the 266 nm photolysis of single CF_3I molecules isolated in the interior of ^4He droplets. At a stagnation temperature $T_o = 15\text{ K}$ the mean size of the pure droplets is estimated as $\bar{N} = 6080$ atoms (see Table 2.2).

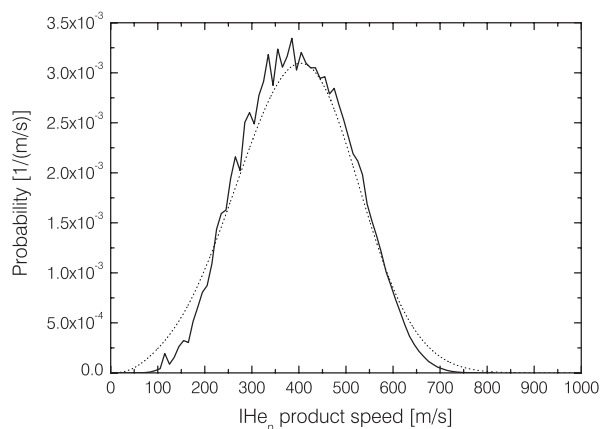


FIGURE 4.54: Simulated speed distribution of escaping iodine radicals from the 266 nm dissociation of CF_3I embedded in ^4He droplets (solid curve). The graph also shows the experimentally obtained overall speed distribution of all detected IHe_n products (dotted curve). The mean droplet size and the radial distribution of the parent molecule inside the droplets is unchanged with respect to Figure 4.53.

This way, a consistent picture incorporating both fragments could be obtained. Since the iodine fragments escape in reality as IHe_n complexes of various sizes, the simulated speed distribution was matched to the *overall* IHe_n speed distribution, which incorporates all individual IHe_n ($n = 0, 1, 2, \dots$) speed distributions according to their experimentally found product intensities in a similar way as the overall kinetic energy distribution shown in Figure 4.16. All optimization processes were done manually and interrupted once the result seemed satisfactory. A somewhat better χ^2 value may therefore be obtained upon further variation of the parameters.

As can be seen from the illustrations, simulated and experimental speed distributions show an excellent agreement. The calculated speed distribution of the CF_3 fragments fully reproduces even details, such as the particular shape of the high-speed tail. Remarkably, also the overall speed distribution of the IHe_n products is well approximated both in position and width, although only a single parameter was varied. Moreover, the I–He collision cross section $\sigma(\text{I}) = 31.0\text{ \AA}^2$ found in our the simulations is entirely reasonable and compares well to the hard-sphere collision cross section of 30.2 \AA^2 for the translational relaxation of spin-orbit excited iodine atoms in a room-temperature ^4He bath gas.²⁵¹ The calculated anisotropy parameters of the escaping CF_3 and iodine fragments (not shown) are, however, close to the gas phase value and virtually constant over the full range of speeds. This is in stark contrast to the pronounced speed dependence of the anisotropy parameters of the escaping CF_3 fragments found experimentally (see Figure 4.28). Possible reasons for this unsatisfactory result will be given below.

In view of the successful simulation of the speed distributions of both CF_3 and the iodine-containing products, we are confident that the calculated escape time distributions are equally

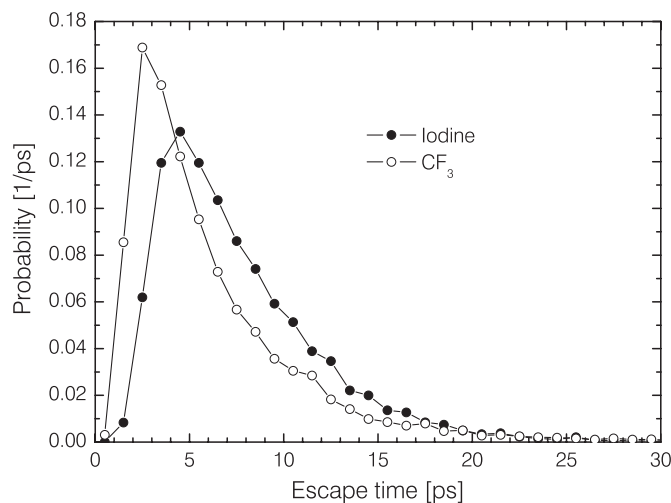


FIGURE 4.55: Simulated escape time distributions of departing CF_3 and I fragments from the 266 nm photodissociation of CF_3I in the interior of ^4He clusters. The calculations were performed for a helium stagnation temperature of 15 K.

realistic. Figure 4.55 illustrates the outcome of the simulations. On average, the CF_3 fragments are predicted to escape somewhat more rapidly than the iodine fragments. While the most probable escape time scales are as short as some picoseconds, the simulations show that an appreciable amount of reaction products depart from the helium droplets as late as a few tens of picoseconds after the photon-induced rupture of the C–I bond. The simulations thus confirm the previously made estimate of a typical escape time scale of about 10 ps.

Compared to CF_3I , a consistent simulation of product speed distributions associated with the 266 nm photolysis of CH_3I in helium clusters turned out to be less successful. As indicated above, we attribute this mainly to a comparatively high degree of trapping occurring in this system. For this reason, we focus on results obtained for a relatively small mean droplet size where trapping should be reduced. Figures 4.56 and 4.57 show experimental and simulated distributions for CH_3 fragments escaping from droplets formed at a helium stagnation temperature of 18 K. While Figure 4.56 illustrates the speed distributions, we plot in Figure 4.57 the anisotropy parameters β as a function of fragment speed v . The experimental distributions correspond to escaping CH_3 in the vibrational ground state and do *not* include the (small) contributions from the relatively weak CH_3He_n progression. As usually, 10^9 trajectories were computed for these graphs. The parameters used in this simulation are put together in Table 4.10. It is important to bear in mind that, as before, these parameters were optimized only with respect to the observed speed distribution. This way, the calculated anisotropy parameters emerge as a largely unbiased result of the simulations. Note that the radial distribution assumed for the CH_3I parent molecules at $T_o = 18$ K is centered about comparatively low radii. This is in qualitative agreement with the results found by Lehmann for a neutral SF_6 impurity in ^4He clusters of various sizes.⁸² His calculations show that the RMS displacement of the dopant molecule from the cluster center, expressed as fraction of the droplet radius, grows with increasing droplet

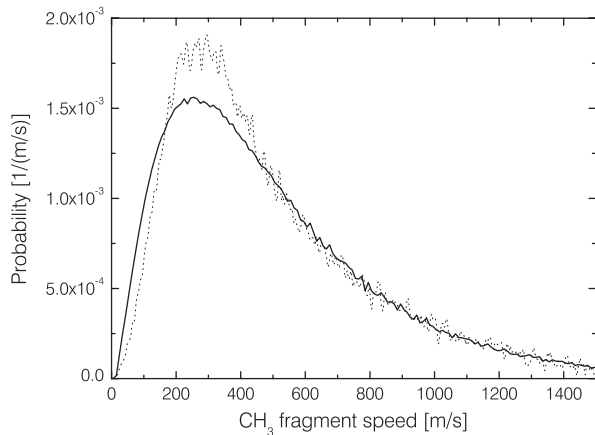


FIGURE 4.56: Measured speed distribution (dotted line) and calculated (solid line) of bare CH_3 fragments escaping in the vibrational ground state from ^4He droplets produced at a stagnation temperature of 18 K. The calculated distribution (solid line) does not refer to any specific vibrational state.

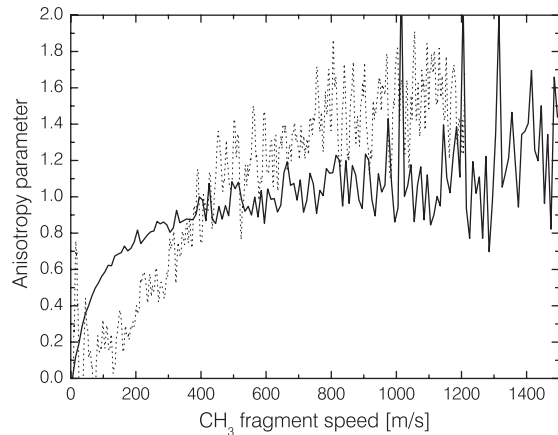


FIGURE 4.57: Measured (dotted line) and calculated (solid line) anisotropy parameters as a function of CH_3 fragment speed. The curves correspond to the same conditions as the speed distributions displayed in Figure 4.56.

size N .

The simulated speed distribution shows a reasonable agreement with the experimental result. More important, however, are the findings for the speed dependence of the simulated anisotropy parameters. Although the experimental function $\beta(v)$ is only roughly approximated, we note two important features. At low product speeds, the simulated anisotropy parameters β increase with fragment speed v , starting with a virtually isotropic distribution at $v = 0$. At larger speeds, the function $\beta(v)$ reaches an approximately constant and finite value that is substantially lower than the initial anisotropy parameter $\langle\beta\rangle = 1.87$ assumed in the calculations. Qualitatively, the simulated distribution $\beta(v)$ thus has *very similar* characteristics as the measured anisotropy parameter distribution displayed in the same graph.

4.6.3 Discussion

The simulations on the basis of a simple hard-sphere scattering model yield surprisingly good results. In particular, the experimentally observed speed distributions could largely be reproduced on the basis of reasonable model parameters. In accord with our interpretation of the experimental data this result strongly suggests that the escape processes of *all* departing prod-

Parent molecule	\bar{N}	r_c	w_r	$\sigma(\text{CH}_3)$ [\AA^2]
CH_3I	2750	0.05	0.01	15.5

TABLE 4.10: Parameters used for the classical Monte Carlo simulation of the escape of CH_3 fragments from helium droplets produced at a stagnation temperature of 18 K.

ucts studied here, including the fragment– He_n complexes, are indeed predominantly “direct”. Moreover, collisions between the traveling fragments and individual ^4He atoms emerge as the most likely origin of the kinetic energy losses observed.

The simulation of the anisotropy parameter distributions $\beta(v)$ still is unsatisfactory, even though the calculations on the light methyl fragments revealed the essential features of the $\beta(v)$ functions typically observed for escaping bare CF_3 , bare CH_3 and CH_3He_n complexes (compare Figures 4.28, 4.34 and (partially) 4.41). Independent of the speed distributions, the latter fact points again to a mainly “direct” escape of the methyl fragments and the methyl– He_n complexes with individual fragment– He collisions as the most probable source of the angular broadening found experimentally. We believe that quantitatively more accurate distributions $\beta(v)$ should emerge from the simulations if the thermal motion of the helium atoms was included. As shown in Section 4.4, the typical kinetic energy transfer from a pair of traveling fragments to the surrounding helium droplet can heat an average size droplet well above the λ -point. At a temperature of 2.5 K, for instance, ^4He atoms would have an appreciable RMS velocity of 125 m/s. Compared to the stationary target atoms used in our current model, incorporating the thermal motion should result in more washed-out angular distributions. In such a model, fewer collisions are necessary to cause a similar average scattering angle and fragments born close to the surface and escaping with relatively high speeds are more likely to experience significant trajectory deflections. If thermal motion is included in the model, the rising part of the simulated function $\beta(v)$ should therefore extend to larger speeds, in agreement with the experiment. Moreover, heavier fragments, such as CF_3 , should experience more significant trajectory deflections than predicted by our current model. Therefore, we are confident such an improved model would also better reproduce the characteristic shape of the experimental $\beta(v)$ function of the escaping CF_3 fragments.

In order to reasonably describe the thermal motion of the helium atoms in an individual helium cluster, a good knowledge of the droplet temperature is indispensable. Since this temperature evolves as the nascent fragments travel through the medium and lose kinetic energy, an improved model should incorporate this time dependence. Such an approach would require to simultaneously trace the trajectories of *both* fragments through the finite-size droplet and to estimate the instantaneous cluster temperature, e.g. on the grounds of the heat capacities introduced in Section 2.2. Such a model can also be expected to provide a better description of the trapping processes which currently are crudely modeled using a fixed critical translational temperature (the trapping probabilities calculated with the current model are smaller than 10^{-3} for the parameters given in Tables 4.9 and 4.10). Since both fragments have to be propagated simultaneously, such a model also opens the door to describing recombination processes.

A noteworthy aspect presently disregarded in the model is a possible change of collision cross-section and mass as helium atoms attach to a moving fragment. Based on the speed-size correlation seen for the escaping fragment– He_n complexes, one may attempt to adjust both the mass and the collision cross section of the traveling structure as a function of its speed relative to the medium. Since the microscopic properties of the complex formation process are, however, presently not fully understood, such an empirical approach has to be taken with care and is likely to oversimplify the underlying mechanisms.

We finally emphasize that the simulations yield good results *although* second and higher-order He–He and He–fragment collisions are entirely neglected. The latter approximation

should constitute a major simplification of the helium dynamics in the vicinity of the traveling fragment. One may, however, argue that the extraordinarily high heat conductivity of the quantum liquid efficiently impedes any localization of kinetic energy. In this sense the simplified hard-sphere collision model used in this work may actually mimic quantum properties of liquid ^4He .

4.7 Other experimental results

Independent from the results presented and discussed in Sections 4.1–4.6 we show in this section selected experimental results that illustrate the proper working of our setup. Firstly, we present measurements of the droplet beam speed as a function of helium stagnation temperature and compare our results to literature values. Secondly, we illustrate the effect of the measures taken to reduce the presence of unsolvated dopant species in the residual gas of the detection chamber.

4.7.1 Droplet beam speed

All ion images of products from photodissociation events in the interior of helium clusters exhibit a displacement from the origin of the imaging setup from which the droplet beam speed in the laboratory frame can be derived. This is illustrated in Figure 4.58 where we show velocity map images of IHe_1 complexes escaping from CF_3I -doped droplets produced at the two different stagnation temperatures $T_o = 11$ and 19 K. Clearly, the displacement is larger for $T_o = 19$ K which indicates an increase of the droplet beam speed with rising stagnation temperature. A thorough analysis of IHe_1 velocity map images recorded at other stagnation temperatures leads to the droplet beam speeds reported in Figure 4.59. The graphical comparison with speeds measured in the Toennies group¹²⁰ shows a good agreement and is a further piece of evidence that our setup provides experimental conditions similar to those of other groups working in this field.

4.7.2 Background reduction

In order to obtain low background signal levels in the velocity map images of bare photodissociation products, it is important to reduce the partial pressure of the dopant species in the residual gas. For this reason, both active and passive measures were taken. As described in detail in Section 3.4, we actively reduce the effusive flux of unsolvated dopant molecules into the detection chamber by using a cross beam instead of a gas-filled scattering cell to introduce impurities into the helium droplets. Passively, the partial pressure of dopant species in the detection chamber is lowered by means of liquid nitrogen (LN_2) reservoirs (see Figure 3.1) which act as cryopumps.

We illustrate the effect of these measures with the aid of velocity map images of methyl radicals in the vibrational ground state. These bare products from the 266 nm photodissociation of CH_3I were detected using the previously described $[2 + 1]$ REMPI scheme around 333.5 nm. In order to map both the droplet signal as well as the high-energy fragments from the dissociation of gas phase molecules onto the position-sensitive detector we used a repeller voltage $V_R = 3000$ V and no einzel lens. Figure 4.60 shows three representative ion images that

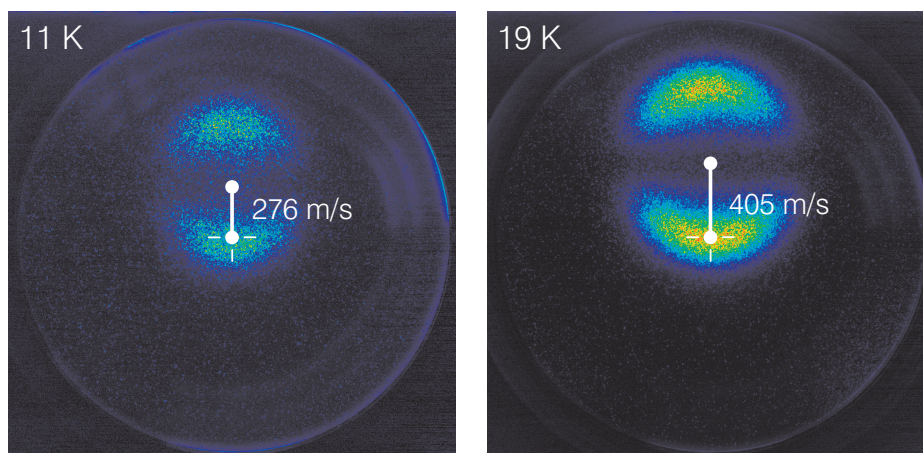


FIGURE 4.58: (Color) Measurement of the droplet beam speed v_D from the displacement of $(\text{IHe}_1)^+$ ion images with respect to the origin of the imaging setup. The origin of the setup was determined beforehand from two ion images recorded with and without using the image-inverting einzel lens. The products were produced by photodissociating CF_3I molecules solvated in the droplets and were non-resonantly ionized using ultrashort laser pulses. The einzel lens voltage used during the acquisition of the displayed images was $V_{\text{lens}} = 6200$ V. Both images were recorded using an integration time of 1 hour. The temperatures given in the upper left corners of the images denote the helium stagnation temperature T_o .

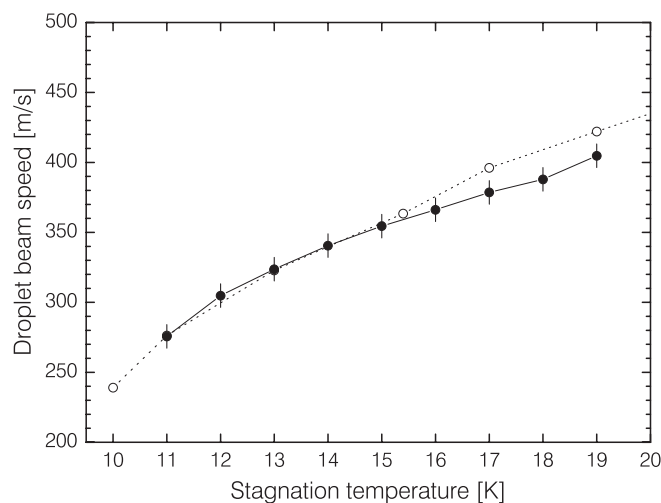


FIGURE 4.59: Plot of the measured droplet beam speed v_D versus the helium stagnation temperature T_o . The solid symbols illustrate the speeds derived from the displacement of the IHe_1 velocity map images at a stagnation pressure $p_o = 30$ bar. For comparison the graph also shows droplet beam speeds measured by Schilling¹²⁰ at $p_o = 20$ bar (open symbols, compare Figure 2.2). All expansion conditions belong to the subcritical expansion regime.

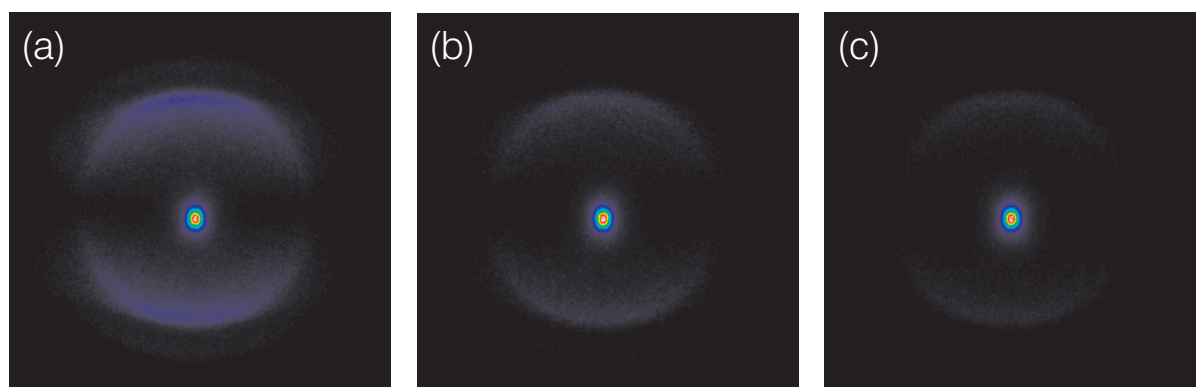


FIGURE 4.60: (Color) Velocity map images of CH_3 fragments in the vibrational ground state, detected using a $[2 + 1]$ REMPI scheme. The images show both the relatively slow fragments escaping from droplets produced at $T_o = 15$ K and signal from the dissociation of unsolvated parent molecules in the detection chamber residual gas. The experimental conditions were (a) scattering cell doping, LN_2 reservoirs warmed up, (b) scattering cell doping, LN_2 reservoirs cooled down, and (c) cross beam doping, LN_2 reservoirs cooled down. The displayed ion images were recorded using a repeller voltage $V_R = 3000$ V, no einzel lens, and an integration time of 15 min. The pictures illustrate a 500×500 pixel sector of the total image. As the einzel lens is on ground potential, the droplet beam velocity vector exceptionally points downwards in these images.

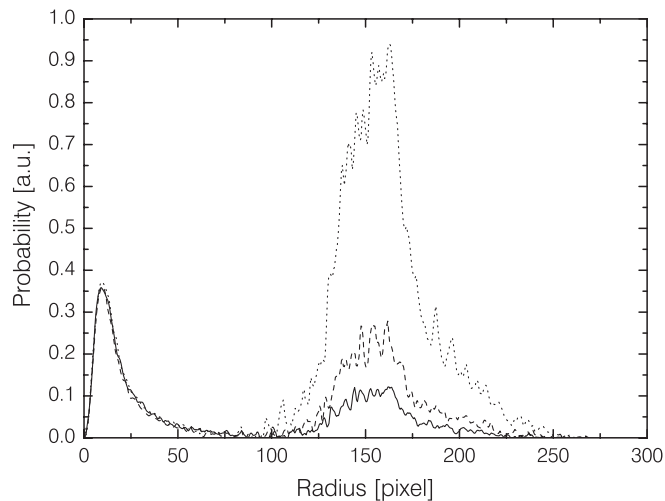


FIGURE 4.61: Speed distributions in the droplet frame (here in units of pixels) obtained by performing Abel inversions on the ion images shown in Figure 4.60. The displayed distributions correspond to Figure 4.60 (a) (dotted line), Figure 4.60 (b) (dashed line), and Figure 4.60 (c) (solid line). In order to compare the gas phase contributions, the distributions have been scaled such that the droplet signals have the same amplitude. Due to the finite droplet beam speed in the laboratory frame the speed distributions of methyl fragments from gas phase parents are artificially broadened in this representation.

were recorded at our standard helium stagnation temperature of 15 K. Clearly, the intensity of the gas phase background decreases from left to right, *i.e.* as the measures to remove unsolvated parent molecules from the detection region of the imaging setup are “switched on”. More quantitatively, this effect can be inferred from the corresponding speed distributions in the droplet frame which are put together in Figure 4.61. An integration of these speed distributions shows that the cryopumps alone reduce the background signal by a factor of ≈ 3.8 , while both measures together result in a reduction by a factor of ≈ 7.9 . Owing to these measures the experimental signal-to-background ratio hence could be improved by almost one order of magnitude.

Chapter 5

Summary and Outlook

5.1 Summary

We have described the details of a new experimental apparatus to investigate the photodissociation and -ionization dynamics of species residing in the interior or at the surface of helium nanodroplets by means of ion and electron imaging techniques. This droplet beam machine was designed, constructed and made operational as part of this thesis work. We furthermore have presented and discussed first experimental results obtained with the said apparatus. In these studies we investigated the 266 nm A band photodissociation of CH₃I and CF₃I inside ⁴He droplets with estimated mean sizes ranging from ≈ 2000 to ≈ 20000 atoms. In order to assess the translational dynamics of the CH₃, CF₃ and iodine photofragments in the quantum fluid, the three-dimensional speed and angular distributions of various departing reaction products were measured using a velocity map imaging setup. Depending on the product under study, quantum state-selective as well as non-resonant ionization schemes were employed. To the best of our knowledge this work is the first experimental study of photodissociation events in the interior of helium nanodroplets and constitutes an original approach to investigating translational particle dynamics in liquid helium. The key results of our studies can be summarized as follows:

1. **Fragments *do* escape**

At all examined mean droplet sizes photofragments of any species created by the 266 nm photolysis of CH₃I or CF₃I can *escape* from the ⁴He clusters they were born into. Compared to “classical” solid clusters where already a few solvation shells around the parent molecule cause virtually complete caging of typical photolysis reactions,^{103–107} liquid helium droplets thus reveal extraordinary dynamical properties. Although it is presently still unclear whether these properties give evidence of quantum behaviour, the measured speed and angular distributions of the departing products should constitute a valuable benchmark for numerical many-body simulations of the fragment escape. As demonstrated by Takayanagi *et al.*¹⁰² such calculations allow one to artificially switch off quantum effects and, together with the experimental results, should ultimately enable us to assess their importance.

2. **The escape processes are predominantly non-thermal and therefore mainly “direct”**

We have demonstrated that the departing fragments leave the helium droplets either bare or as partially solvated fragment–He_n complexes. The measured speed and angular distributions show that the escape of all of these product species is dominated by *non-thermal* processes, regardless of the mean droplet size under study. In accord with the recent simulations by Takayanagi *et al.*¹⁰² the vast majority of departing products thus is thought to leave the helium clusters via “direct” escape. As opposed to thermally, *i.e.* evaporatively released products, “directly” escaping fragments are assumed to push away ⁴He atoms by virtue of their larger mass and their initial kinetic energy until they reach the droplet surface and depart into the gas phase. Whereas thermal contributions to the escape of CF₃ and iodine-containing products are most certainly negligible, our data is compatible with a small thermal contribution to the escape of the lighter CH₃ fragments and CH₃He_n complexes.

3. **Droplet rotations are of minor relevance for “directly” escaping products**

By comparing the anisotropy parameters of “directly” escaping products with different escape times we have demonstrated that droplet rotations in the laboratory frame definitely do not dominate the broadening seen in the angular distributions of those products. This important result enhances the value of our experimental approach as angular distributions derived from velocity map images of “directly” escaping products should, to a good degree of approximation, immediately reveal trajectory deflections occurring inside the finite-size quantum liquid.

4. **The fragment mass strongly influences the speed and angular relaxation**

Compared to the photolysis of free parent molecules in the gas phase, the photodissociation in the interior of helium droplets results in broader angular distributions, *i.e.* smaller mean anisotropy parameters, and lower mean kinetic energies of the escaping products. The fragment mass is found to have a profound impact on the relaxation of both of these observables. The comparison of the data on escaping CH₃, CF₃ and iodine fragments clearly shows that *lighter* fragments departing from the droplets experience *higher* kinetic energy losses and *more smearing* in the angular coordinate. At least qualitatively, the fragment motion through liquid helium droplets thus shows properties similar to a simple billiard-ball type system which encouraged us to carry out numerical simulations on the basis of binary hard-sphere scattering (see 6.). The said mass-dependence does however not apply to the different-size complexes within the IHe_n or the CH₃He_n progressions. Due to the well-established speed-size correlation (see 8.) fragments embedded in larger complexes show higher kinetic energy losses and therefore are thought to have traveled longer distances through the liquid before escaping into the gas phase. The higher degree of angular broadening found for bigger complexes consequently is assumed to result from larger trajectory deflections associated with longer distances of travel inside the helium clusters.

5. **Droplet size effects**

Varying the mean droplet size affects both the mean kinetic energy transfer to the helium

clusters and the loss of angular structure of the escaping products. In general, larger mean droplet sizes result on average in higher kinetic energy losses and more washed-out angular distributions of the departing products. While the photolysis of CF_3I in helium droplets appears to follow this general behaviour, the droplet size effects on the various products from the photodissociation of solvated CH_3I frequently are considerably weaker. The latter effect is attributed to a higher probability of fragment trapping and recombination in CH_3I -doped helium droplets (see 9.).

6. Binary hard-sphere scattering simulations yield remarkably good results

In order to further substantiate the picture of a largely “direct” fragment escape and to investigate the microscopic origin of the observed translational and angular relaxation, we have carried out classical Monte Carlo calculations as a complement to the experimental studies. These simulations treat the fragment motion in the finite-size liquid as a sequence of independent binary hard-sphere collisions with initially stationary ^4He atoms. Most remarkably, the speed distributions of both the departing CF_3 and the iodine fragments created by the photolysis of CF_3I in ^4He droplets of a selected mean size could largely be reproduced on the basis of reasonable and consistent model parameters. Qualitatively, the model also correctly predicts the behaviour of the anisotropy parameter β of escaping CH_3 fragments as a function of fragment speed v . This evidence strongly suggests that elastic collisions between the moving radicals and *individual* ^4He atoms are at the origin of both the translational and angular relaxation of the photofragments inside the ^4He liquid. Fully quantum-mechanical simulations are however desirable to further confirm these findings.

7. Dynamics of vibrationally excited fragments

Using a state-selective ionization scheme we have recorded ion images of departing bare methyl fragments in the first umbrella mode (ν_2) excited vibrational state. These experiments clearly demonstrate that a possible vibrational cooling in the course of the fragment escape is definitely not complete. Both the relative kinetic energy loss and the angular broadening of departing umbrella mode excited methyl fragments are virtually identical to the results found for escaping CH_3 in the vibrational ground state, indicating a very similar interaction with the liquid environment.

8. Complex formation with speed-size correlation

Using non-resonant product ionization by ultrashort 800 nm laser pulses we have shown that both iodine and CH_3 fragments escaping from the helium clusters appear in the gas phase as IHe_n or CH_3He_n complexes with sizes n of up to 15 and more helium atoms. The experimental evidence strongly suggests that the helium atoms attach to the translationally excited neutral radicals prior to their departure from the droplets. Velocity map imaging experiments on size-selected IHe_n complexes revealed that each complex size n can be associated with characteristic speeds that are little affected by changes in the initial kinetic energy of the iodine fragments, *i.e.* parent molecule substitution, or by variations of the mean droplet size. Instead, changing these two parameters strongly influences the size distribution of the departing IHe_n complexes. Moreover, both the escaping IHe_n and CH_3He_n complexes exhibit a marked correlation between their most

probable speeds and their sizes n : In all cases *larger* complexes are found to leave the helium clusters with *lower* most probable speeds. Finally, the most probable speeds of the departing IHe_n and CH_3He_n complexes appear to become virtually identical for complex sizes $n \gtrsim 12$, that correspond roughly to an entirely filled first solvation shell. This data suggests that the number of helium atoms attached to a moving fragment inside the droplet is to a first order of approximation determined by the instantaneous *speed* of the fragment relative to the helium bath and the strength of the fragment–He interaction. Accordingly, we proposed that the complex formation in the droplet interior should be regarded as the *dynamical* development of helium solvation shells around the translationally excited radicals under the destructive influence of the helium flow associated with the relative motion.

9. Recombination

By velocity map imaging bare parent molecules we have demonstrated that CH_3I molecules can recombine in the aftermath of the 266 nm photolysis in the interior of ^4He nanodroplets. The proposed recombination mechanism involves a complete translational relaxation of both photofragments inside the droplets followed by an approach of the fragment pair due to dispersion interactions and therefore is probably unique to liquid clusters. The observed bare $(\text{CH}_3\text{I})^+$ ion signal is thought to arise from *complete evaporation* of helium clusters due to internal relaxation of the recombined parent molecules, and is found to appear with a time constant of ≈ 5 ns. The CH_3I recombination signal has its onset around $T_o = 18$ K, *i.e.* for clusters with mean sizes of about ≈ 3000 atoms, and initially grows as the mean droplet size increases. The virtual absence of a recombination signal for CF_3I is attributed to the different fragment masses and the dissimilar partitioning of the total kinetic energy in the photolysis reaction.

10. No evidence of Landau’s critical velocity

Despite our capability to measure the speed distribution of departing products with a high level of resolution, the photodissociation experiments presented in this work have *not* revealed anomalies that could be linked to the Landau critical velocity of ≈ 58 m/s in bulk He II. In view of the high kinetic energy release associated with the photolysis reactions studied here this is no surprise, as the vast majority of fragments do not translationally relax to speeds below this critical value or propagate through helium droplets heated above the λ -point. Suggestions for experiments where a critical velocity is more likely to be observed will be made below.

5.2 Outlook

The results of this thesis work open up a number of new long-term research directions. Particularly intriguing is the possibility to use the *in-situ* photolysis of chromophores to produce doped helium droplets containing a single *radical* impurity. As indicated in this work, two different photofragment species will generally escape with different average probabilities from helium clusters of a certain mean size which should in many cases enable us to establish experimental conditions under which a significant fraction of the fragments with the lower escape probability

become trapped inside the droplet they were born into. Downstream of the photodissociation experiment one then may introduce other species into the droplets to study radical-involving chemical reactions at ultralow temperatures.

In addition to the trapped fragments the escaping photoproducts also constitute highly interesting systems. Based on the results presented in Chapter 4 many photofragments are expected to leave the helium droplets together with an appreciable number of attached helium atoms. Our results also suggest that the size distribution of these small radical-He_n complexes can be systematically modified by changing the mean size of the original droplets, *i.e.* by varying the expansion conditions. Accordingly, the departing complexes may be of great value for systematically investigating the solvation of *radicals* in small helium clusters, for example with respect to the onset of quantum phenomena. Unlike the closed-shell molecules recently studied by McKellar, Jäger and coworkers,^{92–94} radical species can generally not be co-expanded with helium to produce doped clusters and the making of radical-He_n complexes therefore is associated with substantial experimental difficulties. The photodissociation of suitable parent molecules in the interior of helium droplets constitutes a new and, possibly, advantageous way to produce such species.

Regarding our research in the near future it seems desirable to further elucidate yet unsettled properties of the translational dynamics of neutral photofragments in the ⁴He quantum liquid by means of the techniques presently at hand. Towards this goal we suggest the following:

Improving the apparatus

The experiments clearly show that our capacity to measure the speed and angular distributions of escaping *bare* photofragments is significantly impaired by the presence of unsolvated parent molecules in the detection volume of the ion imaging setup. Our efforts to reduce this background by installing cryopumps in the detection chamber and by fitting a cross beam setup into the doping chamber have brought about a considerable improvement of the signal-to-background ratio (see Section 4.7.2), but still are not fully satisfactory. We therefore propose to add a further differential pumping stage of small length in between the current doping and detection chambers. Such a pumping stage should reduce the effusive transport of dopant species into the detection chamber by about three orders of magnitude and therefore definitely remove the said background from our ion images. The improved apparatus will enable us not only to record speed and angular distributions of departing bare fragments with lower uncertainties but also to more easily obtain reliable intensities of unsolvated products. Furthermore, we should then be able to provide quantitative answers to questions like the degree of internal relaxation of the various escaping bare fragments. Without background it will also be possible to extend our studies to smaller clusters, *i.e.* higher stagnation temperatures, and to monitor bare fragments escaping with speeds close or equal to those observed in the photodissociation of free gas phase molecules. The latter point is particularly important for a future interaction with theory as the presently studied medium-size helium droplets containing a few thousand atoms are theoretically much more difficult to handle.

Imaging studies with enhanced temporal resolution

Although the results presented in this work have enabled us to deduce many important properties of the fragment dynamics in the interior of helium clusters, some issues could not be fully clarified due to the insufficient temporal resolution of the experiments. Presently, the time resolution of the non-state-selective imaging experiments is limited by the finite duration of the UV photolysis laser pulses which have a typical width (FWHM) of 5–6 ns. We therefore propose to carry out experiment using ultrashort pulses from our femtosecond laser system for both the UV photodissociation of the parent molecules and the non-resonant IR ionization of the products. Since the photolysis wavelength of 266 nm can conveniently be obtained by frequency-tripling the amplified output of the Ti:Sa laser system, it should be possible to achieve a temporal resolution of the order of 100 fs in our laboratory. In a first series of experiments we plan to utilize the thus enhanced time resolution to determine whether evaporative escape processes play indeed a significant role in the release of the light CH_3 and CH_3He_n products from the droplets. Whereas directly escaping products should typically leave the helium clusters within about 10 ps, evaporative processes are thought to occur on a time scale of 10^{-9} – 10^{-7} s and therefore should be separable in time with respect to the former escape processes. Secondly, such experiments are expected to provide more precise information on the formation times of recombined bare parent molecules and therefore could help to disentangle the various physical processes that probably play a role in creating these products (see Section 4.5). Thirdly, these experiments may reveal the existence of metastable fragment– He_n complexes escaping from the droplets. As suggested in Section 4.4, helium solvation shells may form temporarily around the “directly” escaping CF_3 radicals and subsequently detach as a result of coupling to the vibrational or rotational motion of the trifluoromethyl radicals. Consequently, a better time resolution may also shed light on aspects of the internal cooling of the departing fragments.

Internal relaxation

Using an improved droplet beam machine with an additional vacuum stage we should be able to quantitatively address the electronic relaxation of the escaping bare iodine fragments and the vibrational relaxation of the departing bare methyl and trifluoromethyl radicals. Unfortunately, we cannot hope to measure the rotational cooling of the escaping CH_3 and CF_3 products as efficient rotationally resolved REMPI schemes are presently not available for these radicals. Investigating the rotational cooling of the escaping fragments should however be particularly rewarding since, compared to the other internal degrees of freedom, rotations can be expected to relax more efficiently in collisions with helium atoms. Accordingly, we propose to extend the photodissociation studies to other dopant species with molecular fragments that can more easily be ionized in a rotationally resolved fashion. A particular interesting molecule meeting this requirement is nitrosyl chloride (NOCl), the gas phase photodissociation dynamics of which have been well characterized.^{252–257} Similar to the alkyl iodides studied in this thesis work, this molecule promptly dissociates with a lifetime of only ≈ 50 fs²⁵⁶ upon excitation of the first electronically excited singlet state S_1 in the spectral region from ≈ 425 to ≈ 510 nm.²⁵⁵ The rapid rupture of the relatively weak N–Cl bond results in the creation of Cl and NO fragments, both of which can be substantially internally excited. In the gas phase the latter

radicals are produced in the two spin-orbit states (${}^2\Pi_{1/2}$ and ${}^2\Pi_{3/2}$),²⁵⁵ with an excitation of the N–O stretch vibration that depends strongly on the photolysis wavelength,²⁵⁵ and with a rotational state distribution that peaks at high rotational quantum numbers $J \approx 30.5$.^{252–255} Moreover, NO radicals can readily be ionized using the well-known rotationally resolved $[1 + 1]$ REMPI scheme via the $A\ {}^2\Sigma^+ \leftarrow X\ {}^2\Pi$ transition.^{258–260} For these reasons, the NO fragment from the photolysis of NOCl presumably is a good candidate for investigating the relaxation of *all* internal degrees of freedom in the course of the fragment escape through liquid ${}^4\text{He}$.

Complex formation

The photolysis experiments presented in Chapter 4 have shown that both atomic and molecular photofragments may depart from the helium clusters as fragment– He_n complexes. Although the microscopic mechanisms governing the formation of these structures are not yet fully understood, the experimental evidence indicates that the complexes develop in the helium droplet interior and that both the fragment–He interaction and the relative speed of the fragment with respect to the droplet environment are important factors in determining the instantaneous size of the traveling complexes. Due to the possibility of rotational and vibrational cooling, complex formation around molecular fragments may however require a more sophisticated description than the development of solvation shells around translationally excited atomic radicals. In order to shed light on the details of the complex formation accompanying the translational motion of fragments in the quantum liquid, more experimental data is indispensable. In particular, atomic and molecular fragments with *known* fragment–He interaction potentials would allow us to further test and to refine the basic complex formation model suggested in this thesis. Also in this respect photodissociation experiments on NOCl in ${}^4\text{He}$ droplets should provide most valuable information, since the interaction of *both* fragments with helium is well-characterized. Recent *ab initio* calculations have determined the interaction potentials of Cl with most rare gas atoms to a high level of accuracy.^{245,261} Additionally, calculated potential energy surfaces of the NO–He,²⁶² NO–Ne²⁶³ and NO–Ar²⁶⁴ systems are available. Since we furthermore should be able to state-selectively ionize these NO–(rare gas) species by means of sensitive REMPI schemes,²⁶⁵ NO fragments open the door to studying the complex formation around molecular radicals in a systematic and state-specific manner.

Landau’s critical velocity

One of the important motivating factors for studying the photodissociation dynamics of molecules embedded in ${}^4\text{He}$ droplets is the possibility of observing Landau’s critical velocity, a phenomenon most directly related to superfluidity, in a finite-size quantum system. However, the photodissociation experiments carried out in this work have not revealed a clear signature of such a critical velocity. As already pointed out above, this is attributed to the fact that only a small minority of the escaping products probe the speed region around 60 m/s. Additionally, the few products that translationally relax to those speeds very probably propagate, at least in the last part of their escape process, through thermally excited helium droplets heated above the λ -point. In view of this evidence one may argue that the experimental sensitivity for a critical velocity could be enhanced simply by increasing the mean droplet size. Due to the higher

kinetic energy losses associated with larger droplets, more fragments could be expected to probe the relevant speed region, while at the same time the increased droplet heat capacities should largely prevent the clusters from reaching temperatures greater than T_λ . Unfortunately, at a constant helium atom flux increased mean cluster sizes are equivalent to lower droplet densities in the detection region, which will rapidly reduce the absolute signal to an unacceptable extent. An alternative and more promising strategy to experimentally monitor Landau's critical velocity lies therefore in choosing a different photolysis reaction with less kinetic energy release and lower initial fragment speeds. Particularly interesting systems in this respect are parent molecules with alkali fragments, since the binding energy of alkali atoms to helium droplets is known to be only of the order of 10 cm^{-1} .^{266,267} In contrast to other less well-characterized radicals, a heavy alkali fragment, e.g. rubidium, that approaches the surface of a helium droplet from the interior with speeds around 60 m/s will therefore most certainly overcome any solvation barrier and escape into the gas phase. Accordingly, the speed distributions of escaping alkali fragments could possibly bare a signature of the critical velocity we are interested in.

Photoionization studies

In the future we also plan to investigate the photoionization of dopant species residing either on the surface or in the interior of helium droplets. Using the velocity map imaging technique the spectrum of released photoelectrons can be measured. Since electrons interact strongly with helium,²⁶⁸ such spectra should be extremely sensitive to the position of the ionized particle and therefore are expected to reliably indicate whether a particular species solvates in the droplet interior or binds to the surface of the helium cluster. Following a recent suggestion by Ancilotto *et al.*²⁶⁹ we mention that photoelectron spectroscopy may therefore shed light on the still unresolved question of whether ^4He clusters can carry quantized linear vortices. Their DFT calculations indicate that Ca atoms should principally reside on the helium cluster surface, but localize in the interior if a vortex is present. In order to elucidate the *dynamics* of the electron escape from the droplets we furthermore intend to carry out time-resolved studies by means of a streak camera. Such an instrument with an expected time-resolution of about 1 ps ²⁷⁰ has recently been built in our group and can simply be inserted into the detection chamber instead of the presently used velocity imaging setup.

Appendix A

Properties of the log-normal distribution

The log-normal distribution $f(N)$, $N \in [0 \infty]$, has two parameters, $\delta > 0$ and μ , and is defined as

$$f(N) = \frac{1}{N\delta\sqrt{2\pi}} \exp\left[-\frac{(\ln N - \mu)^2}{2\delta^2}\right]. \quad (\text{A.1})$$

It can be shown that $f(N)$ is normalized, *i.e.* $\int_0^\infty f(N) dN = 1$. The distribution has one maximum at

$$N_{\max} = \exp(\mu - \delta^2) \quad (\text{A.2a})$$

with

$$f(N_{\max}) = \frac{1}{\delta\sqrt{2\pi}} \exp(\delta^2/2 - \mu). \quad (\text{A.2b})$$

Most conveniently, the p^{th} moment of the log-normal distribution can be calculated analytically:

$$\overline{N^p} = \int_0^\infty N^p f(N) dN = \exp\left(p\mu + \frac{p^2\delta^2}{2}\right). \quad (\text{A.3})$$

A log-normal distribution usually is characterized by its mean \overline{N} and its standard deviation S . These are easily obtained using equation (A.3) and given by

$$\overline{N} = \int_0^\infty N f(N) dN = \exp\left(\mu + \frac{\delta^2}{2}\right) > N_{\max} \quad (\text{A.4a})$$

and

$$S = \left[\int_0^\infty (N - \overline{N})^2 f(N) dN \right]^{\frac{1}{2}} = \overline{N} \sqrt{\exp(\delta^2) - 1}. \quad (\text{A.4b})$$

It often is useful to express the p^{th} moment of the log-normal distribution in terms of the mean value \overline{N} . Combining equations (A.3) and (A.4a) one obtains

$$\overline{N^p} = \overline{N}^p \cdot \exp\left(\frac{p(p-1)}{2}\delta^2\right). \quad (\text{A.5})$$

Inverse to equations (A.4), δ and μ can be expressed as a function of \bar{N} and S :

$$\mu = \ln \left(\bar{N}^2 / \sqrt{\bar{N}^2 + S^2} \right) \quad (\text{A.6a})$$

and

$$\delta^2 = \ln \left(S^2 / \bar{N}^2 + 1 \right) . \quad (\text{A.6b})$$

The full width at half maximum $\Delta N_{1/2}$ of the log-normal distribution is given by

$$\Delta N_{1/2} = \exp \left(\mu - \delta^2 + \delta \sqrt{2 \ln 2} \right) - \exp \left(\mu - \delta^2 - \delta \sqrt{2 \ln 2} \right) \quad (\text{A.7a})$$

or

$$= 2 \exp \left(\mu - \delta^2 \right) \sinh \left(\delta \sqrt{\ln 4} \right) . \quad (\text{A.7b})$$

The relative width can therefore be written as

$$\frac{\Delta N_{1/2}}{\bar{N}} = 2 \exp \left(-\frac{3\delta^2}{2} \right) \sinh \left(\delta \sqrt{\ln 4} \right) . \quad (\text{A.7c})$$

A convenient relation between the two relative widths S/\bar{N} and $\Delta N_{1/2}/\bar{N}$ is obtained from equations (A.6b) and (A.7c):

$$\frac{\Delta N_{1/2}}{\bar{N}} = 2 \left(\frac{S^2}{\bar{N}^2} + 1 \right)^{-\frac{3}{2}} \sinh \left[\sqrt{\ln 4 \cdot \ln \left(\frac{S^2}{\bar{N}^2} + 1 \right)} \right] . \quad (\text{A.8})$$

More information on the log-normal distribution can be found in references [271] and [272].

Appendix B

Abel inversion

Consider a three-dimensional distribution $f(r, z)$ of cylindrical symmetry about the z -axis of a Cartesian coordinate system (x, y, z) . Let $r = \sqrt{x^2 + y^2}$ denote the distance from the z -axis. A projection along the x -axis yields a two-dimensional distribution $p(y, z)$ in the yz -plane. Mathematically, the projection along the x -axis can be written as

$$p(y, z) = \int_{-\infty}^{+\infty} dx f(\sqrt{x^2 + y^2}, z) = 2 \int_0^{\infty} dx f(\sqrt{x^2 + y^2}, z) = 2 \int_{|y|}^{\infty} \frac{f(r, z) r dr}{\sqrt{r^2 - y^2}} \quad (\text{B.1})$$

which is the common definition of the Abel transform.²⁰⁹ Note that the cylindrical symmetry of $f(r, z)$ leads to projection $p(y, z)$ of *even* symmetry in the y -coordinate. *i.e.* $p(-y, z) = p(y, z)$.

In order to recover the distribution $f(r, z)$ from the projection $p(y, z)$ the *inverse* Abel transform is required which usually is given in the form²⁰⁹

$$f(r, z) = -\frac{1}{\pi} \int_r^{\infty} \frac{\frac{d}{dy} p(y, z)}{\sqrt{y^2 - r^2}} dy . \quad (\text{B.2})$$

For numerical purposes equation (B.2) is however of little use since the derivative involved greatly enhances any experimental noise. Moreover, the singularity at the lower limit of the integral is difficult to handle.

A much more robust numerical inversion scheme^{273,274} can be obtained by reconsidering equation (B.1). The one-dimensional Fourier transform of $p(y, z)$ can be written as

$$\mathcal{F}\{p(y, z)\}(q, z) = \int_{-\infty}^{+\infty} dy \int_{-\infty}^{+\infty} dx f(\sqrt{x^2 + y^2}, z) \exp(-i2\pi yq) . \quad (\text{B.3})$$

Since the Fourier transform of a real and even function must again be real and even, all imaginary and odd terms drop and we obtain

$$\mathcal{F}\{p(y, z)\}(q, z) = \int_{-\infty}^{+\infty} dx \int_{-\infty}^{+\infty} dy f(\sqrt{x^2 + y^2}, z) \cos(2\pi xq) , \quad (\text{B.4})$$

where the integration variables x and y were interchanged for convenience. Changing from Cartesian to polar integration variables (r, ϕ) using $r = \sqrt{x^2 + y^2}$ and $x = r \cos \phi$ results in

$$\mathcal{F}\{p(y, z)\}(q, z) = \int_0^{\infty} dr r f(r, z) \int_0^{2\pi} d\phi \cos(2\pi r q \cos \phi) \quad (\text{B.5})$$

which can be simplified considerably with the aid of the zero-order Bessel function of the first kind J_0 given by

$$J_0(x) = \frac{1}{\pi} \int_0^\pi d\phi \cos(x \cos \phi) . \quad (\text{B.6})$$

This results in

$$\mathcal{F}\{p(y, z)\}(q, z) = 2\pi \int_0^\infty dr r f(r, z) J_0(2\pi r q) = \mathcal{H}\{f(r, z)\}(q, z) , \quad (\text{B.7})$$

where the middle expression of equation B.7 is identified as the one-dimensional (zero-order) Hankel transform of $f(r, z)$. Since forward and inverse Hankel transforms are identical, *i.e.* $\mathcal{H} \circ \mathcal{H} = 1$, one finally has

$$f(r, z) = \mathcal{H} \circ \mathcal{F}\{p(y, z)\} , \quad (\text{B.8})$$

where \mathcal{H} and \mathcal{F} stand for the *one-dimensional* Hankel and Fourier transforms, respectively, applied to the *first* dimension of $p(y, z)$.

It is important to realize that equation (B.8) only yields a *real* distribution $f(r, z)$, *i.e.* has a physical meaning, if the projection $p(y, z)$ is indeed even in y as assumed when deriving the transform identity. Before applying these transforms to an experimentally acquired image it is thus indispensable to first locate the symmetry axis of the recorded, noise-affected projection and secondly to process the data such that the input projection to the integral transforms is symmetric about this axis. Experimentally, this is greatly facilitated by orienting the camera such that an axis of the CCD chip, say the columns, is parallel to the symmetry axis of the projection. In this case the coordinates y and z can be taken as indices to the rows and columns of the discrete image and a further introduction of noise by a mathematical rotation of the image is avoided. The inversion formula given by equation (B.8) then represents simply a sequence of one-dimensional and independent integral transforms applied to the rows of the discrete image. Once the symmetry axis is located, a symmetric input $p(y, z)$ to the transforms (B.8) can be obtained by averaging the left ($y < 0$) and right ($y > 0$) side of the recorded image or by calculating separate Abel inversions for the left and right side for the purpose of comparison.

These integral transforms are widely used and computationally efficient as one can make use of the fast Fourier transform (FFT) algorithm developed by Cooley and Tukey.²⁷⁵ However, this so-called Fourier-Hankel method is sensitive to experimental noise which affects the computed Abel inversion particularly at small distances r to the symmetry axis. For especially noisy images this so-called “center-line noise” may reach such an intensity that an inversion by the integral transforms becomes impracticable. Other known problematical inputs to the Fourier-Hankel method include images of a large dynamic range or with highly peaked angular or radial distributions.^{208, 276}

An alternative method to compute an Abel inversion is forward convolution. In this approach a simulated projection is calculated from a three-dimensional trial distribution and compared to the experimental image. Based on the comparison the trial distribution may be iteratively improved until a reasonable agreement between the simulated and the experimental image is achieved. The advantage of this approach is that the Abel transform, in contrast to its inversion, is computationally cheap and numerically straightforward. A particularly powerful forward convolution algorithm that overcomes many limitations of the Fourier-Hankel method

has been proposed by Vrakking.²⁰⁸ His method explicitly makes use of the similarities between the radial and angular distributions of the two-dimensional (2D) projection and the three-dimensional (3D) velocity distribution with cylindrical symmetry axis. Transforming both the experimental and the simulated projection into 2D polar coordinates is one of the key steps of this algorithm. This way useful corrections to the radial and angular part of the 3D trial distribution are calculated directly from the differences between both projections, using empirical feedback coefficients. Note that in contrast to the Fourier-Hankel method the Abel inversion is not obtained from a sequence of independent one-dimensional transforms, but is brought about by true 2D→2D data processing. An important consequence of this treatment concerns the appearance of noise in the inverted distribution. Contrary to the Fourier-Hankel method which projects the experimental noise towards the symmetry axis, Vrakking's algorithm condenses the noise around the *center* of the inversion, where it is less likely to impair the observation of relevant structures. Although numerically costly (typically about 50 iterations are required) this particular forward convolution algorithm has the benefit of great versatility, since satisfactory solutions are obtained for virtually all Abel inversion problems.

The Abel inversion software created as part of this work includes both the Fourier-Hankel method and Vrakking's algorithm. Although the forward convolution method is preferred, computer time can be saved by using the result of the rapid Fourier-Hankel technique as a first guess for the iterative procedure. As a consequence of the identity (B.8) the implementation of the integral transform technique involves computing an one-dimensional FFT on each line of the experimental image, followed by a discrete Hankel transform. In order to suppress numerical artifacts, the argument of each FFT is padded with trailing zeros to four times the length of the original vector. For the Hankel transform we use a fast FFT-based algorithm developed by Candel.²⁷⁷ The implementation of Vrakking's forward convolution method is straightforward. A minor change to the original algorithm was made by introducing a dynamical adjustment of the feedback coefficients between two iterations of the inversion process. In many cases the thus modified algorithm is found to converge faster. Moreover, over-corrections of the trial distribution, which in certain cases can lead to an oscillatory behaviour, are avoided.

We illustrate the performance of our software by inverting a noise-free synthetic image that was calculated using the Abel transform as defined in equation (B.1). The synthetic projection is based on a 3D distribution $P(R, \theta)$ defined as

$$\begin{aligned}
 P(R, \theta) = & 2000 \left(7e^{[-(R-10)^2/4]} \sin^2 \theta + 3e^{[-(R-15)^2/4]} + 5e^{[-(R-20)^2/4]} \cos^2 \theta \right) + \\
 & 200 \left(e^{[-(R-70)^2/4]} + 2e^{[-(R-85)^2/4]} \cos^2 \theta + e^{[-(R-100)^2/4]} \sin^2 \theta \right) + \\
 & 50 \left(2e^{[-(R-145)^2/4]} \sin^2 \theta + e^{[-(R-150)^2/4]} + 3e^{[-(R-155)^2/4]} \cos^2 \theta \right) + \\
 & 20 e^{[-(R-45)^2/3600]} , \tag{B.9}
 \end{aligned}$$

where we use spherical coordinates R and θ for convenience. These coordinates are related to the previously used cylindrical coordinates r and z by $r = R \sin \theta$ and $z = R \cos \theta$. The distribution (B.9) is a good candidate to test a particular implementation since some of its features, such as the high-intensity rings close to the center as well as the superposition of broad low-intensity and radially sharp high-intensity structures, are known to cause problems to the Fourier-Hankel method. Moreover, the distribution was used previously by Dribinski *et al.*²⁷⁶

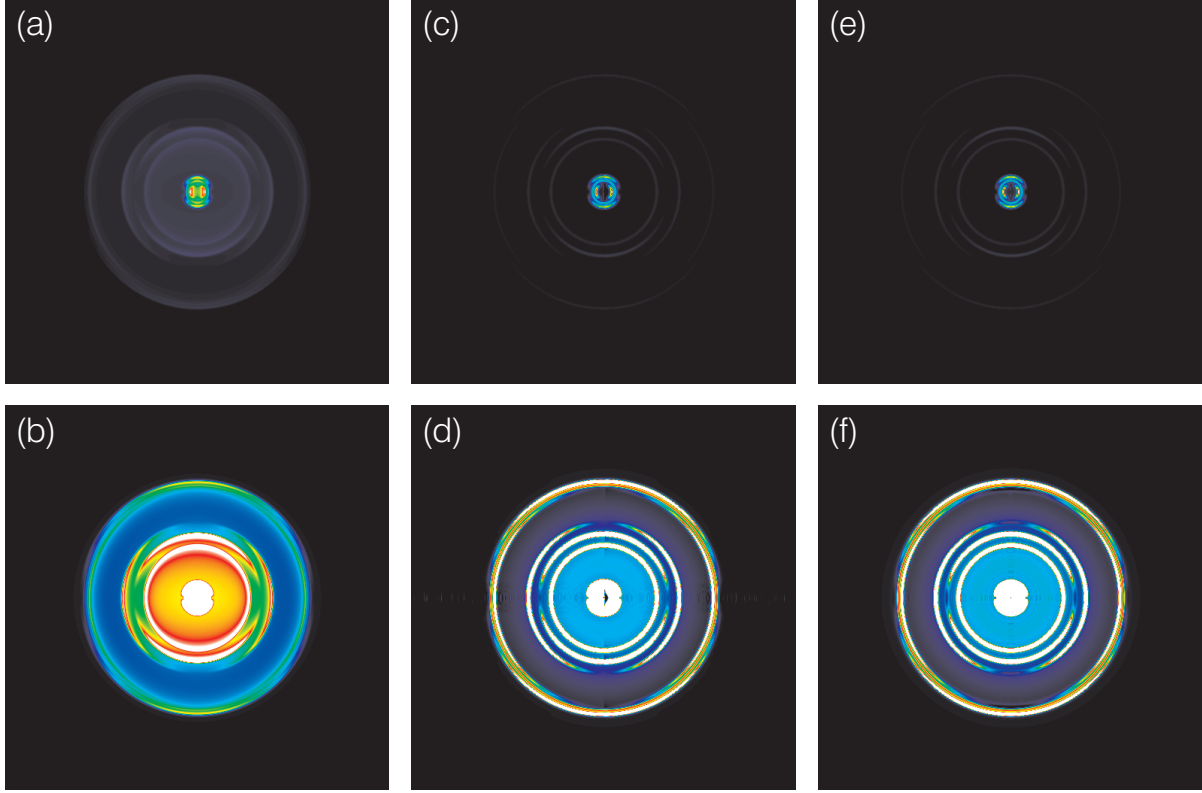


FIGURE B.1: (Color) Synthetic projection image ((a) and (b)) and sections through the recovered three-dimensional distribution ((c)–(f)). The sections are obtained by the Fourier-Hankel method ((c) and (d)), and by 50 additional iterations using the forward convolution algorithm by Vrakking ((e) and (f)). The intensities of the images (b), (d) and (f) are enhanced by factors of 22.5, 240, and 240, respectively, in order to bring low-intensity structures to light. All images are nominally symmetric about a vertical axis and have a size of 512×512 pixels.

to illustrate shortcomings of the Abel inversion by integral transforms. Comparing the obtained inversions thus gives us the possibility to better judge the performance of our particular implementation of the Fourier-Hankel algorithm.

Figure B.1 illustrates the synthetic projection ((a) and (b)), a section through the reconstructed 3D distribution obtained by the Fourier-Hankel method ((c) and (d)), and the section after an additional 50 iterations using the algorithm by Vrakking ((e) and (f)). In order to reveal low-intensity features, the intensities of the images (b), (d) and (f) are enhanced by factors of 22.5, 240, and 240, respectively. The color scale is identical to the one shown in Figure 4.1. It becomes clear that the inversion obtained by the Fourier-Hankel method shows some left-right asymmetries as well as some low-intensity artifacts. These features are largely removed by the subsequent iterative process. Note that in this particular case further iterations will lead to even better results. The improvement of the Abel inversion by the forward convolution method is highlighted in Figure B.2 which shows the radial dependence of the anisotropy parameter β . While the Fourier-Hankel method introduces a prominent artifact at a radius of about 70 pixels

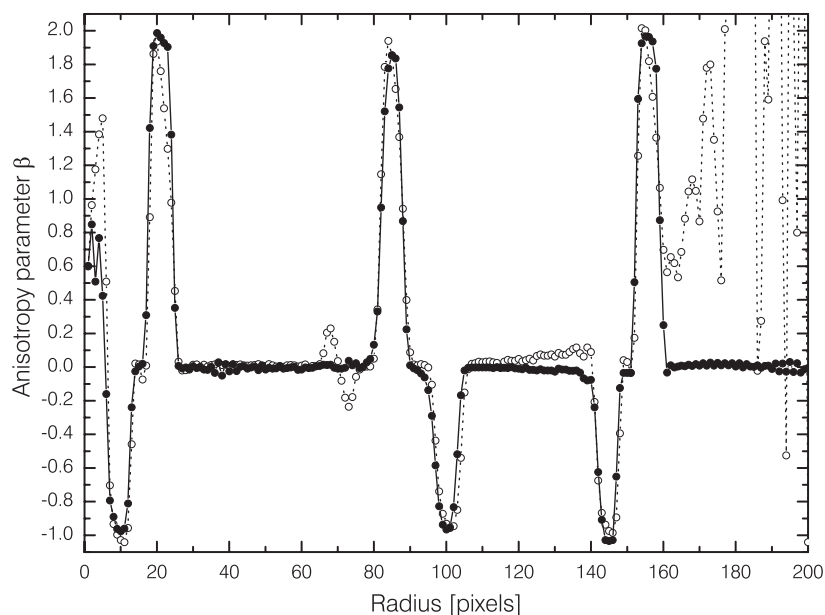


FIGURE B.2: Radial dependence of the anisotropy parameter β obtained by the Fourier-Hankel technique (dashed line, open circles) and after an additional 50 iterations using the forward convolution method by Vrakking (solid line, closed circles). The radial resolution was set to 1 pixel in all computations. All angular distributions were sampled on a grid of 256 points.

and has problems to obtain the correct isotropic distribution at large radii, these inaccuracies are eliminated by the subsequent iterations. Regarding the performance of our Fourier-Hankel method we note that compared to the implementation used by Dribinski *et al.* in reference [276] substantially better results are obtained.

Figure B.3 shows the graphical user interface of the Abel inversion software. The user interface is coded in *MATLAB* language, whereas all time-critical computations are programmed in speed-optimized *C* subroutines. This way the numerically extensive iterations of the forward convolution method can be accomplished in a reasonable amount of time. One iteration on a $512 \text{ pixel} \times 512 \text{ pixel}$ image thus takes about 45 seconds on a personal computer with a 1 GHz Pentium III processor.

Aside from the Abel inversion routines discussed above the software includes an extensive set of image processing and analysis tools. All common image processing tasks prior or subsequent to the inversion process, as well as many analysis calculations, can thus be carried out within a single application. Moreover, a large variety of viewing options permit revealing many aspects of the data prior, during or after the (iterative) inversion process. The most frequently used image processing subroutines permit cosmic ray filtering, image cropping and automatic determination of the symmetry axis and the image origin. Although not used for this work, various smoothing techniques are available. These include 2D linear filters with Gaussian convolution kernel and 2D order-statistical filters. Moreover, the software can perform a radially-resolved Fourier moment analysis of the angular intensity distribution of the experimental projection (see reference [278]) from which noise-reduced low-frequency components may be selected as an input to the Abel

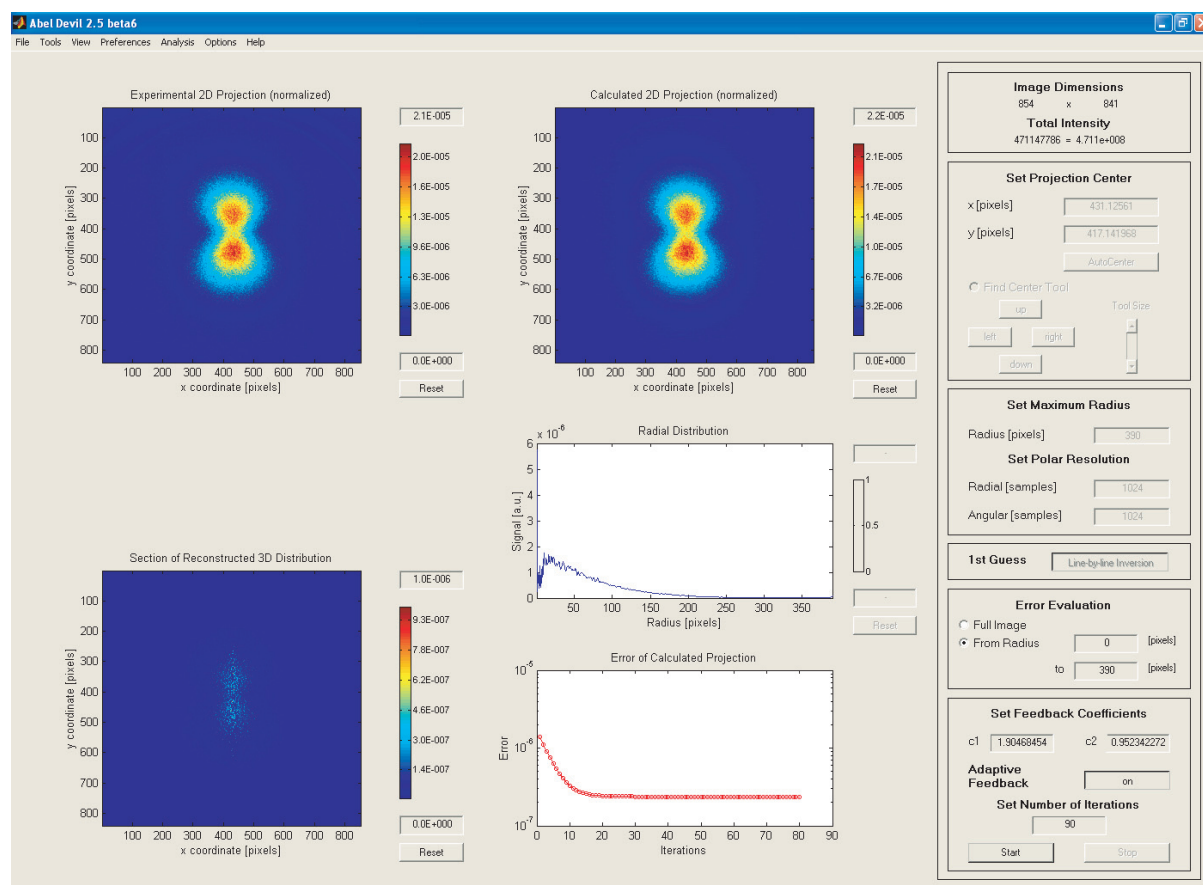


FIGURE B.3: (Color) Screen shot showing the graphical user interface of the Abel inversion software programmed as part of this thesis work. The data corresponds to CF_3 fragments departing from liquid helium clusters in the aftermath of the 266 nm photolysis of solvated CF_3I molecules. Other features of the data may be displayed by choosing different view options.

inversion. Once a reconstructed 3D distribution is available the anisotropy parameter may be calculated as a function of the 3D radius. All calculated distributions can be written to file in various formats to be read, processed or displayed by other applications.

Appendix C

Pick-up induced droplet angular momenta

An off-center collision between a helium cluster and a gas phase molecule will give angular momentum to the droplet. In this section we will estimate the resulting rotational period τ of droplets that underwent a single fully inelastic collision with a foreign particle. A knowledge of this time scale is vital to the interpretation of the imaging data since a rapid rotation of the droplets could potentially wash-out the angular distribution of escaping photofragments. Residual angular momentum from collisions in the expansion process is neglected.

For the benefit of simplicity the following description treats the droplets as homogeneous spheres of bulk ^4He density. In most cases it is safe to assume that the colliding particle is much lighter than the helium droplet and that therefore the center of mass of the system coincides with the droplet center. In this frame a particle of mass m_S impinging with relative speed v and impact parameter b onto the droplet thus carries an angular momentum $L = m_S v b$. If the angular momentum is transferred entirely to the then doped helium cluster the collision event generates a droplet angular speed of

$$\omega = \frac{m_S v b}{I} = \frac{2\pi}{\tau}, \quad (\text{C.1})$$

where I denotes the droplet's moment of inertia. It is assumed that the angular momentum L received in the pick-up process is preserved, although the droplet will lose some angular momentum in the ensuing evaporation of helium atoms from its surface. Furthermore, we will neglect the vector character of the angular velocities $\boldsymbol{\omega}$ and calculate only scalar quantities ω . In reality, however, the distribution of $\boldsymbol{\omega}$ in the laboratory frame will not be isotropic. This effect is brought about by the anisotropy of the droplet speed v_D which, when traversing a scattering cell, leads to an enhanced probability for collisions with the front side of the helium clusters. As a result, collisions preferentially excite rotations about any axis perpendicular to the propagation direction of the droplet beam, while rotations about an axis parallel to the beam axis are somewhat suppressed.

For a rigid and uniform sphere the moment of inertia about an axis through its center is given by $I = \frac{2}{5}MR^2$, where M and R denote the droplet mass and radius, respectively. With

the aid of equation (1.6) and the mass m_4 of individual ^4He atoms obtains

$$I = \frac{2}{5} m_4 r_0^2 N^{\frac{5}{3}} \quad (\text{C.2})$$

for a ^4He droplet of size N . The change of droplet mass and moment of inertia due to the impurity is negligible for large droplets and light impurities. Accordingly, ω may be written as

$$\omega = \frac{5}{2} \frac{m_S}{m_4} \frac{vb}{r_0^2} N^{-\frac{5}{3}}. \quad (\text{C.3})$$

For a given droplet size N the angular speed ω hence is solely determined by the impact parameter b and the relative speed v . Consequently, an upper estimate $\omega_{\max}(N)$ can be obtained by evaluating equation (C.3) for the largest impact parameter and the most elevated relative speed that may occur experimentally. Similarly, we will calculate a statistical mean $\langle\omega\rangle(N)$ from the distributions of impact parameters and relative speeds in a gas-filled scattering cell.

Usually the dimensions of the scattering particle will be negligible compared to the droplet size. In this limit $b = R$ constitutes the maximum impact parameter. The Maxwell-Boltzmann speed distribution predicts that more than 99% of the scattering particles have speeds inferior to $2\sqrt{3k_B T_S/m_S}$, where T_S denotes the kinetic temperature of the gas. Furthermore, the most elevated relative speeds occur if the velocity vectors of droplet and impinging particle are anti-parallel. A reasonably safe upper estimate $\omega_{\max}(N)$ may therefore be written as

$$\omega_{\max}(N) \cong \frac{5}{2} \frac{m_S}{m_4} \frac{N^{-\frac{4}{3}}}{r_0} \left(v_D + 2\sqrt{\frac{3k_B T_S}{m_S}} \right), \quad (\text{C.4})$$

where v_D is the droplet beam speed.

Equation (C.3) is linear in both b and v . The average angular speed $\langle\omega\rangle(N)$ can thus conveniently be calculated from the mean impact parameter $\langle b \rangle$ and the mean relative speed $\langle v \rangle$. Using the statistical distribution

$$g(b) db = \frac{2\pi b}{\pi R^2} db = \frac{2b}{R^2} db \quad (\text{C.5})$$

of impact parameters $b \in [0, R]$, one finds

$$\langle b \rangle = \int_0^R b g(b) db = \frac{2}{3} R = \frac{2}{3} r_0 N^{\frac{1}{3}}. \quad (\text{C.6})$$

A very good approximation to the mean relative speed $\langle v \rangle$ in a scattering cell is given by

$$\langle v \rangle \cong \sqrt{v_D^2 + \langle v_S \rangle^2}, \quad (\text{C.7})$$

where

$$\langle v_S \rangle = \sqrt{\frac{8}{\pi} \frac{k_B T_S}{m_S}} \quad (\text{C.8})$$

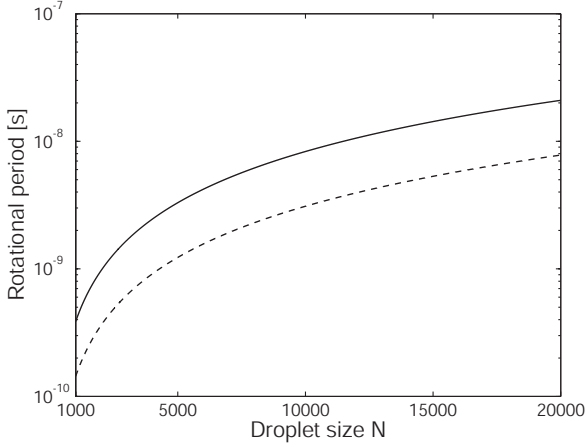


FIGURE C.1: Rotational period of size N helium droplets resulting from a single sticking collision with the scattering gas. The graph shows rotational periods corresponding to the most elevated (dashed line) and the mean angular speed (solid line) as obtained from equations (C.4) and (C.9), respectively. The displayed curves were calculated for $v_D = 405$ m/s, $T_S = 295$ K and $m_S = 196$ amu.

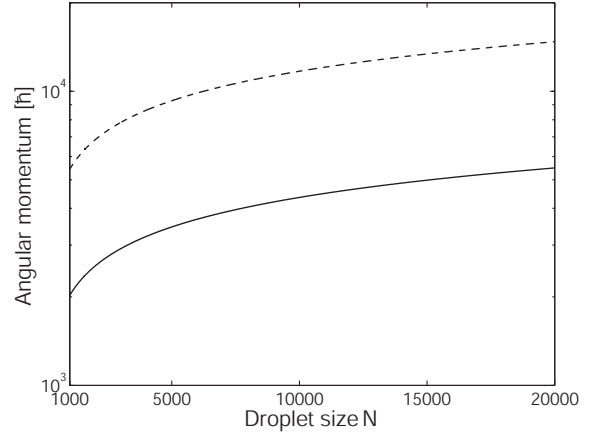


FIGURE C.2: Angular momentum of singly doped helium clusters of size N . Angular momenta are given in units of \hbar . The curves show both the maximum (dashed line) and the average value (solid line). The data was obtained using the same parameters as in Figure C.1.

denotes the mean thermal speed of the scattering particles. One therefore has finally

$$\langle \omega \rangle(N) = \frac{5}{3} \frac{m_S}{m_4} \frac{N^{-\frac{4}{3}}}{r_0} \sqrt{v_D^2 + \frac{8}{\pi} \frac{k_B T_S}{m_S}}. \quad (\text{C.9})$$

We note again that due to the anisotropy introduced by the droplet velocity the angular speeds about a particular axis will generally deviate from the mean value derived here. Rotational periods τ and angular momenta L calculated directly from the maximum and mean angular speeds are shown in Figure C.1 and Figure C.2 as a function of droplet size N . The computed rotational period is found to increase with the clusters size. In the droplet size range $1000 \leq N \leq 20000$ rotational periods τ in excess of 100 ps and angular momenta of several thousand \hbar are predicted.

In order to provide a more realistic description equation (C.9) may also be averaged over the experimental droplet size distribution. For moderate scattering cell pressures one may neglect the pick-up of two and more impurities. The probability of picking-up one impurity then is roughly proportional to the classical geometrical cross section and hence to $N^{\frac{2}{3}}$ (see Section 2.4 for a more detailed discussion). The normalized size distribution $h(N)$ of singly doped droplets thus becomes

$$h(N) = \frac{N^{\frac{2}{3}} \cdot f(N)}{\int_0^\infty N^{\frac{2}{3}} f(N) dN} = (N/\bar{N})^{\frac{2}{3}} \cdot f(N) \cdot \exp(\delta^2/9), \quad (\text{C.10})$$

where, as usual, $f(N)$ denotes the log-normal atom number distribution of pure helium droplets of mean size \bar{N} prior to entering the scattering cell. Accordingly, the size-distribution-averaged

mean angular speed $\overline{\langle \omega \rangle}$ of *doped* droplets can be written as

$$\overline{\langle \omega \rangle} = \int_0^\infty h(N) \langle \omega \rangle(N) dN . \quad (\text{C.11})$$

By applying equation (A.5) one finds:

$$\overline{\langle \omega \rangle} = \frac{5 m_S}{3 m_4} \frac{\overline{N}^{-\frac{4}{3}}}{r_0} \sqrt{v_D^2 + \frac{8 k_B T_S}{\pi m_S}} \cdot \exp(2\delta^2/3) . \quad (\text{C.12})$$

Here δ stands for a parameter of the log-normal distribution as defined in Appendix A. For the experimentally determined value of $\delta \approx 0.55$ (see Section 2.3) the average angular speed $\overline{\langle \omega \rangle}$ therefore is 22 % higher than the possible approximation $\langle \omega \rangle(\overline{N})$.

Appendix D

Modeling fragment motion in helium droplets

In this section we present two simplistic models for the motion of particles in liquid ^4He . Based on the macroscopic notion of viscous flow the first description permits one to estimate the kinetic energy losses experienced by the traveling particle as a function of distance. The second model predicts both the energy losses and the trajectory deflections assuming independent elastic hard-sphere collisions with single helium atoms. In this highly simplified microscopic picture the helium atoms are assumed to be initially at rest in the droplet frame, *i.e.* their thermal motion is neglected.

D.1 Viscous flow

Approximating the geometry of the particle by a sphere one may apply Stokes' formula²⁷⁹

$$F_d = -6\pi\eta vr \quad (\text{D.1})$$

to calculate the drag force F_d on the particle of mass m . In this formula η denotes the viscosity of the liquid, v is the speed of the particle relative to the droplet frame and r stands for the impurity radius. Introducing the traveled distance L in the medium one finds

$$v(L) = v_i - 6\pi\eta r L/m, \quad (\text{D.2})$$

where v_i denotes the initial speed of the particle. Obviously, the maximal travel L_{\max} in the liquid is given by

$$L_{\max} = \frac{mv_i}{6\pi\eta r} = \frac{\sqrt{2mT_i}}{6\pi\eta r}, \quad (\text{D.3})$$

where we use $T_i = mv_i^2/2$ to denote the particle's initial kinetic energy. One therefore may write

$$v(L) = v_i \cdot (1 - L/L_{\max}) \quad (\text{D.4a})$$

or

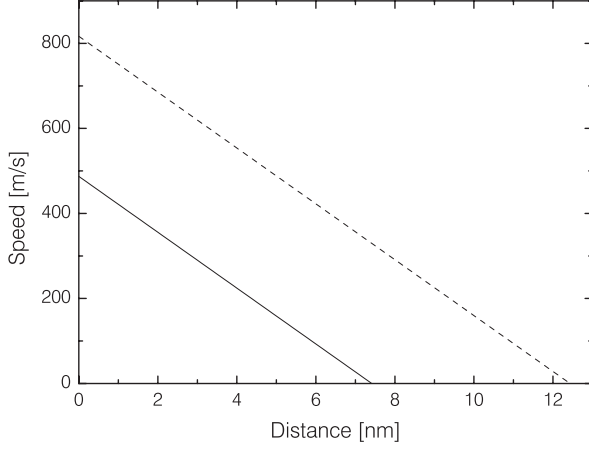


FIGURE D.1: Speed of iodine fragments traveling through liquid ${}^4\text{He}$ as a function of distance. The graph illustrates the predictions of Stokes' law for two different initial kinetic energies. These energies correspond to the mean initial kinetic energies of iodine fragments created by dissociating CF_3I (dashed line) and CH_3I (solid line) with 266 nm light.

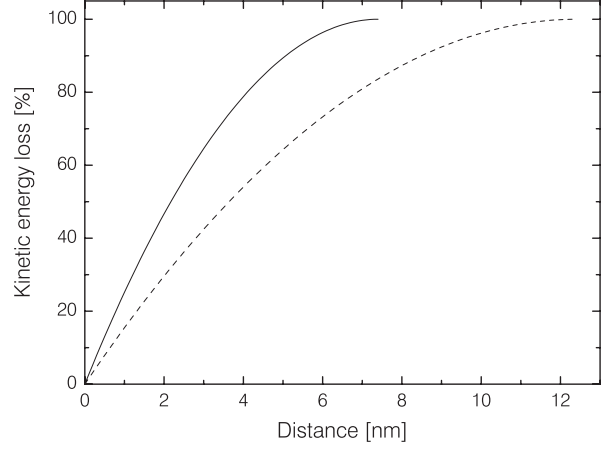


FIGURE D.2: Kinetic energy loss of iodine fragments traveling through liquid ${}^4\text{He}$ as a function of distance. The graph illustrates the predictions of Stokes' law for two different initial kinetic energies. These energies correspond to the mean initial kinetic energies of iodine fragments created by dissociating CF_3I (dashed line) and CH_3I (solid line) with 266 nm light.

$$T(L) = T_i \cdot (1 - L/L_{\max})^2, \quad (\text{D.4b})$$

where $T(L)$ is the position dependent kinetic energy. Note that the travel L_{\max} is a function of the initial kinetic energy T_i .

As an example, we use the expressions (D.4) to describe the motion of iodine fragments from the 266 nm dissociation of CF_3I and CH_3I in helium droplets. Since the droplet environment is thermally excited by the traveling fragment we base the calculations on the viscosity of liquid ${}^4\text{He}$ at 3.5 K, given as⁸ $\eta = 3.5 \cdot 10^{-6} \text{ kg m}^{-1} \text{ s}^{-1}$. The spin-orbit state averaged initial kinetic energies can be taken from Table 4.1 and are given as 3540 cm^{-1} (CF_3I) and 1260 cm^{-1} (CH_3I). Using a van der Waals radius²⁸⁰ of 2.1 \AA the maximal distance L_{\max} can be calculated as 12.4 nm (CF_3I) and 7.4 nm (CH_3I). The resulting fragment speed $v(L)$ and relative energy loss are plotted in Figures D.1 and D.2 as a function of distance. Owing to their smaller initial kinetic energy, iodine fragments from CH_3I are predicted to experience higher relative energy losses for any distance L traveled.

D.2 Elastic hard-sphere collisions

In this description the incident particle of mass m undergoes a series of independent elastic collisions with helium atoms of mass m_4 assumed to be at rest. Each collision causes a transfer of kinetic energy to the target atoms and consequently slows down the incident particle. At the same time each collision deflects the incident particle from its original direction of motion. The

kinetic energies T and T' of the incident particle before and after such a collision are related by²⁸¹

$$T' = T \cdot \frac{1 + 2\varrho \cos \Theta + \varrho^2}{(1 + \varrho)^2}, \quad (D.5a)$$

where $\varrho = m/m_4$ denotes the mass ratio of the particles involved, and Θ is the scattering angle in the center-of-mass frame. The scattering angle ϑ of the incident particle in the laboratory frame can be calculated from²⁸¹

$$\cos \vartheta = \frac{\cos \Theta + \varrho}{\sqrt{1 + 2\varrho \cos \Theta + \varrho^2}}. \quad (D.5b)$$

In case of hard-sphere scattering it is convenient to express the center-of-mass scattering angle Θ in the more general equations (D.5) by the impact parameter b . Introducing the sum of the hard-sphere radii of incident and target particle R we note that in order for a collision to occur the condition

$$0 \leq b \leq R \quad (D.6)$$

has to be fulfilled. The desired connection between Θ and b is established by the geometric relation²⁸²

$$b = R \cos (\Theta/2). \quad (D.7)$$

Using the identity

$$\cos \Theta = 2 \cos^2 (\Theta/2) - 1 \quad (D.8)$$

the equations (D.5) transform to

$$T' = T \cdot \frac{1 + 2\varrho [2 (b/R)^2 - 1] + \varrho^2}{(1 + \varrho)^2} \quad (D.9a)$$

and

$$\cos \vartheta = \frac{2 (b/R)^2 - 1 + \varrho}{\sqrt{1 + 2\varrho [2 (b/R)^2 - 1] + \varrho^2}}. \quad (D.9b)$$

These equations can be used to model the three-dimensional trajectory of a particle moving through a gas of non-interacting and initially stationary target atoms.

It is instructive to examine the *mean* kinetic energy change $\langle T'/T \rangle$ and the *mean* laboratory-frame scattering angle $\langle \vartheta \rangle$ per collision. For this purpose we average equations (D.9) over all impact parameters $b \in [0 R]$. Using the geometrical weight $2\pi b$ of each impact parameter one obtains the expressions

$$\langle T'/T \rangle = \frac{\int_0^R 2\pi b (T'/T) db}{\int_0^R 2\pi b db} = \frac{1 + \varrho^2}{(1 + \varrho)^2} \quad (D.10a)$$

and

$$\langle \vartheta \rangle = \frac{\int_0^R 2\pi b \vartheta db}{\int_0^R 2\pi b db} = 2 \int_0^1 a \arccos \left(\frac{2a^2 - 1 + \varrho}{\sqrt{1 + 2\varrho [2a^2 - 1] + \varrho^2}} \right) da, \quad (D.10b)$$

Fragment	Mass [amu]	$\langle T'/T \rangle$ %	$\langle \vartheta \rangle$ [deg]
I	127	94.1	1.42
CF ₃	69	89.6	2.61
CH ₃	15	66.8	12.00

TABLE D.1: Mean change of kinetic energy and mean laboratory frame scattering angle calculated for single elastic hard-sphere collisions of relevant photofragments with initially stationary ⁴He atoms.

the latter of which can easily be calculated numerically. The evaluation of equations (D.10) for the relevant photofragments yields the results displayed in Table D.1. It becomes clear that the light photofragment CH₃ loses a far higher proportion of its kinetic energy per collision than the relatively heavy iodine atoms. At the same time a collision with a ⁴He atom is predicted to cause a substantial deflections to the trajectory of the CH₃ fragments, while the direction of motion of iodine is little affected.

It is important to note that this description predicts fragments of equal mass and equal collision cross section traveling the same distance, *i.e.* undergoing the same number of collisions, to transfer on average an equal proportion of their initial kinetic energy to the medium. This is in stark contrast to Stokes' formula where these relative energy losses were found to depend on the initial kinetic energy.

List of Figures

1.1	Specific heat capacity of liquid ${}^4\text{He}$ as a function of temperature at saturated vapor pressure	2
1.2	Dispersion curve of bulk He II at a temperature of 1.1 K and under its saturated vapor pressure	2
1.3	Drag force on negative ions moving through highly pressurized He II kept at a temperature of 0.35 K as a function of the ions' mean speed	4
2.1	Phase diagram of ${}^4\text{He}$ in a logarithmic pressure-temperature representation . . .	14
2.2	Droplet beam speeds in the subcritical expansion regime	17
2.3	Cooling of large ${}^4\text{He}$ droplets due to evaporation from the surface	19
2.4	Size and evaporation rate of a thermally excited ${}^4\text{He}$ droplet as a function of cooling time	19
2.5	Internal energy of a $N = 10000$ ${}^4\text{He}$ droplet at elevated temperatures	20
2.6	Evaporation rates of ${}^4\text{He}$ clusters as a function of droplet temperature	20
2.7	Mean droplet size as a function of the scaling parameter Γ	22
2.8	Prediction of mean droplet sizes produced in subcritical expansions from a stagnation pressure of 30 bar and various stagnation temperatures T_o	22
2.9	Predicted atom number distributions $f(N)$ for a stagnation pressure of $p_o = 30$ bar and stagnation temperatures $T_o = 12, 15$ and 18 K	23
2.10	Distributions of droplet radii for a stagnation pressure of $p_o = 30$ bar and various stagnation temperatures	23
2.11	Calculated radial density profiles of various small and medium size ${}^4\text{He}$ and ${}^3\text{He}$ droplets	24
2.12	Plot of the surface thickness correction parameter Δr as a function of mean droplet size \bar{N}	25
2.13	Prediction of the mean classical total scattering cross section $\bar{\sigma}$ as a function of the mean droplet size \bar{N}	25
2.14	Plot of the correction factor $F_{a_0}(\infty, x)$	27
2.15	Contour plot of the correction factor $F_{a_0}(\infty, x)$ as a function of impurity mass and droplet speed	27
2.16	Comparison of the relative intensities $\overline{P}_k(ps)$ and $P_{\overline{N},k}(ps)$ for singly ($k = 1$) and doubly ($k = 2$) doped helium droplets	29

2.17	Intensity ratio of doubly to singly doped helium clusters as a function of the scattering cell pressure p_S	29
2.18	Plot of the relative intensities P_k of k -mer doped ^4He clusters as a function of the scattering cell pressure p_S	31
2.19	Schematic illustration of potential energy surfaces relevant to the photodissociation of CH_3I	37
2.20	Mean internal energy of the CF_3 fragments as measured in the red wing of the A band and at 248 nm	40
3.1	Accurate scale vertical cross section of the helium droplet machine through the axis of the molecular beam	44
3.2	Photograph of the helium droplet machine	46
3.3	Mass spectrum of the residual gas in the baked detection chamber	48
3.4	Arrangement of apertures and resulting beam geometry	50
3.5	Attenuation of a helium droplet beam as a function of helium pressure in the doping chamber	50
3.6	Partial helium pressure and particle flux into the source chamber	51
3.7	Partial helium pressure and particle flux into the detection chamber	51
3.8	Estimated droplet flux into the detection chamber as a function of stagnation temperature	51
3.9	Load map of the <i>RDK-205D</i> cold head (60 Hz)	52
3.10	Load map of the <i>RDK-205D</i> cold head (50 Hz)	52
3.11	Details of the cryogenic cluster source	53
3.12	Details of the orifice assembly	54
3.13	Photograph of the orifice assembly	55
3.14	Cross section of the platinum-iridium disk into which the orifice is drilled	56
3.15	Scanning electron microscope image of a typical $5\ \mu\text{m}$ orifice	56
3.16	Ion currents for the droplet fragment ions He^+ and He_2^+ for expansion conditions in the vicinity of the critical point of ^4He	61
3.17	First derivative of the He_2^+ ion currents with respect to the temperature measured on the orifice assembly for various stagnation pressures p_o	62
3.18	Temperatures of the maxima shown in Figure 3.17 versus nominal temperatures given by the isentrope through the critical point	62
3.19	Typical refrigeration behaviour of the helium droplet source	63
3.20	Typical minimum sustainable stagnation temperatures for a $5\ \mu\text{m}$ orifice	63
3.21	Plot of the ion current ratio $R_{2,1}(p_S)$	68
3.22	Plot of the ion current ratio $\tilde{R}_{2,1}(p_{\text{cross}})$	68
3.23	Ratio of the slopes $\tilde{\alpha}(\bar{N}) \bar{\sigma}_{\text{cap}}(\bar{N})$ and $\alpha(\bar{N}) \bar{\sigma}_{\text{cap}}(\bar{N})$	69
3.24	Contour plot of the intensity ratio P_2/P_1 of dimer and monomer doped helium droplets as a function of helium stagnation temperature T_o and scattering gas pressure p_S	69
3.25	Conventional single-grid ion imaging apparatus as developed by Chandler and Houston	71

3.26	Sensitivity of the MCP detector used in our imaging setup as a function of repeller voltage V_R	74
3.27	Ion optics assembly of the velocity map imaging setup with einzel lens	76
3.28	Experimentally found optimal extractor voltages V_E for various repeller voltages V_R	81
3.29	Raw and Abel inverted image of aniline photoelectrons created by [1 + 1'] REMPI processes	82
3.30	Internal calibration of the imaging setup without einzel lens	83
3.31	Kinetic energy distribution of photoelectrons created via [1 + 1'] REMPI in jet-cooled aniline	83
3.32	Experimentally determined optimal extractor voltages V_E for various einzel lens voltages V_{lens}	84
3.33	Magnification of the einzel lens at a repeller voltage of $V_R = -4000$ V and various einzel lens voltages V_{lens}	84
3.34	Electronic schematics for the ion and electron imaging experiments	87
4.1	Color scale used to display two-dimensional intensity distributions	94
4.2	Time-of-flight mass spectra of ions produced by irradiating CF_3I -doped helium droplets with various laser pulse sequences	96
4.3	Time-of-flight mass spectra of ions produced by irradiating CH_3I -doped helium droplets with various laser pulse sequences	96
4.4	Effect of the time delay Δt between ns and fs laser pulses on the time-of-flight mass spectrum of products created by the A band photolysis of CH_3I in the interior of ^4He droplets	99
4.5	Droplet size effect on the relative signals of the IHe_n products created by the 266 nm photodissociation of CF_3I in helium droplets	100
4.6	Droplet size effect on the relative signals of the IHe_n products created by the 266 nm photodissociation of CH_3I in helium droplets	100
4.7	Velocity map images of escaping bare iodine fragments from the 266 nm photodissociation of CF_3I and CH_3I in ^4He droplets	102
4.8	Velocity map images of departing IHe_n products ($n = 1, 2, \dots, 12$) from the 266 nm photodissociation of CF_3I in ^4He droplets	103
4.9	Velocity map images of departing IHe_n products ($n = 1, 2, \dots, 12$) from the 266 nm photodissociation of CH_3I in helium droplets	104
4.10	Measured and fitted speed distribution of departing IHe_2 complexes from the photolysis of CF_3I in helium droplets	105
4.11	Measured and fitted speed distribution of departing IHe_9 complexes from the photolysis of CH_3I in helium droplets	105
4.12	Most probable speeds of the departing IHe_n products from the 266 nm photolysis of CF_3I and CH_3I in helium droplets	106
4.13	Widths (FWHM) of the speed distributions of departing IHe_n products from the 266 nm photolysis of CF_3I and CH_3I in helium droplets	106
4.14	Comparison of the speed distributions of departing IHe_n products from the 266 nm photolysis of CF_3I and CH_3I embedded in helium droplets, measured at a helium stagnation temperature of 15 K	110

4.15	Mean kinetic energy of individual departing IHe_n products from the 266 nm photolysis of CF_3I and CH_3I in helium droplets	110
4.16	Overall kinetic energy distribution of all IHe_n product complexes escaping from CF_3I -doped ^4He droplets produced at the stagnation temperature $T_o = 15$ K	111
4.17	Overall kinetic energy distribution of all IHe_n product complexes escaping from CH_3I -doped ^4He droplets produced at the stagnation temperature $T_o = 15$ K	111
4.18	Overall mean kinetic energy of the IHe_n products escaping from CF_3I -doped ^4He droplets as a function of the helium stagnation temperature	113
4.19	Overall mean kinetic energy of the IHe_n products escaping from CH_3I -doped ^4He droplets as a function of the helium stagnation temperature	113
4.20	Mean anisotropy parameters of individual departing IHe_n products from the photolysis of CF_3I in the interior of ^4He droplets	114
4.21	Mean anisotropy parameters of individual departing IHe_n products from the photolysis of CH_3I in the interior of ^4He droplets	114
4.22	Energy available in a two-body I–He collision as a function of relative speed	121
4.23	Outcome of the 266 nm A band photolysis of CH_3I in ^4He droplets additionally doped with on average two extra Ar atoms	121
4.24	Typical velocity map images of escaping bare CF_3 photofragments	124
4.25	Typical speed distributions of escaping bare CF_3 fragments	124
4.26	Typical kinetic energy distributions of escaping bare CF_3 fragments	124
4.27	Mean kinetic energy of escaping bare CF_3 radicals as a function of the helium stagnation temperature	126
4.28	Anisotropy parameter distribution $\beta(v)$ and speed distribution of bare CF_3 fragments escaping from ^4He droplets produced at $T_o = 15$ K	127
4.29	Averaged and limiting anisotropy parameters of escaping CF_3 radicals as a function of the stagnation temperature T_o	127
4.30	Typical velocity map images of escaping bare CH_3 fragments in the vibrational ground state	129
4.31	Typical speed distributions of escaping bare CH_3 fragments in the vibrational ground state	129
4.32	Typical kinetic energy distributions of escaping bare CH_3 fragments in the vibrational ground state	129
4.33	Mean kinetic energy of escaping bare vibrational ground state CH_3 radicals as a function of the helium stagnation temperature	131
4.34	Anisotropy parameter β as a function of fragment speed v and the speed distribution of bare CH_3 fragments in the vibrational ground state escaping from ^4He droplets produced at $T_o = 15$ K	132
4.35	Averaged and limiting anisotropy parameters of escaping bare CH_3 radicals in the vibrational ground state as a function of stagnation temperature T_o	132
4.36	Speed distributions of vibrational ground state and umbrella mode excited ($\nu_2 = 1$) CH_3 fragments escaping from ^4He droplets produced at a helium stagnation temperature of 15 K	133

4.37	Plot of the anisotropy parameter versus speed for vibrational ground state and umbrella mode excited ($\nu_2 = 1$) CH_3 fragments escaping from ^4He droplets produced at a helium stagnation temperature of 15 K	133
4.38	Time-of-flight mass spectrum illustrating the formation of CH_3He_n complexes in the aftermath of the photolysis of CH_3I in the interior of ^4He droplets	134
4.39	Most probable speed and FWHM of the CH_3He_n speed distributions observed at a helium stagnation temperature of 15 K	134
4.40	Velocity map image of escaping CH_3He_1 products created by the 266 nm photolysis of CH_3I in ^4He droplets produced at a stagnation temperature of 15 K.	135
4.41	Anisotropy parameter β of escaping CH_3He_1 complexes as a function of product speed, observed at a stagnation temperature of 15 K	135
4.42	Mean kinetic energy of various escaping products as fraction of the gas phase value, observed at a stagnation temperature of 15 K	139
4.43	Mean anisotropy parameter of various escaping products as fraction of the gas phase value, observed at a stagnation temperature of 15 K	139
4.44	Velocity map images of CH_3I parent molecules in the detection volume of the ion imaging setup at various stagnation temperatures	145
4.45	Velocity map images of CF_3I parent molecules in the detection volume of the ion imaging setup at various stagnation temperatures	146
4.46	Experimentally observed and decomposed speed distributions of both recombined CH_3I molecules and “directly” escaping IHe_4 complexes at the stagnation temperature $T_o = 18$ K	148
4.47	Experimentally observed and decomposed speed distributions of both recombined CH_3I molecules and “directly” escaping IHe_4 complexes at the stagnation temperature $T_o = 15$ K	148
4.48	Contribution of the recombination signal to the total detected ion signal as a function of stagnation temperature	148
4.49	Translational temperature of the recombination signal as a function of stagnation temperature	148
4.50	Velocity map images illustrating the change of the CH_3I recombination signal with the time delay Δt between UV photolysis and femtosecond ionization laser pulses	149
4.51	Contribution of the recombination signal to the total ion signal as a function of the time delay Δt between photolysis and ionization laser pulses	150
4.52	Translational temperature of the recombination signal as a function of the time delay Δt between photolysis and ionization laser pulses	150
4.53	Measured and simulated speed distribution of escaping CF_3 radicals from the 266 nm photolysis of single CF_3I molecules isolated in the interior of ^4He droplets ($T_o = 15$ K)	159
4.54	Measured and simulated speed distribution of escaping iodine-containing products from the 266 nm photolysis of single CF_3I molecules embedded in ^4He droplets ($T_o = 15$ K)	159
4.55	Simulated escape time distributions of departing CF_3 and I fragments from the 266 nm photodissociation of CF_3I in the interior of ^4He clusters ($T_o = 15$ K)	160

4.56	Measured and simulated speed distributions of CH ₃ fragments escaping from ⁴ He droplets produced at a stagnation temperature T_o of 18 K	161
4.57	Measured and simulated anisotropy parameter distributions $\beta(v)$ of CH ₃ fragments escaping from ⁴ He droplets produced at a stagnation temperature T_o of 18 K	161
4.58	Measurement of the droplet beam speed v_D from the displacement of (IHe ₁) ⁺ ion images with respect to the origin of the imaging setup	164
4.59	Plot of the droplet beam speed v_D measured by velocity map imaging as a function of the helium stagnation temperature T_o	164
4.60	Velocity map images of CH ₃ fragments in the vibrational ground state showing both the droplet and the gas phase contribution for different experimental conditions	165
4.61	Comparison of the gas phase background signal in the ion images of vibrational ground state CH ₃ fragments for various experimental conditions	165
B.1	Synthetic projection image and sections through the three-dimensional distribution recovered by different methods	180
B.2	Anisotropy parameters β obtained by performing an Abel inversion of a synthetic model image using different methods	181
B.3	Graphical user interface of the Abel inversion software	182
C.1	Rotational periods of singly doped ⁴ He clusters as a function of droplet size N .	185
C.2	Angular momenta of singly doped ⁴ He clusters as a function of droplet size N .	185
D.1	Speed of iodine fragments traveling through liquid ⁴ He as a function of distance as predicted by Stokes' law	188
D.2	Kinetic energy loss of iodine fragments traveling through liquid ⁴ He as a function of distance as predicted by Stokes' law	188

List of Tables

2.1	Internal energy of ^4He clusters as a function of droplet size N and droplet temperature T	20
2.2	Prediction of the mean droplet size \overline{N} for a stagnation pressure $p_o = 30$ bar and various stagnation temperatures T_o	20
2.3	Correction factor $F_{a_0}(\infty, x)$ for various scattering gases at room temperature . .	28
2.4	Molecular constants of CH_3I and CF_3I	33
2.5	Available energy following a collision between a helium droplet and a CH_3I or CF_3I molecule	33
2.6	Quantum yields, anisotropy parameters and energy partitioning in the 266 nm photodissociation of CH_3I	38
2.7	Quantum yields, anisotropy parameters and energy partitioning in the 266 nm photodissociation of CF_3I	41
3.1	Base and typical operating pressures of the differentially pumped vacuum stages of the helium droplet machine	49
3.2	Estimated contribution of the different heat transport mechanisms to the total heat load on first and second stage of the cold head.	60
3.3	Cold-cathode gauge correction factors for CH_3I and CF_3I	68
3.4	Typical cross beam backing pressures for various helium expansion conditions . .	70
3.5	Vibrational energy levels in the aniline cation used for the internal calibration of the velocity map imaging setup without einzel lens	82
3.6	Maximum laboratory frame kinetic energies observable with the velocity map imaging setup without einzel lens	85
3.7	Maximum laboratory frame kinetic energies observable with the velocity map imaging setup einzel lens	85
3.8	List of HV power supplies used in the imaging experiments	88
3.9	Typical voltages applied to the MCP and phosphor screen assembly for imaging experiments	88
4.1	Spin-orbit state averaged kinetic energies and estimated mean speeds of iodine fragments from the 266 nm A band dissociation of free CH_3I and CF_3I molecules in the gas phase	108

4.2	Overall mean kinetic energy of the escaping IHe_n products averaged over all complex sizes n and over the internal state distribution of iodine	112
4.3	Spin-orbit state averaged mean anisotropy parameters associated with the 266 nm A band dissociation of free CH_3I and CF_3I molecules in the gas phase	115
4.4	Dissociation channel averaged mean kinetic energy and estimated mean speed of CF_3 fragments produced by the 266 nm photolysis of free CF_3I molecules in the gas phase	125
4.5	Mean kinetic energy of escaping bare CF_3 fragments for selected stagnation temperatures	126
4.6	Dissociation channel averaged mean kinetic energy and estimated mean speed of CH_3 fragments in specific vibrational states created by the 266 nm photolysis of free CH_3I molecules in the gas phase	130
4.7	Mean kinetic energy and mean relative kinetic energy loss of escaping bare CH_3 radicals in the vibrational ground state for selected helium stagnation temperatures T_o	130
4.8	Mean total kinetic energy transfer ΔE from a pair of created photofragments to helium droplets of selected mean sizes	140
4.9	Parameters used for the classical Monte Carlo simulation of the escape of CF_3 and iodine fragments from helium droplets produced at a stagnation temperature of 15 K	158
4.10	Parameters used for the classical Monte Carlo simulation of the escape of CH_3 fragments from helium droplets produced at a stagnation temperature of 18 K	161
D.1	Mean change of kinetic energy and mean laboratory frame scattering angle calculated for single elastic hard-sphere collisions of relevant photofragments with initially stationary ^4He atoms	190

List of abbreviations

AWG	American wire gauge
CCD	Charge-coupled device
DFT	Density functional theory
DMC	Diffusion Monte Carlo
ETP	Electrolytic tough pitch
FFT	Fast Fourier transform
FWHM	Full width at half maximum
HENDI	Helium nanodroplet isolation spectroscopy
HV	High voltage
IR	Infrared
KDP	Potassium dihydrogen phosphate
LN ₂	Liquid nitrogen
MCP	Microchannel plate
MPI	Multi-photon ionization
OFHC	Oxygen-free high conductivity
PC	Personal computer
PTFE	Poly-tetra-fluoro-ethylene
QMS	Quadrupole mass spectrometer
REMPI	Resonance enhanced multi-photon ionization
RMS	Root mean squared
SEM	Secondary electron multiplier
TOF	Time of flight
UHV	Ultra high vacuum
UV	Ultra violet
VUV	Vacuum ultra violet
ZEKE	Zero kinetic energy

Bibliography

- [1] Fritz London. *Macroscopic Theory of Superfluid Helium*, volume 2 of *Superfluids*. Wiley, New York, 1954.
- [2] J. Wilks and D. S. Betts. *An Introduction to Liquid Helium*. Clarendon Press, Oxford, 2nd edition, 1987.
- [3] D. R. Tilley and J. Tilley. *Superfluidity and Superconductivity*. IOP Publishing, Bristol, 3rd edition, 1990.
- [4] L. Tisza. Transport phenomena in helium II. *Nature*, 141:913, 1938.
- [5] L. Landau. The theory of superfluidity of helium II. *Journal of Physics USSR*, 5:71–90, 1941.
- [6] L. Landau. On the theory of superfluidity of helium II. *Journal of Physics USSR*, 11:91–92, 1947.
- [7] E. Andronikashvili. Direct observation of two kinds of motion in helium II. *Journal of Physics USSR*, 10(3):201–206, 1946.
- [8] R. J. Donnelly and C. F. Barenghi. The observed properties of liquid helium at the saturated vapor pressure. *Journal of Physical and Chemical Reference Data*, 27(6):1217–1274, 1998.
- [9] R. A. Cowley and A. D. B. Woods. Inelastic scattering of thermal neutrons from liquid helium. *Canadian Journal of Physics*, 49(2):177–200, 1971.
- [10] D. G. Henshaw and A. D. B. Woods. Modes of atomic motions in liquid helium by inelastic scattering of neutrons. *Physical Review*, 121(5):1266–1274, 1961.
- [11] D. R. Allum, P. V. E. McClintock, A. Phillips, and R. M. Bowley. The breakdown of superfluidity in liquid ^4He : An experimental test of Landau’s theory. *Philosophical Transactions of the Royal Society of London A*, 284(1320):179–223, 1977.
- [12] J. Poitrenaud and F. I. B. Williams. Precise measurement of effective mass of positive and negative charge carriers in liquid helium II. *Physical Review Letters*, 29(18):1230–1232, 1972.

- [13] J. Poitrenaud and F. I. B. Williams. Erratum. *Physical Review Letters*, 32(21):1213–1213, 1974.
- [14] M. Takami. Spectroscopic study of atoms and molecules in liquid helium. *Comments on Atomic and Molecular Physics*, 32(4):219–231, 1996.
- [15] I. F. Silvera. Ultimate fate of a gas of atomic hydrogen in a liquid-helium chamber: Recombination and burial. *Physical Review B*, 29(7):3899–3904, 1984.
- [16] B. Tabbert, H. Günther, and G. zu Putlitz. Optical investigation of impurities in superfluid ^4He . *Journal of Low Temperature Physics*, 109(5-6):653–707, 1997.
- [17] V. Ghazarian, J. Eloranta, and V. A. Apkarian. Universal molecule injector in liquid helium: Pulsed cryogenic doped helium droplet source. *Review of Scientific Instruments*, 73(10):3606–3613, 2002.
- [18] S. Stringari and J. Treiner. Systematics of liquid helium clusters. *Journal of Chemical Physics*, 87(8):5021–5027, 1987.
- [19] M. Lewerenz, B. Schilling, and J. P. Toennies. Successive capture and coagulation of atoms and molecules to small clusters in large liquid helium clusters. *Journal of Chemical Physics*, 102(20):8191–8207, 1995.
- [20] J. P. Toennies and A. F. Vilesov. Spectroscopy of atoms and molecules in liquid helium. *Annual Review of Physical Chemistry*, 49:1–41, 1998.
- [21] S. Grebenev, M. Hartmann, A. Lindinger, N. Pörtner, B. Sartakov, J. P. Toennies, and A. F. Vilesov. Spectroscopy of molecules in helium droplets. *Physica B*, 280(1-4):65–72, 2000.
- [22] E. Lugovoj, J. P. Toennies, S. Grebenev, N. Pörtner, A. J. Vilesov, and B. Sartakov. Spectroscopy of single molecules and clusters inside superfluid helium droplets. In Roger Campargue, editor, *Atomic and Molecular Beams, The State of the Art 2000*, pages 755–774. Springer, Berlin, 2001.
- [23] J. A. Northby. Experimental studies of helium droplets. *Journal of Chemical Physics*, 115(22):10065–10077, 2001.
- [24] F. Stienkemeier and A. F. Vilesov. Electronic spectroscopy in He droplets. *Journal of Chemical Physics*, 115(22):10119–10137, 2001.
- [25] Philippe Sindzingre, Michael L. Klein, and David M. Ceperley. Path-integral Monte Carlo study of low-temperature ^4He clusters. *Physical Review Letters*, 63(15):1601–1604, 1989.
- [26] M. V. R. Krishna and K. B. Whaley. Structure and excitations of quantum liquid clusters. *Modern Physics Letters B*, 4(14):895–904, 1990.
- [27] R. N. Barnett and K. B. Whaley. Molecular impurities in helium clusters. *Zeitschrift für Physik D*, 31(1-2):75–84, 1994.

- [28] K. B. Whaley. Structure and dynamics of quantum clusters. *International Reviews in Physical Chemistry*, 13(1):41–84, 1994.
- [29] F. Dalfovo, A. Lastrì, L. Pricauenko, S. Stringari, and J. Treiner. Structural and dynamical properties of superfluid helium: A density-functional approach. *Physical Review B*, 52(2):1193–1209, 1995.
- [30] S. A. Chin and E. Krotscheck. Systematics of pure and doped ^4He clusters. *Physical Review B*, 52(14):10405–10428, 1995.
- [31] K. B. Whaley. Spectroscopy and microscopic theory of doped helium clusters. In J. M. Bowman and Z. Bačić, editors, *Advances in Molecular Vibrations and Collision Dynamics*, volume 3, pages 397–451. JAI Press, Stamford, Connecticut, 1998.
- [32] Y. Kwon, P. Huang, M. V. Patel, D. Blume, and K. B. Whaley. Quantum solvation and molecular rotations in superfluid helium clusters. *Journal of Chemical Physics*, 113(16):6469–6501, 2000.
- [33] P. Huang, Y. Kwon, and K. B. Whaley. The finite-temperature path integral Monte Carlo method and its application to superfluid helium clusters. In Eckhard Krotscheck and Jesus Navarro, editors, *Microscopic approaches to quantum liquids in confined geometries*, volume 4 of *Series on advances in quantum many-body theory*, chapter 3, pages 91–128. World Scientific, Singapore, 2002.
- [34] H. Kamerlingh Onnes. Experiments on the condensation of helium by expansion. *Communications from the Physical Laboratory at the University of Leiden*, 105:1–6, 1908.
- [35] H. Kamerlingh Onnes. The liquefaction of helium. *Communications from the Physical Laboratory at the University of Leiden*, 108:1–23, 1908.
- [36] P. Kapitza. Viscosity of liquid helium below the λ -point. *Nature*, 141:74, 1938.
- [37] J. F. Allen and A. D. Misener. Flow of liquid helium II. *Nature*, 141:75, 1938.
- [38] E. W. Becker, K. Bier, and W. Henkes. Strahlen aus kondensierten Atomen und Molekeln im Hochvakuum. *Zeitschrift für Physik*, 146:333–338, 1956.
- [39] E. W. Becker, R. Klingelhöfer, and P. Lohse. Über die Möglichkeit der gerichteten Einführung von Deuterium und Tritium bei Kernfusionsexperimenten. *Zeitschrift für Naturforschung*, 15a:644–645, 1960.
- [40] E. W. Becker. Beams of condensed matter in high vacuum. Presentation at the Brookhaven Conference on Molecular Beams, Heidelberg, 11 June 1959.
- [41] E. W. Becker. On the history of cluster beams. *Zeitschrift für Physik D*, 3:101–107, 1986.
- [42] E. W. Becker, R. Klingelhöfer, and P. Lohse. Strahlen aus kondensiertem Wasserstoff, kondensiertem Helium und kondensiertem Stickstoff im Hochvakuum. *Zeitschrift für Naturforschung*, 17a:432–438, 1962.

- [43] E. W. Becker, R. Klingelhöfer, and P. Lohse. Strahlen aus kondensiertem Helium im Hochvakuum. *Zeitschrift für Naturforschung*, 16a:1259, 1961.
- [44] E. W. Becker, J. Gspann, and G. Krieg. Scattering of cesium atoms by ^4He clusters. In M. Krusius, editor, *Proceedings of the 14th International Conference on Low Temperature Physics, Otaniemi, Finland, 14–20 August 1975*, pages 426–428, Amsterdam, 1975. North-Holland.
- [45] J. Gspann, G. Krieg, and H. Vollmar. Atomic interaction with quantum fluid clusters: ^3He -cluster beam generation and Cs-scattering by ^4He -clusters. *Journal de Physique, Colloque C2*, 38:171–173, 1977.
- [46] J. Gspann and H. Vollmar. Momentum transfer to helium-3 and helium-4-microdroplets in heavy atom collisions. *Journal de Physique, Colloque C6*, 39:330–331, 1978.
- [47] J. Gspann. Helium microdroplet transparency in heavy atom collisions. *Physica B*, 108:1309–1310, 1981.
- [48] J. Gspann. Electronic and atomic impacts on large clusters. In S. Datz, editor, *Physics of electronic and atomic collisions*, pages 79–96. North-Holland, 1982.
- [49] J. Gspann and R. Ries. ^3He and ^4He clusters colliding with Cs atoms: Total cross sections for varying impact speed. *Surface Science*, 156:195–200, 1985.
- [50] J. Gspann. Atomic impact experiments with free helium-3 and helium-4 clusters. *Zeitschrift für Physik B*, 98(3):405–411, 1995.
- [51] A. P. J. van Deursen and J. Reuss. Experimental investigation of small He clusters. *Journal of Chemical Physics*, 63(10):4559, 1975.
- [52] P. W. Stephens and J. G. King. Experimental investigation of small helium clusters: Magic numbers and the onset of condensation. *Physical Review Letters*, 51(17):1538–1541, 1983.
- [53] J. Gspann and H. Vollmar. Metastable excitations of large clusters of ^3He , ^4He or Ne atoms. *Journal of Chemical Physics*, 73(4):1657–1664, 1980.
- [54] T. E. Gough, M. Mengel, P. A. Rowntree, and G. Scoles. Infrared spectroscopy at the surface of clusters: SF_6 on Ar. *Journal of Chemical Physics*, 83(10):4958–4961, 1985.
- [55] J. P. Toennies. Helium clusters. In G. Scoles, editor, *Proceedings of the international school of physics “Enrico Fermi”, Course CVII, The Chemical Physics of Atomic and Molecular Clusters, Varenna, 28 June - 7 July 1988*, pages 597–617, Amsterdam, 1990. Italian Physical Society, North-Holland.
- [56] A. Scheidemann, J. P. Toennies, and J. A. Northby. Capture of neon atoms by ^4He clusters. *Physical Review Letters*, 64(16):1899–1902, 1990.
- [57] A. Scheidemann, B. Schilling, J. P. Toennies, and J. A. Northby. Capture of foreign atoms by helium clusters. *Physica B*, 165:135–136, 1990.

- [58] S. Goyal, D. L. Schutt, and G. Scoles. Vibrational spectroscopy of sulfur hexafluoride attached to helium clusters. *Physical Review Letters*, 69(6):933–936, 1992.
- [59] S. Goyal, D. L. Schutt, and G. Scoles. Infrared spectroscopy in highly quantum matrices: Vibrational spectrum of $(\text{SF}_6)_{n=1,2}$ attached to helium clusters. *Journal of Physical Chemistry*, 97(10):2236–2245, 1993.
- [60] S. Goyal, D. L. Schutt, and G. Scoles. Errata: Vibrational spectroscopy of sulfur hexafluoride attached to helium clusters [Phys. Rev. Lett. 69, 933 (1992)]. *Physical Review Letters*, 73(18):2512–2512, 1994.
- [61] R. Fröchtenicht, J. P. Toennies, and A. Vilesov. High-resolution infrared spectroscopy of SF_6 embedded in He clusters. *Chemical Physics Letters*, 229(1-2):1–7, 1994.
- [62] M. Hartmann, R. E. Miller, J. P. Toennies, and A. Vilesov. Rotationally resolved spectroscopy of SF_6 in liquid helium clusters: A molecular probe of cluster temperature. *Physical Review Letters*, 75(8):1566–1569, 1995.
- [63] J. Harms, M. Hartmann, J. P. Toennies, A. F. Vilesov, and B. Sartakov. Rotational structure of the IR spectra of single SF_6 molecules in liquid ^4He and ^3He droplets. *Journal of Molecular Spectroscopy*, 185(1):204–206, 1997.
- [64] M. Barranco, M. Pi, S. M. Gatica, E. S. Hernandez, and J. Navarro. Structure and energetics of mixed ^4He - ^3He drops. *Physical Review B*, 56(14):8997–9003, 1997.
- [65] M. Pi, R. Mayol, and M. Barranco. Structure of large ^3He - ^4He mixed drops around a dopant molecule. *Physical Review Letters*, 82(15):3093–3096, 1999.
- [66] D. M. Brink and S. Stringari. Density of states and evaporation rate of helium clusters. *Zeitschrift für Physik D*, 15(3):257–263, 1990.
- [67] A. Guirao, M. Pi, and M. Barranco. Finite size effects in the evaporation rate of ^3He clusters. *Zeitschrift für Physik D*, 21(2):185–188, 1991.
- [68] M. Hartmann, R. E. Miller, J. P. Toennies, and A. F. Vilesov. High-resolution molecular spectroscopy of van der Waals clusters in liquid helium droplets. *Science*, 272(5268):1631–1634, 1996.
- [69] M. Hartmann, F. Mielke, J. P. Toennies, and A. F. Vilesov. Direct spectroscopic observation of elementary excitations in superfluid He droplets. *Physical Review Letters*, 76(24):4560–4563, 1996.
- [70] L. Pitaevskii and S. Stringari. Superfluid effects in rotating helium clusters. *Zeitschrift für Physik D*, 16(4):299–301, 1990.
- [71] M. V. R. Krishna and K. B. Whaley. Collective excitations of helium clusters. *Physical Review Letters*, 64(10):1126–1129, 1990.

- [72] M. V. Rama Krishna and K. B. Whaley. Microscopic studies of collective spectra of quantum liquid clusters. *Journal of Chemical Physics*, 93(1):746–759, 1990.
- [73] S. A. Chin and E. Krotscheck. Structure and collective excitations of ^4He clusters. *Physical Review B*, 45(2):852–874, 1992.
- [74] M. Casas, F. Dalfovo, A. Lastri, L. Serra, and S. Stringari. Density functional calculations for ^4He droplets. *Zeitschrift für Physik D*, 35(1):67–75, 1995.
- [75] S. Grebenev, J. P. Toennies, and A. F. Vilesov. Superfluidity within a small helium-4 cluster: The microscopic Andronikashvili experiment. *Science*, 279(5359):2083–2086, 1998.
- [76] S. Grebenev, M. Hartmann, M. Havenith, B. Sartakov, J. P. Toennies, and A. F. Vilesov. The rotational spectrum of single OCS molecules in liquid ^4He droplets. *Journal of Chemical Physics*, 112(10):4485–4495, 2000.
- [77] J. P. Toennies. Microscopic superfluidity of small ^4He and para- H_2 clusters inside helium droplets. In Eckhard Krotscheck and Jesus Navarro, editors, *Microscopic approaches to quantum liquids in confined geometries*, volume 4 of *Series on advances in quantum many-body theory*, chapter 9, pages 379–417. World Scientific, Singapore, 2002.
- [78] D. Blume, M. Lewerenz, F. Huisken, and M. Kaloudis. Vibrational frequency shift of HF in helium clusters: Quantum simulation and experiment. *Journal of Chemical Physics*, 105(19):8666–8683, 1996.
- [79] R. Fröchtenicht, M. Kaloudis, M. Koch, and F. Huisken. Vibrational spectroscopy of small water complexes embedded in large liquid helium clusters. *Journal of Chemical Physics*, 105(15):6128–6140, 1996.
- [80] Matthias Hartmann, Nikolas Pörtner, Boris Sartakov, J. Peter Toennies, and Andrej F. Vilesov. High resolution infrared spectroscopy of single SF_6 molecules in helium droplets. I. Size effects in ^4He droplets. *Journal of Chemical Physics*, 110(11):5109–5123, 1999.
- [81] C. Callegari, A. Conjusteau, I. Reinhard, K. K. Lehmann, and G. Scoles. First overtone helium nanodroplet isolation spectroscopy of molecules bearing the acetylenic chromophore. *Journal of Chemical Physics*, 113(23):10535–10550, 2000.
- [82] K. K. Lehmann. Potential of a neutral impurity in a large ^4He cluster. *Molecular Physics*, 97(5):645–666, 1999.
- [83] K. K. Lehmann. Rotation in liquid ^4He : Lessons from a highly simplified model. *Journal of Chemical Physics*, 114(10):4643–4648, 2001.
- [84] C. Callegari, A. Conjusteau, I. Reinhard, K. K. Lehmann, G. Scoles, and F. Dalfovo. Superfluid hydrodynamic model for the enhanced moments of inertia of molecules in liquid ^4He . *Physical Review Letters*, 83(24):5058–5061, 1999.

- [85] C. Callegari, A. Conjusteau, I. Reinhard, K. K. Lehmann, G. Scoles, and F. Dalfovo. Erratum: Superfluid hydrodynamic model for the enhanced moments of inertia of molecules in liquid ^4He [Phys. Rev. Lett. 83, 5058 (1999)]. *Physical Review Letters*, 84(8):1848–1848, 2000.
- [86] M. Chester and L. C. Yang. Superfluid fraction in thin helium films. *Physical Review Letters*, 31(23):1377–1380, 1973.
- [87] G. A. Csáthy and M. H. W. Chan. Substrate dependence of the superfluid onset of ^4He films. *Journal of Low Temperature Physics*, 121(5-6):451–458, 2000.
- [88] Y. K. Kwon and K. B. Whaley. Atomic-scale quantum solvation structure in superfluid helium-4 clusters. *Physical Review Letters*, 83(20):4108–4111, 1999.
- [89] R. P. Feynman. Atomic theory of the λ transition in helium. *Physical Review*, 91(6):1291–1301, 1953.
- [90] U. Even, J. Jortner, D. Noy, N. Lavie, and C. Cossart-Magos. Cooling of large molecules below 1 K and He clusters formation. *Journal of Chemical Physics*, 112(18):8068–8071, 2000.
- [91] U. Even, I. Al-Hroub, and J. Jortner. Small He clusters with aromatic molecules. *Journal of Chemical Physics*, 115(5):2069–2073, 2001.
- [92] J. Tang, Y. J. Xu, A. R. W. McKellar, and W. Jäger. Quantum solvation of carbonyl sulfide with helium atoms. *Science*, 297(5589):2030–2033, 2002.
- [93] J. Tang and A. R. W. McKellar. High-resolution infrared spectra of carbonyl sulfide solvated with helium atoms. *Journal of Chemical Physics*, 119(11):5467–5477, 2003.
- [94] Y. J. Xu, W. Jäger, J. Tang, and A. R. W. McKellar. Spectroscopic studies of quantum solvation in $^4\text{He}_N\text{-N}_2\text{O}$ clusters. *Physical Review Letters*, 91(16):3401, 2003.
- [95] S. Moroni, A. Sarsa, S. Fantoni, K. E. Schmidt, and S. Baroni. Structure, rotational dynamics, and superfluidity of small OCS-doped He clusters. *Physical Review Letters*, 90(14):3401, 2003.
- [96] F. Paesani, A. Viel, F. A. Gianturco, and K. B. Whaley. Transition from molecular complex to quantum solvation in $^4\text{He}_N\text{OCS}$. *Physical Review Letters*, 90(7):3401, 2003.
- [97] K. Nauta and R. E. Miller. Nonequilibrium self-assembly of long chains of polar molecules in superfluid helium. *Science*, 283(5409):1895–1897, 1999.
- [98] K. Nauta and R. E. Miller. Formation of cyclic water hexamer in liquid helium: The smallest piece of ice. *Science*, 287(5451):293–295, 2000.
- [99] G. W. Rayfield and F. Reif. Quantized vortex rings in superfluid helium. *Physical Review*, 136(5A):1194–1208, 1964.

- [100] M. Lewerenz, B. Schilling, and J. P. Toennies. A new scattering deflection method for determining and selecting the sizes of large liquid clusters of ^4He . *Chemical Physics Letters*, 206(1-4):381–387, 1993.
- [101] J. Harms and J. P. Toennies. Experimental evidence for the transmission of ^3He atoms through superfluid ^4He droplets. *Physical Review Letters*, 83(2):344–347, 1999.
- [102] T. Takayanagi and M. Shiga. Photodissociation of Cl_2 in helium clusters: An application of hybrid method of quantum wavepacket dynamics and path integral centroid molecular dynamics. *Chemical Physics Letters*, 372(1-2):90–96, 2003.
- [103] V. Vorsa, P. J. Campagnola, S. Nandi, M. Larsson, and W. C. Lineberger. Photofragmentation of $\text{I}_2^- \cdot \text{Ar}_n$ clusters: Observation of metastable isomeric ionic fragments. *Journal of Chemical Physics*, 105(6):2298–2308, 1996.
- [104] J. M. Papanikolas, J. R. Gord, N. E. Levinger, D. Ray, V. Vorsa, and W. C. Lineberger. Photodissociation and geminate recombination dynamics of I_2^- in mass-selected $\text{I}_2^- (\text{CO}_2)_n$ cluster ions. *Journal of Physical Chemistry*, 95(21):8028–8040, 1991.
- [105] S. Nandi, A. Sanov, N. Delaney, J. Faeder, R. Parson, and W. C. Lineberger. Photodissociation of $\text{I}_2^- (\text{OCS})_n$ cluster ions: Structural implications. *Journal of Physical Chemistry A*, 102(45):8827–8835, 1998.
- [106] M. L. Alexander, N. E. Levinger, M. A. Johnson, D. Ray, and W. C. Lineberger. Recombination of Br_2^- photodissociated within mass selected ionic clusters. *Journal of Chemical Physics*, 88(10):6200–6210, 1988.
- [107] U. Buck. Photodissociation of hydrogen halide molecules in different cluster environments. *Journal of Physical Chemistry A*, 106(43):10049–10062, 2002.
- [108] P. Slavíček, P. Žďánková, P. Jungwirth, R. Baumfalk, and U. Buck. Size effects on photodissociation and caging of hydrogen bromide inside or on the surface of large inert clusters: From one to three icosahedral argon layers. *Journal of Physical Chemistry A*, 104(33):7793–7802, 2000.
- [109] H. Buchenau, E. L. Knuth, J. Northby, J. P. Toennies, and C. Winkler. Mass-spectra and time-of-flight distributions of helium cluster beams. *Journal of Chemical Physics*, 92(11):6875–6889, 1990.
- [110] R. D. McCarty. Thermodynamic properties of helium-4 from 2 to 1500 K at pressures up to 10^8 Pa. *Journal of Physical and Chemical Reference Data*, 2:923, 1973.
- [111] S. Angus and K. M. de Reuck, editors. *Helium-4*, volume 4 of *International thermodynamic tables of the fluid state*. Pergamon, Oxford, 1977.
- [112] T. Jiang and J. A. Northby. Fragmentation clusters formed in supercritical expansions of ^4He . *Physical Review Letters*, 68:2620–2623, 1992.

- [113] B. E. Callicoatt, K. Förde, T. Ruchti, L. L. Jung, K. C. Janda, and N. Halberstadt. Capture and ionization of argon within liquid helium droplets. *Journal of Chemical Physics*, 108(22):9371–9382, 1998.
- [114] H. Buchenau, J. P. Toennies, and J. A. Northby. Excitation and ionization of ^4He clusters by electrons. *Journal of Chemical Physics*, 95(11):8134–8148, 1991.
- [115] U. Henne and J. P. Toennies. Electron capture by large helium droplets. *Journal of Chemical Physics*, 108(22):9327–9338, 1998.
- [116] E. L. Knuth and U. Henne. Average size and size distribution of large droplets produced in a free-jet expansion of a liquid. *Journal of Chemical Physics*, 110(5):2664–2668, 1999.
- [117] J. P. Toennies and K. Winkelmann. Theoretical studies of highly expanded free jets: Influence of quantum effects and a realistic intermolecular potential. *Journal of Chemical Physics*, 66(9):3965–3979, 1977.
- [118] J. Harms, J. P. Toennies, and E. L. Knuth. Droplets formed in helium free-jet expansions from states near the critical point. *Journal of Chemical Physics*, 106(8):3348–3357, 1997.
- [119] David R. Miller. Free jet sources. In Giacinto Scoles, editor, *Atomic and Molecular Beam Methods*, volume 1. Oxford University Press, Oxford, 1988.
- [120] B. Schilling. *Molekularstrahlexperimente mit Helium-Clustern*. Bericht 14/1993, Max-Planck-Institut für Strömungsforschung, Göttingen, 1993.
- [121] V. Weisskopf. Statistics and nuclear reactions. *Physical Review*, 52(4):295–303, 1937.
- [122] S. Stringari. Clusters of quantum liquids. In G. Scoles, editor, *Proceedings of the international school of physics “Enrico Fermi”, Course CVII, The Chemical Physics of Atomic and Molecular Clusters, Varenna, Italy, 28 June – 7 July 1988*, pages 199–236, Amsterdam, 1990. Italian Physical Society, North-Holland.
- [123] J. P. Toennies and A. F. Vilesov. Novel low-energy vibrational states of foreign particles in fluid ^4He clusters. *Chemical Physics Letters*, 235(5-6):596–603, 1995.
- [124] M. Hartmann. *Hochauflösende Spektroskopie von Molekülen in $^4\text{Helium}$ - und $^3\text{Helium}$ -Clustern*. Bericht 10/1997, Max-Planck-Institut für Strömungsforschung, Göttingen, 1997.
- [125] J. Harms, J. P. Toennies, and F. Dalfovo. Density of superfluid helium droplets. *Physical Review B*, 58(6):3341–3350, 1998.
- [126] Eldon L. Knuth, Bernard Schilling, and J. P. Toennies. On scaling parameters for predicting cluster sizes in free jets. In Gordon Lord and John Harvey, editors, *Proceedings of the 19th International Symposium on Rarefied Gas Dynamics*, pages 270–276, Oxford, 1995. Oxford University Press.
- [127] Otto F. Hagen. Nucleation and growth of clusters in expanding nozzle flows. *Surface Science*, 106:101–116, 1981.

- [128] O. F. Hagena. Condensation in free jets: Comparison of rare gases and metals. *Zeitschrift für Physik D*, 4:291–299, 1987.
- [129] E. L. Knuth. Size correlations for condensation clusters produced in free-jet expansions. *Journal of Chemical Physics*, 107(21):9125–9132, 1997.
- [130] V. R. Pandharipande, J. G. Zabolitzky, S. C. Pieper, R. B. Wiringa, and U. Helmbrecht. Calculations of ground-state properties of liquid ^4He droplets. *Physical Review Letters*, 50(21):1676–1679, 1983.
- [131] V. R. Pandharipande, S. C. Pieper, and R. B. Wiringa. Variational Monte Carlo calculations of ground states of liquid ^4He and ^3He drops. *Physical Review B*, 34(7):4571–4582, 1986.
- [132] R. N. Barnett and K. B. Whaley. Variational and diffusion Monte Carlo techniques for quantum clusters. *Physical Review A*, 47(5):4082–4098, 1993.
- [133] M. A. McMahon, R. N. Barnett, and K. B. Whaley. Dopant location in $\text{SF}_6\text{He}_{39,40}$. *Journal of Chemical Physics*, 104(13):5080–5093, 1996.
- [134] Michel Macler and Young K. Bae. Comment on: “successive capture and coagulation of atoms and molecules to small clusters in large liquid helium clusters” [J. Chem. Phys. 102, 8191 (1995)]. *Journal of Chemical Physics*, 106(13):5785–5786, 1997.
- [135] M. Lewerenz, B. Schilling, and J. P. Toennies. Response to “comment on: ‘successive capture and coagulation of atoms and molecules to small clusters in large liquid helium clusters’ ” [J. Chem. Phys. 106, 5785 (1997)]. *Journal of Chemical Physics*, 106(13):5787, 1997.
- [136] H. Hess, D. S. Larsen, and A. A. Scheidemann. Measurement of pick-up cross-sections of ^4He clusters: Polar versus non-polar molecules. *Philosophical Magazine B*, 79(9):1437–1444, 1999.
- [137] K. Berkling, R. Helbing, K. Kramer, H. Pauly, Ch. Schlier, and P. Toschek. Effektive Stoßquerschnitte bei Streuversuchen. *Zeitschrift für Physik*, 166:406, 1962.
- [138] M. Behrens, R. Frochtenicht, M. Hartmann, J. G. Siebers, U. Buck, and F. C. Hagemester. Vibrational spectroscopy of methanol and acetonitrile clusters in cold helium droplets. *Journal of Chemical Physics*, 111(6):2436–2443, 1999.
- [139] K. Nauta and R. E. Miller. Solvent mediated vibrational relaxation: Superfluid helium droplet spectroscopy of HCN dimer. *Journal of Chemical Physics*, 111(8):3426–3433, 1999.
- [140] A. Scheidemann, B. Schilling, and J. P. Toennies. Anomalies in the reactions of He^+ with SF_6 embedded in large helium-4 clusters. *Journal of Physical Chemistry*, 97(10):2128–2138, 1993.

- [141] T. Ruchti, K. Förde, B. E. Callicoatt, H. Ludwigs, and K. C. Janda. Charge transfer and fragmentation of liquid helium clusters that contain one or more neon atoms. *Journal of Chemical Physics*, 109(24):10679–10687, 1998.
- [142] B. E. Callicoatt, D. D. Mar, V. A. Apkarian, and K. C. Janda. Charge transfer within He clusters. *Journal of Chemical Physics*, 105(17):7872–7875, 1996.
- [143] U. Buck, G. Hoffmann, J. Kesper, D. Otten, and M. Winter. Scattering analysis of NO clusters in a new molecular beam machine. *Chemical Physics*, 126(1):159–168, 1988.
- [144] H. Burger, K. Burczyk, H. Hollenstein, and M. Quack. Vibrational spectra and force constants of symmetric tops. 46. High resolution FTIR spectra of $^{12}\text{CF}_3\text{I}$, $^{13}\text{CF}_3\text{I}$ and $^{12}\text{CF}_3^{79}\text{Br}$ near 1050 cm^{-1} and 550 cm^{-1} . *Molecular Physics*, 55(2):255–275, 1985.
- [145] André T. J. B. Eppink and D. H. Parker. Energy partitioning following photodissociation of methyl iodide in the A band: A velocity mapping study. *Journal of Chemical Physics*, 110(2):832–844, 1999.
- [146] Gerhard Herzberg. *III. Electronic Spectra and Electronic Structure of Polyatomic Molecules*. Molecular Spectra and Molecular Structure. Van Nostrand Reinhold Company, New York, 1966.
- [147] F. Dalfovo. Atomic and molecular impurities in ^4He clusters. *Zeitschrift für Physik D*, 29(1):61–66, 1994.
- [148] Richard N. Zare. Photoejection dynamics. *Molecular Photochemistry*, 44(1):1–37, 1972.
- [149] G. N. A. Vanveen, T. Baller, A. E. Devries, and M. Shapiro. Photofragmentation of CF_3I in the A-band. *Chemical Physics*, 93(2):277–291, 1985.
- [150] H. Guo. Three-dimensional photodissociation dynamics of methyl iodide. *Journal of Chemical Physics*, 96(9):6629–6642, 1992.
- [151] B. R. Johnson, C. Kittrell, P. B. Kelly, and J. L. Kinsey. Resonance Raman spectroscopy of dissociative polyatomic molecules. *Journal of Physical Chemistry*, 100(19):7743–7764, 1996.
- [152] J. L. Knee, L. R. Khundkar, and A. H. Zewail. Picosecond monitoring of a chemical-reaction in molecular beams: Photofragmentation of $\text{R-I} \rightarrow \text{R}^\ddagger + \text{I}$. *Journal of Chemical Physics*, 83(4):1996–1997, 1985.
- [153] D. P. Zhong, P. Y. Cheng, and A. H. Zewail. Bimolecular reactions observed by femtosecond detachment to aligned transition states: Inelastic and reactive dynamics. *Journal of Chemical Physics*, 105(17):7864–7867, 1996.
- [154] M. Dzvonik, S. Yang, and R. Bersohn. Photodissociation of molecular-beams of aryl halides. *Journal of Chemical Physics*, 61(11):4408–4421, 1974.

- [155] A. Furlan, T. Gejo, and J. R. Huber. Probing curve crossing by wavelength-dependent recoil anisotropy: The photodissociation of CF_3I at 275–303 nm studied by photofragment translational spectroscopy. *Journal of Physical Chemistry*, 100(19):7956–7961, 1996.
- [156] JANAF Thermochemical Tables. *J. Phys. Chem. Ref. Data*, 14, 1985. Suppl. 1.
- [157] Robert S. Mulliken. Intensities in molecular electronic spectra. X. Calculations on mixed halogen, hydrogen halide, alkyl halide and hydroxyl spectra. *Journal of Chemical Physics*, 8:382–395, 1940.
- [158] A. Gedanken and M. D. Rowe. Magnetic circular dichroism spectra of the methyl halides. Resolution of the $n \rightarrow \sigma^*$ continuum. *Chemical Physics Letters*, 34(1):39–43, 1975.
- [159] A. Gedanken. The magnetic circular-dichroism of the A-band in CF_3I , $\text{C}_2\text{H}_5\text{I}$ and $t\text{-BuI}$. *Chemical Physics Letters*, 137(5):462–466, 1987.
- [160] André T. J. B. Eppink and D. H. Parker. Methyl iodide A-band decomposition study by photofragment velocity imaging. *Journal of Chemical Physics*, 109(12):4758–4767, 1998.
- [161] P. Felder. Photodissociation of CF_3I at 248 nm: Kinetic energy dependence of the recoil anisotropy. *Chemical Physics*, 155(3):435–445, 1991.
- [162] F. Aguirre and S. T. Pratt. Velocity map imaging of the photodissociation of CF_3I : Vibrational energy dependence of the recoil anisotropy. *Journal of Chemical Physics*, 118(3):1175–1183, 2003.
- [163] F. G. Godwin, P. A. Gorry, P. M. Hughes, D. Raybone, T. M. Watkinson, and J. C. Whitehead. Two-photon VUV laser-induced fluorescence detection of $\text{I}^*(^2P_{1/2})$ and $\text{I}^*(^2P_{3/2})$ from alkyl iodide photodissociation at 248 nm. *Chemical Physics Letters*, 135(1-2):163–169, 1987.
- [164] M. D. Person, P. W. Kash, and L. J. Butler. The influence of parent bending motion on branching at a conical intersection in the photodissociation of CX_3I (X=H, D, F). *Journal of Chemical Physics*, 94(4):2557–2563, 1991.
- [165] Y. Amatatsu, K. Morokuma, and S. Yabushita. Ab initio potential energy surfaces and trajectory studies of A-band photodissociation dynamics: $\text{CH}_3\text{I}^* \rightarrow \text{CH}_3 + \text{I}$ and $\text{CH}_3 + \text{I}^*$. *Journal of Chemical Physics*, 94(7):4858–4876, 1991.
- [166] Y. Amatatsu, S. Yabushita, and K. Morokuma. Full nine-dimensional ab initio potential energy surfaces and trajectory studies of A-band photodissociation dynamics: $\text{CH}_3\text{I}^* \rightarrow \text{CH}_3 + \text{I}$, $\text{CH}_3 + \text{I}^*$, and $\text{CD}_3\text{I}^* \rightarrow \text{CD}_3 + \text{I}$, $\text{CD}_3 + \text{I}^*$. *Journal of Chemical Physics*, 104(24):9783–9794, 1996.
- [167] C. Yamada, E. Hirota, and K. Kawaguchi. Diode laser study of the ν_2 band of the methyl radical. *Journal of Chemical Physics*, 75(11):5256–5264, 1981.

- [168] F. Bernardi, W. Cherry, S. Shaik, and N. D. Epiotis. Structure of fluoromethyl radicals. conjugative and inductive effects. *Journal of the American Chemical Society*, 100(5):1352–1356, 1978.
- [169] S. J. Riley and K. R. Wilson. Excited fragments from excited molecules: Energy partitioning in photodissociation of alkyl iodides. *Faraday Discussions of the Chemical Society*, 53:132–146, 1972.
- [170] W. P. Hess, S. J. Kohler, H. K. Haugen, and S. R. Leone. Application of an InGaAsP diode laser to probe photodissociation dynamics: I* quantum yields from *n*- and *i*-C₃F₇I and CH₃I by laser gain vs absorption spectroscopy. *Journal of Chemical Physics*, 84(4):2143–2149, 1986.
- [171] A. V. Baklanov, M. Aldener, B. Lindgren, and U. Sassenberg. R2PI detection of the quantum yields of I(²P_{1/2}) and I(²P_{3/2}) in the photodissociation of C₂F₅I, *n*-C₃F₇I, *i*-C₃F₇I and CH₃I. *Chemical Physics Letters*, 325(4):399–404, 2000.
- [172] R. A. Hertz and J. A. Syage. Detection of the perpendicular \tilde{A} state transitions of CH₃I by imaging of photofragment angle-velocity distributions. *Journal of Chemical Physics*, 100(12):9265–9268, 1994.
- [173] N. E. Triggs, M. Zahedi, J. W. Nibler, P. Debarber, and J. J. Valentini. High-resolution study of the ν_1 vibration of CH₃ by coherent Raman photofragment spectroscopy. *Journal of Chemical Physics*, 96(3):1822–1831, 1992.
- [174] Z. H. Huang and H. Guo. Theoretical modeling of photodissociation dynamics of CH₃I on LiF(001). *Journal of Chemical Physics*, 98(4):3395–3409, 1993.
- [175] A. D. Hammerich, U. Manthe, R. Kosloff, H. D. Meyer, and L. S. Cederbaum. Time-dependent photodissociation of methyl iodide with five active modes. *Journal of Chemical Physics*, 101(7):5623–5646, 1994.
- [176] D. Q. Xie, H. Guo, Y. Amatatsu, and R. Kosloff. Three-dimensional photodissociation dynamics of rotational state selected methyl iodide. *Journal of Physical Chemistry A*, 104(5):1009–1019, 2000.
- [177] R. O. Loo, H. P. Haerri, G. E. Hall, and P. L. Houston. Methyl rotation, vibration, and alignment from a multiphoton ionization study of the 266 nm photodissociation of methyl iodide. *Journal of Chemical Physics*, 90(8):4222–4236, 1989.
- [178] D. W. Chandler, J. W. Thoman, M. H. M. Janssen, and D. H. Parker. Photofragment imaging: The 266 nm photodissociation of CH₃I. *Chemical Physics Letters*, 156(2-3):151–158, 1989.
- [179] K. Kavita and P. K. Das. Dynamics of I*(²P_{1/2}) production from fluorinated alkyl iodides at 266, 280, and \sim 305 nm. *Journal of Chemical Physics*, 112(19):8426–8431, 2000.
- [180] P. Felder. Photodissociation of CF₃I at 248 nm: Internal energy distribution of the CF₃ fragments. *Chemical Physics*, 143(1):141–150, 1990.

- [181] Y. S. Kim, W. K. Kang, and K. H. Jung. State-selective photofragment imaging of iodine atoms via photodissociation of CF_3I at 277 nm. *Journal of Chemical Physics*, 105(2):551–557, 1996.
- [182] R. L. Asher and B. Ruscic. On the heats of formation of trifluoromethyl radical CF_3 and its cation CF_3^+ . *Journal of Chemical Physics*, 106(1):210–221, 1997.
- [183] Janis Research Company, Inc., Wilmington, MA. *Sumitomo (SHI) 4 K Refrigerator*. <http://www.janis.com>.
- [184] Sumitomo Heavy Industries, Ltd., Tokyo, Japan. *Cold head RDK-205D*. <http://www.shi.co.jp>.
- [185] J. G. Weisend II, editor. *Handbook of Cryogenic Engineering*. Taylor & Francis, Philadelphia, 1998.
- [186] Thomas M. Flynn. *Cryogenic Engineering*. Marcel Dekker, New York, 1996.
- [187] Ulrich Henne. *Untersuchung großer durch Elektronenstoß erzeugter negativer und positiver Helium-Clusterionen*. Bericht 5/1996, Max-Planck-Institut für Strömungsforschung, Göttingen, 1996.
- [188] B. E. Callicoatt, K. Forde, L. F. Jung, T. Ruchti, and K. C. Janda. Fragmentation of ionized liquid helium droplets: A new interpretation. *Journal of Chemical Physics*, 109(23):10195–10200, 1998.
- [189] P. W. Atkins. *Physical Chemistry*. Oxford University Press, Oxford, 6th edition, 1998.
- [190] Wolfgang Demtröder. *Laser Spectroscopy*, chapter 9, pages 516–551. Springer, Berlin, 2nd edition, 1996.
- [191] Y. B. Fan, K. L. Randall, and D. J. Donaldson. Photochemistry of alkyl halide dimers. *Journal of Chemical Physics*, 98(6):4700–4706, 1993.
- [192] F. Ito and T. Nakanaga. Photodissociation of methyl iodide clusters in the A-band excitation: Photofragmentation excitation spectra of $(\text{CH}_3\text{I})_n$ by ultraviolet pump-CRD probe measurement. *Journal of Chemical Physics*, 119(11):5527–5533, 2003.
- [193] Franco Bottiglioni, Jacques Coutant, and Mario Fois. Ionization cross sections for H_2 , N_2 and CO_2 clusters by electron impact. *Physical Review A*, 6(5):1830–1843, 1972.
- [194] Claire Vallance, Sean A. Harris, James E. Hudson, and Peter W. Harland. Absolute electron impact ionization cross sections for CH_3X , where $\text{X}=\text{H}$, F , Cl , Br , and I . *Journal of Physics B*, 30:2465–2475, 1997.
- [195] C. Q. Jiao, B. Ganguly, C. A. DeJoseph Jr., and A. Garscadden. Comparisons of electron impact ionization and ion chemistries of CF_3Br and CF_3I . *International Journal of Mass Spectrometry*, 208:127–133, 2001.

- [196] U. Onthong, H. Deutsch, K. Becker, S. Matt, M. Probst, and T. D. Märk. Calculated absolute electron impact ionization cross-section for the molecules CF_3X ($\text{X}=\text{H}, \text{Br}, \text{I}$). *International Journal of Mass Spectrometry*, 214:53–56, 2002.
- [197] Donald Rapp and Paula Englander-Golden. Total cross sections for ionization and attachment in gases by electron impact. I. Positive ionization. *Journal of Chemical Physics*, 43(5):1464–1489, 1965.
- [198] A. J. R. Heck and D. W. Chandler. Imaging techniques for the study of chemical reaction dynamics. *Annual Review of Physical Chemistry*, 46:335–372, 1995.
- [199] P. L. Houston. Snapshots of chemistry: Product imaging of molecular reactions. *Accounts of Chemical Research*, 28(11):453–460, 1995.
- [200] P. L. Houston. New laser-based and imaging methods for studying the dynamics of molecular collisions. *Journal of Physical Chemistry*, 100(31):12757–12770, 1996.
- [201] D. W. Chandler and P. L. Houston. Two-dimensional imaging of state-selected photodissociation products detected by multiphoton ionization. *Journal of Chemical Physics*, 87(2):1445–1447, 1987.
- [202] W. C. Wiley and I. H. McLaren. Time-of-flight mass spectrometer with improved resolution. *Review of Scientific Instruments*, 26:1150–1157, 1955.
- [203] André T. J. B. Eppink and D. H. Parker. Velocity map imaging of ions and electrons using electrostatic lenses: Application in photoelectron and photofragment ion imaging of molecular oxygen. *Review of Scientific Instruments*, 68(9):3477–3484, 1997.
- [204] D. H. Parker and A. T. J. B. Eppink. Photoelectron and photofragment velocity map imaging of state-selected molecular oxygen dissociation/ionization dynamics. *Journal of Chemical Physics*, 107(7):2357–2362, 1997.
- [205] Miklos Szilagyi. *Electron and Ion Optics*. Plenum Press, New York, 1988.
- [206] H. L. Offerhaus, C. Nicole, F. Lépine, C. Bordas, F. Rosca-Pruna, and M. J. J. Vrakking. A magnifying lens for velocity map imaging of electrons and ions. *Review of Scientific Instruments*, 72(8):3245–3248, 2001.
- [207] H. B. Michaelson. The work function of the elements and its periodicity. *Journal of Applied Physics*, 48(11):4729–4733, 1977.
- [208] M. J. J. Vrakking. An iterative procedure for the inversion of two-dimensional ion/photoelectron imaging experiments. *Review of Scientific Instruments*, 72(11):4084–4089, 2001.
- [209] Ronald N. Bracewell. *The Fourier Transform and Its Applications*. McGraw-Hill, New York, 2nd edition, 1986.

- [210] L. V. Keldysh. Ionization in the field of a strong electromagnetic wave. *Soviet Physics JETP*, 20(5):1307–1314, 1965.
- [211] M. Takahashi, H. Ozeki, and K. Kimura. Vibrational spectra of aniline- Ar_n van der Waals cations ($n=1$ and 2) observed by two-color “threshold photoelectron” [zero kinetic energy (ZEKE)-photoelectron] spectroscopy. *Journal of Chemical Physics*, 96(9):6399–6406, 1992.
- [212] X. B. Song, M. Yang, E. R. Davidson, and J. P. Reilly. Zero kinetic energy photoelectron spectra of jet-cooled aniline. *Journal of Chemical Physics*, 99(5):3224–3233, 1993.
- [213] J. W. Hudgens, T. G. Digiuseppe, and M. C. Lin. Two photon resonance enhanced multiphoton ionization spectroscopy and state assignments of the methyl radical. *Journal of Chemical Physics*, 79(2):571–582, 1983.
- [214] P. Chen, S. D. Colson, W. A. Chupka, and J. A. Berson. Flash pyrolytic production of rotationally cold free radicals in a supersonic jet. Resonant multiphoton spectrum of the $3p^2A_2'' \leftarrow X^2A_2''$ origin band of CH_3 . *Journal of Physical Chemistry*, 90(11):2319–2321, 1986.
- [215] I. Powis and J. F. Black. Rotational population and alignment of CD_3 ($v = 0$) photofragments from the A-band excitation of methyl- d_3 iodide. *Journal of Physical Chemistry*, 93(6):2461–2470, 1989.
- [216] A. Gedanken, M. B. Robin, and Y. Yafet. The methyl iodide multiphoton ionization spectrum with intermediate resonance in the A-band region. *Journal of Chemical Physics*, 76(10):4798–4808, 1982.
- [217] M. T. Duignan, J. W. Hudgens, and J. R. Wyatt. Multiphoton ionization of the trifluoromethyl radical. *Journal of Physical Chemistry*, 86(21):4156–4161, 1982.
- [218] R. J. Levis and M. J. DeWitt. Photoexcitation, ionization, and dissociation of molecules using intense near-infrared radiation of femtosecond duration. *Journal of Physical Chemistry A*, 103(33):6493–6507, 1999.
- [219] S. Augst, D. Strickland, D. D. Meyerhofer, S. L. Chin, and J. H. Eberly. Tunneling ionization of noble gases in a high-intensity laser field. *Physical Review Letters*, 63(20):2212–2215, 1989.
- [220] F. Ancilotto, P. B. Lerner, and M. W. Cole. Physics of solvation. *Journal of Low Temperature Physics*, 101(5-6):1123–1146, 1995.
- [221] F. Stienkemeier, J. Higgins, C. Callegari, S. I. Kanorsky, W. E. Ernst, and G. Scoles. Spectroscopy of alkali atoms (Li, Na, K) attached to large helium clusters. *Zeitschrift für Physik D*, 38(3):253–263, 1996.
- [222] J. Reho, C. Callegari, J. Higgins, W. E. Ernst, K. K. Lehmann, and G. Scoles. Spin-orbit effects in the formation of the Na-He excimer on the surface of He clusters. *Faraday Discussions*, 108:161–174, 1997.

- [223] C. Callegari, J. Higgins, F. Stienkemeier, and G. Scoles. Beam depletion spectroscopy of alkali atoms (Li, Na, K) attached to highly quantum clusters. *Journal of Physical Chemistry A*, 102(1):95–101, 1998.
- [224] U. Kleinekathöfer, M. Lewerenz, and M. Mladenović. Long range binding in alkali-helium pairs. *Physical Review Letters*, 83(23):4717–4720, 1999.
- [225] K. T. Tang and J. P. Toennies. The van der Waals potentials between all the rare gas atoms from He to Rn. *Journal of Chemical Physics*, 118(11):4976–4983, 2003.
- [226] K. E. Kürten and M. L. Ristig. Atomic impurities in liquid helium. *Physical Review B*, 27(9):5479–5485, 1983.
- [227] R. N. Barnett and K. B. Whaley. Molecules in helium clusters: SF₆He_N. *Journal of Chemical Physics*, 99(12):9730–9744, 1993.
- [228] A. Viel and K. B. Whaley. Quantum structure and rotational dynamics of HCN in helium clusters. *Journal of Chemical Physics*, 115(22):10186–10198, 2001.
- [229] F. Paesani, F. A. Gianturco, and K. B. Whaley. Microsolvation and vibrational shifts of OCS in helium clusters. *Journal of Chemical Physics*, 115(22):10225–10238, 2001.
- [230] M. Mella, M. C. Colombo, and G. Morosi. Ground state and excitation dynamics in Ag doped helium clusters. *Journal of Chemical Physics*, 117(21):9695–9702, 2002.
- [231] V. A. Apkarian and N. Schwentner. Molecular photodynamics in rare gas solids. *Chemical Reviews*, 99(6):1481–1514, 1999.
- [232] Q. Li and J. R. Huber. The photodissociation of ClNO₂ in argon and water clusters studied at 235 nm by the REMPI-TOF method. *Chemical Physics Letters*, 354(1-2):120–127, 2002.
- [233] C. Cohen-Tannoudji, B. Diu, and F. Laloë. *Quantum Mechanics*, volume 1. Wiley, New York, 1990.
- [234] N. Pörtner, A. F. Vilesov, and M. Havenith. Spontaneous alignment of tetracene molecules in ⁴He droplets. *Chemical Physics Letters*, 368(3-4):458–464, 2003.
- [235] Y. Jiang, M. R. Giorgiarnazzi, and R. B. Bernstein. Concurrent photodissociation and multiphoton ionization processes in CH₃I from 266–307 nm. *Chemical Physics*, 106(1):171–178, 1986.
- [236] K. R. Atkins. Ions in liquid helium. *Physical Review*, 116(6):1339–1343, 1959.
- [237] S. P. Sapers, V. Vaida, and R. Naaman. Multiphoton ionization study of intramolecular and intermolecular effects on the photodissociation of methyl iodide. *Journal of Chemical Physics*, 88(6):3638–3645, 1988.

- [238] Y. K. Choi, Y. M. Koo, and K. W. Jung. Multiphoton ionization and fragmentation processes of methyl iodide clusters at 266 and 355 nm. *Journal of Photochemistry and Photobiology A: Chemistry*, 127(1-3):1–5, 1999.
- [239] J. Park, N. Shafer, and R. Bersohn. The time evolution of the velocity distribution of hydrogen atoms in a bath gas. *Journal of Chemical Physics*, 91(12):7861–7871, 1989.
- [240] G. Nan and P. L. Houston. Velocity relaxation of $S(1D)$ by rare gases measured by Doppler spectroscopy. *Journal of Chemical Physics*, 97(11):7865–7872, 1992.
- [241] M. Baba, M. Brouard, S. P. Rayner, and J. P. Simons. Elastic scattering dynamics of translationally and rotationally aligned molecular fragments via Doppler-resolved laser spectroscopy. $\text{OH}(X^2\Pi_{3/2})+\text{Ar}/\text{He}$. *Chemical Physics Letters*, 220(6):411–416, 1994.
- [242] Y. Matsumi, S. M. Shamsuddin, Y. Sato, and M. Kawasaki. Velocity relaxation of hot $\text{O}(1D)$ atoms by collisions with rare gases, N_2 , and O_2 . *Journal of Chemical Physics*, 101(11):9610–9618, 1994.
- [243] H. Partridge, J. R. Stallcop, and E. Levin. Potential energy curves and transport properties for the interaction of He with other ground-state atoms. *Journal of Chemical Physics*, 115(14):6471–6488, 2001.
- [244] M. P. de Lara-Castells, R. V. Krems, A. A. Buchachenko, G. Delgado-Barrio, and P. Villarreal. Complete basis set extrapolation limit for electronic structure calculations: Energetic and nonenergetic properties of HeBr and HeBr₂ van der Waals dimers. *Journal of Chemical Physics*, 115(22):10438–10449, 2001.
- [245] R. Burcl, R. V. Krems, A. A. Buchachenko, M. M. Szczeniński, G. Chałasiński, and S. M. Cybulski. $\text{RG}+\text{Cl}(2P)$ ($\text{RG} = \text{He}, \text{Ne}, \text{Ar}$) interactions: Ab initio potentials and collision properties. *Journal of Chemical Physics*, 109(6):2144–2154, 1998.
- [246] P. Casavecchia, G. He, R. K. Sparks, and Y. T. Lee. Interaction potentials for $\text{Br}(2P) + \text{Ar}, \text{Kr},$ and $\text{Xe}(1S)$ by the crossed molecular beams method. *Journal of Chemical Physics*, 75(2):710–721, 1981.
- [247] R. J. Donovan and D. Husain. Electronically excited iodine atoms. Part 2. $\text{I}(5^2P_{1/2})$ in the photolysis of hydrogen iodide. *Transactions of the Faraday Society*, 62:1050–1055, 1966.
- [248] D. Husain and R. J. Donovan. Electronically excited halogen atoms. *Advances in Photochemistry*, 8:1–75, 1971.
- [249] L. E. Brus and V. E. Bondybey. Cage effects and steric hindrance in van der Waals solids, with application to alkyl iodide photolysis in rare gas hosts. *Journal of Chemical Physics*, 65(1):71–76, 1976.
- [250] G. Marsaglia and A. Zaman. Toward a universal random number generator. Technical Report FSU-SCRI-87-50, Florida State University, 1987.

- [251] J. I. Cline, C. A. Taatjes, and S. R. Leone. Diode laser probing of I^* ($^2P_{1/2}$) Doppler profiles: Time evolution of a fast, anisotropic velocity distribution in a thermal bath. *Journal of Chemical Physics*, 93(9):6543–6553, 1990.
- [252] A. E. Bruno, U. Brühlmann, and J. R. Huber. Photofragmentation LIF spectroscopy of NOCl at dissociation wavelengths > 450 nm. Parent electronic spectrum and spin state and Λ -doublet populations of nascent NO and Cl fragments. *Chemical Physics*, 120(1):155–167, 1988.
- [253] A. Ogai, C. X. W. Qian, L. Iwata, and H. Reisler. Photodissociation dynamics of NOCl: State-specific Λ -doublet ratios in the $^2\Pi_{1/2}$ and $^2\Pi_{3/2}$ states of NO. *Chemical Physics Letters*, 146(5):367–374, 1988.
- [254] A. Ticktin, A. E. Bruno, U. Brühlmann, and J. R. Huber. NO($X^2\Pi$) rotational distributions from the photodissociation of NOCl and NOBr at 450 and 470 nm. *Chemical Physics*, 125(2-3):403–413, 1988.
- [255] A. Ogai, C. X. W. Qian, and H. Reisler. Photodissociation dynamics of jet-cooled ClNO on S_1 ($1^1A''$): An experimental study. *Journal of Chemical Physics*, 93(2):1107–1115, 1990.
- [256] A. Untch, K. Weide, and R. Schinke. The direct photodissociation of ClNO(S_1): An exact three-dimensional wave packet analysis. *Journal of Chemical Physics*, 95(9):6496–6507, 1991.
- [257] J. Y. Cao, Y. F. Wang, and C. X. W. Qian. Product fine structure state populations and nonadiabatic dissociation dynamics: Cl^* ($^2P_{1/2}$)/ Cl ($^2P_{3/2}$) branching ratio in the visible and near ultraviolet photodissociation of nitrosyl chloride. *Journal of Chemical Physics*, 103(22):9653–9660, 1995.
- [258] R. Engleman, Jr. and P. E. Rouse. The β and γ bands of nitric oxide observed during the flash photolysis of nitrosyl chloride. *Journal of Molecular Spectroscopy*, 37(2):240–251, 1971.
- [259] H. Zacharias, R. Schmiedl, and K. H. Welge. State selective step-wise photoionization of NO with mass spectroscopic ion detection. *Applied Physics*, 21(2):127–133, 1980.
- [260] W. G. Mallard, J. H. Miller, and K. C. Smyth. Resonantly enhanced two-photon photoionization of NO in an atmospheric flame. *Journal of Chemical Physics*, 76(7):3483–3492, 1982.
- [261] A. A. Buchachenko, R. V. Krems, M. M. Szczyński, Y. D. Xiao, L. A. Viehland, and G. Chałasiński. Collision and transport properties of $Rg+Cl(^2P)$ and $Rg+Cl(^1S)$ ($Rg = Ar, Kr$) from ab initio potentials. *Journal of Chemical Physics*, 114(22):9919–9928, 2001.

- [262] J. Kłos, G. Chałasiński, M. T. Berry, R. Bukowski, and S. M. Cybulski. Ab initio potential-energy surface for the $\text{He}(^1S) + \text{NO}(X^2\Pi)$ interaction and bound rovibrational states. *Journal of Chemical Physics*, 112(5):2195–2203, 2000.
- [263] M. H. Alexander, P. Soldán, T. G. Wright, Y. S. Kim, H. Meyer, P. J. Dagdigian, and E. P. F. Lee. The $\text{NO}(X^2\Pi)$ –Ne complex. II. investigation of the lower bound states based on new potential energy surfaces. *Journal of Chemical Physics*, 114(13):5588–5597, 2001.
- [264] M. H. Alexander. A new, fully ab initio investigation of the $\text{NO}(X^2\Pi)$ Ar system. I. Potential energy surfaces and inelastic scattering. *Journal of Chemical Physics*, 111(16):7426–7434, 1999.
- [265] Y. Kim and H. Meyer. Multiphoton spectroscopy of NO–Rg (Rg = rare gas) van der Waals systems. *International Reviews in Physical Chemistry*, 20(3):219–282, 2001.
- [266] F. Ancilotto, E. Cheng, M. W. Cole, and F. Toigo. The binding of alkali atoms to the surfaces of liquid helium and hydrogen. *Zeitschrift für Physik B*, 98(3):323–329, 1995.
- [267] A. Nakayama and K. Yamashita. Path integral Monte Carlo study on the structure and absorption spectra of alkali atoms (Li, Na, K) attached to superfluid helium clusters. *Journal of Chemical Physics*, 114(2):780–791, 2001.
- [268] D. S. Peterka, A. Lindinger, L. Poisson, M. Ahmed, and D. M. Neumark. Photoelectron imaging of helium droplets. *Physical Review Letters*, 91(4):3401, 2003.
- [269] F. Ancilotto, M. Barranco, and M. Pi. Probing vortices in ^4He nanodroplets. *Physical Review Letters*, 91(10):5302, 2003.
- [270] G. M. Lankhuijzen and L. D. Noordam. Atomic streak camera. *Optics Communications*, 129(5-6):361–368, 1996.
- [271] J. Aitchison and J. A. C. Brown. *The Lognormal Distribution*, volume 5 of *Department of Applied Economics Monographs*. Cambridge University Press, Cambridge, 1957.
- [272] A. L. Koch. The logarithm in biology. 1. Mechanisms generating the log-normal distribution exactly. *Journal of Theoretical Biology*, 12(2):276–290, 1966.
- [273] Eric W. Hansen. Fast Hankel transform algorithm. *IEEE Transactions on Acoustics, Speech, and Signal Processing*, 33(3):666–671, 1985.
- [274] L. Montgomery Smith and Dennis R. Keefer. Abel inversion using transform techniques. *Journal of Quantitative Spectroscopy and Radiative Transfer*, 39(5):367–373, 1988.
- [275] J. W. Cooley and J. W. Tukey. An algorithm for the machine computation of the complex fourier series. *Mathematics of Computation*, 19:297–301, 1965.
- [276] V. Dribinski, A. Ossadtchi, V. A. Mandelshtam, and H. Reisler. Reconstruction of abel-transformable images: The gaussian basis-set expansion abel transform method. *Review of Scientific Instruments*, 73(7):2634–2642, 2002.

- [277] S. M. Candel. An algorithm for the Fourier-Bessel transform. *Computer Physics Communications*, 23:343–353, 1981.
- [278] M. J. Bass, M. Brouard, A. P. Clark, and C. Vallance. Fourier moment analysis of velocity-map ion images. *Journal of Chemical Physics*, 117(19):8723–8735, 2002.
- [279] H. Ockendon and J. R. Ockendon. *Viscous Flow*. Cambridge University Press, Cambridge, 1995.
- [280] S. S. Batsanov. Van der Waals radii of elements. *Inorganic Materials*, 37(9):871–885, 2001.
- [281] H. Goldstein. *Classical Mechanics*. Addison-Wesley, Reading, Massachusetts, 2nd edition, 1980.
- [282] L. D. Landau and E. M. Lifshitz. *Mechanics*. Pergamon, Oxford, 1976.

Acknowledgements

I would like to express my sincere gratitude to the people mentioned below. In many ways they all have made valuable contributions to this thesis work.

Dr. Marcel Drabbels, my advisor, who developed the helium droplet project, for prompt assistance, the sharing of scientific experience as well as his encouragement and cheerful company in and outside the lab.

Prof. Tom Rizzo for accepting me as a graduate student in the LCPM group and for providing an outstanding scientific environment.

The members of the mechanical workshop, most notably *Jean-Luc Passard* and *André Fattet*, for rapid and reliable advice, high-quality work, and countless machining hours.

Gabriel Roch and *Olivier Noverraz* from the electronic workshop for their technical assistance and many useful “boxes”.

Prof. Majed Chergui, *Prof. Ursula Röthlisberger*, *PD Dr. Alkwin Slenczka*, and *Prof. Jan Peter Toennies* for serving on the thesis examination committee.

Dr. Aziz Kasimov for assistance in the lab as well as teaching me about bulk liquid helium.

Dr. Rainer Beck, *Dr. Oleg Boiarkine*, *Richard Bossart*, *Cédric Bovet*, *Christelle Cardon*, *Rachele Chianese*, *Thanh Tung Dang*, *Prof. Tino Gäumann*, *Anthi Kamariotis*, *Dr. Monika Kowalczyk*, *Dr. Joachim Makowe*, *Pavel Maksyutenko*, *Sébastien Mercier*, *Antoine Milon*, *Dr. Dimitrios Papageorgopoulos*, *Mikhail Polianski*, *Dr. Julia Rebstein*, *Dr. David Rueda*, *Amanz Ruf*, *Marco Sacchi*, *Dr. Mathieu Schmid*, past and present members of the LCPM, for the enjoyable atmosphere and fruitful discussions.

Our secretary *Marianne Dang* for caring beyond administrative matters.

My former and current flatmates *Dr. Patrice Theulé*, *Plinio Maroni* and *Evgeniy Loginov* for fun and friendship.

My friends and family for their love and support.

CURRICULUM VITAE

- 1999-2004 ECOLE POLYTECHNIQUE FÉDÉRALE DE LAUSANNE
Ph.D. in physical chemistry with Dr. M. Drabbels and Prof. Dr. Th. Rizzo
Photodissociation studies of CH₃I and CF₃I in fluid ⁴He nanodroplets
- 1997-1999 FRITZ-HABER INSTITUT DER MAX-PLANCK-GESELLSCHAFT, BERLIN
Diploma work in physical chemistry with Prof. Dr. H.-J. Freund
Laser desorption of NO from nickel oxide surfaces
- 1996-1999 FREIE UNIVERSITÄT BERLIN
Studies leading to the diploma in physics
Options in environmental management and meteorology
- 1995-1996 UNIVERSITY OF EDINBURGH, UK
Studies in computational and atmospheric physics
- 1992-1995 GEORG-AUGUST-UNIVERSITÄT, GÖTTINGEN, GERMANY
Undergraduate studies
- 1991 WIGBERT GYMNASIUM, HÜNFELD, GERMANY
Abitur